TSUNAMIS PROVOKED BY FAST GRANULAR LANDSLIDES: 3D LABORATORY EXPERIMENTS ON GENERATION AND INITIAL PROPAGATION OF WAVES

by

Francesco Bregoli

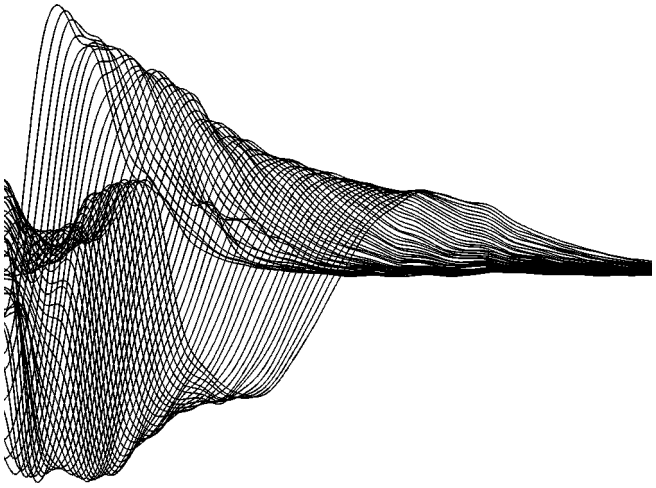

DOCTORATE in CIVIL ENGINEERING

UNIVERSITAT POLITÈCNICA DE CATALUNYA

GRUP D'INVESTIGACIÓ EN MODELITZACIÓ DE CONQUES I TRANSPORT DE SEDIMENTS

Supervisor: Prof. Dr. Allen Bateman Pinzón

Co-supervisor: Dr. Vicente Medina Iglesias

Barcelona,

September 2015

Funded by: UNIVERSITAT POLITÈCNICA DE CATALUNYA BARCELONATECH · GOBIERNO DE ESPAÑA · MINISTERIO DE EDUCACIÓN, CULTURA Y DEPORTE

A mio nonno

Abstract

Landslides and debris flows falling into reservoirs, natural lakes, fjords or seas can generate impulsive waves, which can be assimilated to tsunamis. This phenomenon, also known as "landslide tsunami", can be highly destructive with respect to dams, other structures and infrastructures as well as to people living along shorelines.

The aftermath observation of destructive past events, such as the Vajont Dam in Italy (1963), is not enough to describe and finally to furnish sufficient information to help in adequately preventing the recurrence of the phenomenon. Several authors have carried out experimental studies on the topic in straight channels and wave basins with different landslide generators. Due to the lack of studies on the effects of granular landslides falling in a basin, and in order to explore new ranges of governing parameters for further experiments, the present research work was conceived and undertaken.

To this effect, a facility to study that phenomenon was set up in the fluvial-morphodynamics laboratory of the Technical University of Catalonia. The system consists of a steep-slope flume releasing granular material in a wave basin. To achieve a high-speed mass movement, a metallic wheeled box was designed and built, sliding along the flume over rails having a very low surface roughness. The box, filled with gravel, accelerates down the slope. At the end of the run the box's flaps open to launch the granular material into the wave basin. A system was designed to be able to measure the high velocity and the geometry of the sliding mass. It employs the treatment of images captured by a high-speed camera which records the granular material at entry into the water. A grid on the water surface was set up employing laser sheets. Thus, by filming the water surface at impact and successively processing the resulting images, it was possible to accurately measure the produced waves.

In the present work a number of 41 experiments, changing the main governing parameters, were carried out. The analysis of the experimental results has permitted to define empirical relationships between the landslides parameters and the produced wave amplitude, propagation and energy, as a tool useful for risk assessment. The empirical relationships were successfully tested on two real events: the Vajont Dam (Italy, 1963) and the Chehalis Lake (Canada, 2007).

Particularly, the transfer of energy between landslide and water waves was examined. A newel 1D forward Euler model, including the 3D landslide deformations, was created with the aim of measuring the mentioned energy transfer. The result shows that about 52% of the landside energy is dissipated by Coulomb basal friction, about 42% is dissipated by other processes (mainly turbulence) and only the remaining 6% is transferred to the wave train thus formed.

Resumen

Cuando un deslizamiento o un flujo de detritos con elevada velocidad entra en un embalse, un lago, un fiordo o en el mar, se pueden generar una serie de olas de impulso que se definen como una tipología de tsunami. Este fenómeno puede ser extremamente destructivo, afectando a población, presas y cualquier tipo de estructura que se encuentre en la proximidad de las orillas.

Los análisis a posteriori de desastrosos eventos históricos, como el caso del embalse del Vajont en Italia (1963), no son suficientes para describir y prevenir el fenómeno. Por estos motivos, varios autores han conducido experimentos sobre olas de impulso usando diferentes generadores de deslizamientos. Debido a la escasez de experimentos sobre el efecto de la entrada de deslizamientos granulares en un tanque de oleaje, y para explorar un rango más amplio de los parámetros involucrados, se ha planteado el presente trabajo de investigación.

En el laboratorio de morfodinámica fluvial de la Universitat Politècnica de Catalunya, se ha instalado un nuevo dispositivo experimental utilizando un canal de alta pendiente que descarga en un tanque de oleaje. Para reproducir adecuadamente el fenómeno, se ha desarrollado un sistema capaz de acelerar la masa granular construyendo un carro de acero con ruedas encajadas en unos raíles montados sobre el canal de alta pendiente. El carro, cargado de grava, acelera durante la bajada. Sus puertas se abren al final del recorrido lanzando el material granular en el tanque. La velocidad y geometría del deslizamiento se han medido a través del procesado de imágenes procedentes de una cámara de fotos de alta velocidad de toma. Para medir las olas producidas, se ha instalado un sistema de planos láseres incidentes sobre la superficie del agua, creando una malla de líneas. Filmando la malla y posteriormente tratando las imágenes, se pudieron medir las olas producidas.

Se han realizado 41 experimentos, cambiando los principales parámetros de gobierno del proceso. El análisis experimental ha permitido definir relaciones empíricas entre los parámetros del deslizamiento y la amplitud, propagación y energía de las olas producidas, como herramientas útiles para la evaluación del riesgo. Las fórmulas empíricas se han aplicado satisfactoriamente a dos casos reales: el embalse de Vajont (Italia, 1963) y el lago Chehalis (Canadá, 2007).

En particular, con el objetivo de cuantificar la conversión de energía desde el deslizamiento hasta las olas, se ha creado un nuevo modelo numérico. El resultado muestra que la energía del deslizamiento viene disipada de un 52% por fricción basal y de un 42% por otros procesos (principalmente turbulencia). Solamente el 6% restante se transfiere a la serie de olas.

Resum

Quan una esllavissada o una corrent d'arrossegalls entra a gran velocitat en un embassament, en un llac, en un fiord, o al mar, es poden generar una sèrie d'onades d'impuls que es defineixen com a una tipologia de tsunami. Aquest fenomen, conegut com a "landslide tsunami", pot ser extremadament destructiu, afectant a població, preses, o qualsevol tipus d'estructura que es trobi a la proximitat de les ribes.

Els anàlisis a posteriori de desastrosos esdeveniments històrics, com el de l'embassament de Vajont a Itàlia (1963), no són suficients per descriure i preveure adequadament el fenomen. Per aquesta raó, varis autors han dirigit experiments sobre onades d'impuls en canals rectilinis o en dipòsits d'aigua utilitzant diferents generadors de esllavissades. Degut a l'escassetat d'estudis sobre els efectes de l'entrada de material granular en un dipòsit, i a causa de la necessitat d'explorar un rang més ampli dels paràmetres involucrats, s'ha plantejat el present treball d'investigació.

En el laboratori de morfo-dinàmica fluvial de la Universitat Politècnica de Catalunya, s'ha instal·lat un nou sistema per estudiar el fenomen. La instal·lació consta d'un canal amb pendent acusada que descarrega en un dipòsit d'aigua. Per accelerar suficientment la massa granular, s'ha construït un carro d'acer amb rodes que llisca sobre uns rails fixats al canal. El carro, omplert de grava, accelera en la baixada. Les seves portes s'obren al final del recorregut llençant la grava al dipòsit. Es va definir un sistema capaç de mesurar la velocitat i la geometria del material granular a través del processament d'imatges procedents d'una càmera de fotografiar d'alta velocitat de tir. Finalment, es va instal·lar un sistema de plans làser incidents sobre la superfície d'aigua, creant una malla de línies. Filmant la malla i tractant posteriorment les imatges, es van poder mesurar les onades produïdes.

En el present treball es van realitzar 41 experiments, canviant cada vegada els principals paràmetres de govern del procés. L'anàlisi experimental ha permès definir relacions empíriques entre els paràmetres de la esllavissada i l'amplitud, propagació i energia de les onades produïdes com eina útil per l'avaluació del risc associat. Les relacions empíriques s'han aplicat satisfactòriament a dos casos reals: l' embassament de Vajont (Itàlia, 1963) i el llac Chehalis (Canada, 2007).

En particular, amb l'objectiu d'analitzar la conversió d'energia des de la esllavissada fins a les onades, s'ha creat un nou model numèric. El resultat demostra que l'energia del lliscament ve dissipada de un 52% per fricció basal i de un 42% per altres processos dissipatius (principalment la turbulència). Tan sols el 6% restant es transfereix a les onades.

Preface

The research reported in this document was carried out in the Sediment Transport Research Group (GITS) of the Department of Hydraulic, Marine and Environmental Engineering in the Technical University of Catalonia (UPC), between 2011 and 2015.

The dissertation is the result of my own work and the scientific discussions held with my supervisors, Prof. Allen Bateman and Dr. Vicente Medina, who are both members of the GITS research group, as well as Prof. Hermann Fritz of the Georgia Institute of Technology, with whom I spent 3 months of internship as part of my PhD program.

Manuel Rast, supported by his advisors of ETH-VAW of Zurich, crucially helped us in the initial set-up during his internship in the aforementioned laboratory of the UPC.

Partial contents of chapters 2 and 3 have been presented in 4 international congresses and 1 seminar listed below in chronological order:

Bateman, A., Bregoli, F., Medina, V. & Rast, M. (2011), Setup of an experimental device for high-speed debris flows generating 2D impulse waves *in* 'RCEM 2011: Proceedings of the 7th IAHR Symposium of River, Coastal and Estuarine Morphodynamics', pp. 841-852, Tsinghua University Press (Ed.), Beijing;

Bregoli, F., Bateman, A. & Medina, V. (2012), High-speed debris-flows generating 2D impulse waves: experimental analysis *in* 'River Flow 2012 - Proceedings of the International Conference on Fluvial Hydraulics, San José, Costa Rica', pp. 987-991, Murillo, R. (Ed.), Taylor & Francis Group, London, 2012;

Bregoli, F. Bateman, A. & Medina, V. (2012), Olas de impulsión generadas por corrientes de detritos rápidas: estudio experimental, *in* 'XXV Congreso Latinoamericano de Hidráulica, San José, Costa Rica', Murillo, R. (Ed.);

Bregoli, F., Bateman, A., Medina, V. & Gomez, D. R. (2013), Experimental studies on 3D impulse waves generated by rapid landslides and debris flows, *in* 'Italian Journal of Engineering Geology and Environment, Proceedings of the International Conference on Vajont - 1963-2013 - Thoughts and analyses after 50 years since the catastrophic landslide, Padua, Italy', pp. 115-122, Genevois, A. P. (Ed.);

Bregoli, F., Overview of activities carried out at BarcelonaTech. Focus on 3D tsunami waves generated by granular landslides, Environmental Fluid Mechanics and Water Resource Seminar, 14/3/2014, School of Civil and Environmental Engineering, Georgia Institute of Technology, Atlanta (US).

Chapter 4 is an edited version of an article planned to be submitted to the Journal of Hydraulic Research.

Chapter 5 is an edited version of an article planned to be submitted to the Journal of Geophysical Research.

All experimental work was carried out by myself in the laboratories of the aforementioned Department, with the help of Prof. Allen Bateman and Dr. Vicente Medina. Moreover, Clara Bentz, Victor de Cagny and Louis Dussarps, three internship students of ParisTech, and Eudald Bonet, undergraduate student of (UPC), assisted me during the laboratory activity.

Table of contents

List of Tables

List of Figures

List of Symbols

Variable	Description
a	wave amplitude of the first crest
a_d	major axis of the final deposit of the landslide
a_e	major axis of the elliptical wave front
a_{max}	maximum wave amplitude
a_{sol}	amplitude, or height, of solitary wave
$a_{sol,0}$	initial amplitude, or height, of solitary wave
A_d	basal area of the final deposit of the landslide
b_d	minor axis of the final deposit of the landslide
b_e	minor axis of the elliptical wave front
c	wave celerity
C	centroid of landslide
C_d	landslide drag coefficient
c_{sol}	solitary wave's celerity
d_{16}	grain diameter associated with the 16^{th} percentile of the particle size distribution
d_{30}	grain diameter associated with the 30^{th} percentile of the particle size distribution
d_{50}	median grain diameter of the sliding material
d_{84}	grain diameter associated with the 84^{th} percentile of the particle size distribution
d_{90}	grain diameter associated with the 90^{th} percentile of the particle size distribution
d_m	mean grain diameter of the sliding material
d_{max}	maximum grain diameter of the sliding material
d_{min}	minimum grain diameter of the sliding material
D	distance of the landslide final deposit's farthest grain
e	eccentricity of the elliptical wave's front

Variable	Description
E_d	total energy of drag transferred to the water body
E_f	total dissipated energy by means of basal friction
E_s	total landslide energy
$E_{s,kin}$	landslide kinetic energy
$E_{s,pot}$	landslide potential energy
E_t	total dissipated energy of turbulence at water - granular material boundaries
E_w	total wave first crest energy
$E_{w,kin}$	wave first crest kinetic energy
$E_{w,pot}$	wave first crest potential energy
$E_{w,hydrostatic}$	hydrostatic energy of still water
f	focus of the elliptical wave front
F_c	Coulomb forces at landslide bottom
F_d	landslide drag force
Fr	Froude number of landslide
g	gravity
h	wave height
h_s	average thickness of the landslide
h_w	water depth in the basin
k	parameters of empirical relationships
l	wavelength
L	water tank length
l_{1c}	length of the 1st crest of the wave
l_s	length of the landslide
$l_{s,ini}$	initial length of the landslide

Variable	Description
M	total mass of granular material per unit width
m_s	mass of the sliding material
m'_s	submerged mass of the sliding material
n	ratio between axes of the elliptical wave front
O	order of lowpass digital Butterworth filters
p	percentage of η of initiation of wave reflection
p_{front}	percentage of η of initiation of front wave reflection
p_{lat}	percentage of η of initiation of lateral wave reflection
P_1	wave first up-crossing point
P_2	wave first down-crossing point
P_3	wave second up-crossing point
P_t	power of turbulences at water - granular material boundaries
r	momentum of granular material per width unit
Re	impulsive Reynolds number
Re^*	Reynolds number of grain
Ru	Run-up
s_b	basal area of landslide
s_{front}	frontal area of landslide
t	elapsed time from impact
t_{max}	time of maximum wave amplitude
t_{splash}	elapsed time from impact to splash exhaustion
t_{stop}	elapsed time from impact to landslide stop
v_s	velocity of the landslide
V_s	volume of the landslide

Variable	Description
V_w	volume of 1st crest of the wave
W	water tank width
w_c	cutoff normalized frequency in low-pass digital Butterworth filters
We	impulsive Weber number
w_s	width of landslide
x	distance from impact along sliding direction
x_{max}	distance of maximum wave amplitude
$\underset{\sim}{x}$	landslide propagation path
$\underset{\sim}{x}_{stop}$	distance of landslide stop along the propagation path (runout)
y	lateral distance from sliding direction
$z_{s,c}$	landslide drop height referred to the centroid of mass
α	impact angle
β	angular wave direction
γ	run-up slope
δ	relative error of landslide run-out distance
η	water surface displacement
η_{ref}	water surface displacement, corresponding to the initiation of reflection
$\eta_{ref,front}$	water surface displacement, corresponding to the initiation of frontal wave reflection
$\eta_{ref,lat}$	water surface displacement, corresponding to the initiation of lateral wave reflection
θ_s	porosity of the granular material
μ_w	dynamic viscosity of water
μ_m	sliding friction coefficient for mass point model
ν_w	kinematic viscosity of water

Variable	Description
ξ	turbulence coefficient or “mass-to-drag ratio” for mass point model
ρ_s	density of landslide rock
$\rho_{s,bulk}$	bulk density of landslide
$\rho_{s,bulk,sat}$	saturated bulk density of landslide
$\rho'_{s,bulk,sat}$	submerged saturated bulk density of landslide
ρ_w	density of water
σ_w	surface tension of water
τ	Coulomb shear stress
φ_s	internal friction angle of the granular material
$\varphi_{s\text{-}b}$	basal friction angle between granular material and bottom of slope

List of Abbreviations

ALE FEM	Arbitrary Lagrangian-Eulerian Finite Element Method
AOI	Area Of Interest of images for the High Speed camera
asl	Above the sea level
CFD-DEM	Computational Fluid Dynamics / Discrete Element Method model
CMOS	Complementary Metal–Oxide–Semiconductor image sensor
DLT	Direct Linear Transformation
ENEL	Ente Nazionale per l'Energia Elettrica
FEM	Finite Element Method
GITS	Grupo de Investigación en Transporte de Sedimentos (Sediment Transport Research Group)
GT	Georgia Institute of Technology (GeorgiaTech)
HD	High Definition
HS	High Speed
MSE	Mean Squared Error
openFOAM	Open source Field Operation And Manipulation: computational fluid dynamics, simulation software
PIV	Particle Image Velocimetry
STD	Standard Deviation
UPC	Universitat Politècnica de Catalunya - BarcelonaTech
USGS	U.S. Geological Survey

Acknowledgements

Throughout my doctoral studies I have been encouraged by many people. I would like to thank all of them for the great support I have received.

First and foremost I am pleased to express my deepest gratitude to my supervisor and director of the GITS team Prof. Allen Bateman, who pulls me towards the research world. I have spent wonderful years with him learning, travelling and always trying to solve mysteries of hydraulics no matter being in or out the lab or in a jungle of Central America!

Dr. Vicente Medina has been the handyman-co-supervisor of my investigations. Are you short of ideas? Ask him a question, you will receive an answer! Are you programming and do not know how to do? Give him a problem, you will have a solution! Are you lost in Barcelona? Ask him a direction and you cannot be wrong. Do not expect the answer before 24:00; he is mostly active during night! Thanks Vicente!

I would like to address a special gratitude to Prof. Hermann Fritz, who hosts me for three months in his office down in the GeorgiaTech campus. He has been a guide and a reference during and after my internship over there. I cannot forget the interesting and essential conversations, not only about landslide tsunamis, we had on the 5th floor in front of a large coffee.

I want to kindly thank the team of the VAW-ETH laboratory of Zurich, and especially Mr. Manuel Rast, for the cooperation and the initial set-up of the experimental device. Without his help this thesis would have been not initiated.

Throughout these years at the Department of Hydraulic Engineering of the UPC I have had the pleasure of sharing exciting moments with extraordinary people. I have already mentioned Allen Bateman and Vicente Medina, now is the turn of Dr. Guillaume Chevalier. *Chevalier* by name and by nature, he has been always present helping me in the geological and Shakespearian side of the duty. With him I spent days in the field looking for debris flows and other kind of flows. He is not only a schoolmate but a friend!

How forget the other members of the GITSian community: *ironman* Dr. Alberto Herrero, the *ironmother* Doctora Anna Mujal and the *parce* - and soon Doctor - Andres Diaz with whom I sheared memorable moments in office, lab and some hidden parts of *Latinoamerica*. They have been together with Allen, Vicente, Guillaume, Khaled Hamad and Cristina Fernandez the most heterogenic, and at the same time bracing, team I have ever been involved.

La Doctora Anaïs Ramos has been a unique companion with whom I have shared an unforgettable part of my life. She has been always willing to push me forward wisely with her strong sense of honesty and perseverance.

Dr. Fabio Ciervo of CUGRI (Salerno, Italy) has been a great mate since he came in our office in Barcelona. We have tackled together some of the more stochastic problems in flows from the Catalonian city to the peak of Jebel Toubkal.

I want to address a special thanks to Alba Mellado, Francisco Nuñez, Sergi Capapé, Gonzalo Olivares and Anna Maria Obando, colleagues of my department with whom I have shared days in and outside the campus.

I would like to thanks the students Clara Bentz, Victor de Cagny and Louis Dussarps from ParisTech, and Eudald Bonet from UPC. They all spent a trainee period, seriously helping me in the shadows of the laboratory.

Some months ago I was thinking about who can help me in proofreading this large manuscript. I needed a person with perfect English, some knowledge in technology and in natural hazards. Once I summed these characteristics I saw only one solution: my uncle Franco. Thanks so much *zio* Franco for your immeasurable help. You not only review my English but you struggle to fully understand the contents of this thesis. This is the best way to proofreading.

My life in Barcelona has been pleasant thanks to the many friends I have been the pleasure to meet. I cannot mention all of them. But certainly I want to thanks for the company the member of my football team Lleida3 with whom I won many "cups". I address a huge gratitude to *el capitá* Toni who open twice the doors of his house to host me. He is a great friend more than the perfect housemate.

I would like to give a special thanks to Gemma to bear me in the long and worm days of the thesis typing, when one can certainly lost a part of social interaction. She helps me in the Catalan side of this thesis. But this is the minor act. Instead, she has been always present in the last months and I cannot find an appropriate word to say thanks to her.

Among the Catalan friends there is a special one, the girl that convinces me to land in Barcelona back in 2007: Eva. She has been the first guide and companion of life for the first years. I will never forget that.

Last but not least the greatest thanks are for my family. My father transmits to me the serenity of the greatest men, my mother the strength of the women that never give up. I know that it is not easy to have a son far away but they have always supporting me from the other side of Mediterranean See. The last words are for the origins: the grandparents. Special thanks are for

my tireless *nonna* Bruna, my polyglot *nonna* Noemi, literally a font of knowledge, and my *nonno* Virio, who has recently passed away. I will never forget his teachings on the backyard of his house.

This thesis was funded by the 4 years grant FPU2009 of the Spanish Ministry of Education.

The laboratory set-up was founded by the 3 year Spanish national project DEBRIS FLOW (CGL 2009-13039) of the Spanish Ministry of Education.

Chapter 1: Introduction

This introductive chapter contains the problem description of landslide tsunamis, a detailed review of historical events, followed by the motivations that drove the present doctoral thesis. The chapter continues with the current state-of-the-art related to the topic. After identifying gaps in past researches, the objectives of the thesis are exposed.

1.1 Landslide tsunamis

The word “tsunami”, literally “harbor wave” in Japanese, is generally associated with a destructive set of giant gravity waves provoked by large mass movements.

In common parlance, the source of a tsunami is often associated with submarine earthquakes, due to their considerably high destructivity. However, a tsunami can be potentially triggered by any other mass movement able to displace a large mass of water.

A specific tsunami can be created when a sufficient quantity of solid, or liquid and solid mixture, slides into or through a reservoir, a natural lake, a fjord, a river or the sea. The momentum of the sliding mass is transferred to the mass of water, turning the latter into a set of giant waves able to travel relatively large distances.

This particular phenomenon, known within the scientific community as "impulse waves" (Kamphuis & Bowering, 1970) or “landslide tsunamis” (Mader, 1999; Ward, 2001) or displacement wave (Hermanns et al., 2013), can be highly destructive and unlikely to be predicted, as witnessed by past events in which thousands of people perished (see Table 1.1).

The term "landslide" in "landslide tsunami" follows the definition of Cruden (1991) and is commonly referred to any sliding process as landslides, rock falls, rock avalanches, debris flows, pyroclastic flows, lava, ice calving or snow avalanches. Therefore the tsunamigenic landslide can be composed by blocks or loose granular material with different density and with the presence or absence of water at the basis of its formation.

The initial configuration of landslides such as can provoke a tsunami could be one of those mentioned in the following list (Fritz, 2002).

- Sub-aerial landslide: a landslide starting on a certain elevation over the water surface;
- partially submerged landslide: a landslide starting partially outside the water and partially inside the water body;
- underwater landslide: a landslide starting completely under the water surface.

Normally a sub-aerial landslide is more destructive, the slide having the possibility to accelerate considerably. Underwater landslides, frequent at oceans and great lakes, can involve a larger amount of sliding material with respect to their sub-aerial counterparts, but they usually produce smaller waves and run up.

A clear nomenclature of the phenomenon is still under discussion. “Landslide tsunamis” and “impulse waves” are terms often used in a general meaning to represent either sub-aerial or underwater landslide initiation affecting any water body. Whereas the term “displacement waves” is generally limited to describe rock- and/or ice avalanche/fall - triggered waves in mountain lakes (Hermanns et al. 2013).

The behavior of the entire phenomenon can be synthesized into four phases.

1. The mass movement initiation and propagation: the landslide is triggered and slides along a slope.
2. The wave generation: the landslide enters in the water body, forming the wave.
3. The wave propagation: the wave propagates into the water body.
4. The wave run-up: the wave hits the shorelines, “climbs” flanks and enters into the territory.

The phenomenon of landslide tsunami takes place especially in mountainous zones where slope instability is more frequent. In particular, a landslide or a debris flow can be triggered by various behaviors such as the increase of water pore pressure in the soil due to heavy rainfall or snow melting, earthquakes, volcanic eruptions and defrosting of alpine permafrost, among others (Coussot & Meaunier, 1996; Iverson, et al., 1997; Hungr, et al., 2001).

Once the mass movement is initiated, it starts to propagate along the slope. When such sliding mass having a relatively high velocity hits a water body, a set of giant waves can be generated and it can propagate over a long distance.

Although having a high destructive potential, landslides seem to produce a tsunami wave that rapidly decays if compared with earthquake tsunamis (Heller & Hager, 2010). This observation does, in fact, bear relation to the different scale of the processes and the forces involved: crustal blocks that move during large earthquakes are incomparably larger than any landslide.

Nevertheless, relatively close to impact and especially in confined or narrow water bodies, the generated waves can produce a very large run-up of hundreds of meters in elevation, having the effect of destroying the shoreline or easily overtopping dams (Panizzo et al., 2005). Two historical examples can attest the power of this behavior: Lituya Bay (Alaska, 1958) where a wave run-up of 524 m has been recorded close to impact; Vajont Dam (Italy, 1963) where a

wave run-up of 210 m has been observed and where the waves, overtopping the dam, killed 2000 people. Other infamous past events show evidence of the potential risk of tsunamis triggered by landslides, but their limited number entails that aftermath analyses are not sufficient in number to properly predict the effects of similar future occurrences. For this reasons, experimental studies were carried out by different researchers in the last four decades. The experiments concern rigid bodies or granular material plunging in straight channels (two-dimensional, 2D) or in a water basin (three-dimensional, 3D). Numerical models have received a boost in the last 20 years thanks to their versatility. But the complexity of simulating a 3D phenomenon that involves the 3 phases (solid, liquid and gaseous) implies that experimental works are still attractive both to describe the process itself, and to provide data for model validation.

1.1.1 Historical events

In the past, different events of sub-aerial landslides generating tsunamis have taken place all over the world. In many cases, the destructive power of the process makes the population quite sensitive to the topic. It also elicits much scientific interest, mostly under the form of detailed reports.

Worldwide catalogs of landslide tsunamis are under definition. More than 250 events have been observed from the 14th century to the present time. The distribution of documented events (see Figure 1.1) shows correlations with the environmental factors that increase the local susceptibility to landslide tsunamis: geology, geomorphology and climate all influence the spatial distribution. However, the regional concentrations in Norway (156 Events), the Pacific Northwest of North America (18 events), and the European Alps (12 events) likely reflect the high level of landslide research in these regions and the availability of pertinent studies (Roberts et al., 2014). For the same reason the risk cannot be discarded *a priori* in other regions.

Tsunamigenic landslides can be triggered by means of different mechanisms as explained previously. In Table 1.1 it is possible to appreciate a list of the main historical events observed, and the corresponding triggering mechanisms. Some of the most significant events on record are analyzed hereinafter.

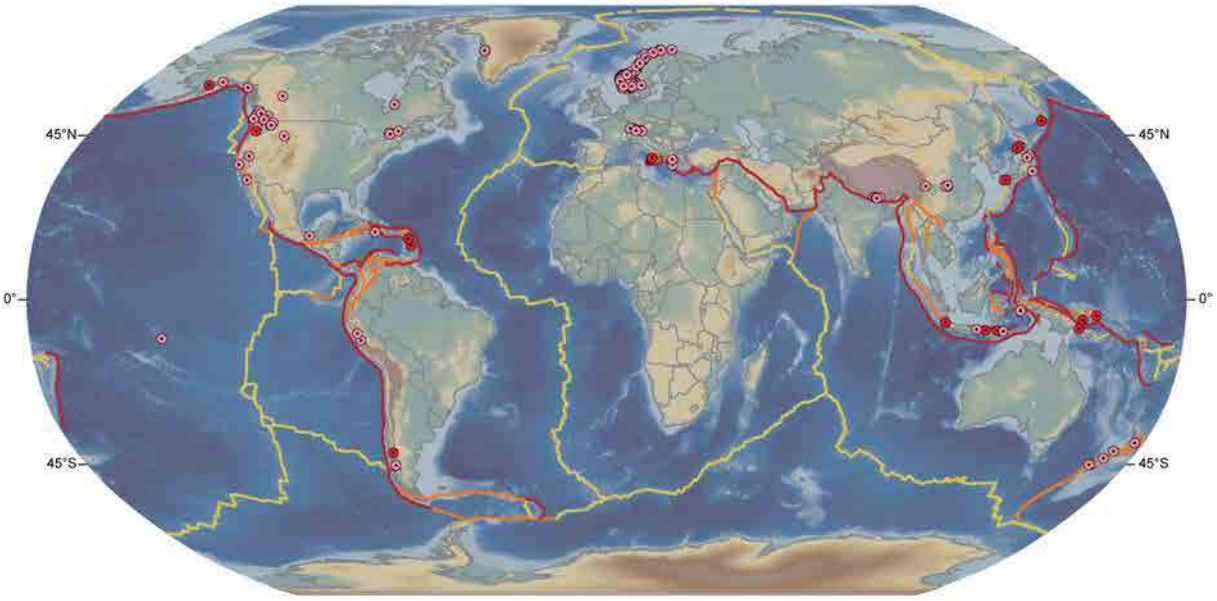

Figure 1.1. World map of landslide-generated tsunamis: pink circles are non-volcanic landslides; red circles are volcanic landslides; lines represent convergent (red), divergent (yellow) and transforming (orange) plat boundaries (in Roberts et al., 2014).

Table 1.1. Characteristics of the main worldwide historical events of sub-aerial landslide tsunamis by means of different triggering factors.

Year and Location	Triggering factor	Mass movement type	Landslide volume (m^3)	Max. run-up (m)	Fatalities	Reference
1792, Mt. Mayuyama (JP)	Volcanic eruption	Pyroclastic and debris flow	$150x10^6$ to $400x10^6$	22	14300	Miyamoto (2010)
1905, Disenchantment Bay (USA)	Glacier fall	Ice calving	$29x10^6$	35	0	Slingerland & Voight (1979)
1905, Loen Lake (NO)	Water infiltration	Rockslide	$0.35x10^6$	40.5	61	Grimstad (2005)
1934, Tafjord Fjord (NO)	Water infiltration	Rock avalanche	$1.5x10^6$	60	41	Sælevik et. al (2009)
1936, Loen Lake (NO)	Water infiltration	Rockslide	$1x10^6$	74	73	Grimstad (2005)
1958, Lituya Bay (USA)	Earthquake	Rockslide	$300x10^6$	524	2	Slingerland & Voight (1979)
1959, Pontesei Reservoir (IT)	Water infiltration	Silt landslide	$5x10^6$	20	1	Panizzo et al. (2005)
1963, Vajont Reservoir (IT)	Water infiltration	Limestone landslide	$270x10^6$	210	2000	Semenza (2001)
1965 Cabrera Lake (CL)	Rainfall infiltration	Debris flow	$10x10^6$	60	27	Watt et al. (2009)

Year and Location	Triggering factor	Mass movement type	Landslide volume (m^3)	Max. run-up (m)	Fatalities	Reference
1971, Yanahuin Lake (PE)	Moraine fall	Granular landslide	$0.1x10^6$	30	600	Slingerland & Voight (1979)
2002, Stromboli Island (IT)	Volcanic eruption	Pyroclastic flow	$5.6x10^6$	10	0	Bonaccorso et al. (2003)
2007,Chehalis Lake (CA)	Rainfall infiltration	Landslide	$3x10^6$	37.8	0	Brideau & Stead. (2012)

The most destructive disaster induced by a landslide tsunami ever observed has been the Mount Mayuyama collapse in 1792. Mount Mayuyama is a peak of the Mount Unzen system that lies in the peninsula of Shimbara (prefecture of Nagasaki, Japan). Due to a volcanic eruption, a huge slope of the Mayuyama collapsed, causing a landslide (pyroclastic flow and sediments) of more than $150x10^6$ m^3 (see Figure 1.2a).

The landslide velocity has been estimated as 100 m/s and the thickness of the front, about 30 m. The landslide passed through Shimbara City, destroying everything in its path, and entered into the Ariake Bay, provoking a tsunami with an initial height of 20 m. It propagates for approximately 30 km (see Figure 1.2b). The disaster provoked 14300 victims (Miyamoto, 2010).

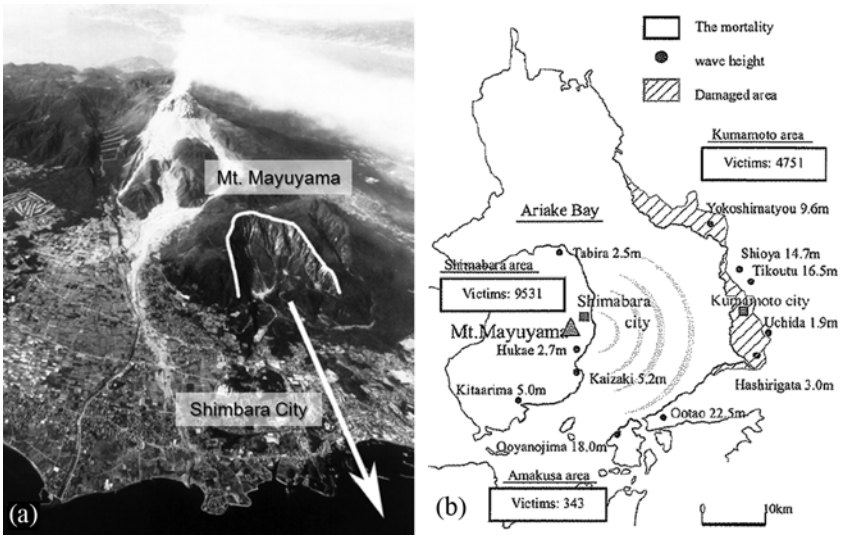

Figure 1.2. The Mount Mayuyama disaster (1792, Japan): a) the ancient slope failure and its path (courtesy of Asia Air Survey Co. Ltd.); b) map of the area with synthetic information of wave height and victims (in Miyamoto, 2010).

Landslide tsunami threat due to volcanic eruption, possibly followed by flank collapses, is a well-known behavior. Several instances have occurred in the Mediterranean area, and especially

in the Aeolian Islands (Italy), where at least 8 events have been recognized in the last century (Maramai et al., 2005). Within the Aeolian Archipelago, the Stromboli Volcano forms a conic island. The volcano retains a regular activity, mainly explosive. Occasionally, an effusive eruption occurs, with lava usually flowing along a path known as "Sciara del Fuoco" (Figure 1.3a).

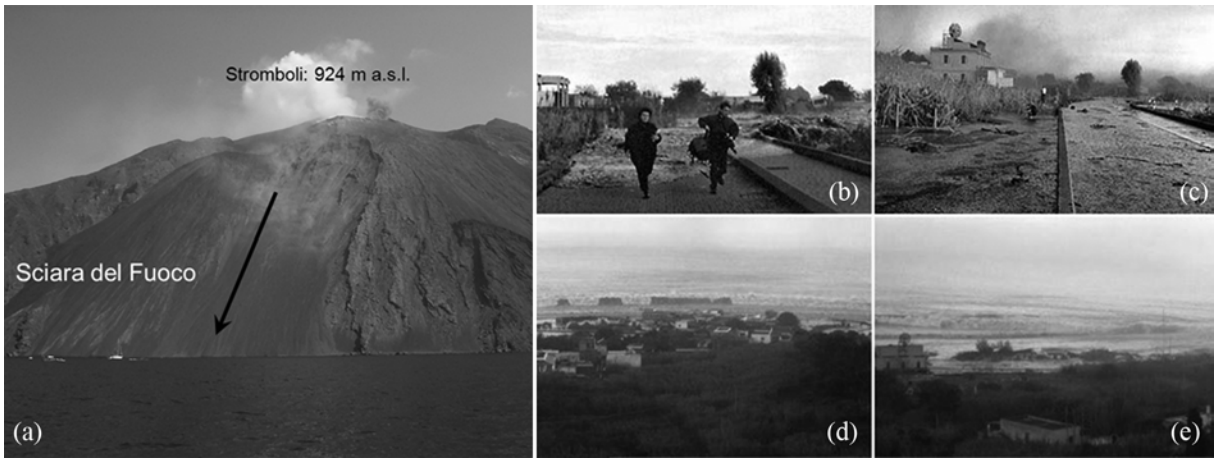

Figure 1.3. The Stromboli Island (Italy) under landslide tsunami threat: a) the volcano and the path of the lava and pyroclasts "Sciara del Fuoco" (Photo by D.Barthel, 2003); b) people escaping from the waves of the 2002 tsunami in Stromboli Island; c) inland flooded by the tsunami; d) and e) waves approaching the coastline of the island (b, c, d and e: photos by Philippe Guillemin and Dave Rothery).

In the last 100 years various effusive eruptions took place (in 1916, 1919, 1930, 1944, 1954 and 2002) and 5.6×10^6 m^3 of material reached the sea provoking tsunamis (Bonaccoroso et al., 2003, Maramai et al., 2005). The last one (2002) is well documented by photos, videos (http://www.iahrmedialibrary.net) and field evidence. The lava flowed in the sea and provoked a tsunami that reached urban areas. It caused damages but fortunately no fatalities (see Figure 1.3b, Figure 1.3c, Figure 1.3d and Figure 1.3e).

Others potential failures of volcanic islands' flanks prone to generate landslide tsunamis are presented in section 1.1.2. An exhaustive list of tsunamis provoked by volcanic activity can be consulted at the Oregon State University web page (http://volcano.oregonstate.edu/volcanogenic-tsunamis).

Water infiltration due to rainfall, snow melting (often combined with rainfall) or human activity, is probably the most frequent trigger of landslides and thus of landslide tsunamis.

The most infamous event of a tsunamigenic landslide, triggered by human activity-induced water infiltration, is the Vajont reservoir disaster (1963).

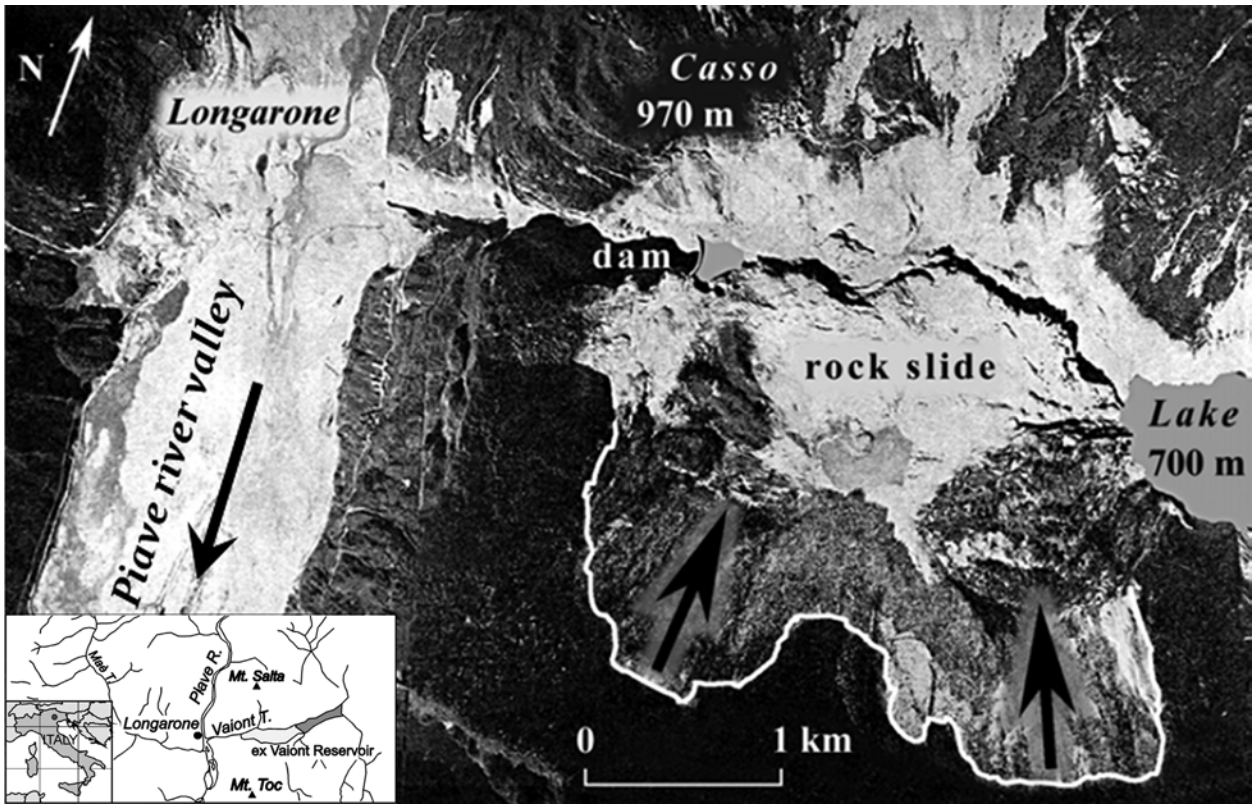

Figure 1.4. Descriptive Map of Vajont Dam (Italy) after the 1963 landslide (ENEL 1963, after Fritz 2002). Location map after Genevois & Ghirotti (2005).

The Vajont Dam was built in the region of Veneto (North East of Italy) between 1956 and 1960, on the homonym creek that, after a narrow gorge, flows into the Piave River. The town of Longarone is located at the confluence. The dam was erected in correspondence of the gorge, having a structure in the form of a double arc and a height of 265.5 m (See Figure 1.4 and Figure 1.5b).

As soon as the construction was completed, the filling operation was started (February 1960). On November 1960 a first slope failure was triggered in the south side: the infiltration of water in a permeable layer mobilized a volume of $7x10^5$ m^3 of limestone sliding into the reservoir (see Figure 1.5a). The slide provoked a 2 m wave and a run-up on the dam of 10 m, fortunately without overtopping it (Semenza, 2001). At the same time a visible fissure on the slope flank was left open: a sign of a potential future failure.

Partially rejecting the advice of scientists and researchers, the dam was filled and emptied several times in order to test the reservoir, thus widening the crack. On the 9th of October 1963 an enormous landslide with an estimated volume of $300x10^6$ m^3 and a front of 2 km was mobilized and entered the reservoir (see Figure 1.5c).

The resulting observed wave run up in the front flank was around 210 m above the lake level, very close to the town of Casso (Datei, 2002). The wave overtopped the dam and propagated down into the Piave Valley entirely destroying Longarone and other towns/villages along its path (see Figure 1.6a and Figure 1.6b). 2000 people were killed. The dam itself did not suffer damage and is still visible today.

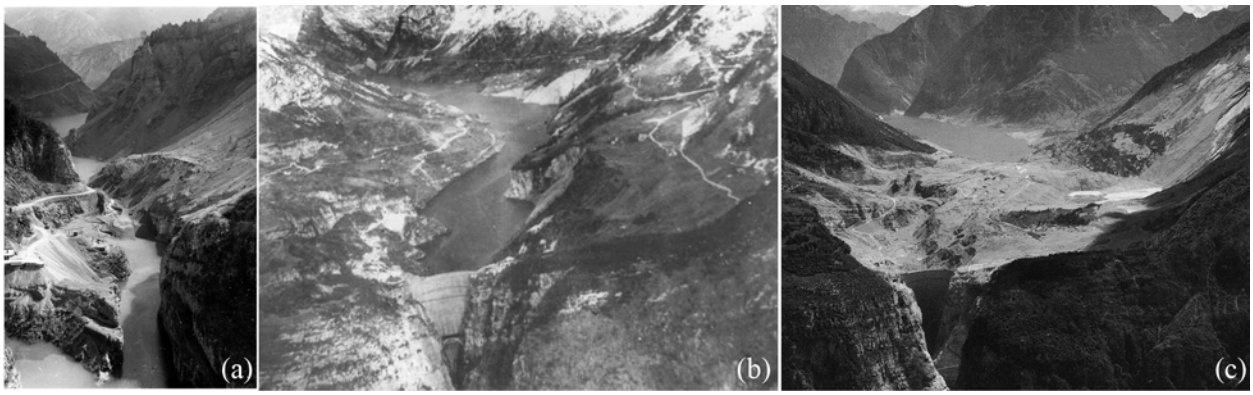

Figure 1.5. Photo collection of the Vajont dam disaster: a) Vajont reservoir looking upstream after the preliminary 1960 landslide (in Semenza, 2001); b) the Vajont Reservoir before the event of 1963 (in Semenza, 2001); the reservoir after the event (U.S. Geological Survey - USGS, 1963).

Figure 1.6. Effects on the town of Longarone: (a) before and (b) after the event of 1963 (source: Vajont Survivors' Committee).

The Vajont event is unfortunately famous for the terrible impact on both the population and social texture of the affected area, but it also contributed to increase the sensitivity of citizens at large concerning such types of anthropogenic disasters. However, around the world other examples exist of reservoirs actually under landslide tsunami-associated risk. Some of them are reported in section 1.1.2.

A recent and well documented example of landslide tsunami, triggered by water infiltration, is the event of Lake Chehalis (British Columbia, Canada, 2007). The landslide occurred on the 4th

December 2007, when rainfall combined with snow melting increased the pore pressure and trigger the landslide. The mass released by the failure, with a volume in the order of $3x10^6$ m^3, entered the lake, provoking a tsunami wave that buried three local campgrounds and stripped the vegetation on the opposite shore of the lake to a maximum height of 37.8 m (see Figure 1.7). Fortunately no victims occur as the campgrounds were running in low season. However the woody debris formed a dam at the lake outlet elevating the lake level and exposed a downstream community to a potential outburst flood. An 8 month removal project eventually eliminated this hazard (Wang et al., 2015).

Fortunately, no casualties were incurred as the campgrounds were operating in low-season.

Detailed field measurements, terrestrial photogrammetric 3D models and an airborne LiDAR digital elevation model were conducted to describe the landslide pre and post event as well as the mechanism of failure (Brideau et al., 2012).

The headscarp is located at an elevation of 840 m asl while the lake shoreline is at 240 m asl. The headscarp measures 210 m in width and 40m in thickness. The landslide travelled a horizontal sub-aerial distance of 950 m before entering the lake. The inclined sub-aerial path is about 1,115 m in length and the mean slope is 32°. Brideau et al. (2012) estimated the basal friction angle between the slide and the bedrock in between 25° and 30°. Recently Wang et al. (2015) calculated the landslide velocity at impact in 60 m/s. The framework of the Lake Chehalis event provides crucial information for evaluating and improving empirical and numerical models of landslide tsunamis.

Landslides are often triggered by earthquakes. One impressive example of tsunami provoked by an earthquake-triggered landslide is the event of Lituya Bay (Alaska, USA, 1958). The bay has the morphology of a U-shaped fjord with a T form, having two inlets at the upper part (see Figure 1.8a and Figure 1.8b). The width of the bay varies from 1.2 km to 3.3 km, the depth from 220 m to 10 m at the mouth. The spot has suffered different landslide-tsunami events in recent times. On the 9th of July 1958, the most important event started at the Gilbert Inlet where a giant rock slide was triggered by an intense tectonic movement: a fault is situated right by and longitudinally to both inlets (see Figure 1.8b). This event is also one of the most studied by, for instance and among others, Miller 1960, Mader 1999, Fritz et al. 2001 and Fritz et al. 2009.

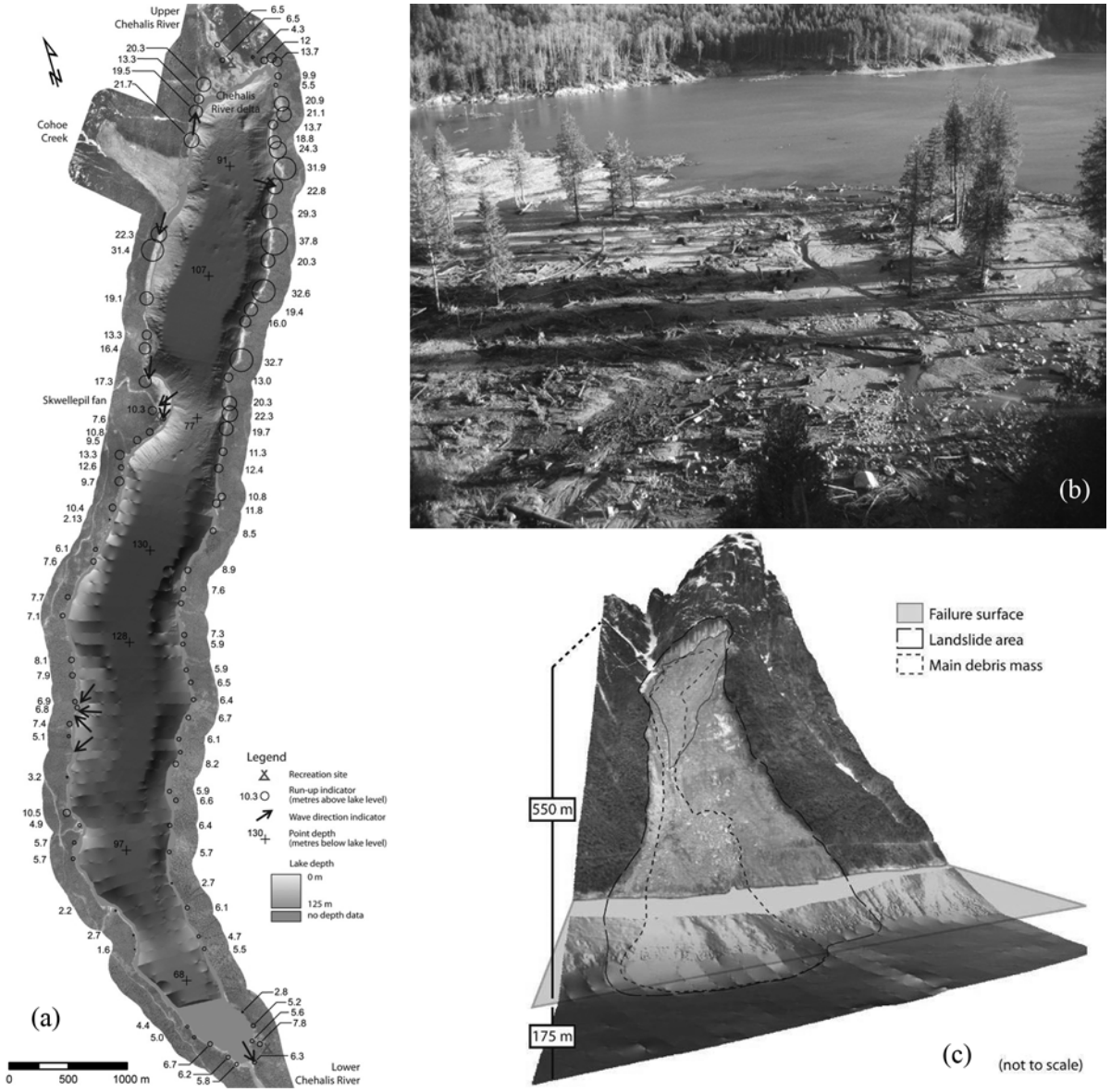

Figure 1.7. Lake Chehalis event of 2007 (Canada): a) map of wave impacts along the shoreline of the lake (after Lawrence et al., 2013); b) damages at the campground on the upper Chehalis River delta at 1 km from the landslide (after Lawrence et al., 2013); c) 3D view of the landslide based on orthophotography, LiDAR and SONAR data (after Roberts et al., 2013).

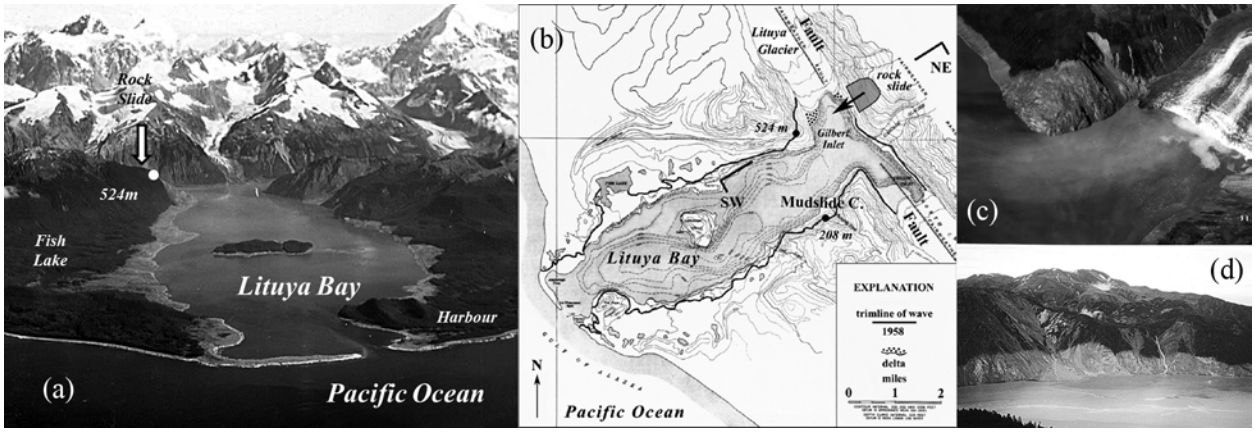

Figure 1.8. Description of the event of Lituya Bay (Alaska, USA, 1958) and evidences of impulse-wave effects on shorelines: a) aerial photo of the spot after the 1958 event (USGS, 1958); b) map of Lituya Bay where in dotted line the fault, in continuous line the trim line of the wave and heights of run-up are represented (in Miller, 1960).; c) stripped woods at Gilbert Inlet revealing a run-up of 524 m (USGS, 1958), d) run-up of 208 m at Mudslide Creek (USGS, 1958).

The power of the wave chopped the pine forest along the shoreline drawing a trim line, which makes possible the post evaluation of the wave's run-up. The trim line is reported in the map of Figure 1.8b and visible in the aerial photo in Figure 1.8c and Figure 1.8d.

The triggered rockslide had an estimated volume of 31×10^6 m^3, sliding along a slope of around 40° (Miller, 1960). A maximum velocity at impact with water of 110 m/s has been estimated by Fritz et al (2009), neglecting friction. Once the slide reached the water body, a huge wave was created, crossing the inlet, here only 1350 m wide, and provoking a run-up of 524 m, which is the highest recorded in history on earth (see Figure 1.8c). Two fishermen perished during this event.

1.1.2 Locations potentially under risk

Although a number of past events spreading in different area of the world were examined in the previous section, landslide tsunamis are not as frequent as other natural hazards. Nevertheless, they certainly constitute intense events. The hazard related to landslides is a combination of probability (return period), magnitude (mobilized volume) and intensity (velocity, force or energy) of a potential event (Fell et al., 2008). In evaluating the hazard presented by landslide tsunamis, there is an additional, and not yet fully solved, step to be considered, i.e. that related to the energy transfer from landslide to waves. However, it can be immediately seen that an event of low probability and high intensity can pose a high hazard and

a potentially high risk when the various elements at risk (population, buildings and infrastructures) become involved.

It is a known fact that the sensitivity of the population has increased in the last 50-60 years as an effect of disasters of significant impact. However, the lesson learned has not prevented the rise of new risky situations. Some of them are certainly related to natural hazards and are concentrated in those territories that are more prone to landslides. But locations still exist that are potentially under a landslide tsunami risk induced by human activity. Some of these are presented in this section.

Reservoirs are certainly the infrastructures under the closest observation, following the Vajont event. These infrastructures are frequently placed in mountainous areas where slope instabilities are more common. Within a relatively short time-frame, China has energetically pursued the construction of many of the largest reservoirs in the world. The famous Three Gorges Reservoir (Western China) has already suffered some minor landslide-induced tsunami events. The main event involved the well-known Gongjiafang landslide, located on the left bank of the Yangtze River, which occurred on 23 November 2008 when a rock fall of 3.8×10^5 m^3 entered the basin. The maximum run-up generated was 13 m in the opposite bank. In the course of the slide, the structure of the rock mass disintegrated into granular clusters (Huang et al., 2012). At least two other locations are currently at risk in the same reservoir and, for this reason, Huang et al. (2013) have conducted experiments to improve the knowledge of the phenomenon.

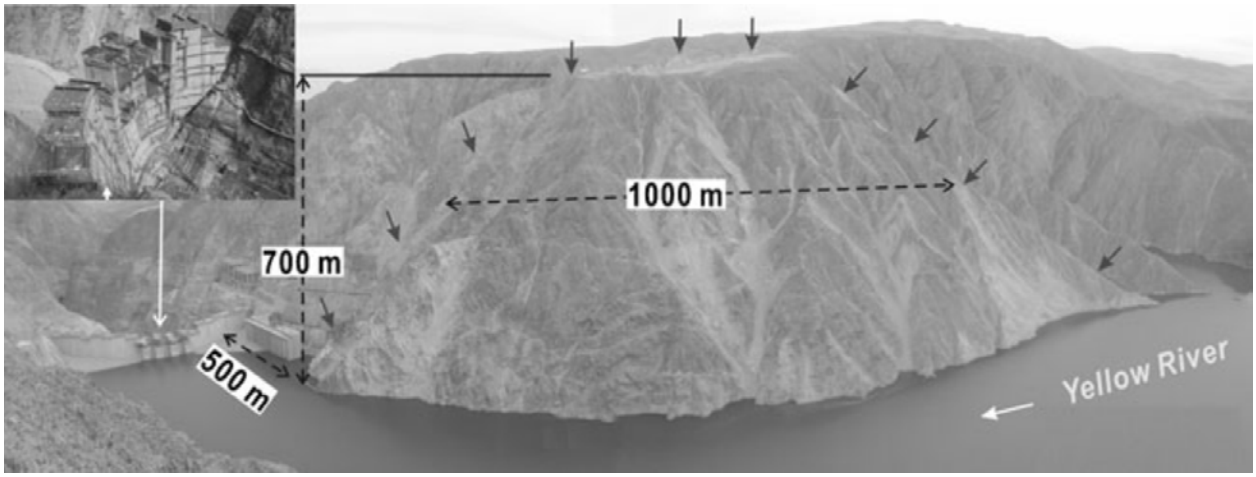

Figure 1.9. Geometry of the Guobu slope close to the Laxiwa dam after impoundment in a photo of 14 January 2010. The Arrows are the boundary of the potential landslide (in Zhang et al., 2013).

However, the Three Gorges is not the only endangered Chinese reservoir. Recently, there has been discussion over the risk that a portion of the flank of the Laxiwa Hydropower Station in the

upper part of the Yellow River may collapse (Zhang et al., 2013). The potential landslide, called Guobu (see Figure 1.9) has a mean width of 1 km and a height of 700 m.

For what concerns Spain, around 1100 reservoirs are currently in place within the Country, with concentrations in mountainous areas such as the Pyrenees range. Examples of those reservoirs prone to slope instability are the Itoiz and Yesa in Aragon (Sainz & Herrero, 1999) or the Baserca Reservoir. A special attention is reserved to the last one, as an example of neglected potential risk.

The Baserca Reservoir is situated at the border between the Aragon and Catalonia Regions, on the Noguera Ribagorçana River. The mean water depth is 23.8 m while the highest is 69.5 m.

Applying the task of reconnaissance of debris-flows and their susceptibility on a regional scale (Chevalier, 2012; Bregoli et al., 2014) some possible sources, paths and fans of past events can be observed entering the reservoir (see Figure 1.10). Especially two fans of debris flows are fairly evident, while a third one, near the dam, seems to be originating from fluvial activities. The spot has a certain interest in the study of impulse waves generated by debris flows that can provoke damage to the dam or to the roads bordering the lake's edge or eventually to the towns of Senet and Aneto situated downstream. However, more detailed studies should be performed to identify and quantify the potential risk.

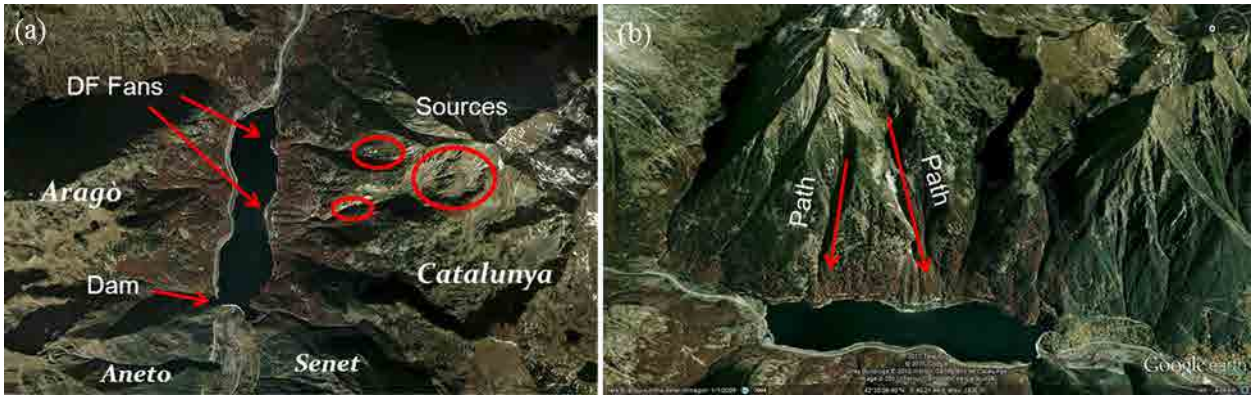

Figure 1.10. Baserca Reservoir, Spain: a) descriptive map of the reservoir with sources and fans of debris flows (DF) (aerial photo of Institut Cartografic de Catalunya, 2011); b) oblique image of the spot with the debris-flows paths (Google Earth, 2009).

Natural hazards related to landslide tsunamis are certainly frequent in fjords and glacial bays where the flanks are steep due to their typical U-shape morphology (see, for instance, the example of Lituya Bay in the previous section). The Atlantic coast of Norway is one of the areas most prone to those hazards. Hundreds of past events have been detected and described

(Hermanns et al., 2014) and some dedicated experiments has been carried out by Sælevik et al. (2009). Currently a potential rockslide with an estimated volume of more than $50x10^6$ m^3 has been detected in the Åkerneset rock slope in the narrow Storfjorden in Western Norway (Harbitz et al., 2014; see Figure 1.11). Its probability of failure has been estimated in a return period between 1000 and 5000 years.

Figure 1.11. The potential Åkerneset rock slope (Norway) in shaded area (in Harbitz et al., 2014)

Volcanic islands' flanks are other areas where landslide tsunamis can potentially occur. The examples of Mount Mayuyama and Stromboli have been presented in the previous section, but many other cases can be recognized around the globe.

La Palma is a volcanic island of the Canary Archipelago in Spain. It is situated in the Atlantic Ocean, in front of Morocco. The peak of the volcano is 2423 m asl, but the total height from the ocean floor to the summit is about 7000 m. The south part of the island is dominated by the Cumbre Vieja volcano, which is active but dormant (see Figure 1.12). The last eruption was in 1971. Recent studies have assessed that the Cumbre Vieja can potentially collapse and provoke a mega-tsunami that could reach and devastate the East Coast of the United States (Masson, 1996; Carracedo et al., 1999; Moss et al., 1999). Ward and Day (2001) pointed out that "*Geological evidence suggests that during a future eruption, Cumbre Vieja Volcano on the Island of La Palma may experience a catastrophic failure of its west flank, dropping 150 to 500 km^3 of rock into the sea. Using a geologically reasonable estimate of landslide motion, we model tsunami waves produced by such a collapse. Waves generated by the run-out of a 500 km^3 (150 km^3) slide block at 100 m/s could transit the entire Atlantic Basin and arrive on the coasts of the Americas with 10-25 m (3-8 m) height*". The discussion in the scientific community on this delicate

problem is under continuous development, as the potential failure can endanger a huge portion of the population living along the Atlantic coasts.

Similar discussions concern the Montserrat volcanic island in the Lesser Antilles. It has been demonstrated that the island's edifice experienced past failures, a finding that has alarmed the scientific community (Watt et al., 2012).

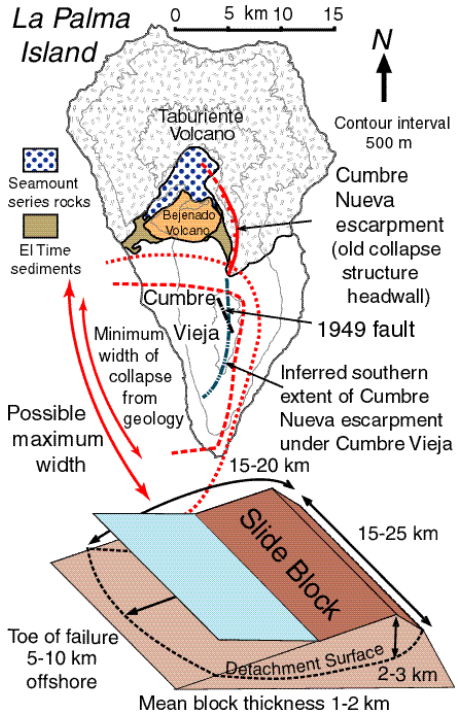

Figure 1.12. Map of La Palma Island (Canary Islands, Spain) showing the major geological deposits and the potential slide block geometry pictured at the bottom (in Ward and Day, 2001).

1.2 Motivations

In the previous section it was pointed out that tsunamis provoked by landslides are a serious threat. After particularly destructive events the sensitivity of the population to the issue has increased, but many sites are still in danger. The risk can be reduced only with an effective and quick response by the local authorities, but they certainly need appropriate tools. The scientific community, on its part, has the obligation to provide instruments to evaluate and thus mitigate or eliminate potential hazards.

Landslide tsunamis involve solid and liquid phases. The solid one is usually deformable (granular material). Thus, the numerical modelling of the phenomenon is still an open challenge. A proper model needs to simulate the process with at least a biphasic and 3D approach. In the last decade, in Spain as well as in other parts of the world, considerable efforts have been made

in the area of numerical modelling of landslide tsunamis (Quecedo et al., 2004; Pastor et al., 2009; Serrano-Pacheco et al. 2009; Crosta et al. 2015). But, contrary to other countries, no experimental work was carried out. This thesis aims to improve the understanding of landslide-provoked tsunamis, with the intent to preserve the lessons learned and to offer tools intended to help avoid repeating past errors in the survey and management of the territory.

When the problem being faced is still too complex to be addressed solely from a numerical approach, experimental works can provide tools to local authorities which can be promptly applied to protect the population, or to civil engineers and project managers in general, when planning new infrastructure.

In 2009 the GITS team started collaborating with the Laboratory of Hydraulics, Hydrology and Glaciology (VAW) of the Technical University of Zurich. They have a long tradition in studying landslide tsunamis and when they suggested this new path of investigation, there was no hesitation in pursuing it.

This research intends to be an advance in the topic, offering predictors for hazard assessment related to landslide tsunamis, in the belief that experimental data, can be of interest for the calibration and validation of numerical models.

1.3 State-of-the-art

Despite some pioneer studies, it is only in the last 40 years that the research on tsunamis generated by landslides has received a boost through laboratory experiments, scale models of real events and numerical approximations of the problem. Focusing on experiments, blocks or granular material were used to simulate the landslide, while water basins were reproduced by straight channels (2D) and rectangular tanks (3D). The principal experimental researches are reported in Table 1.2 below. These past studies are then described, differentiating between the ones using blocks and the ones using granular material to simulate landslides.

Table 1.2. List of the principal researches on landslide tsunamis and their main features. EF=Empirical Formulations; PIV= Particle Image Velocimetry; SPH= Smoothed-Particle Hydrodynamics; ND=No Data found.

Researchers	Model Type	Wave Tank or Channel $L \times W \times h_w$ (m)	Slope of impact α (°)	Froude number of impact	Purpose
Scott-Russell (1844)	2D block	6.10 × 0.30 × 0.09 to 0.14	90	ND	solitary wave investigation
Noda (1970)	2D block	32.00 × 0.30 × 0.15 to 0.61	90	ND	wave type classification

Researchers	Model Type	Wave Tank or Channel $L \times W \times h_w$ (m)	Slope of impact α (°)	Froude number of impact	Purpose
Kamphuis & Bowering (1970)	2D block	45.00 × 1.00 × 0.23 to 0.46	20 to 90	0.90 to 3.10	EF
Slingerland & Voight (1979)	various	various	ND	ND	state-of-the-art
Huber (1980)	2D granular	30.40 × 0.50 × 0.12 to 0.36	28 to 50	0.53 to 3.69	EF
Huber (1980)	3D granular	6.00 × 10.00 × 0.12 to 0.36	28 to 50	0.53 to 3.69	EF
Huber & Hager (1997)	2D/3D granular	same as Huber (1980)	28 to 50	0.53 to 3.69	data reanalysis of Huber (1980)
Fritz (2002)	2D granular	11.00 × 0.50 × 0.30 to 0.67	45	1.08 to 4.66	EF, PIV
Walder et al., (2003)	2D block	0.30 × 0.285 × 0.05 to 0.13	11.2 to 19.5	1.00 to 4.10	numerical model calibration
Zweifel (2004)	2D block/granular	11.00 × 0.50 × 0.15 to 0.60	45	1.08 to 4.89	EF, comparison block/slide
Panizzo et al. (2005)	3D block	12.00 × 6.00 × 0.40 to 0.80	16 to 36	1.00 to 2.20	EF, SPH
Heller (2008)	2D granular	11.00 × 0.50 × 0.075 to 0.60	30 to 90	0.86 to 6.83	study of scale effects
do Carvalho & do Carmo (2007)	2D Block	12.00 ×1.50 ×1.00	30.7, 39.5	ND	EF
Ataie-Ashtiani & Nik-Khah (2008)	2D block/granular	3.60 × 2.50 × 0.50 to 0.80	15 to 60	ND	EF
Sælevik et al. (2009)	2D block	25.00 × 0.50 × 0.60	35	1.00 to 1.50	PIV, scaled model
Di Risio et al. (2009)	3D block	50.00 × 30 × 0.80	90	0.29 to 2.64	run-up on conical island
Mohammed (2010)	3D granular	48.80 × 26.50 × 0.60 to 1.35	27.1	1.00 to 4.00	EF

1.3.1 Experiments with blocks as wave generator

The pioneer researcher and naval engineer, the Scotsman John Scott-Russell, was probably the first to address wave generation with a rigid body plunged into water.

His purpose was to reproduce and study the solitary wave, which he observed in an experiment (Scott-Russell, 1837): by pulling a boat with horses in a large straight channel and suddenly stopping the boat, a solitary wave was created and it propagated for kilometers without important changes in height and velocity. He followed the wave along the channel on horseback, recording data.

In 1844, Scott-Russell successfully tried to reproduce in the laboratory a solitary wave, dropping a block at the header of a channel (Scott-Russell, 1844). No relationship between block

features and water wave features was assessed, due to lack of interest in this topic, but comments on wave generation were detailed. His important conclusion was that the celerity c_{sol} of the solitary wave can be approximated by

$$c_{sol} = \sqrt{g\left(h_w + a\right)} \tag{1.1}$$

where h_w is the water depth and a the solitary wave amplitude. This fundamental result was later confirmed by different authors, such as Boussinesq (1872) and Laitone (1960).

Noda (1970) used linear theory to predict the form of the wave motion produced by a body falling vertically into a tank. He was the first to relate the features of the wave being produced to those of the falling body. The Noda solution is not consistent under the assumption of linear motion, especially in the zone relatively close to the falling box. Nevertheless, the study identifies the important relationship existing between the slide's Froude number (*Fr)* and the relative slide thickness (*S)*. The regions of wave types, as defined by a synthesis of the theoretical solution (Noda, 1970) and experimental results (Wiegel et al., 1970) are shown in Figure 1.13. The wave type was determined by the slide's Froude number.

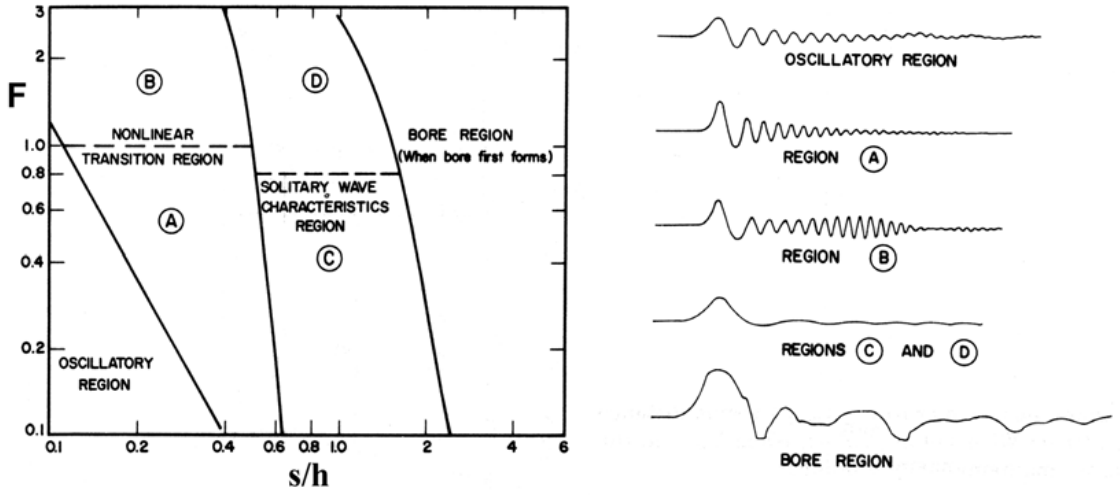

Figure 1.13. Wave type classification as Noda (1970). The waves are classified by the slide Froude number F and the relative slide thickness s/h.

In their experiments, Kamphuis & Bowering (1970) used a sliding block entering a straight channel. They observed interesting behaviors such as the decay of the wave height and of the velocity of propagation affirming: "*It may be seen that the characteristics of this wave depend mainly on the slide volume and the Froude number of the slide upon impact with the water. The resulting wave goes through a transition period. For the highest wave (usually the first), the wave height becomes stable relatively quickly and decays exponentially during the period of*

transition, the wave period continues to increase for a long time, the velocity of propagation may be approximated very closely by solitary wave theory" (Kamphuis & Bowering, 1970). They also investigated the effects of changes in the features – such as the thickness of the block and the slope of the slide (see Figure 1.14a and Figure 1.14b) – of the sliding block on the waves thus being generated.

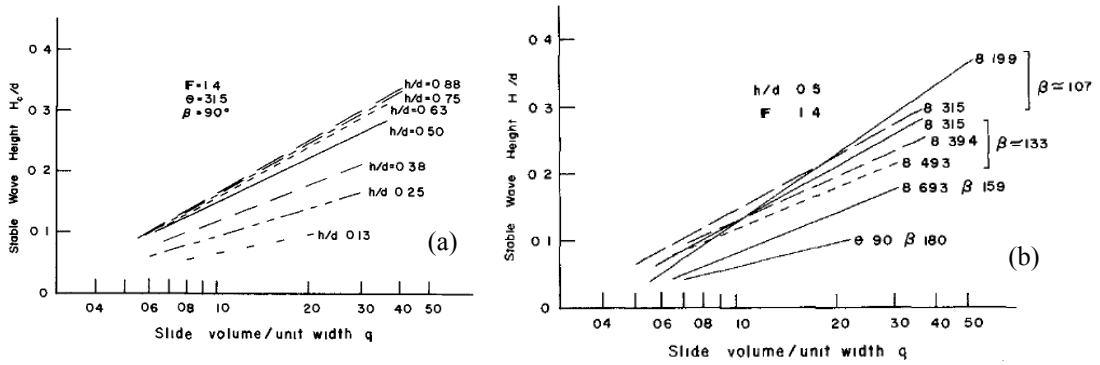

Figure 1.14. a) Effect of the thickness of the block on the wave height: the wave height increases as the thickness of the block is increased; b) effect of the slide slope on the wave height: the wave height increases as the slide slope is increased (Kamphuis & Bowering, 1970).

Walder et al (2003), conducted comprehensive experiments employing a block sliding in a straight channel, focusing on the entrance. The experiments have been used to design a simplified numerical model and to understand the block motion. They conclude that "... *submerged block-landslide motion is resisted primarily by frictional forces and only to a minor degree by hydrodynamic drag."* A similar result, but with granular deformable material, was produced in the present work, as described in chapter 5.

Some studies on both the three dimensional physical model and the wave run-up on plane slopes were carried out in the Laboratory of Environmental and Maritime Hydraulic (LIAM) of L'Aquila University by Panizzo (2004). The studies focused on empirical formulations able to correlate the main parameters of impulse-generated water waves to those of the landslide movement and the reservoir. The landslides were modelled as solid blocks with zero porosity entering a wave tank. The improvement brought about by Panizzo (2004) was to take into account the effect of radial expansion of the wave. He included the angle of propagation into the empirical equations. Based on the experimental analysis he also created a relatively simple Smoothed-Particle Hydrodynamics (SPH) numerical model to describe the propagation of the impulse wave in a reservoir, and tested the results in some well-known cases like those of the Vajont Reservoir and the Pontesei Reservoir. Panizzo et al. in 2005 built the following empirical relationship between the wave height and the slide parameters, depending on the distance from

impact and the direction of propagation. He included a new main parameter based on time, named the "nondimensional time of the landslide underwater motion" defined as $T_s = t_s\sqrt{g/h_w}$ where t_s is the elapsed time from impact to landslide stop. Some concerns exist on the stoppage of a rigid, not deformable block.

$$T_s = 0.43\left(\frac{B_s h_s}{h_w^{\,2}}\right)^{-0.27} F^{-0.66}\left(\sin\alpha\right)^{-1.32} \tag{1.2}$$

The nondimensional wave height is empirically expressed as:

$$H\left(r/h_w,\Gamma\right) = 0.07\left[T_s\Big/\left(B_s h_s/h_w^{\,2}\right)\right]^{-0.45}\left(\sin\alpha\right)^{-0.88}\exp\left(0.6\cos\Gamma\right)\left(r/h_w\right)^{-0.44} \tag{1.3}$$

The study offers an important remark on the effect of the slope on the wave height. In equation (1.3) the trend is that increasing α, the wave height decreases. This trend is completely opposite to the case of the similar 3D study by Huber & Hager (1997), where the increase in α corresponds to an increase in the wave height. A comparison between the empirical formulas of Panizzo (2005) and Huber & Hager (1997) is given in Figure 1.15, showing an overestimation of the Huber & Hager formula with respect to the other.

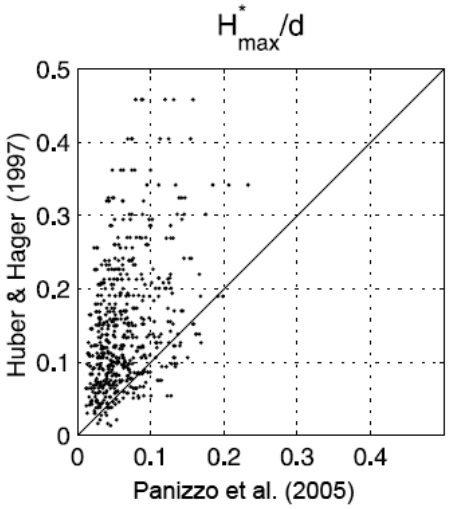

Figure 1.15. Comparison between experimental results by Huber and Hager (1997) and Panizzo et al. (2005): Huber & Hager formula overestimates the Panizzo formula (in Panizzo et al., 2005).

The recent events of the Stromboli Island (see section 1.1.1) generated the demand for an early warning system. Bellotti et al. (2009), starting from the recent experiments of Di Risio et al (2009), built a 3D model with FLOW-3D (a commercial code), implemented for a conical island. Di Risio et al (2009) conducted experiments in the LIAM laboratory in consortium with the

University of Roma Tre. The experiments consist in a block sliding along the slope of a cone, entering a water tank. The results focused on the calibration of the FLOW-3D model.

1.3.2 Experiments with granular material as wave generator

Slingerland and Voight introduced for the first time granular material instead of a sliding block. They used scaled models of the Lake Koocanusa and of the Mica reservoirs (both in Canada) to simulate the behavior of a landslide entering a water body (Slingerland & Voight, 1979; Slingerland & Voight, 1982). They derived an empirical regression relating the first wave amplitude to the dimensionless kinetic energy E_{sk} of the slide:

$$\log\left(a/h_w\right) = -1.25 + 0.71E_{sk} \tag{1.4}$$

$$E_{sk} = \frac{1}{2}\frac{\rho_s}{\rho_w}\frac{V_s}{h_w^{\,3}}\frac{v_s^{\,2}}{gh_w} \tag{1.5}$$

The measurements were taken at a certain distance $x/h_w = 4$. As they used a water basin, the wave was propagating radially, but only the main direction was taken into account in the measurements.

Various researchers at the Laboratory of Hydraulics, Hydrology and Glaciology (VAW) of the Swiss Federal Institute of Technology of Zurich (ETH Zurich), have studied impulse waves from the beginning of the ’80. The VAW-ETH laboratory also greatly contributed to the present work by exchanging experience and information.

Their works are summarized here, giving more prominence to the latest work by Heller et al. 2010, who collated all the previous ones.

Huber (1980) ran experiments using a granular sliding material into a channel and was able to derive some empirical relationships. During the runs he observed different kinds of waves like sinusoidal, cnoidal or solitary, as well as transitory. An interesting conclusion was that the celerity associated to all types of waves was approximated quite well by the celerity of a solitary wave, as in equation (1.1). Huber & Hager (1997) further elaborated on the experiments of 1980, deriving the following empirical relationship, where H is the dimensionless wave height, V_s and B_s the dimensionless landslide volume and thickness, α the slope and ρ_s the landslide density:

$$H = 0.88\sin\alpha\left(\frac{\rho_s}{\rho_w}\right)^{1/4}\left(\frac{V_s}{B_s}\right)^{1/2}\left(\frac{h_w}{x}\right)^{1/4} \tag{1.6}$$

They also ran 150 experiments in a basin and corrected the previous relationship in case of a 3D propagation as follows where γ is the wave direction:

$$H = 2 \cdot 0.88 \sin\alpha \cos^2\left(\frac{2\gamma}{3}\right)\left(\frac{\rho_s}{\rho_w}\right)^{1/4}\left(\frac{V_s}{B_s h_w^{\,2}}\right)^{1/2}\left(\frac{r}{h_w}\right)^{-2/3} \tag{1.7}$$

An analysis on the effect of the radial propagation of waves can be appreciated in Figure 1.16. In the Huber research, the radial effect of wave propagation is taken into account as well as the wave decay along the distance. Nevertheless, it should be noted that the main slide parameter considered was the sliding volume, thus neglecting its thickness and velocity.

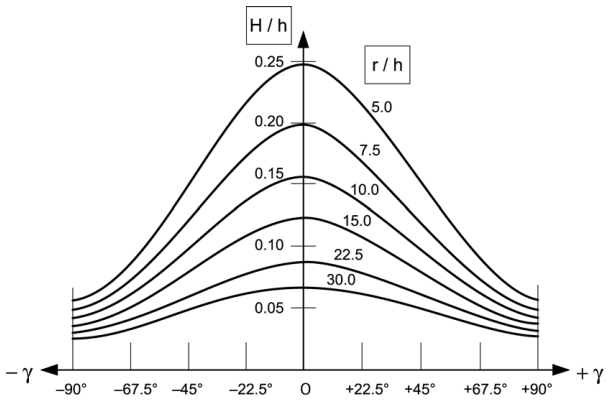

Figure 1.16. Radial impulse wave propagation: relative wave heights H/h_w as a function of relative propagation distance r/h_w and lateral wave propagation direction γ (in Huber and Hager, 1997).

The need to increase control over the main parameters of the granular sliding mass led Fritz (2002) to devise and create a "pneumatic landslide generator" (see Figure 1.17). This generator also allowed the exploration of higher slide velocities with respect to Huber (1980).

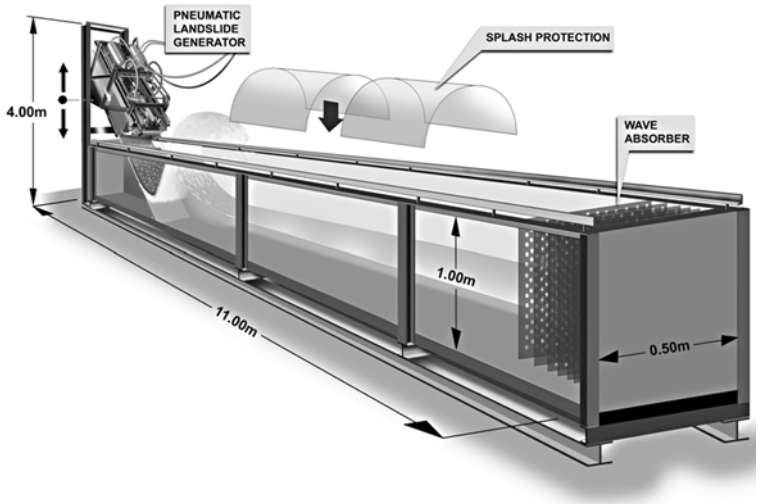

Figure 1.17. The pneumatic landslide generator of the WAV-ETH laboratory (in Fritz, 2002).

The important advancement introduced by this approach was the study of the near field of impact. Fritz (2002) divides the process of wave formation onto 4 phases, namely: "no flow separation", "local flow separation", "backward collapsing impact craters", and "outward collapsing impact craters" (see Figure 1.18). To describe the phenomenon he used different dimensionless parameters:

- Slide Froude Number $F = v_s / \sqrt{g h_w}$
- Relative Slide Mass $M = m_s / \left(\rho_w B_s h_w^{\,2} \right)$
- Relative Slide Thickness $S = h_s / h_w$

For the study of the velocity field, he introduced the Particle Image Velocimetry (PIV), with which he characterized the near field of impact. He differentiated between the maximum wave amplitude (found in the near field) and the wave amplitude in the propagation field.

The landslide generator was also used by other researchers of the main institute such as Zweifel et al. (2006) and Heller (2008). The resulting empirical relationships were later summarized in Heller (2008), who included all the experiments of the VAW-ETH laboratory.

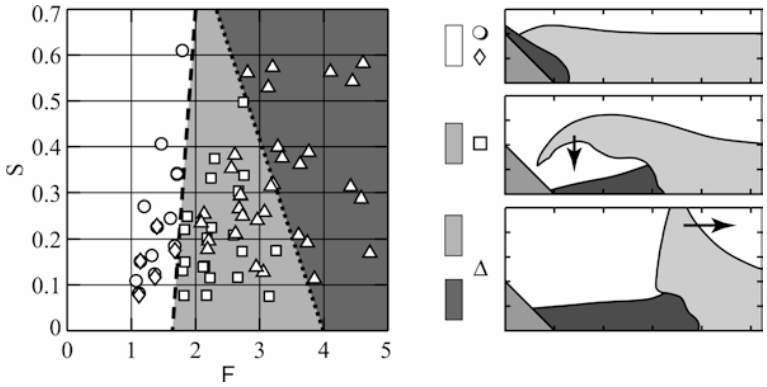

Figure 1.18. Flow separation and crater type formation: slide thickness S vs. slide Froude number F. Open circle, no flow separation; open diamond, local flow separation; open square, backward collapsing impact craters; open triangle, outward collapsing impact craters; light grey, complex transition region with backward and outward collapsing craters, dark grey, only outward collapsing craters (in Fritz, 2002)

Heller ran different experiments, widening the range of parameters investigated by the previous researchers. The latest available results of the empirical models are given by Heller & Hager (2010) and shown here in Figure 1.19 and Figure 1.20. In the Figure 1.19 the maximum wave amplitude $A_M = a_M / h_w$ and the maximum wave height $Y_M = h_M / h_w$ are both related to a parameter, P that is a product of different dimensionless parameters as shown below.

$$P = F S^{1/2} M^{1/4} \left(\cos\left((6/7)\alpha \right) \right)^{1/2} \tag{1.8}$$

$$A_M = (4/9)P^{4/5} \tag{1.9}$$

$$Y_M = (5/9)P^{4/5} \tag{1.10}$$

Figure 1.20 illustrates the wave decay along the distance from impact, relating parameter P to the wave amplitude and height at the dimensionless distance $X=x/h_w$. The formulas, describing the relationships between the wave amplitude and height with the distance, are reported in equations (1.11) and (1.12), where $A=a/h_w$ is the dimensionless wave amplitude and $H=h/h_w$ the dimensionless wave height:

$$A(X) = (3/5)\left(PX^{-1/3}\right)^{4/5} \tag{1.11}$$

$$A(X) = (3/4)\left(PX^{-1/3}\right)^{4/5} \tag{1.12}$$

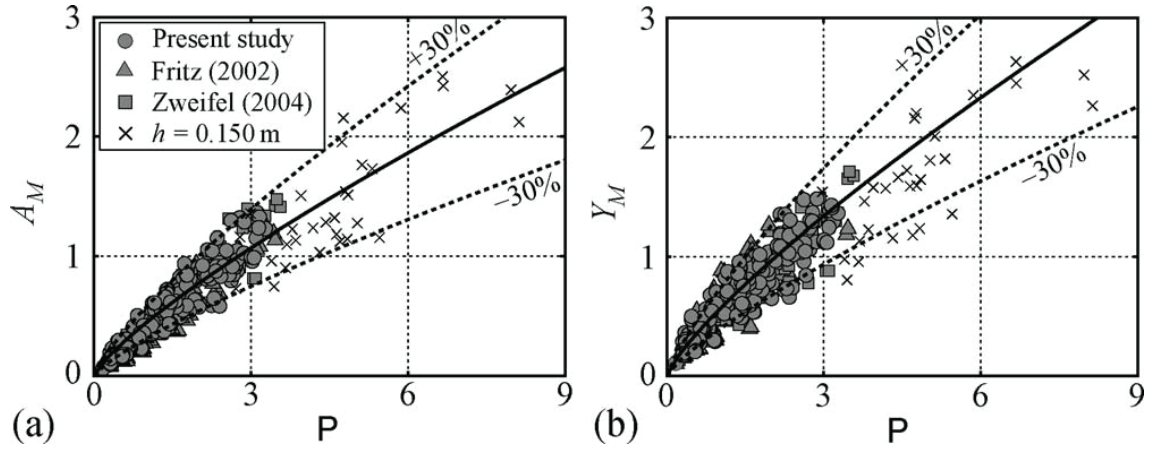

Figure 1.19. Data from all VAW runs: (a) relative maximum wave amplitude versus P and (b) relative maximum wave height versus P (in Heller & Hager, 2010).

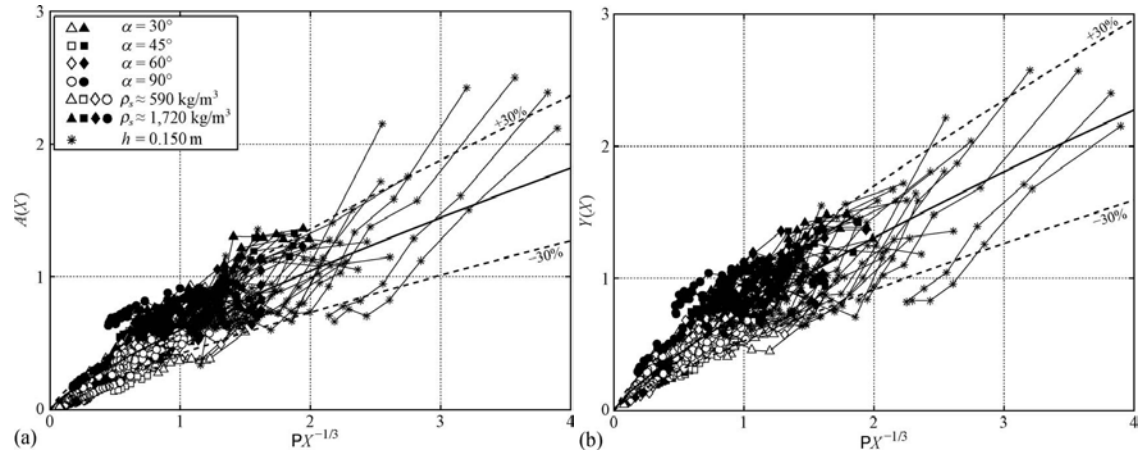

Figure 1.20. Data from all VAW runs: (a) relative maximum wave amplitude versus P along the distance (b) relative maximum wave height versus P along the distance (in Heller & Hager, 2010).

In the Wave Research Laboratory of the Oregon State University (USA), experiments on granular sub-aerial landslides were carried out by Mohammed (2010) in a large wave tank (Figure 1.21), normally used for tsunami's simulation.

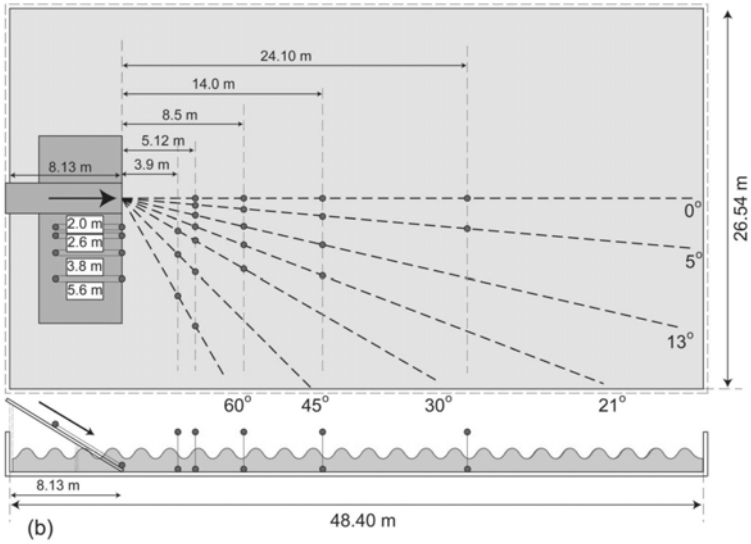

Figure 1.21. The wave gauge array used to measure the water surface elevation of tsunami wavefronts generated by three-dimensional deformable granular landslides (Oregon State University, Corvallis; in Mohammed & Fritz, 2012).

The experiments, collated in Mohammed & Fritz (2012), consist in releasing a great quantity of material (in the order of 10^3 kg), sliding along a slope of 27.1°. The experiments, having a good similarity in parameters with the ones carried out in this thesis, were used as a test of the wave form, according to the authors. The work ends up with different empirical predictors, which are, among others:

$$\frac{a}{h_w} = k_a \left(\frac{r}{h_w} \right)^{n_a} \cos\theta \tag{1.13}$$

$$k_a = 0.31 F^{2.1} S^{0.6} \tag{1.14}$$

$$n_a = -1.2 F^{0.25} S^{-0.02} B^{-0.33} \tag{1.15}$$

In particular, they provide a predictor for the energy conversion between landslide and first wave crest at a specific location, as follows:

$$\frac{E_{crest}\left(\frac{r}{h_w} = 10 \right)}{E_{s,kin}} = 0.02 S^{0.9} F^{0.7} V^{-0.1} \tag{1.16}$$

1.3.3 Numerical modelling

During the last two decades a considerable effort was made in modelling tsunamis generated by landslides. Being the phenomenon multiphasic and fully 3D close to impact, the task of modelling such behaviors is not straightforward. The models used are of different types and are often applied to experiments or past events for validation purposes or hazard assessment.

Quecedo et al. (2004) affirm that depth-integrated Navier-Stokes equations are not sufficient in describing the phenomenon in the near field. Therefore they use full Navier-Stokes solved with FEM for the solution of hyperbolic equations and complemented with indicator functions that assign the material properties (they use 3 phases: solid, liquid, air) to each spatial point in the domain. With the mentioned FEM method they ensure to correctly simulate the process at high slope. They successfully test the method with results obtained in the physical model by Fritz et al. (2001) simulating the event of Lituya Bay (1958).

Tinti et al. (2006) model the event of Stromboli Island (2002) by dividing the landslide and the tsunami in two phases. The landslide is simulated by means of a Lagrangian approach, the tsunami is simulated with depth-averaged Navier-Stokes equations.

Waythomas et al. (2006) simulate the possible debris flow provoked by the eruption of the Augustine Volcano, located in the Cook Inlet (Alaska, USA). They use the method of center-of-mass translation, similarly to Walder et al. (2003) to simulate the landslide, and a Boussinesq approach for waves. The method, applied to a past event which occurred in the 19th century at the same spot, does not fit properly with the available data.

Serrano-Pacheco et al. (2009) use a FVM method to solve Navier-Stokes equations over complex topography.

Pastor et al. (2009) give an interesting framework to model landslide tsunamis. They affirm that no single model able to reproduce all involved phenomena exists, and it is necessary to use a series of sub-models. Thus, they divide the analysis into: (1) initiation of landslide; (2) propagation of landslide; (3) entry of landslide in water (near field); (4) far field propagation of waves. For (1) they use a coupled model in displacements and pore pressures, together with a constitutive model describing soil behavior. Landslide propagation (2) is analyzed with a depth integrated model incorporating fluidized soil rheology. The interaction of landslide and water (3) is modelled with a fully 3D model composed of a level-set algorithm which keeps track of the multiphase interfaces (solid, air and water). Propagation in the far field (4) is performed using depth-integrated Navier-Stokes equations. They apply the model to the experiments by Fritz et al. (2001) and to a hypothetical case in Santa Liestra Reservoir (Spain). However they conclude

that "*...in addition to the difficulties of each sub model, there is the additional problem of linking them, passing the pertinent data from one to another, […]. All models described in this paper present advantages and limitations, and much research is still needed in the four areas described."*

Abadie et al. (2010) in simulating landslide tsunamis present a multiple-fluid Navier-Stokes model of waves generated by rigid and deformable slides. In their framework, the computational domain is divided into water, air, and slide regions, all treated as Newtonian fluids. For rigid slides, a penalty method allows for parts of the fluid domain to behave as a solid. They implement the rigid slide law validated by Grilli & Watts (2005) for underwater motion, which is governed by slide acceleration, fluid added mass, gravity, buoyancy and drag. The drag coefficient C_d is estimated to be 0.2 by Grilli & Watts (2005). However it concerns a rigid ellipsoid-shaped body triggered under the water surface. Therefore the deformability of the sliding mass is not supported. In chapter 5 of this thesis a discussion of this issue can be found. Abadie et al. (2010) also include a representation of granular landslides, which reproduces with partial success the experiments of Fritz (2002). The conclusion affirms that the problem is *"... still far from being satisfactorily solved, which in particular stresses the need for a careful and thorough model validation process.*"

Mazzanti & Bozzano (2009) adapt common numerical models and software that were originally designed for sub-aerial landslides in order to simulate the propagation of combined sub-aerial/subaqueous and completely subaqueous landslides. Drag and buoyancy forces, the causes of energy loss at the landslide-water impact, are substituted by two synthetic coefficients similarly to the Voëllmy (1955) fluid rheology (see the discussion on the topic in section 5.4). The coefficients are estimated by back-analysis of past events.

Panizzo (2004) and Capone (2010) use the SPH method in simulating landslide tsunamis.

Considerable advancements in modeling landslide tsunamis were recently presented by Zhao et al. (2015) and Crosta et al. (2015). The first, use quasi-3D DEM analyses in plane strain by a coupled DEM-CFD code to simulate rockslides from onset to impact with still water and the subsequent wave generation. The second, use an ALE FEM approach to model and analyze the near-field evolution of landslides generating tsunamis, under different 2D and 3D conditions. The sliding mass is simulated as an elasto-plastic Mohr–Coulomb material and the lake water as a Newtonian fluid. Both Zhao et al. (2015) and Crosta et al. (2015) are successfully validated by some 2D and 3D experiments and by simulating the Vajont Dam case (1963). Both methods are of particular interest because they include landslide deformation, a fundamental feature in the

near field analysis. Eventually, both methods are compared and discussed in the same issue. The DEM-CFD needs a rescaling of properties and particle size in order to support a low computational demand. A high hydraulic conductivity results from this assumption. ALE FEM does not need the rescaling. However the DEM-CFD approach also includes rockslide saturation, while ALE FEM does not. Neither model includes air entrainment during impact.

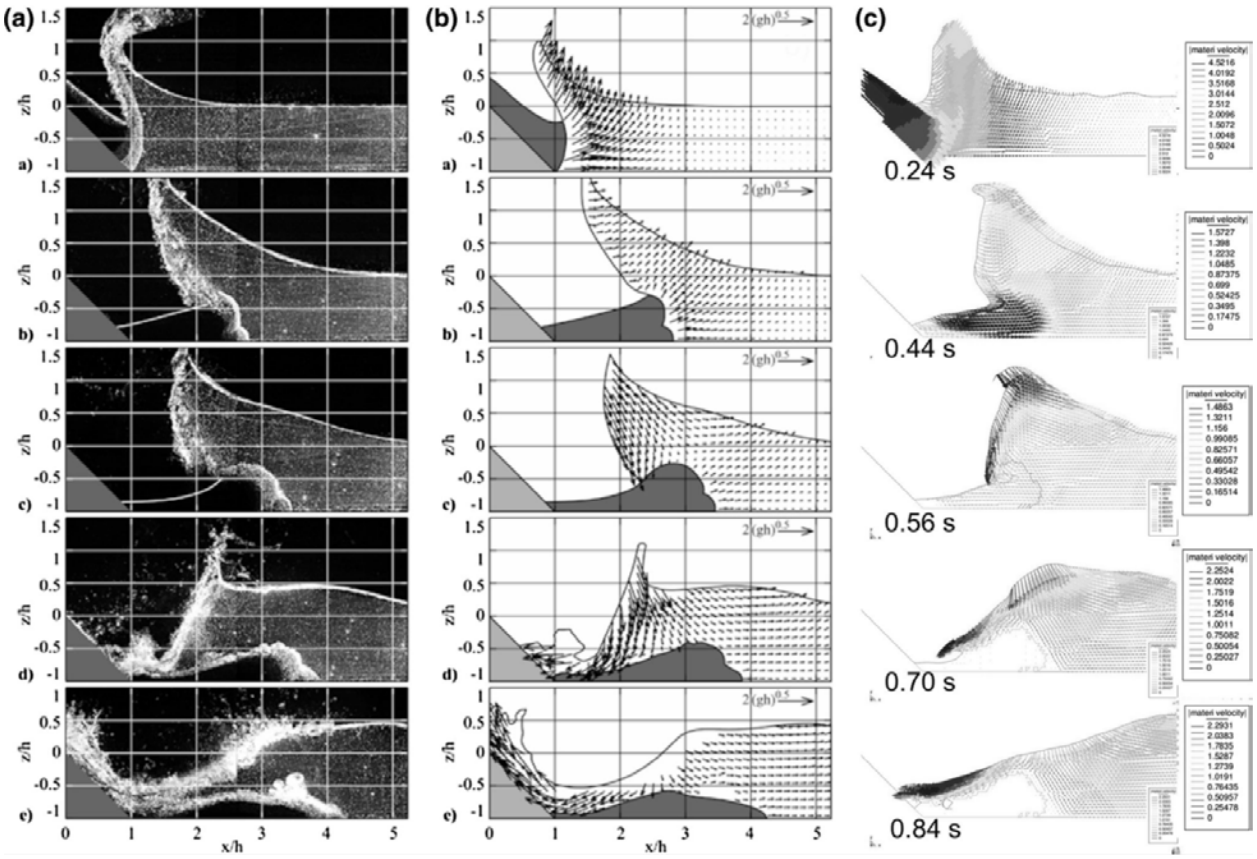

Figure 1.22. Comparison of the observed (left hand and middle panels) and computed (on the right hand side) wave velocity vectors for the 2D experiment by Fritz (2002) (in Crosta et al., 2015).

1.4 Research gaps

Undoubtedly, many authors have addressed the problem over the past 40 years. However, a certain lack of studies was detected within the state-of-the-art. The most significant of such gaps are listed below.

- Only two researches, Huber (1980) and Mohammed (2010) address granular landslides entering a water tank. The first one is an extensive work but, finally, it does not adequately prove the results in a comprehensive way: wave height predictions lack correlation coefficients with the experimental data (Mohammed & Fritz 2012). The second one improves considerably the understanding of the process, but the focus rests

on a unique slope of impact, and measurements are taken mainly at the point of full wave development, neglecting measurements at the zone of initial formation.

- All authors under consideration in the state-of-the-art have used probes to measure wave characteristics. This constrains to making restrictive assumptions of constant wave celerity when measuring wave energy. Moreover, they do not provide continuous measurements of water displacement along the domain.
- The description of the mechanism of energy transfer between landslide and waves, as well as the energy dissipation during motion, have not been sufficiently presented experimentally. Some authors, as Walder et al. (2003) and do Carvalho & do Carmo (2007), propose experiment results describing the sub-aerial and underwater landslide motion, but they simulate the process with a rigid block. Landslide deformation, found here to be an important feature, is ignored.
- The range of landslide Froude and Reynolds numbers employed are frequently limited to relatively low values, while the angles of impact are frequently greater than 25°. Especially in 3D experiments with granular material, there is actually no experience reported of reproducing slides with angles lower than 27.1°.
- A demand exists for experimental results addressing 3D deformable landslide generating tsunamis in a 3D wave tank suitable for validating or calibrating numerical models.

1.5 Objectives of the present thesis

The present work focuses on the study of a granular mass sliding into a water body during the phases of wave generation and initial propagation. The necessity of the study is driven by the lack of field as well as of experimental data on tsunami waves originating from a sliding granular mass and propagating in the three dimensions. Only few authors have addressed this topic in the past.

Deformability is one of the essential features peculiar to a granular mass. This property is not easy to take into account, as the mass rapidly changes its shape during the slide's progress. But, at the same time, deformability is considered important for the triggering behavior of the process.

The other aim of the present work is to consider the effects of 3D wave propagation in a basin. This effect seems to be of primary importance as it can explain - at first instance - the overestimation of empirical formulations such as are produced by experimental studies only made on straight channels.

On the basis of the motivations mentioned earlier in the present study, a new laboratory facility was set up in order to explore a new range of parameters for the presented phenomena, considering a granular sliding mass entering in a water basin. A new measuring system was also set up to observe the mass movement and the wave propagation at high resolution. In designing the measuring method the author intends to pursue the measurement of the produced waves continuously in time and space so as to avoid the classical discontinuous measurements produced by probes.

In civil engineering the task of predicting the effect of natural hazards is fundamental. Thus, an aim of the present work is to give empirical predictors able to quantify the potential hazard due to tsunamis generated by landslides, useful as a basic tool in risk assessment frameworks.

A particular attention is also given to the final deposit of the granular mass, as it is intended to be a measure of the forces the solid material has experienced when hitting the mass of water and transferring its momentum to that medium.

In answering the question of what portion of the momentum, and thus of the energy, is transferred by granular landslides to the water basin, a simplified numerical model will be pursued.

Frictional forces, drag forces as well as turbulence are intended to be quantified. This last task is an "added value" of the work, as it has not been tackled before for the particular configuration of granular deformable landslides.

1.6 Structure of the thesis

The thesis is composed of six chapters. The first introductive chapter helps to present and explain the topic, focusing on historical events, state-of-the-art and the objectives of the research work. The second chapter describes the experimental set-up, examining the laboratory reproduction of the phenomenon and the measurement techniques employed. Special attention is devoted to the avoidance of possible sources of errors and uncertainties in the measurement framework. Within the third chapter the main experimental results are collated and presented in their original form. The elaborations of the experimental results are presented in chapter 4 and 5. Chapter 4 concerns the experimental analysis. It has permitted to generate empirical formulas, relating the landslide characteristics to the produced wave characteristics, as useful tools for risk assessment frameworks. The 5th chapter addresses the definition of a simplified, conceptual numerical model able to describe the energy conversion between the landslides and the produced waves. Finally, the 6th chapter consolidates and presents the conclusions of the thesis.

Chapter 2: Experimental set-up

An experimental device to study landslide tsunamis has been set up in the fluvial-morphodynamics laboratory of the Sediment Transport Research Group (GITS). The facility is located within the laboratories of the Hydraulic, Coastal and Environmental Engineering Department (DEHMA) of the Technical University of Catalonia (UPC), in Barcelona (Spain).

The experimental set-up is described in detail within this chapter.

2.1 Dimensional analysis

The complexity of the phenomenon being researched is highlighted by the considerable number of parameters involved. The problem entails 14 governing parameters described in Figure 2.1 and Table 2.1. Three physical quantities are involved: length, mass and time (Table 2.2). To scale the prototype behavior, the Froude similarity is chosen. The variables to be investigated, also called dependent variables, concern the characteristics of the formed waves. These dependent variables are reported in Table 2.1.

Following the Π-theorem of Buckingham (1914), any property N of the wave, and thus any dependent variable being investigated here, can be expressed as:

$$N = f\left(h_s, l_s, w_s, V_s, m_s, \rho_{s,bulk}, v_s, \alpha, h_w, \rho_w, g, t, x, y\right) \tag{2.1}$$

Only one type of granular material was chosen for this study thus, for simplicity, the granulometry, the porosity θ_s, and the internal friction angle φ_s are not taken as governing parameters. However, it can be seen that $\rho_{s,bulk} = \rho_s\left(1-\theta_s\right)$. The characteristics of the granular material, including the frictional features, are introduced in section 2.3.3.

Being n_1 the number of governing parameters and n_2 the number of physical quantities involved, the Π-theorem states that N can be described by $m = n_1 - n_2$ dimensionless parameters, choosing n_2 repeating parameters, without losing in physical description. In our experiment three physical quantities are involved: length, mass and time (see Table 2.2). The three chosen repeating parameters are h_w, ρ_w and g. Thus the equation (2.1) can be rewritten in dimensionless form as follow:

$$\Pi = f\left(\frac{h_s}{h_w}, \frac{l_s}{h_w}, \frac{w_s}{h_w}, \frac{V_s}{h_w^{\,3}}, \frac{m_s}{h_w^{\,3}\rho_w}, \frac{\rho_{s,bulk}}{\rho_w}, \frac{v_s}{\sqrt{gh_w}}, \alpha, t\sqrt{\frac{g}{h_w}}, \frac{x}{h_w}, \frac{y}{h_w}\right) \tag{2.2}$$

Any convenient combination of the dimensionless parameters in equation (2.2) is valid to describe Π (i.e. Kamphuis & Bowering, 1970). In equation (2.2) one can see the presence of the

landslide Froude number $Fr = v_s / \sqrt{g h_w}$, while Reynolds, Weber and Cauchy numbers are omitted. This is due to the observation that, taking into account the scale of our physical model, the effects of dynamic viscosity μ_w, surface tension σ_w and fluid compressibility K_w of water are sufficiently small to be neglected. However, considerations on the scale effects are presented in section 2.2.

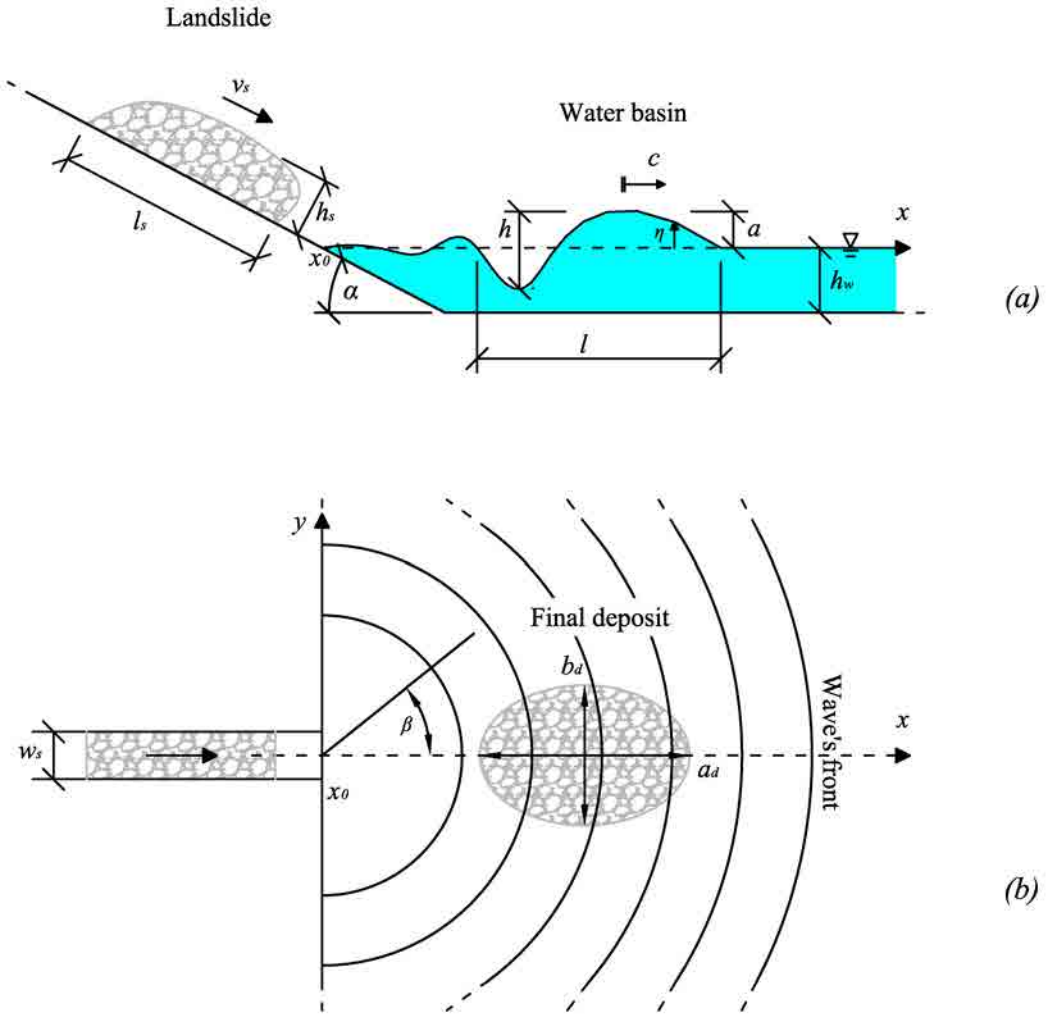

Figure 2.1. Sketch of the phenomenon with coordinate system and parameters involved: a) lateral view; b) aerial view. For the description of parameters see Table 2.1.

Table 2.1. List of landslide tsunamis governing parameters and variables.

List of governing parameters			
Parameter	**Dimension**	**Unit**	**Description**
h_s	[L]	*m*	average thickness of landslide at impact
l_s	[L]	*m*	length of landslide at impact
w_s	[L]	*m*	width of landslide at impact
V_s	[L^3]	m^3	volume of landslide at impact
m_s	[L]	*kg*	mass of sliding material
$\rho_{s,bulk}$	[ML^{-3}]	kg/m^3	bulk density of landslide
v_s	[LT^{-1}]	*m/s*	average velocity of landslide at impact
α	[-]	°	impact angle
h_w	[L]	*m*	water depth in basin
ρ_w	[ML^{-3}]	kg/m^3	density of water
g	[LT^{-2}]	m/s^2	gravity
t	[T]	*s*	elapsed time from impact
x	[L]	*m*	distance from impact along sliding direction
y	[L]	*m*	lateral distance from sliding direction
List of dependent variables			
a_{max}	[L]	*m*	maximum wave amplitude
x_{max}	[L]	*m*	distance of maximum wave amplitude
t_{max}	[T]	*s*	time of maximum wave amplitude
$a(x)$	[L]	*m*	leading wave amplitude along x
$a(t)$	[L]	*m*	leading wave amplitude in time
E_w	[ML^2T^{-2}]	*J*	energy of first wave crest

Table 2.2. List of physical quantities involved in the problem

Name	**Dimension**	**Unit**
Length	[L]	m
Mass	[M]	kg
Time	[T]	s

Particular attention is paid to the energy conversion from landslide energy to the first wave crest energy. Thus, an appropriate energy parameter suitable to define the dimensionless forms of the mentioned energies is the following:

$$E_{w,hydrostatic} = \rho_w g \frac{h_w^{\,2}}{2} w_s l_s \tag{2.3}$$

$E_{w,hydrostatic}$ can be seen as the potential hydrostatic energy that opposes the landslide impact energy. More details on this topic are presented in sections 3.2.7, 4.7 and in chapter 5.

Within this thesis, the empirical predictive formulas were determined by multiple regressions of the measured values in dimensionless form. However, the importance of each governing parameter changes, depending on the predicted variable. Thus, only the more relevant governing parameters are taken, case by case, to define simplified empirical formulas. Similarly, all the combinations of parameters are investigated, but only the more relevant are presented (see chapter 4).

The wave length l and the wave height h are not analyzed in the present study, because wave reflections compromise their measurement (see section 2.4 and 3.2.2). However, l is described in section 3.2.5.

2.2 Scale effects

The dimensionless numbers of interest when considering scale effects on physical models in hydraulics are the Froude number, the Reynolds number and the Weber number. The Cauchy number is not taken into account here, as water is considered as an incompressible fluid. The impulsive Froude number Fr, Reynold number Re and Weber number We are presented below, together with the grain Reynolds number Re^*:

$$Fr = \frac{v_s}{\sqrt{g h_w}} \tag{2.4}$$

$$Re = \frac{\rho_w \sqrt{g h_w^{\,3}}}{\mu_w} \tag{2.5}$$

$$Re^* = \frac{\rho_w d_m v_s}{\mu_w} \tag{2.6}$$

$$We = \frac{\rho_w g h_w^{\,2}}{\sigma_w} \tag{2.7}$$

where d_m is the mean grain size of the landslide granular material.

For the experiments carried out in support of the present thesis, the dimensionless numbers previously listed are in the following ranges, considering values of $\mu_w = 10^{-3}$ kg/(m·s) and $\sigma_w = 7.28 \cdot 10^{-2}$ kg·m·s^{-3} valid for water at 20°C:

- $1.91 \leq Fr \leq 4.17$
- $280143 \leq Re \leq 391511$
- $58334 \leq Re^{*} \leq 114049$
- $5390 \leq We \leq 8422$

Observing that Re and Re^{*} are in the order of magnitude of 10^5, it is possible to affirm that the landslide tsunamis in laboratory simulation are highly turbulent close to impact. A turbulent condition involves less viscous effects than in a laminar flux, because inertial forces clearly overcome viscous forces. Thus close to impact at least, viscous effects are not significant.

However the viscous effects on the propagation of the formed waves could not be discarded *a priori*. Generally, the reduced scale of laboratory tests, run in Froude similarity, can involve possible viscous effects, due to the interaction between the propagated waves and the bed and boundaries of the tank or channel where the same waves are propagated. The generated tsunami waves are typically non-linear. To simplify the problem, the evaluation of transitional solitary wave damping due to viscous effects is taken as reference. Keulegan (1948) provided an analytical solution (equation (2.8)) to evaluate the gradual extinction of solitary waves along a channel:

$$1 - \frac{a_{sol}(x)}{a_{sol,0}} = 1 - \left(1 + \left(\frac{h_w}{a_{sol,0}} \right)^{-1/4} \frac{x}{12 h_w} \left(1 + \frac{2h_w}{W} \right) \sqrt{\frac{\nu_w}{g^{1/2} h_w^{\,3/2}}} \right)^{-4} \tag{2.8}$$

where $a_{sol}(x)$ is the solitary wave amplitude along the distance x, $a_{sol,0}$ is the initial wave amplitude at $x = 0$ and W is the width of the tank. Figure 2.2 shows wave damping following the equation (2.8) for different $a_{sol,0}$ at the farthest measured point of the water tank used in this thesis, being the worst scenario of wave attenuation. For the reference value of $a_{sol,0} = 0.1$m the equation (2.8) shows that the damping due to viscosity effect for a $h_w = 0.2$m is in the order of 1 %. Values of $h_w < 0.1$m start to show a viscous effect of more than 4%. Similar conclusions are presented by Heller et al. (2011): they give a rule of thumb of $h_w \geq 0.2$m to avoid the effect of viscosity in hydraulic models of impulse wave investigation.

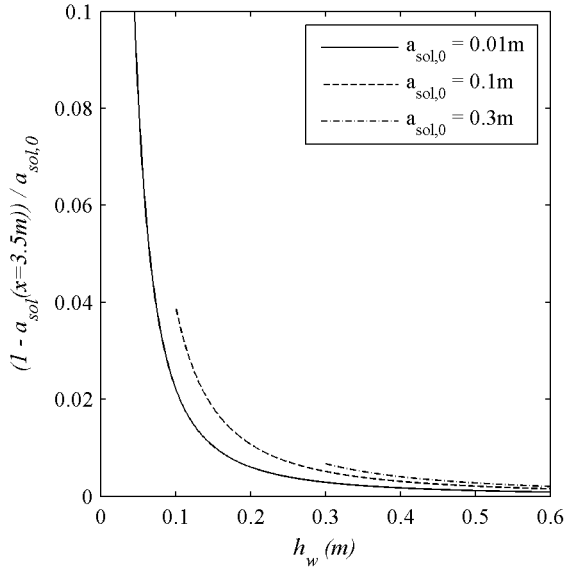

Figure 2.2. Wave damping due to viscous effects, following Keulegan (1948). The equation (2.8) is evaluated at a distance of x=3.5 m from the impact, for different initial wave amplitudes $a_{sol,0}$.

The Weber number has an order of magnitude of 10^3. This means that the fluid's inertia is clearly high compared to its surface tension.

In literature, surface tension effect has found to be negligible on wave propagation for wavelengths greater than about $2x10^{-3}$ m (i.e.: Dean & Dalrymple, 1991; Johnson, 1997; Novak at al., 2010). Moreover Novak et al. (2010) specify that wave celerity c has to be greater than 0.23 m/s to avoid surface tension effects. In our experiments the wavelength l is of the order of 10^0 m (see section 3.2.5), and c is of the order of 10^0 m/s (see section 3.2.4). Surface tension can induce scale effects also on breaking waves, which have been observed in some laboratory runs. Novak et al. (2010) specify that a $Re > 3x10^4$ is sufficient to avoid surface tension effects on breaking waves. In our experiments this condition is met by a wide margin.

Some doubt may arise on the role of surface tension in the splash zone, where droplets and splash occur. While this behavior certainly can exists both in the laboratory and in nature, in laboratory experiments those effects are implicitly taken into account (Walder et al., 2003).

2.3 The facility

The experimental set-up was designed properly to simulate the landslide tsunami behavior in its generation and propagation. Thus, special attention was devoted to reproduce what had been identified as the main features of the problem: the three-dimensional granular landslide deformation and the three-dimensional wave propagation.

It was found necessary to force the landslide to reach such a high velocity, and thus a high *Fr*, so as to both fill gaps in previous researches and achieve similarity with real events occurring in nature. At the same time, adequately high landslide velocity and water depth were selected for the purpose of avoiding viscous and surface tension effects (see section 2.2).

The main characteristics of the experimental device are:

- dimension of the water basin: $L = 4.10$, $W = 2.45$ m
- angle of landslide impact $\alpha \leq 27.5°$
- landslide impact velocity $v_s \leq 7$ m/s
- landslide mass weight $m \leq 150$ kg,
- still water depth range: $0.2 \text{ m} \leq h_w \leq 0.6$ m,

The experiments that were actually carried out do not cover the full ranges of parameters previously listed but, potentially, the full ranges can be explored in future studies.

The set-up was used in the past to study fluvial-morphodynamics and sediment transport in gravel bed creeks (Bregoli, 2008), as well as debris flows (Steiner 2006; Morlotti 2010). For the present study, the facility was modified to investigate the landslide tsunami process.

The resulting experimental set-up is extensively described in all its part hereinafter.

2.3.1 Landslide generator

The system consists of a steep flume, with slope variable from 0 to 27.8°, designed to release the granular material into a rectangular water basin, placed at the exit of the channel (Figure 2.3a).

Observing past studies (Steiner 2006), if the granular material were to be released along the bottom of the channel, the basal friction would considerably reduce its acceleration.

Thus, to give to the granular material a sufficient velocity, a system was developed, able to achieve high-speed mass movement and, at the same time, permitting the measurement of the main landslide parameters. The solution was obtained through the fabrication of a wheeled steel box (Figure 2.3b and details in Figure 2.4), sliding on rails fixed to the lateral walls of the flume. The rails have a very low degree of surface roughness. The box achieves sufficient acceleration along the 6.20 m of rail length (see Figure 2.5). At the end of the flume, a high-resistance shock absorber (hydraulic piston) instantly stops the box, thus forcing the opening of the flaps and the release of the granular material (Figure 2.6).

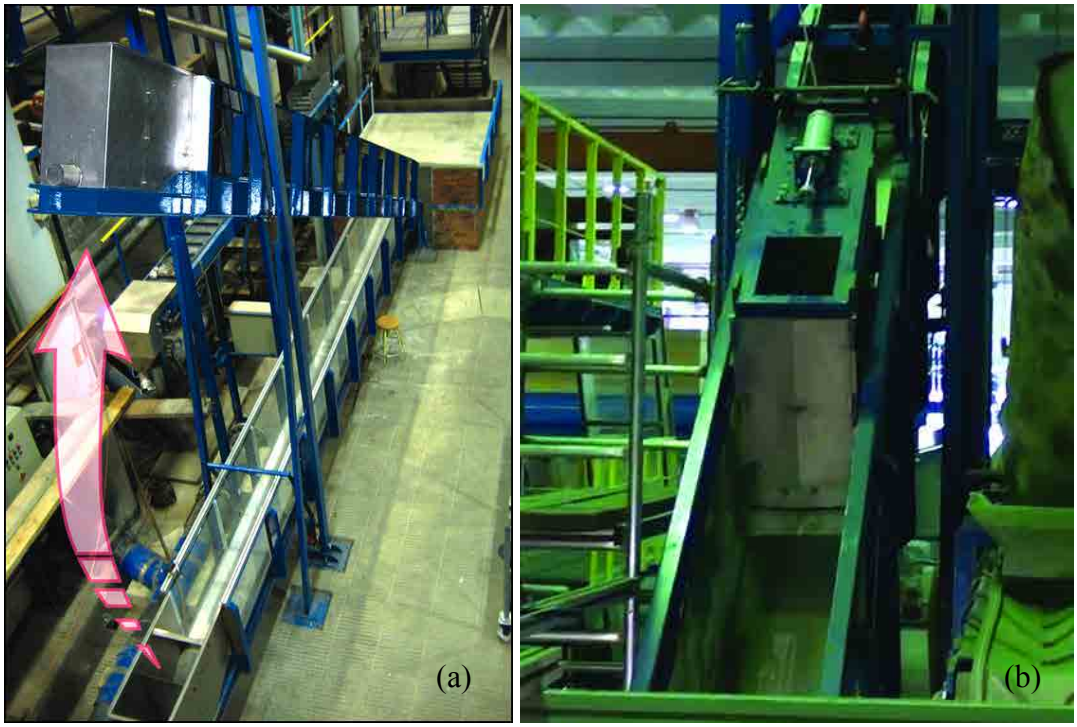

Figure 2.3. Landslide generator: (a) view of the variable slope flume in its maximum (27.8°) and minimum (horizontal) slope configuration; (b) front view of the steel box sliding along the flume at its maximum slope configuration.

The released granular material plunges into the basin (Figure 2.7a), creates a crater and a splash (Figure 2.7b) and eventually triggers a wave train. In its underwater motion the simulated landslide slides along a wedge having the same roughness of the bottom of the tank. Of the 41 conducted experiments, 8 do not include the wedge at the box exit. This configuration is the result of a technical drawback for low angles of impact. But adequate precautions have been taken into account in the evaluation of the results produced by these 8 experiments (see chapter 4 and 5).

The measurement of the geometry and velocity of the landslide is achieved by recording with a high speed camera the released material, properly marked with a powerful laser sheet. More details on landslide measurement are given in section 2.5.

The system allows the independent modification of the landslide main parameters. The mass can be changed by choosing the amount of granular material. The geometry of the landslide can be varied in its initial length, thickness and width within the box maximum internal dimensions: 1.00x0.30x0.34 m (length x thickness x width). The angle of impact can be adjusted by varying the flume slope, between 15° and 27.8°. The velocity at impact can be varied by dropping the

box from different heights, thus changing its initial potential energy. The tank water depth can be set, if required, at 0.20 m, 0.40 m or 0.60 m.

Once the experiment is concluded, the box is filled again for the next experiment with the selected amount of gravel and is lifted back to its initial position by means of a winch.

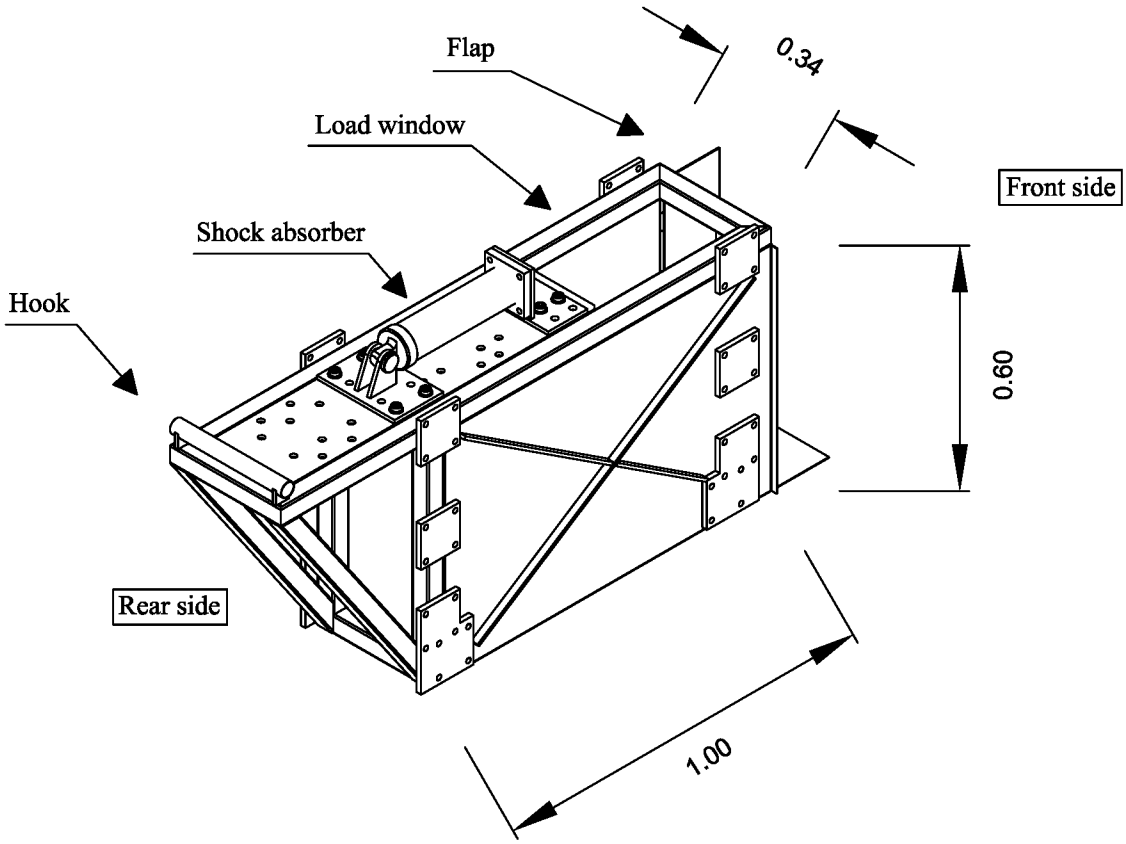

Figure 2.4. Sliding box characteristics. Measures in meters. Technical plans are reported in Appendix A .

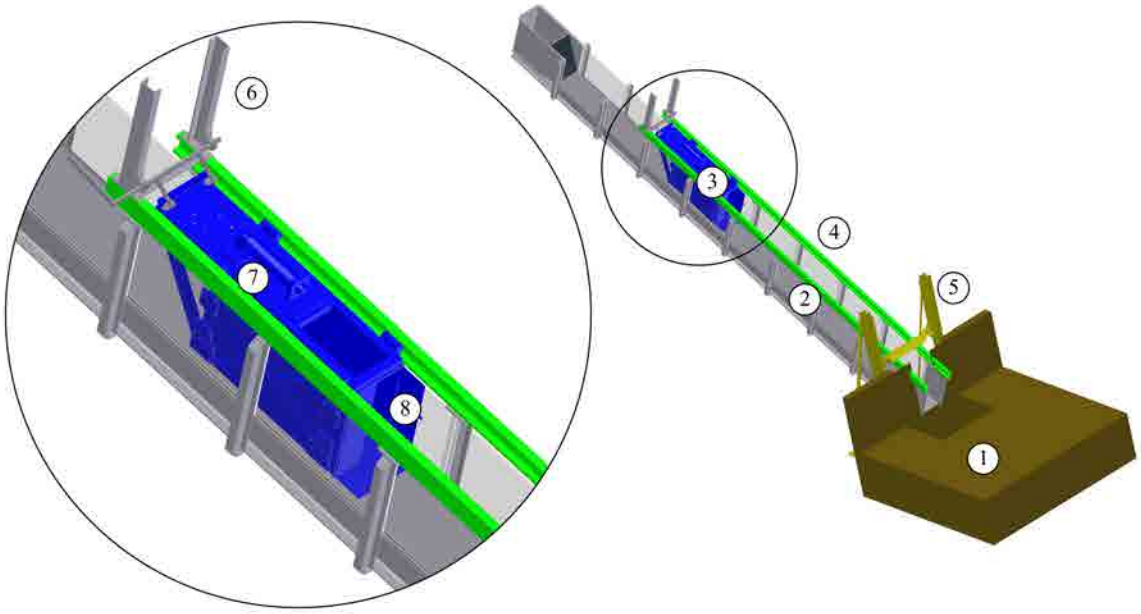

Figure 2.5. 3D view of the flume and details of the sliding box at its initial hooked position: 1) water tank; 2) flume; 3) sliding box; 4) rails; 5) braking bridge structure; 6) triggering hook; 7) hydraulic piston shock absorber; 8) exit door for the granular material.

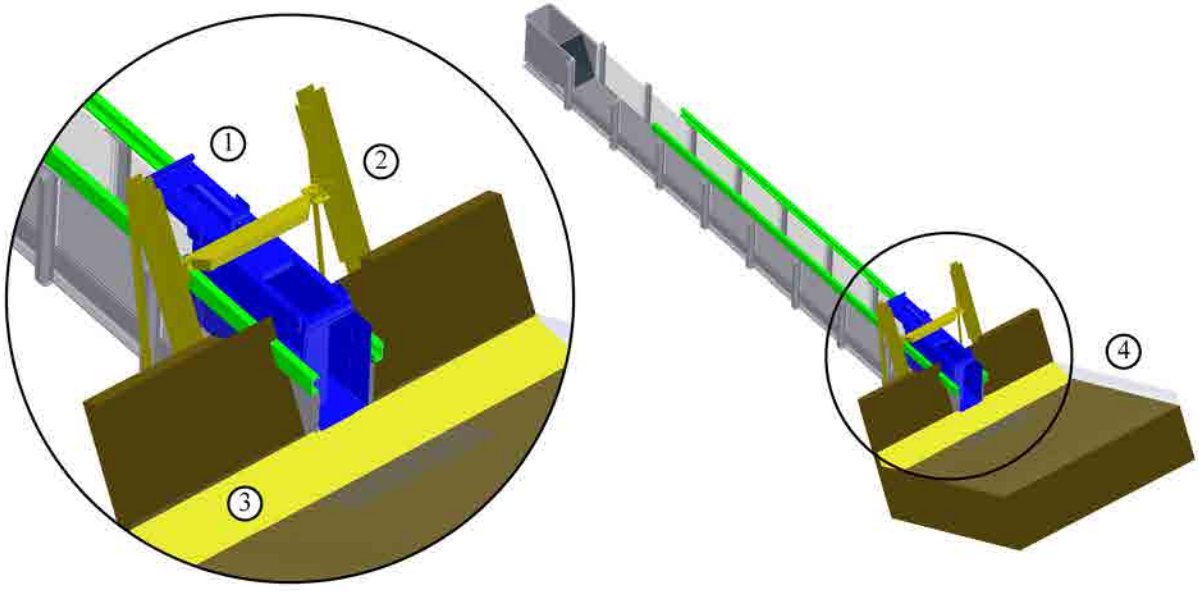

Figure 2.6. 3D view of the flume and details of the final position of the sliding box: 1) hydraulic piston shock absorber; 2) braking bridge structure; 3) wedge; 4) water tank.

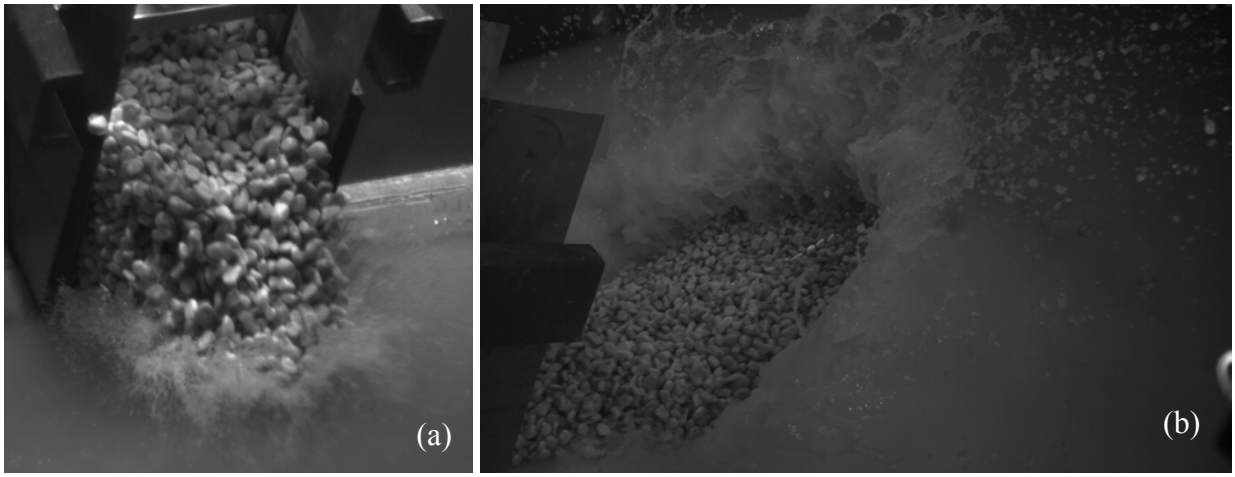

Figure 2.7. Granular material released in water basin after the flaps open. Frames extracted from two video clips from the high speed camera recording at 640 f/s: (a) front view of the granular material entering water for experiment *Type_a_M120_27.8deg* (see Table 3.1); (b) rear view of the granular material sliding into water, creating crater and splash.

2.3.2 Wave tank

The wave tank is set up taking advantage of the multifunctional platform existing at the exit of the aforementioned flume. The tank was used in the past to study debris-flow mobility, debris-flow fans and sediment transport in steep creeks. For the present application, the tank was modified by sealing the manhole used for sediment recovery, adding a wooden wedge and lateral walls and closing the end section with a wooden wall. The tank, the wedge and the additional walls were covered with a water-proof, strong plastic paint. The resulting volume has a width of 2.44m, a length of 4.10m and a possible water depth of 0.60m. The lateral walls have a total height of 1.20m to avoid splash and water spills out of the tank.

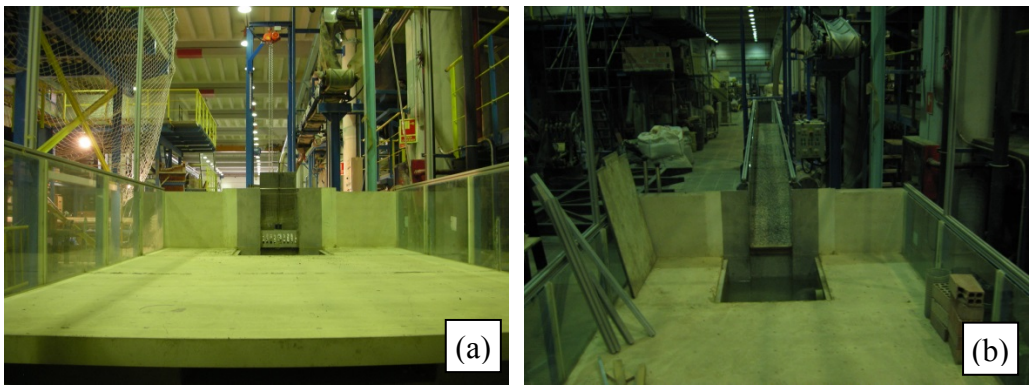

Figure 2.8. (a) View of the platform at the exit of the channel in its previous configuration; (b) general view of channel, manhole for sediment recovery and the platform.

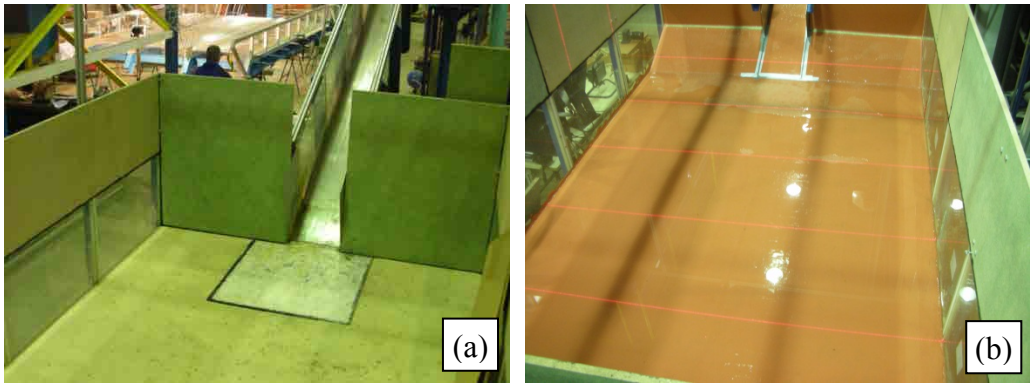

Figure 2.9. Modifications to the water tank: (a) sealed manhole and positioned walls; (b) final configuration of tank with wedge and plastic paint.

2.3.3 Granular material

Gravel samples with different characteristics are available in the laboratory, but only one type was chosen. In this study the selected gravel has a white colour (see Figure 2.10). The white colour better reflects laser light and is easier to recognize when processing binary images. A description of the particle-size distribution of this gravel is given in Table 2.3, while the geotechnical parameters being used are given in Table 2.4.

Table 2.3. Descriptive diameters in mm of the gravel used, after Guevara (2007).

d_{16}	d_{30}	d_{50}	d_{84}	d_{90}	d_m	d_{max}	d_{min}
13.7	14.96	16.9	21.7	22.9	19.5	25.4	12.7

Table 2.4. Geotechnical parameters: ρ_s is the stone density (Guevara, 2007), θ_s is the porosity or void fraction and $\varphi_{s\text{-}b}$ is the basal friction angle between gravel and slope, as evaluated in this study.

ρ_s (kg/m^3)	θ_s (-)	$\varphi_{s\text{-}b}$ (°)
2820	0.4	30

Considering the values of Table 2.4, the following densities can be assessed:

$$\rho_{s,bulk} = \rho_s\left(1-\theta_s\right) = 2820 \cdot 0.6 = 1692\, kg/m^3 \tag{2.9}$$

$$\rho_{s,bulk,sat} = \rho_{s,bulk} + \rho_w\theta_s = 1692 + 1000 \cdot 0.4 = 2092\, kg/m^3 \tag{2.10}$$

$$\rho'_{s,bulk,sat} = \rho_{s,bulk,sat} - \rho_w = 2092 - 1000 = 1092\, kg/m^3 \tag{2.11}$$

where ρ_s is the stone density, θ_s is the porosity or void fraction of the bulk, $\rho_{s,bulk}$, $\rho_{s,bulk,sat}$ and $\rho'_{s,bulk,sat}$ are respectively the bulk density, the saturated bulk density and the submerged saturated bulk density of the gravel, while ρ_w is the water density.

The mass of the bulk m_s is given by the following equation:

$$m_s = V_s \rho_{s,bulk} \tag{2.12}$$

where V_s is the volume of the bulk. The submerged mass of the bulk m'_s is given by the equation (2.13).

$$m'_s = V_s \rho'_{s,bulk,sat} \tag{2.13}$$

Combining equations (2.12) and (2.13) permits to determine m'_s trough known quantities as follows:

$$m'_s = m_s \frac{\rho'_{s,bulk,sat}}{\rho_{s,bulk}} \tag{2.14}$$

The basal friction angle between gravel and slope $\varphi_{s\text{-}b}$ is evaluated here with laboratory tests in dry condition, using the same plastic-painted wedge utilized in our laboratory experiments (see Figure 2.10). Starting from the horizontal plane, the wedge inclination is increased till the gravel starts to slide down. The slope is measured with a digital inclinometer, having an accuracy of 0.05°. The process is repeated 3 times and filmed in order to validate the angle of initial movement. This angle, corresponding to the basal friction angle, is assessed as $\varphi_{s\text{-}b} = 30°$.

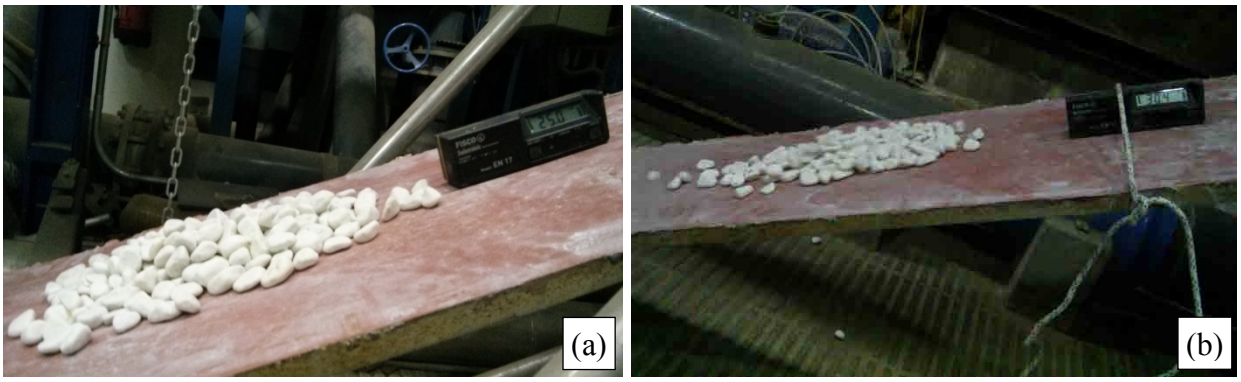

Figure 2.10. Two frames from a video recorded in the laboratory assessing the basal friction angle between slope and gravel by progressively increasing the slope: the gravel is initially stationary on a slope of 25°. (a) and then starts to slide down the wedge when 30°. of slope is exceeded (b).

2.4 Wave reflection issues

The waves propagate trough the tank along the 3 directions and quickly reach the walls, were they are reflected. Having the tank a longitude L = 4.20 m and a width W = 2.44 m, the reflections can produce a strong influence on the experimental data. Thus the reflections must be properly analyzed in order to correctly assess the clean part of the wave signal. Considering, at

first instance, the hypothesis of radial wave, the reflection is assumed to be symmetrical with respect to the walls.

The mass of water starts to be reflected much before the arrival of the peak at the wall. This means that the wave starts to be reflected once its front touches the wall (Figure 2.11). Being the wave large in relation to its amplitude, the evaluation of the arrival of its front is not a foregone issue.

The beginning of the reflection can be assessed when a certain water vertical displacement η_{ref}, having a fixed percentage p of the wave amplitude a, arrives at the wall. p is fixed thanks to available observation.

$$\eta_{ref} = pa \tag{2.15}$$

Two types of reflection are recognized: frontal (the waves reaching the end wall are reflected back); lateral (the waves reaching the lateral walls are reflected symmetrically back to the centerline).

In the case of the frontal reflection $p = p_{front} = 0.15$ is assessed, thanks to the comparison with the Mohammed and Fritz (2012) experimental data (section 3.2.2.1), while $p = p_{lat} = 0.50$ is fixed in case of lateral reflections.

Reflections are credited with compromising the signal, in the worst case after the first crest, and in the best case after the second crest. Therefore, in any case, all measurements in this study realized on the first crest are valid.

More details are given in section 3.2.2, where geometrical concepts are introduced in order to analyze the frontal and lateral reflections.

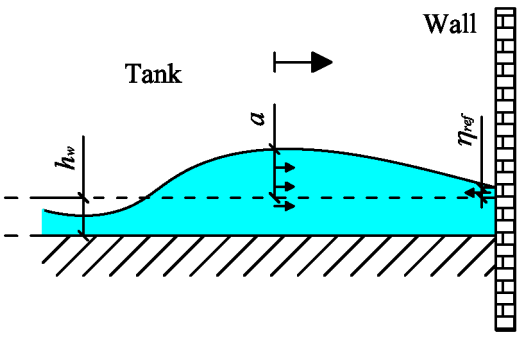

Figure 2.11. Wave reflection

2.5 Measurement system

A measurement system was designed *ad-hoc* for the experimental set-up. It is based upon an extensive use of imagery post-processing. The images are captured trough an array of different video cameras. Due to the high velocity of the simulated landslide, a high-speed camera (HS), able to shoot up to 1000 frames per second (f/s), is focused upon the exit of the sliding box. The camera records the evolution of the granular material (velocity and thickness) on a center line drawn by a laser sheet.

A number of laser sheets project lines on the water surface (Figure 2.12). The water has been previously loaded with a small amount of kaolin that colors the fluid in white, reflecting the lasers at water surface. The amount of kaolin has been set at 5‰ of water volume. This kaolin content does not alter the viscosity of the water. Kaolin is odorless and does not dissolve in water, thus it can be recovered easily after drying the tank.

Three high definition (HD) video cameras focus on the water tank, recording from different points of view the produced water displacement at the laser sheets (see Figure 2.12).

In Figure 2.12 one can observe the hatched area representing the respective angles of view of the two main cameras employed: the HD Camera C, and the HS Camera. The two angles of view overlap at the landslide entrance. This is necessary to connect the observations of Camera C and the HS Camera with the instant of impact.

Through a calibration process employing a mathematical-geometrical transformation algorithm created *ad-hoc* by the GITS team (Bateman et al., 2006), the metrical measurement of the laser lines is achieved.

The final deposit is also measured after each run, once the basin is emptied.

2.5.1 Lasers

The laser generators employed here are of two types: a high-power green laser and a low-power red laser. Both lasers are generated by a laser diode and the produced laser beams have line collimators.

The green laser specifications are as follows:

- manufacturer: Changchun Dragon Lasers Co., Ltd (China)
- wavelength (colour): 532nm (green)
- power: 1W
- stability: 5%
- power control: knob
- optical fibre: 14mm diameter with SMA905 fibre connector

- collimator: focusable line tracer, line size 4m length per 1cm width at 2 meter distance (manufactured by Monocrom, Spain).

The six red lasers' specifications are as follows:

- manufacturer: Laserlands
- wavelength (colour): 650nm (red)
- power: 5mW
- power control: on/off
- collimator: integrated focusable line tracer, line size 1-3m length per 2mm width at 1 meter distance.

The green laser, having a collimator able to project a line of 4 meters of longitude, marks the center line of the water tank along the x coordinate. Moreover, the same laser line marks the surface of the granular material entering the water. The high power of the laser is necessary to properly illuminate the gravel. The choice of white gravel is due to its high reflectivity of light. In fact, the HS camera needs a powerful illumination to be able to capture suitable images, because of the minimal time the shutter stays open.

The main measurements for this thesis are performed along the mentioned green line.

The six red lasers are positioned orthogonally to the green line and are used to evaluate the lateral propagation of the wave.

The final geometrical configuration of the laser sheets is described in Figure 2.12 where it is also possible to observe the position of the four cameras employed.

In this thesis, the measurements taken along the red lines form the basis for the evaluation of the front shape of the produced waves (see section 3.2.2).

As explained before, the laser sheets mark the water surface because the water is loaded with kaolin that adequately reflects the laser light (see Figure 2.13).

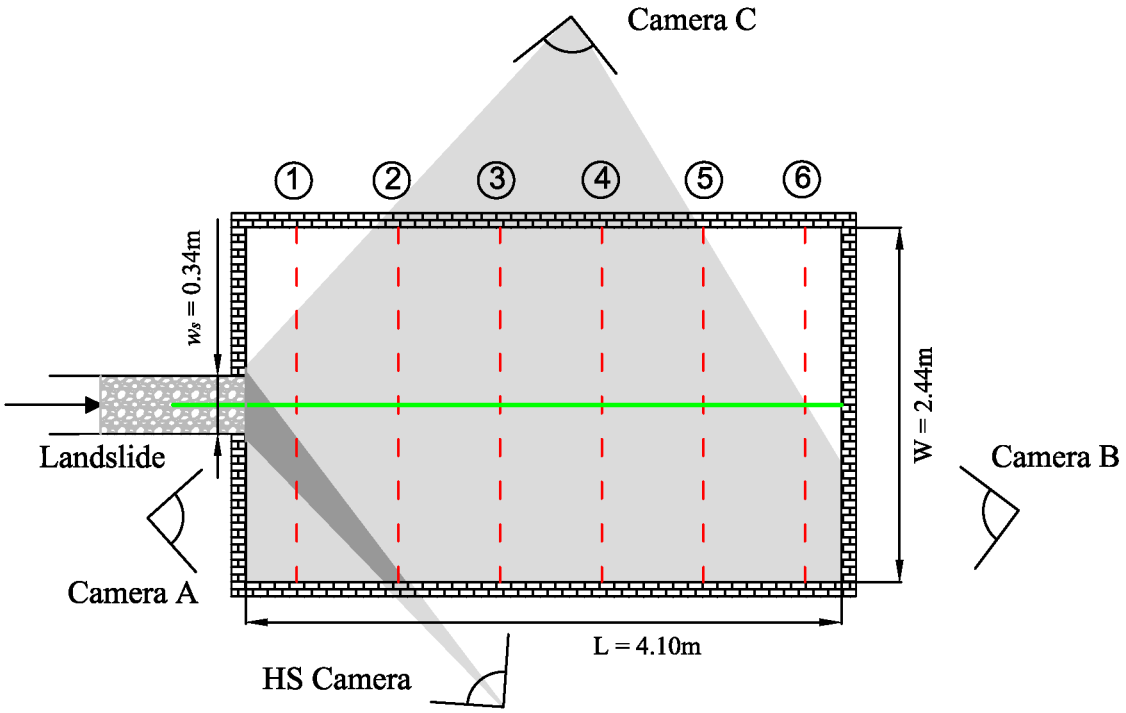

Figure 2.12. Laser sheet position inside the water tank and point of view of the three HD cameras (named Camera A, B and C) focusing on the water tank, as well as of the HS camera recording the granular material. The hatched areas represent the angles of view of Camera C and the HS Camera.

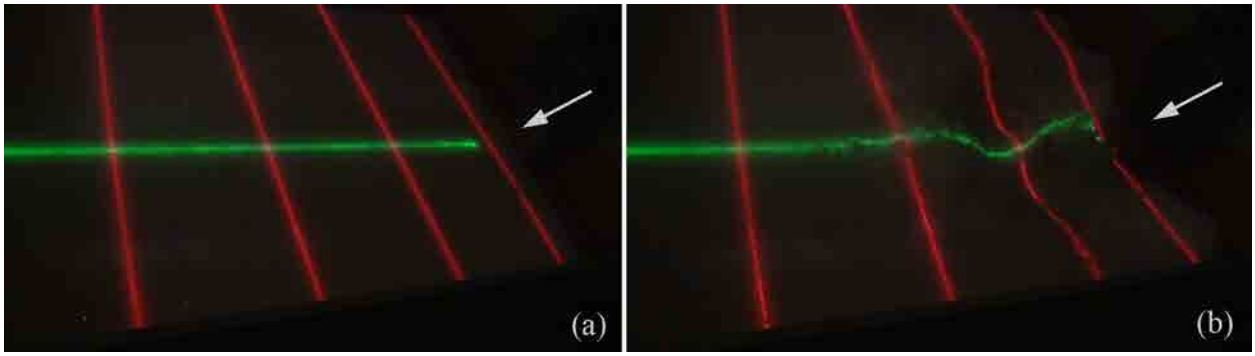

Figure 2.13. Laser grid on the water tank for the experiment *Type_b_M50_27.8deg* (see Table 3.1): a) water surface at time zero, immediately before impact; b) water surface displacement at 0.7s after impact. The arrow points out the impact point and impact direction.

2.5.2 High speed camera

The measurements of the granular material entering the water basin are achieved by recording its progress with a high speed video camera. The device employed is a BASLER A504k area scan camera (Figure 2.14a) with a high speed CMOS sensor (Figure 2.14b), designed for industrial use. The main characteristics are:

- digital sensor: MICRON® MI-MV13 CMOS
- colour: monochrome
- resolution: 1280x1024 pixels (1.3 megapixel)
- pixel size: 12x12 μm
- frame rate at full resolution: 500 f/s (equivalent to a frame period of 1/500 s or 2 ms)
- video output: Camera Link (full), 10 taps, 8 bits each
- RAM dedicated storage: 8 Gb
- lens mount: Nikon

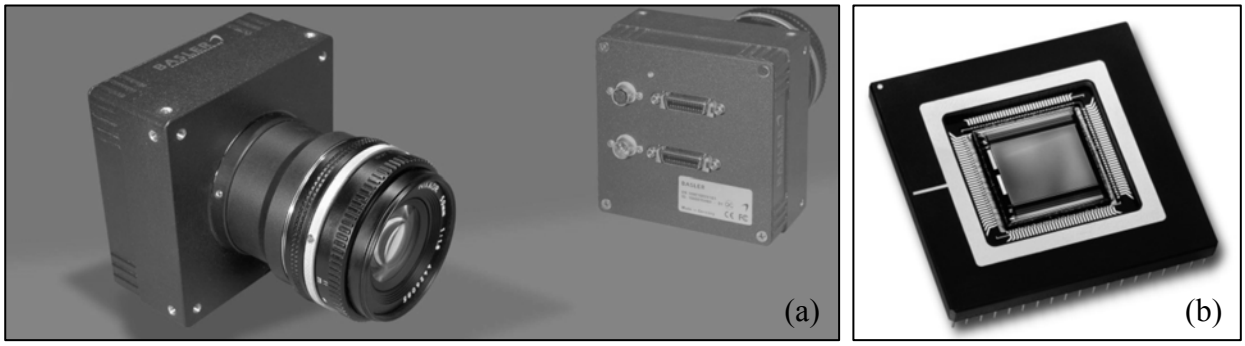

Figure 2.14. BASLER A504k high speed video camera: a) front and rear view of the video camera; b) the MICRON® MI-MV13 CMOS digital image sensor of 1280x1024 pixels (1.3 megapixels) mounted in the camera. (Photos extracted from the Basler A500k user's manual, 2008).

The camera is particularly sensitive to green light (see Figure 2.15) and for this reason a green laser light of 532nm was selected.

The lens used is the Nikon AF Nikkor 50mm f/1.4D. Despite the narrow focal length (50mm, fixed), this lens was selected thanks to its aperture: the high speed camera needs a large amount of light in order to capture readable images at high frequency. The Nikon AF Nikkor 50mm f/1.4D has a maximum aperture of f/1.4 which guarantees high luminosity levels for the required short exposure time. Moreover, this lens has no perspective distortion, which instead characterize wide-angle or telephoto lenses: it does in fact assure a low- distortion image, a basic requirement for the present application.

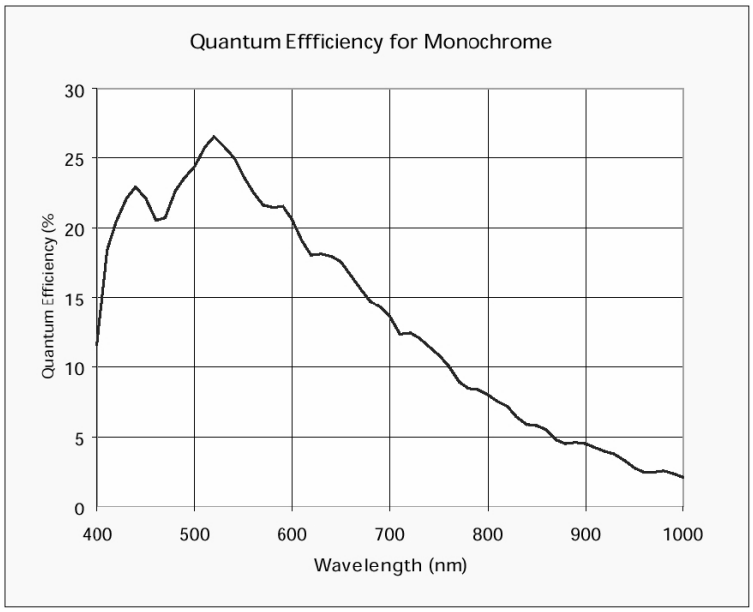

Figure 2.15. Quantum efficiency for the BASLER A504k high speed video camera. The peak corresponds to the green light (532nm). (Graphic extracted from the Basler A500k user's manual, 2008).

The camera is managed with the XCAP™ software, which is the ready-to-run image analysis software for PIXCI® frame grabbers. Through this software it is possible to select the area of interest (AOI) within the photographic frame (thus reducing the image dimensions), the exposure time and the frame rate, amongst other settings. The exposure time is crucial when recording the granular material in our application: it should be long enough to capture sufficient light and short enough to obtain crisp, blur-free images. The exposure time also influences the maximum recording frame period: the camera cannot take photographs at a frame period lower than the exposure time. Increasing the lens aperture could help capture more light and thus decrease the frame period. However, an excessively large aperture produces an extremely shallow depth-of-field, resulting in a strong background blur, which limits clear observation only to the image area where the lens is focused.

The AOI is carefully chosen to ensure the area being recorded is sufficiently large to include the entire process and, at the same time, small enough to limit the image dimensions so as to minimize memory space requirements. Similarly, the frame rate must be chosen so as properly to describe the granular flow while limiting the amount of memory space required.

Based on the analysis of the issues mentioned above, the camera settings have been chosen as follows:

- AOI: 800x800 pixels
- lens aperture: f/1.4
- time of exposition: 2 ms
- frame rate: 500 f/s

Depending on the ambient light available, the previous settings were slightly modified for the different experiments (more details in Appendix D).

The light was a major issue in HS camera recording. For instance, the frame in Figure 2.16a was extracted from a video recorded with the HS camera for the experiment *Type_a_M120_27.8deg* (see Table 3.1). This video was recorded with an AOI of 800x800, a lens aperture of f/1.4, an exposure time of 1.4 ms, and a frame rate of 640 f/s. To make the entire process of the granular material entering the water visible to the camera, 5 halogen lamps of 500W each (2500W in total) had to be used to project sufficient light on the sediment entrance.

Finally the use of a green laser of 1W power collimated on a line over the gravel surface results in an illumination as reproduced in Figure 2.16b. The frames were analyzed in their binary form after conversion from grayscale (8 bit) to black and white (1bit) (see example in Figure 2.16c).

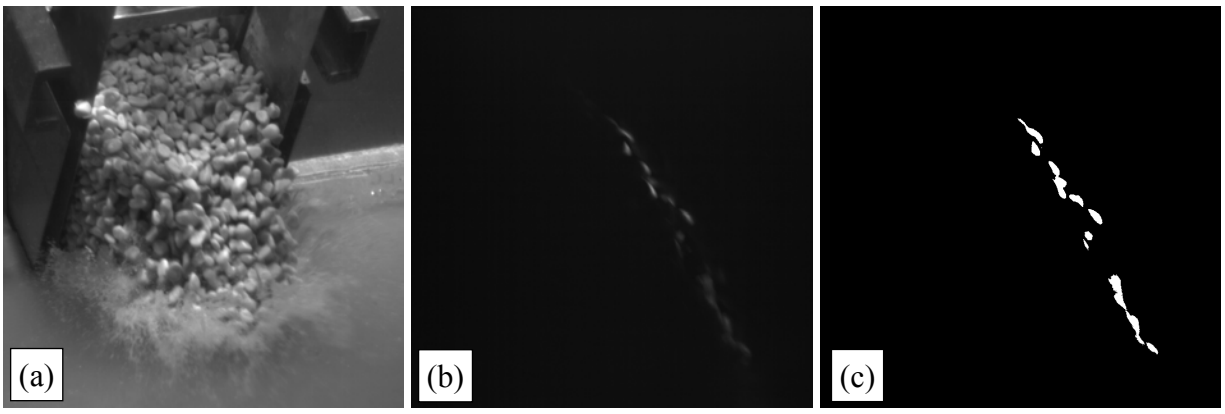

Figure 2.16. Frames extracted from HS camera videos for similar experiments: a) *Type_a_M120_27.8deg* at *t* = 0.042, lighting by 2500 W halogen lights*; b) Unique_M120_27.8deg at t* = 0.042 s lighting by 1W green laser line; c) same as figure b) but at 1bit after applying a threshold on pixel intensity.

2.5.3 High definition cameras

High definition cameras (HD) were employed to record the laser grid projected on the water surface. As explained before, the water was loaded with a small amount of kaolin, thus the

recorded lines mark the water surface elevation. Three full-HD Sony Handycams were employed for the first experiments. The cameras have the following characteristics:

- colour: RGB
- resolution: 1920x1080 pixels (fullHD)
- pixel size: 1.65x1.65 μm
- frame rate at full HD: 24 f/s

The Sony Handycam has a very good performance in capturing red light (see Figure 2.13 a and b).

However, it was decided for the following experiments to use two Canon EOS 550D. Those Canon are reflex photo cameras able to record videos at full-HD as well as at HD. They are quite adaptable to different applications, due to the large number of different lenses available. In general, optics for photo cameras entail less distortions than those for video cameras. The manual settings of the reflex photo cameras also offer an advantage for our application. The Canon EOS 550D is also able to record HD videos at a frame rate of 50 f/s. Unfortunately, the Canon EOS 550D sensor has a poor sensitivity at the wavelength of red lasers and the limits this posed to the observation of the laser-produced red lines was a major drawback.

The HD resolution was chosen for this application. Thus the specifications of the Canon EOS 550D are:

- colour: RGB
- video resolutions: 1920x1080 pixels (full-HD); 1280x720 pixels (HD)
- pixel size: 4.3x4.3 μm
- frame rate: 24 f/s at fullHD; 50 f/s at HD;

The lens mounted is a Tamron 17-135mm zoom. With this lens the following settings have been selected:

- ISO: 400
- lens aperture: f/4.5
- exposure time: 1/160 s
- zoom: 17 mm (wide angle)

An example of a frame extracted from a HD video can be observed in Figure 2.17.

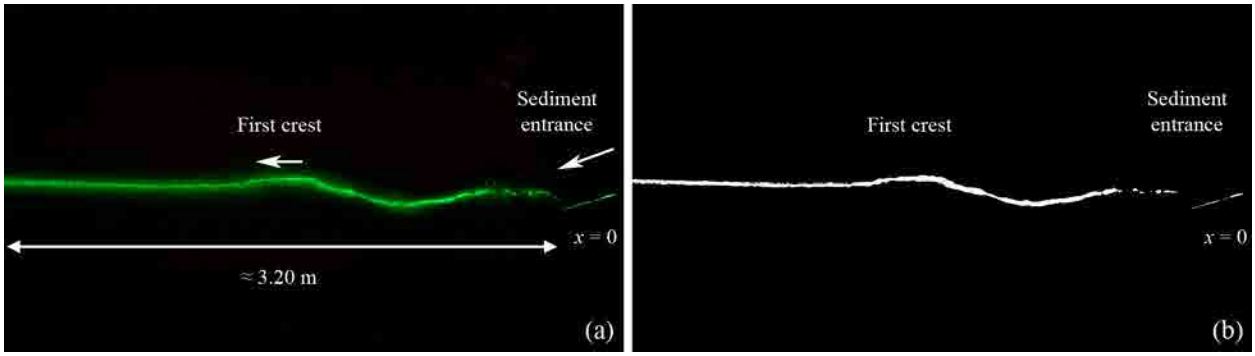

Figure 2.17. Extracted frame from an HD video recorded with the Canon EOS 550D, for the experiment *Unique_M100_27.8deg* (Camera C): a) color frame at t = 0.9 s after impact; b) same frame as in a) but in 1bit after applying a threshold on pixel intensity for the green channel.

2.5.4 Measurement framework

The video frames previously described need a proper calibration to be translated from the spatial references of the camera into the spatial references of the measurements. The calibration methodology, developed here, is based upon the method proposed by Tsai (1987) and was employed by Bregoli (2008) in the fluvial-morphodynamics laboratory of the GITS team, when conducting experiments in bed evolution and sediment transport in creeks. In the following sections the calibration, the image pre-processing and the measurement methodology will be presented.

2.5.4.1 Calibration methodology

Camera calibration in the context of machine vision is a technique extensively used in robotics and automation. This technique allows to define the parameters of transformation between the spatial references of the camera (images) and the spatial references of the measurement (world), through the optimization of a number of parameters (Tsai, 1987).

The parameters are divided in two subsets:

- intrinsic parameters (camera internal geometric and optical characteristics such as the focal and the CMOS sensor characteristics)
- extrinsic parameters (3D position and orientation of the camera frame relative to a certain world system of coordinates)

The optimization can be linear or nonlinear. Linear optimizations require less effort to be solved and are more stable than nonlinear ones. Moreover, in nonlinear optimization, an initial good guess of parameters is required. A popular linear optimization is the DLT (direct linear transformation, Abdel-Aziz & Karara, 1971), which simply solves linear equations but ignores

lens distortions unless an artificial distortion parameter is introduced. The DLT was employed in this laboratory by Bateman et al. (2006). In our experimental application, lens distortion is crucial and unknown because of the use of an inherently distorted commercial lens. Thus, the nonlinear pinhole method of Tsai (1987),), including the optimization of lens distortion, is used.

The pinhole optimization method (see Figure 2.18) is based on the measurement of a known point P in the real world 3D coordinates (x_w, y_w, z_w). The 3D coordinates of the object point P in the 3D camera coordinate system are (x, y, z), which are centered at point O (the optical center) with the z axis the same as the optical axis. (X, Y) is the image coordinate system centered at O_i (intersection of the optical axis z and the front image plane) and parallel to x and y axes. The focal length f is the distance between O and O_i. (X_u, Y_u) would be the image coordinates of (x, y, z) if a perfect pinhole camera model were used. (X_d, Y_d) are the actual image coordinates, which differ from (X_u, Y_u) due to lens distortion. However, since the unit for digital images is the number of pixels, to obtain the coordinates to be used in a computer (X_f, Y_f) additional parameters need to be specified.

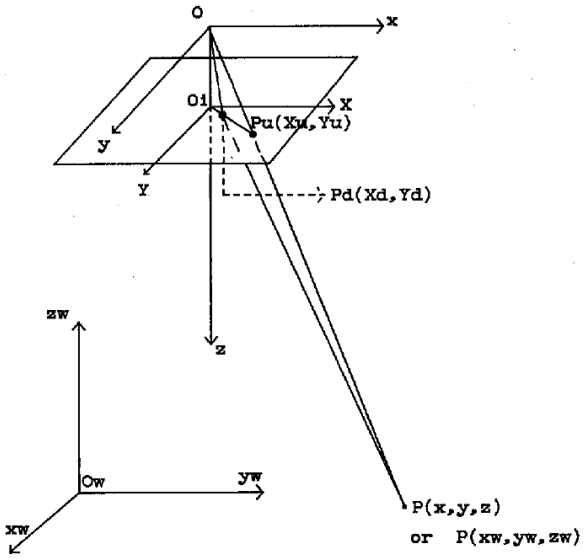

Figure 2.18. Camera geometry references with perspective projection and radial lens distortion for the pinhole method (extracted from Tsai, 1987).

The method is divided in 4 steps described hereafter.

Step 1: rigid body transformation $(x_w, y_w, z_w) \rightarrow (x, y, z)$

It consists of a rigid body translation and rotation from the real world coordinate system (x_w, y_w, z_w) to the camera 3D coordinate system (x, y, z) as follows:

$$\begin{bmatrix} x \\ y \\ z \end{bmatrix} = R \begin{bmatrix} x_w \\ y_w \\ z_w \end{bmatrix} + T \tag{2.16}$$

where R is the rotation matrix

$$R = \begin{bmatrix} r_1 & r_2 & r_3 \\ r_4 & r_5 & r_6 \\ r_7 & r_8 & r_9 \end{bmatrix} \tag{2.17}$$

and T is the translation vector

$$T = \begin{bmatrix} T_x \\ T_y \\ T_z \end{bmatrix} \tag{2.18}$$

The parameters to be optimized are 3 for rotation (yaw, pitch and roll angles) and 3 for translation.

Step 2: perspective projection $(x, y, z) \rightarrow (X_u, Y_u)$

It consists of the transformation from the 3D camera coordinates (x, y, z) to the undistorted image coordinates (X_u, Y_u), using the perspective projection with the pinhole camera geometry as follows:

$$X_u = f \frac{x}{z} \tag{2.19}$$

$$Y_u = f \frac{y}{z} \tag{2.20}$$

The parameter to be optimized here is the focal length f.

Step 3: radial lens distortion $(X_u, Y_u) \rightarrow (X_d, Y_d)$

It consists of the transformation from the undistorted image coordinates (X_u, Y_u) to the distorted ones (X_d, Y_d). It optimizes only the radial lens distortion, neglecting other minor distortions, with the following:

$$X_d + D_x = X_u \tag{2.21}$$

$$Y_d + D_y = Y_u \tag{2.22}$$

where

$$D_x = X_d\left(kr^2\right) \tag{2.23}$$

$$D_y = Y_d\left(kr^2\right) \tag{2.24}$$

$$r = \sqrt{X_d{}^2 + Y_d{}^2} \tag{2.25}$$

The parameter to be optimized here is the radial lens distortion k.

Step 4: digital acquisition $(X_d, Y_d) \rightarrow (X_f, Y_f)$

It consists of moving from the image coordinates (X_d, Y_d) to the digital image coordinates in pixels (X_f, Y_f) using the following transformation:

$$X_f = \frac{X_d}{d_x} + C_x \tag{2.26}$$

$$Y_f = \frac{Y_d}{d_y} + C_y \tag{2.27}$$

where (X_f, Y_f) are the row and column numbers of the image pixel in the computer frame memory, (C_x, C_y) row and column numbers of the center of the computer frame memory (center of image in pixels), d_x is the center to center distance between adjacent sensor elements of the CMOS in X (scan line) direction, d_y is the center to center distance between adjacent sensor elements of the CMOS in Y direction. d_x and d_y are generally known, while C_x and C_y are initially guessed at as the center of the digital image, and successively optimized.

In conclusion, a total number of 10 parameters needs to be optimized.

Operationally, the calibration process of a coplanar set of points (calibration panel) is the same process as the previously described 4 steps, repeated for all the coplanar points. This technique is the proper calibration process, and it allows to define the optimized parameters of transformation from (X_f, Y_f) to the world coordinates (x_w, y_w, z_w) of any objects recorded by the camera in the same geometric plane of the calibration panel.

The coplanar points real world coordinates x_w and y_w are known because they are set by the user (see calibration panels in Figure 2.20 and Figure 2.21). (X_f, Y_f) are known in the digital image, C_x and C_y are initially guessed through the camera resolution settings, d_x and d_y are generally given by the CMOS manufacturer. R, T, f and k are unknown and are optimized by the method.

The calibration technique has been implemented in the software "Calibration_Managed.exe" by the GITS team. It allows defining the parameters of transformation between the spatial references of the camera (images) and the spatial references of the measurement (world).

The measurements are performed on the laser lines drawing the intersection between the laser planes and the surfaces to be measured. Thus the calibration of images is exactly applied to the plane of each laser sheet where the calibration panel must be aligned (see example in Figure 2.19a).

As a consequence of the set-up of the present experimental application, the shooting angle of the cameras with respect to the plane of measurement is necessarily high (see Figure 2.19a). This introduces a massive perspective distortion resulting in non-parallel rows and columns of points in the calibration image. The distortion is so high that it is extremely complicated to automatically detect the main coordinate directions. Thus an *ad-hoc* algorithm intended to label and order the point in the N-E and E-W direction has been implemented as follow:

1. Recognize the 4 corners of the calibration panel
2. Define the mean N-S, E-W axes of the calibration panel
3. Define the local N-S, E-W axes for each point of the calibration panel, starting from the center point (where the axes have a direction similar to that of point 2) and spreading through the adjacent points, with a "flooding" algorithm.

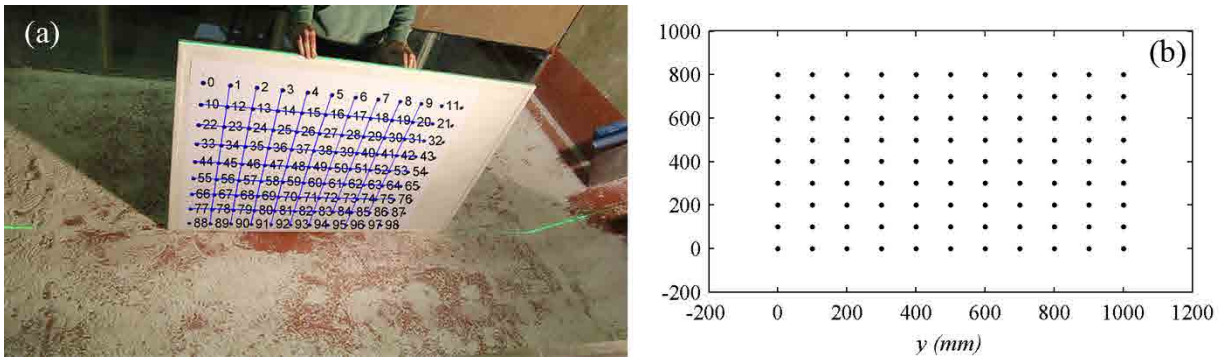

Figure 2.19. Results of the calibration algorithm: a) original image of calibration panel with the recognized and labeled points; b) application of the results of the calibration to the same calibration points (the axes reference is here arbitrary).

Once the points are labeled (see Figure 2.19a) they are ordered and the proper calibration optimization is performed so as to minimize the quadratic error in the known distance between points. The result of the measurement of the same calibration panel is given in Figure 2.19b.

The optimization is extremely complex, entailing a nonlinear system of 8 unknowns. For this reason the robust FORTRAN library MINPACK (Moré et al., 1980; Dennis & Schnabel, 1996) has been employed in optimization.

The inputs of the calibration software are:

1. the binary image in *.bmp format containing only the calibration points in black over a white background (same as the binary version in Figure 2.19a)
2. the distance between calibration points (fixed by user, see Figure 2.20 and Figure 2.21)
3. the input text file "Camera_Parameters.txt".

The "Camera_Parameters.txt" contains the following information: camera model; digital image's horizontal number of pixel; d_x; d_y; centre of the image in pixels along x C_x; centre of the image in pixels along y C_y.

Generally $d_x = d_y$, but also no square CMOS sensor element exists on the market.

The main outputs of the calibration are:

1. "Coordenadas_Laser.txt", the calibration file (the main result of the process)
2. "Calibracion.txt", the intrinsic and extrinsic calibration parameters
3. "Coord.txt", coordinates in pixels of the calibration points
4. "Data.txt", world coordinates of the calibration points
5. "Error.txt", report of calibration process errors (see section 2.6.1).

The main output is "Coordenadas_Laser.txt", that contain the transformation parameters and is used later in the measurement method. The parameters of the calibration are collated in "Calibracion.txt" and are:

- Intrinsic: f, k, r
- Extrinsic: R, T, C_x and C_y

It is essential to note that the calibration is performed for (1) a specific relative position between camera and laser plane (or calibration panel), (2) a specific camera model and (3) specific camera configuration and settings (focus, zoom position, picture size, resolution). If any of this three characteristics changes, the calibration must be repeated for the new configuration.

Accidental movements of the camera, as well as any out-of-alignement position of the calibration panel, could be a source of systematic errors. This issue is taken up in section 2.6.2 where sensitivity to systematic errors and thus a degree of uncertainty in measurement is discussed.

To enhance the optimization of calibration parameters, a good practice is to calibrate the image covering the maximum possible area of the frame with the calibration panel. Moreover a minimum number of calibrating black points should be used to achieve a good result. In this task the minimum number of points is set at 80. Adding more points, would certainly improve the calibration quality. If the required dimensions of the panel render it too large to be handled, the calibration should be performed preferentially in that part of the frame where the measurements are attempted.

The same method of calibration is conducted for the HS and HD cameras, but the difference in size and detail of the images, requires different areas of calibration: the HS camera requires a narrow but detailed calibration (ISO A3 sheet calibration panel, with dimensions of 297x420 mm; see the rescaled panel in Figure 2.20) while the HD cameras require a wider area of calibration but with less detail (ISO A0 sheet calibration panel, with dimensions of 841x1189 mm; see the rescaled panel in Figure 2.21).

The calibration panel should be set up along the direction of movement: for the granular material, the panel is placed along the sliding slope, while for the water surface it is placed horizontally.

The calibration panels are composed of black dots over a white background (Figure 2.20 and Figure 2.21), the point being to be easily recognized: black and white images are used in our calibration and measurement methodologies.

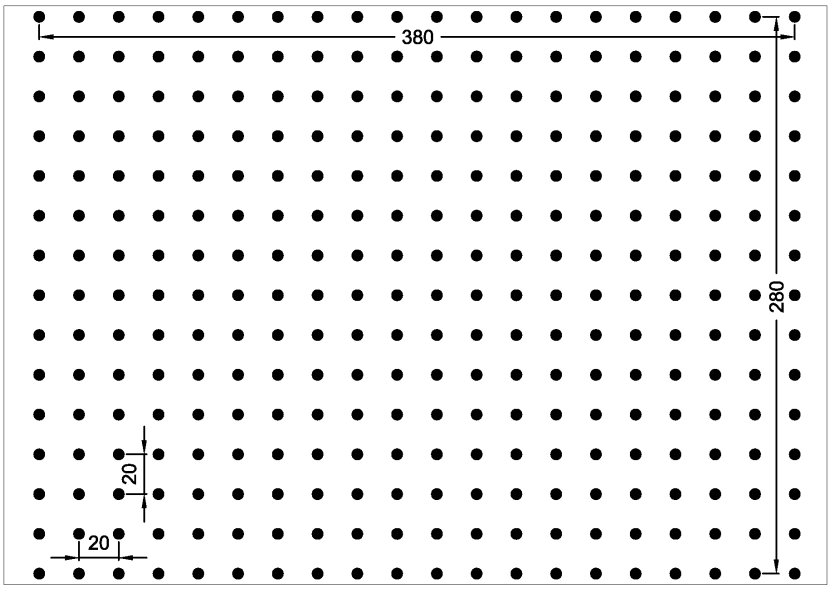

Figure 2.20. Calibration panel with 300 points, for use with the HS camera: ISO A3 paper, rescaled to fit the page (measurements in mm)

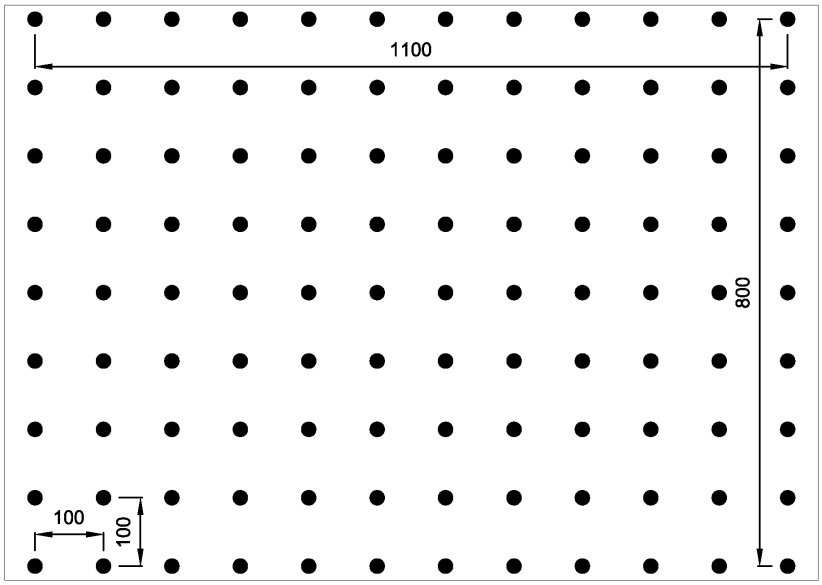

Figure 2.21. Calibration panel with 108 points, for use with the HD camera: ISO A0 paper rescaled to fit the page (measurements in mm)

2.5.4.2 Pre-processing of images

The images to be used in measurements need a certain degree of pre-processing to achieve a satisfactory image quality. To be suitable for our measurement framework, a 3 channels RGB image (24bit) needs to be converted to a grayscale image (8bit-grayscale) by selecting a channel. Obviously, the channel to be selected should be the one corresponding to the laser color being recorded. The choice of green and red laser is made in order to be easily identified within the same RGB images. An 8bit-grayscale image corresponds to a matrix, containing a value of light intensity ranging from 0 to 255 for each element (pixel). A value of 0 corresponds to black pixels, one of 255, to white.

In limiting the measurement to those zones of interest in the image, first a mask is applied and then a threshold on pixels intensity is introduced so as to obtain black and white - or binary - images (1bit). The threshold is chosen depending on the intensity of ambient and laser light.

Morphological operations can be applied only to binary images. The following are the basic morphological operations that are performed to clean and define the zones of interest:

1. removal of isolate pixels
2. dilation
3. majority

After applying the above listed morphological operations, the resulting binary images define exactly the zones of measurement on the originating grayscale image. The result of the combination between the 1bit images and the 8bit-grayscale images, are the masked 8bit-grayscale images. In turn, these 8bit-grayscale images are the input for the measurement methodology (see examples in Figure 2.22).

This post-processing is then applied to each frame of the recorded videos.

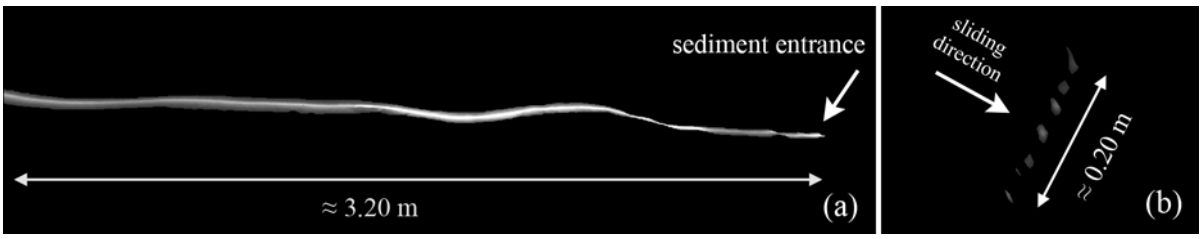

Figure 2.22. Examples of 8bit-grayscale images after pre-processing as input for the measurement methodology: a) frame showing the water profile along the *x* axis for the experiment *Unique_M75_27.8deg*; b) frame showing the vertical front of the granular landslide prior to impact for the experiment *Unique_M50_hs0.20_27.8deg*.

2.5.4.3 Measurements

The "captura blobs.exe" software, designed by the GITS team, is used here to perform the measurements. It uses the "Camera_Parameters.txt" and the "Coordenadas_Laser.txt" to measure the visible objects in the video frames: laser lines projected on gravel and water surface).

As explained before, the grayscale images are the designated input for the measurement. The methodology uses the pixel intensity range from 0 to 255 to ponder the centroid of the line to be measured. Thus, in this framework the centroid is not geometrical but is weighted on the basis of the light intensity: the center of the laser line is meant to be where the intensity of light is the highest.

The measurement framework uses the output parameters of the calibration to define the real world coordinates of each point of the objects visible in the input grayscale frames (i.e. Figure 2.22).

The measurements are different for the granular material and the water surface displacement, and are described separately in the following two sections.

2.5.4.3.1 Granular material measurements

The granular material is filmed with the HS camera at 500 f/s. The high frequency frames are important in capturing the material moving at a velocity in the order of 5 m/s. On this basis,

around 100 frames are an adequate number for the measurements to be effected within the captured length of the process.

For this study, the main parameters of the granular material to be measured are: velocity, thickness and length.

The times of evolution of velocity $\underline{v_s}(t)$ and thickness $\underline{h_s}(t)$ are measured inside an observation Eulerian control volume. Within the same control volume an averaged velocity v_s and thickness h_s. v_s and h_s related to the centroid of the mass at impact are measured. The length of the landslide l_s, similarly to v_s and h_s, is measured as an average value.

The software "captura_blobs.exe" can recognize and enumerate, if requested, blobs within each frame. In computer vision, blob detection methods are aimed at detecting regions in a digital image that differ in properties, in our case brightness, compared to surrounding regions.

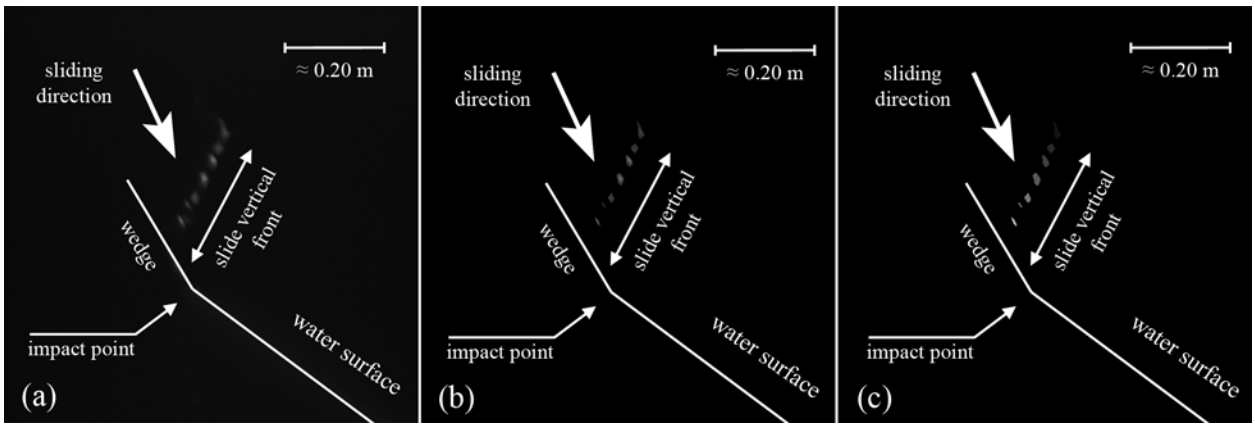

Figure 2.23. Identification of blobs in a landslide front at 0.012s prior to impact with water for experiment *Unique_M50_hs0.20_27.8deg*: a) 8bit-grayscale frame where the slide vertical front approaching the water basin is visible; b) masked 8bit-grayscale image after preprocessing; b) identification of 7 blobs by "captura_blobs.exe".

Identifying blobs is fundamental when it is necessary to recognize and follow an object moving in sub-sequential frames. This technique is called "particle image tracking" and is employed to follow each illuminated grain of the granular mass.

In Figure 2.23 one can observe the steps needed to identify the grains in a single frame, through the blobs definition. Figure 2.23a represent the grayscale image, Figure 2.23b represent the masked grayscale image and finally Figure 2.23c represent the grains each one recognized as a blob. The different intensity of the blobs' color is used to differentiate them. Thus at the following frame the velocity is calculated for each blob, knowing the displacement of the blob's centroid and the time interval Δt. In the example in Figure 2.24 the blobs of frame 1 and frame 2

are compared. Here 6 different blobs, corresponding to 6 different grains, have been identified. Blob number 1 corresponds to a new grain entering in the laser-lit plane and thus its displacement will be measured in the following frame. The yellow arrows identify the displacement vectors of the grains' centroids. In some cases the shape of the blob changes from frame to frame. This is the case of blob number 2. These changes in shape can be attributed to rotations or changes of light reflectivity due to the grain's naturally irregular surface. However, the time step $\Delta t = 0.002$s, resulting from the HS camera frame rate, can be deemed small enough to considerably limit this issue.

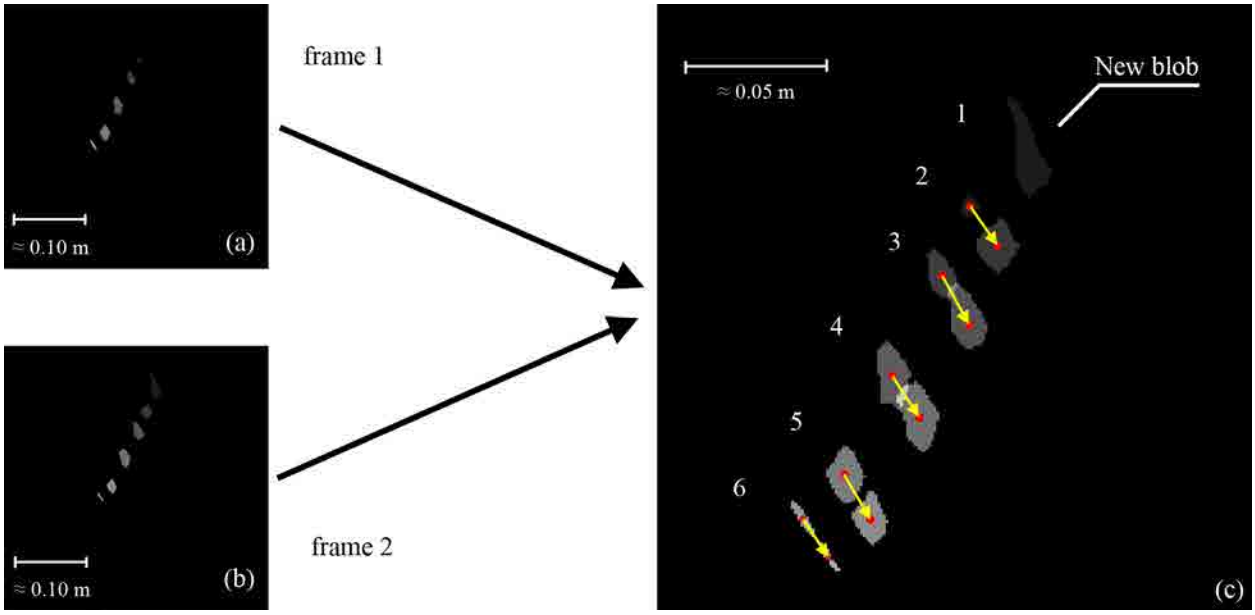

Figure 2.24. Particle tracking framework for the example in Figure 2.23: a) frame 1 of the blobs at landslide front at 0.014s prior to impact with water; b) frame 2 of the blobs at landslide's front at 0.012s prior to impact with water; c) magnified image of combination of frame 1 and frame 2 where red dots are the centroid of grains and yellow arrows are the displacement vectors between frame 1 and frame 2.

To obtain a unique average value of velocity for each time step $\underline{v}_s(t)$, the mean velocity of the different grains travelling inside the observing control volume is calculated.

In researching the averaged properties of the landslide, a Lagrangian average on the entire granular mass passing through the control volume of fixed width is calculated, considering total mass M and momentum r for unit width as follow:

$$M = \sum \left(\underline{h}_{s,i} \cdot \underline{v}_{s,i} \right) \Delta t \tag{2.28}$$

$$r = M \cdot \underline{v}_{s,i} = \sum \left(\underline{h}_{s,i} \cdot \underline{v}_{s,i} \right) \Delta t \cdot \underline{v}_{s,i} \tag{2.29}$$

$$h_s = \frac{M}{\sum \underline{v}_{s,i} \Delta t} = \frac{\sum \left(\underline{h}_{s,i} \cdot \underline{v}_{s,i} \right) \Delta t}{\sum \underline{v}_{s,i} \Delta t} \tag{2.30}$$

$$v_s = \frac{r}{M} = \frac{\sum \left(\underline{h}_{s,i} \cdot \underline{v}_{s,i} \right) \Delta t \cdot \underline{v}_{s,i}}{\sum \left(\underline{h}_{s,i} \cdot \underline{v}_{s,i} \right) \Delta t} \tag{2.31}$$

$$l_s \approx \Delta t \sum_i \underline{v}_{s,i}(t) \tag{2.32}$$

The control volume has a fixed width *d* and it is centered at intersection between wedge and initial water level, as shown in Figure 2.25.

The results of these measurements are reported in section 3.1.

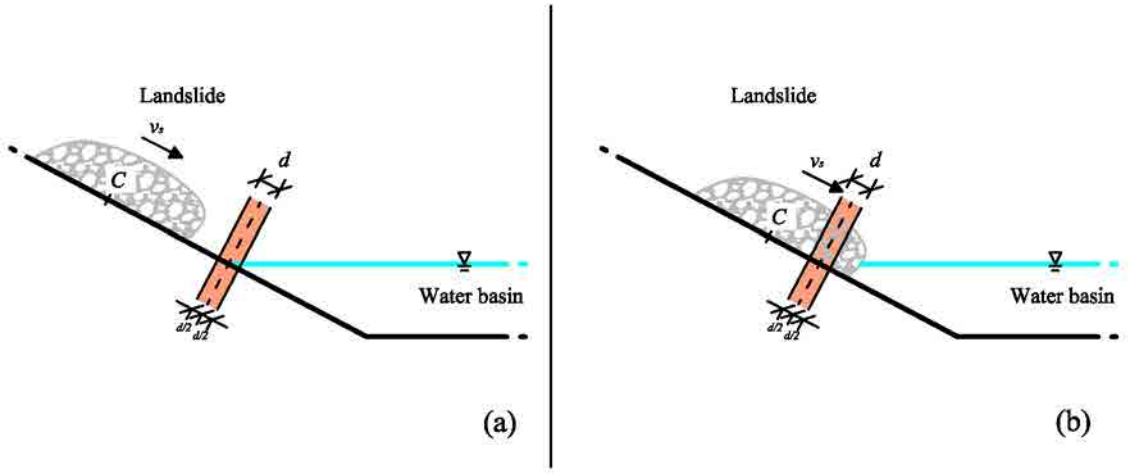

Figure 2.25. Position of control volume of fixed width *d*: a) the control volume in pink color is centered at wedge – water level intersection; b) the landslide is travelling through the control volume where the measurement of thickness and velocity is performed.

2.5.4.3.2 Water surface displacement measurements

The water surface elevation is measured along the direction *x* for each time step. The time step is fixed by the HD camera frame rate as $\Delta t = 1/50 = 0.02$s. The first frame where the contact of landslide with water is detected, corresponds to the frame of initial time $t = 0$. In Figure 2.26 it is possible to observe the main measurements performed for the frame reported in Figure 2.17. The location of the first crest's peak gives the wave amplitude *a* and its location *x* in time. Three key points are recognized: P_1 is the first up-crossing point, P_2 is the first down-crossing point

and P_2 is the second up-crossing point. The first crest longitude and its subtended area are measured between P_1 and P_2. The first wavelength is measured between P_1 and P_3.

In Figure 2.26 it is possible to observe that the measurement starts from x = 1m: the area of measurement was masked close to impact because of splash interferences. Thus the window of observation, constrained by the splash on one side and by the camera angle on the other side, is limited to a width spanning from 2.25m to 2.75m, depending on the experiment. The camera field misses, in any case, a section of about 0.50m before the end of the tank. However, the visual angle of the camera cannot be moved: in order to determine t = 0, it is crucial that the camera films, as a minimum, the landslide entrance.

The results of these measurements are reported in section 3.2.

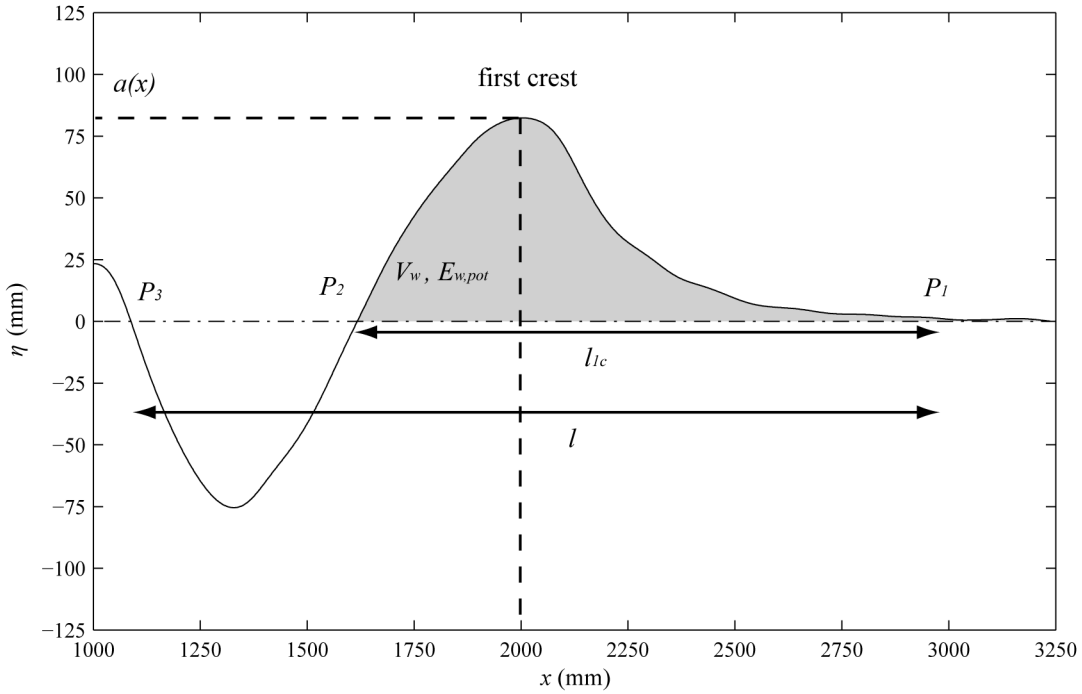

Figure 2.26. Result of measurement after image treatment and signal filtering (see section 2.5.4.4), for the same frame of Figure 2.17 (*Unique_M100_27.8deg*, Camera c). The dash-dot line represents the still water level, while the solid line represents the water surface displacement η at t = 0.9 s after impact. First crest amplitude *a(x)* and position are identified by seeking the first wave crest maximum. The grey area is the 2D integrating area under the first crest, where wave volume and wave potential energy are measured (see section 3.2.6 and 3.2.7).

2.5.4.4 Filtering data

The signals of the water surface profiles resulting from the measurement methodology are noisy due to different factors:

- splash close to impact
- splash drops falling along the laser lines
- landslide grains surfing along the surface

Each of these effects can create a peak or a discontinuity along the wave profile, which must be appropriately filtered.

The filter designed for this application is a lowpass digital Butterworth, named after the physicist who first described this family of filters (Butterworth, 1930).

A lowpass digital Butterworth filter is defined by the filter order O and a normalized cutoff frequency w_c. The transformation function from original to filtered signal is defined by these two parameters.

A Butterworth filter having $O = 2$ and $w_c = 0.01$ is chosen to filter the water surface displacement in x (see example of resulting filtered signal in Figure 2.26). The relative low cutoff frequency is fixed because of the high interferences provoked by the splash close to impact. In the example of Figure 2.27 it is possible to appreciate the relative difference between original $\eta(x)$ and filtered $\eta_{filt}(x)$ water surface displacement averaged along the x and represented in time for one experiment. Close to wave formation the splash and drops are filtered, provoking a maximum mismatch with the measured series of about 0.9%. This is the period of time when the filter is mostly engaged, while after $t = 0.5$ the filtered series deviates less than 0.25%. In any case, the average relative difference between $\eta(x)$ and $\eta_{filt}(x)$ is always less than 1% and it is considered an acceptable maximum mismatch in designing the filter.

A Butterworth filter having $O = 10$ and $w_c = 0.3$ is applied to the water surface displacement in time for selected spots (probe-like measurements; see examples of resulting filtered signal in Figure 3.7). For this last application the choice of a higher order is done because the time series is larger and involves several peaks. Moreover, the cutoff frequency is higher because the signal is less disturbed than in the previously described measurement.

The landslide measurements are not filtered, as the measured quantities are given as averages. However, for plotting purposes, the landslide velocity is filtered with a Butterworth filter having $O = 5$ and $w_c = 0.2$ to avoid showing local unwanted peaks related to grain jumps or massive changes in grain shape observation from images (see section 3.1.1).

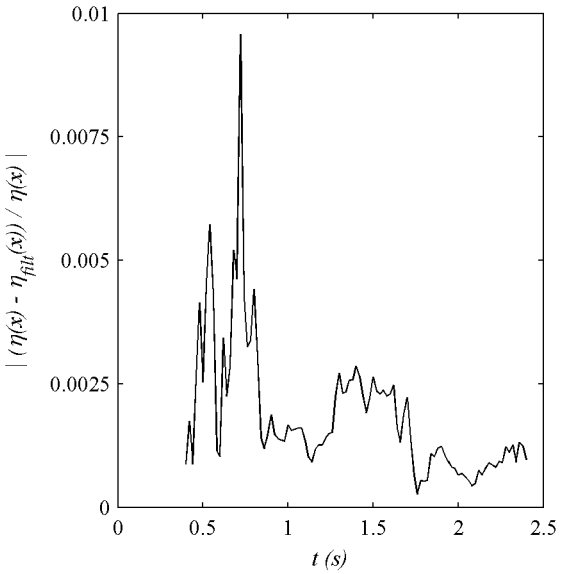

Figure 2.27. Spatial averaged relative difference between original $\eta(x)$ and filtered $\eta_{filt}(x)$ water surface displacement in time for experiment *Unique_M100_27.8deg*. The average relative difference within the total elapsed time is 0.0019.

2.6 Errors and uncertainty of measurement

Generally speaking, different standard quantities have to be mentioned when referring to the errors of measurement in physics (Taylor, 1997):

- the *resolution* is the smallest change in the underlying physical quantity that produces a response in the measurement
- the *accuracy* of a measurement system is the degree of closeness of the mean of the measurement results of a quantity to that quantity's true value
- the *precision* refers to the closeness of agreement within individual results, which can be identified as the standard deviation (SD) of the population of measurements.

In any experimental work the task of evaluating the error of measurement is crucial.

Systematic errors and their influence on the final measurement are important in order to define the degree of uncertainty of the experimental results.

In our measurement methodology two sources of errors exist: (1) errors in the method of calibration optimization, (2) systematic errors of measurement. The first source of errors gives the global degree of accuracy and precision of the measurement tools, while the second source gives the degree of uncertainty. Both are described hereafter.

2.6.1 Accuracy and precision of the measurement tool

The maximum measurement resolution is set by the calibration and measurement framework at 10^{-5} m. The tool was originally designed to work with a higher image resolution than required by the present application. Thus the high measurement resolution can be excessive for this experimental work. Measurements are given in 10^{-5} m resolution but, finally, end results are presented with a 10^{-3} m resolution.

Accuracy and precision can vary depending on image calibration and camera used. The average accuracy and precision for the HS and the HD cameras, which are specified in the output "Error.txt" for each performed calibration, can be found in Table 2.5.

Table 2.5. Maximum resolution and average accuracy and precision of the measurement tool.

	Max resolution (mm)	Accuracy (mm)	Precision (mm)
HS camera	0.01	0.58	0.40
HD camera	0.01	0.90	0.53

On this basis, the accuracy of the measurement tool is attested to ± 0.5mm.

The high performance of the measurement tool contrasts with the significant systematic errors that are presented in the following section.

2.6.2 Systematic errors

Sensitivity analysis is the study of how the uncertainty in the output of a mathematical model or system (numerical or otherwise) can be apportioned to different sources of uncertainty in its inputs (Saltelli et al., 2008).

Here an analysis of the sensitivity of the measuring methodology in response to possible systematic errors is performed. The analysis is performed for the case of the HS camera, which is meant to be the most sensitive camera in our pool, and successively extrapolated to the HD camera.

The systematic errors of measurement that can occur in our laboratory concern the possible rotations and translations of the calibration panel or the video cameras and can be described as:

a) the misaligned position of the calibration panel along the laser plane
b) the accidental movement of the cameras after calibration

The first case is investigated by forcing rotations and translations of the calibration panel. To limit the second case, the calibration is performed for each camera prior to each experiment and thus the associated errors are not analysed here.

The systematic errors due to translations and rotations of the calibrating panel for the HS camera (Figure 2.28a) are investigated independently by measuring a known object. The designated object is the inclinometer of Figure 2.28b.

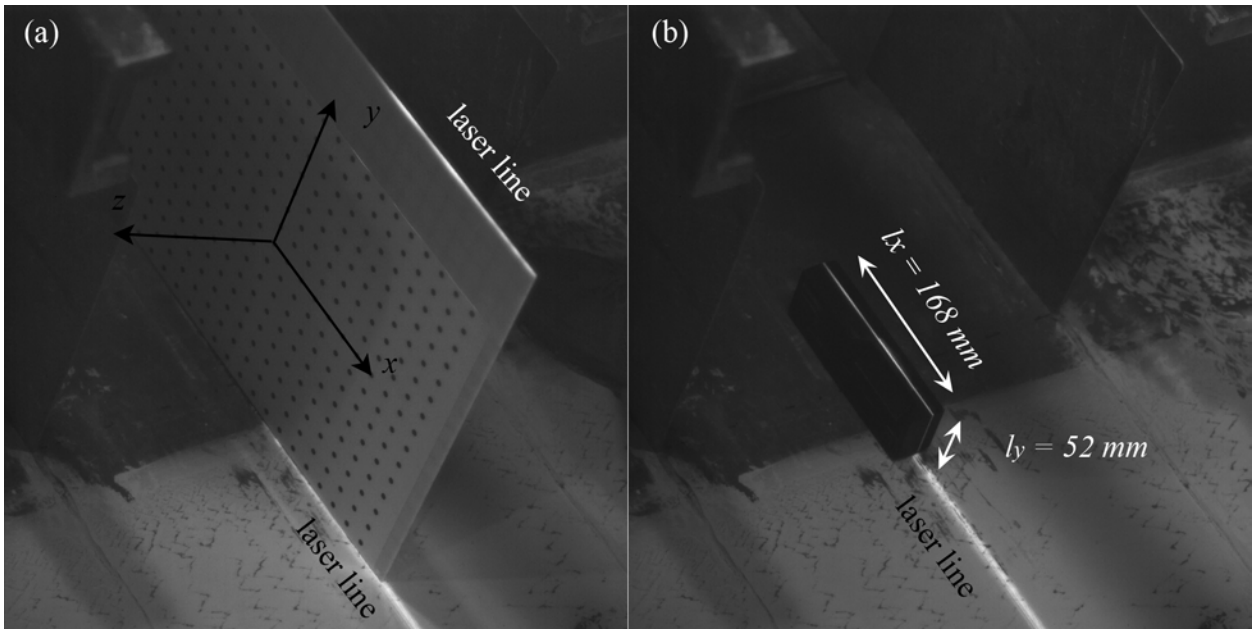

Figure 2.28. Evaluation of systematic errors for the HS camera: a) reference calibration, with the calibration panel aligned with the laser plane, and reference of the induced systematic movements; b) photo of the measured object and its real dimensions along the laser line.

The errors investigated are the rotation in x, the rotation in y and the translation along z. Different positions of the calibration panel are calibrated. Then, the calibration outputs are used to measure the known object. The results of this series of tests produce curves of sensitivity for each family of induced errors (Figure 2.29, Figure 2.30 and Figure 2.31).

The laser sheet has a width of about 1cm. Thus, the maximum estimated error of panel positioning in z is of the order of ±0.5cm. On this basis, the maximum estimated error of panel x rotation and y rotation for the HS camera calibration panel (isoA3 sheet dimensions) are given by the following:

$$x_{rot,max} = \pm \tan^{-1}\left(\frac{0.5}{15}\right) = \pm 1.9\,\text{deg} \tag{2.33}$$

$$y_{rot,max} = \pm \tan^{-1}\left(\frac{0.5}{22.5}\right) = \pm 1.27\,\text{deg} \tag{2.34}$$

Using the same concept, the maximum estimated errors of panel positioning and rotation for the HD camera calibration panel (ISO A0 sheet dimensions) can be deduced. The maximum estimated errors in positioning and rotations are collated in Table 2.6, where also the relative maximum uncertainties per axis are calculated using the linear fits reported in the graphics in Figure 2.29, Figure 2.30 and Figure 2.31. The calculated uncertainties include the accuracy and precision of the measurement tool.

In conclusion, the maximum uncertainty in landslide measurement is estimated in the range of ± 2 % in the horizontal direction and ± 15 % in the vertical direction, while for the water surface displacement it is estimated in the range of ± 1 % in the horizontal direction and ± 15 % in the vertical direction.

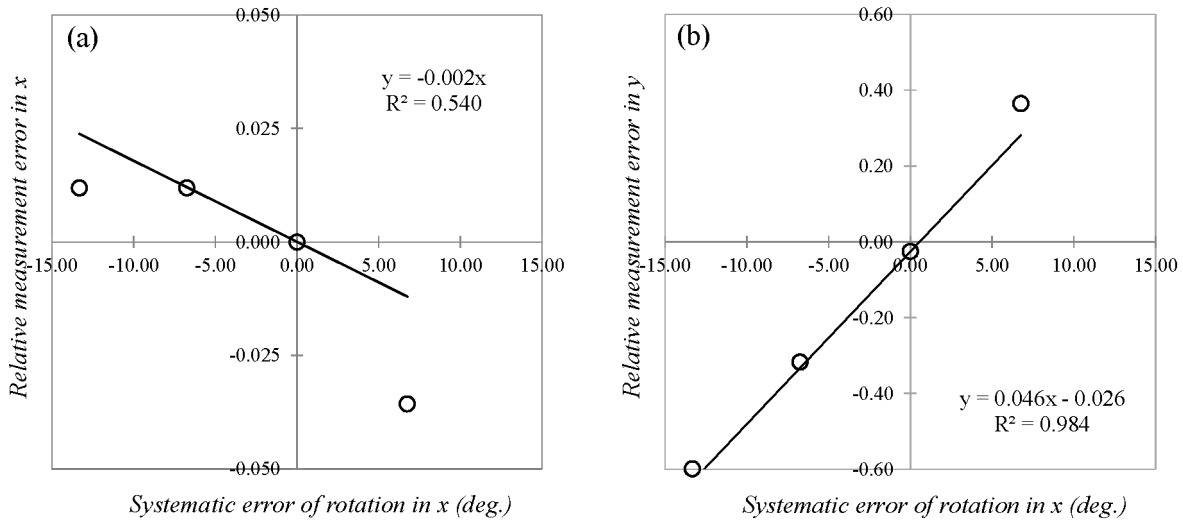

Figure 2.29. Systematic errors of rotation around the *x* axis and linear sensitivities curves: a) object measurement errors in *x* direction; b) object measurement errors in *y* direction.

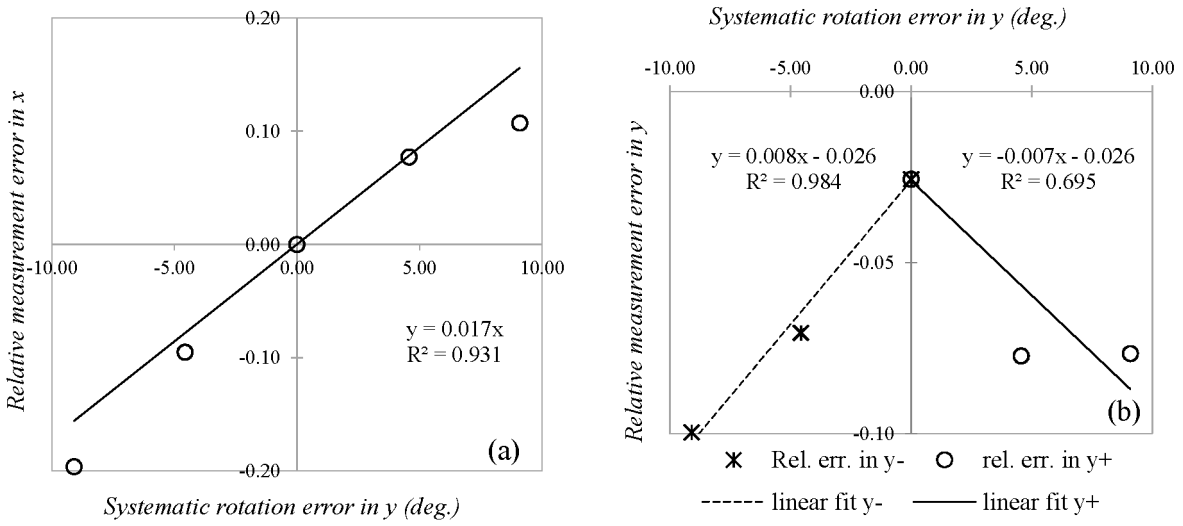

Figure 2.30. Systematic errors of rotation around the *y* axis and linear sensitivities curves: a) object measurement errors in *x* direction; b) object measurement errors in *y* direction.

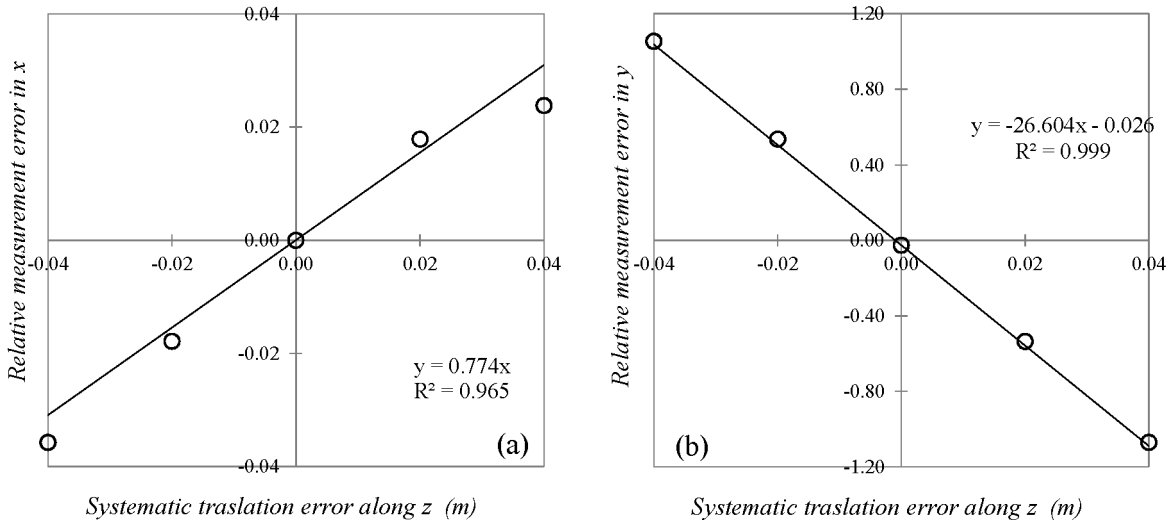

Figure 2.31. Systematic errors of translation along the *z* axis and linear sensitivities curves: a) object measurement errors in *x* direction; b) object measurement errors in *y* direction.

Table 2.6. Maximum estimated errors in position and rotations and the relative maximum uncertainties per axis using equations in Figure 2.29, Figure 2.30 and Figure 2.31.

	HS camera			HD camera		
Reference axes	***x***	***y***	***z***	***x***	***y***	***z***
Max. systematic displ./rot.	± 1.90 °	± 1.27°	± 0.005 m	± 0.57°	± 0.38°	± 0.005 m
Max. uncertainty in *x* (%)	± 0.38	± 2.16	± 0.39	± 0.11	± 0.65	± 0.39
Max. uncertainty in *y* (%)	± 11.00	± 3.62	± 15.02	± 5.22	± 2.90	± 15.02

2.6.3 Test on the reliability of high definition cameras

Due to the observed discontinuity in the evaluation of velocity of wave peak translation performed using the Canon HD camera (see Figure 2.32a), a verification of the capabilities of this device in describing wave peak displacement and velocity became necessary.

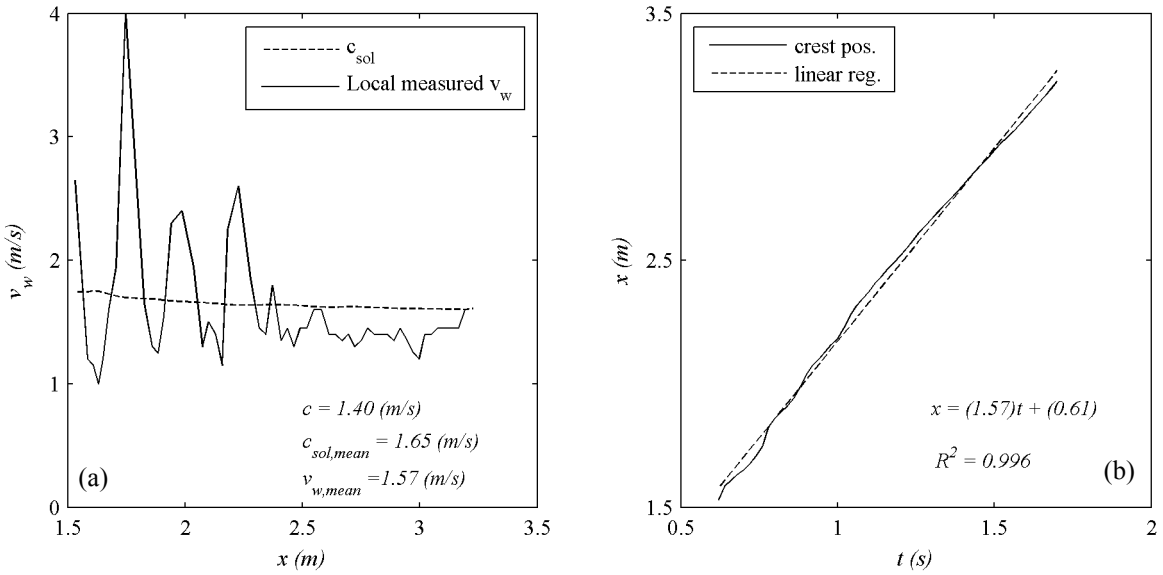

Figure 2.32. Crest position and velocity for the run *Unique_M100_27.8deg*: a) velocity measured with crest peak displacement and celerity of solitary wave for the local wave amplitude; b) position in time of the wave crest peak and the linear regression having as slope the wave peak mean velocity.

The free fall of a penny is filmed and successively the theoretical and the measured velocity are compared. The results reveal a good agreement between theory and observation. In Figure 2.33 it can be observed that the free fall of the object, having an initial zero velocity, is an excellent fit with the theoretical equations of motion. The test was performed 4 times, giving similar results.

On this basis, one can affirm that the camera correctly reproduces the movement of the object and thus the discontinuities are addressed to the high sensibility on the wave crest peak displacement. The peaks of the wave crests are so smooth that it is sometimes difficult to identify them properly. Thus, small errors of position are magnified in the evaluation of velocity and so produce local peaks. The problem is adequately solved by averaging the velocity in space and time, as the average value of the peak seems to be almost constant: the velocity calculated as slope of the linear fit in Figure 2.32b is similar to the average velocity of wave peak translation along the *x* reported in Figure 2.32a.

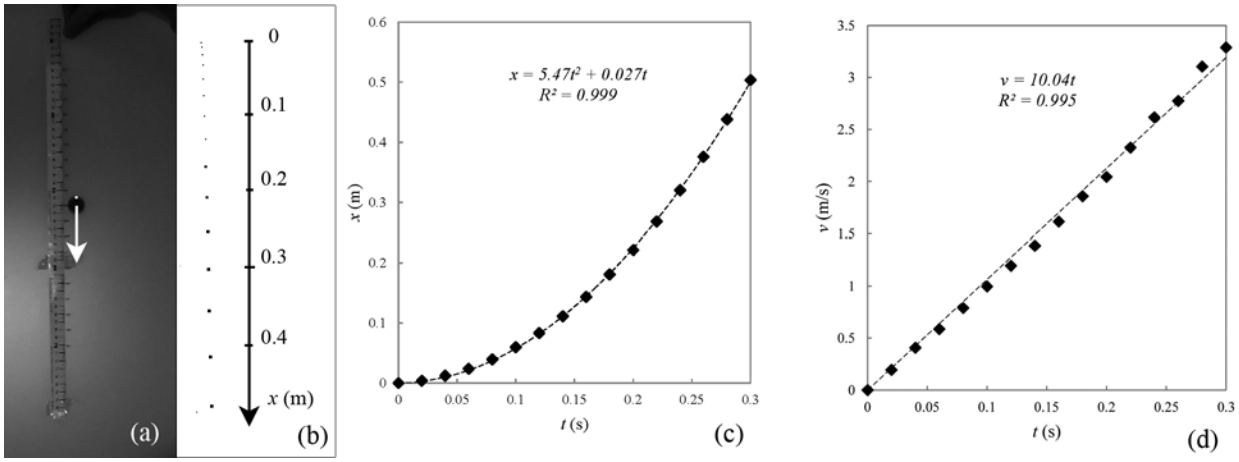

Figure 2.33. Free fall of a penny with initial condition $x = 0$ and $v = 0$ at $t = 0$, recorded by the HD camera at frame rate of 50 f/s: a) a frame of the penny falling along the rule; b) position of the penny for every frame; c) time versus position rescaled thanks to the rule (the diamonds are the data and the dashed line is the quadratic fitting); d) time versus velocity (the diamonds are the data and the dashed line is the linear fitting).

Chapter 3: Experimental results

A total number of 41 experiments was carried out in the present thesis at different wave generator configurations. They are divided in 5 Sets. The first 16 experiments (Set 1 and Set 2) have been conducted with a configuration that did not permit the simultaneous observation of landslides and waves evolution and thus they are omitted from the analysis of results. However, because they include the observation of the landslides evolution, 7 of them, belonging to Set 1, were used for the model introduced in chapter 5. The remaining 25 experiments, belonging to Set 3, Set 4 and Set 5, are employed in the empirical analysis of results (chapter 4) and in the model.

In conclusion, of the 41 experiments, 25 were used in defining the empirical predictors and 32 were used for the energy transfer model. The remaining 9 experiments are used for descriptive purposes but are omitted from analysis because of incompleteness in data measurements. The explained dataset is presented in Table 3.1, while the complete datasets are recollected in tables in Appendix C and in graphics in Appendix D .

The main experimental results are presented in this chapter. First, the observations of landslide characteristics are introduced including form, velocity, energy and final deposit. Then, the wave features are presented, starting from the analysis of the reflections into the wave tank to properly define the range of validity of the wave profiles. Successively, the resulting wave amplitude, celerity, length and period are described, as well as the volume and energy of the first wave's crest.

The experimental results are compared with the empirical predictor results of other researches in order to analyze similarities and differences with the previous experimental studies.

The experimental results presented in this chapter are therefore the basis of the empirical predictor formulas introduced in chapter 4 and are used to calibrate and verify the numerical model presented in chapter 5.

Table 3.1. Experimental datasets and their use along the presented work. ND: no data available.

#	# set	Name	*m (kg)*	*α (°)*	h_w *(m)*	*Fr*	Wedge	Landslide data	Deposit data	Wave data	Empirical use	Model use
1	Set 1	*Type_a_M50_27.8deg*	50	27.8	0.20	3.38	yes	yes	yes	no	no	yes
2	Set 1	*Type_a_M50_27.8deg*	50	27.8	0.16	4.02	yes	yes	yes	no	no	yes
3	Set 1	*Type_a_M75_27.8deg*	75	27.8	0.19	3.94	yes	yes	yes	no	no	yes
4	Set 1	*Type_a_M100_27.8deg*	100	27.8	0.19	3.95	yes	yes	yes	no	no	yes
5	Set 1	*Type_a_M125_27.8deg*	125	27.8	0.19	4.05	yes	yes	yes	no	no	yes
6	Set 1	*Type_a_M140_27.8deg*	140	27.8	0.18	4.10	yes	yes	yes	no	no	yes
7	Set 1	*Type_a_M110_27.8deg*	110	27.8	0.20	4.17	yes	yes	yes	no	no	yes
8	Set 1	*Type_a_M120_27.8deg*	120	27.8	0.20	3.84	yes	yes	no	no	no	no
9	Set 2	*Type_b_M50_27.8deg*	50	27.8	0.20	ND	yes	no	yes	yes	no	no
10	Set 2	*Type_b_M50_27.8deg*	50	27.8	0.16	ND	yes	no	yes	yes	no	no
11	Set 2	*Type_b_M75_27.8deg*	75	27.8	0.19	ND	yes	no	yes	yes	no	no
12	Set 2	*Type_b_M100_27.8deg*	100	27.8	0.19	ND	yes	no	yes	yes	no	no
13	Set 2	*Type_b_M125_27.8deg*	125	27.8	0.19	ND	yes	no	yes	yes	no	no
14	Set 2	*Type_b_M140_27.8deg*	140	27.8	0.18	ND	yes	no	yes	yes	no	no
15	Set 2	*Type_b_M110_27.8deg*	110	27.8	0.20	ND	yes	no	yes	yes	no	no
16	Set 2	*Type_b_M120_27.8deg*	120	27.8	0.20	ND	yes	no	yes	yes	no	no
17	Set 3	*Unique_M50_27.8deg*	50	27.8	0.20	3.86	yes	yes	no	yes	yes	no
18	Set 3	*Unique_M75_27.8deg*	75	27.8	0.20	3.61	yes	yes	yes	yes	yes	yes
19	Set 3	*Unique_M100_27.8deg*	100	27.8	0.20	3.65	yes	yes	yes	yes	yes	yes
20	Set 3	*Unique_M110_27.8deg*	110	27.8	0.20	3.64	yes	yes	no	yes	yes	no
21	Set 3	*Unique_M120_27.8deg*	120	27.8	0.20	3.70	yes	yes	no	yes	yes	no
22	Set 3	*Unique_M125_27.8deg*	125	27.8	0.20	3.66	yes	yes	yes	yes	yes	yes
23	Set 3	*Unique_M130_27.8deg*	130	27.8	0.20	3.68	yes	yes	no	yes	yes	no

#	# set	Name	*m (kg)*	*α (°)*	h_w *(m)*	*Fr*	Wedge	Landslide data	Deposit data	Wave data	Empirical use	Model use
24	Set 3	*Unique_M136_27.8deg*	136	27.8	0.20	3.69	yes	yes	yes	yes	yes	yes
25	Set 3	*Unique_M139.5_27.8deg*	139.5	27.8	0.20	3.70	yes	yes	yes	yes	yes	yes
26	Set 3	*Unique_M50_hs0.10_27.8deg*	50	27.8	0.20	4.12	yes	yes	yes	yes	yes	yes
27	Set 3	*Unique_M50_hs0.15_27.8deg*	50	27.8	0.20	3.86	yes	yes	no	yes	yes	no
28	Set 3	*Unique_M50_hs0.20_27.8deg*	50	27.8	0.20	3.69	yes	yes	no	yes	yes	no
29	Set 3	*Unique_M50_hs0.25_27.8deg*	50	27.8	0.20	3.83	yes	yes	no	yes	yes	no
30	Set 3	*Unique_M75_hs0.10_27.8deg*	75	27.8	0.20	3.85	yes	yes	no	yes	yes	no
31	Set 3	*Unique_M75_hs0.15_27.8deg*	75	27.8	0.20	3.95	yes	yes	no	yes	yes	no
32	Set 3	*Unique_M75_hs0.20_27.8deg*	75	27.8	0.20	4.03	yes	yes	yes	yes	yes	yes
33	Set 3	*Unique_M75_hs0.25_27.8deg*	75	27.8	0.20	3.38	yes	yes	yes	yes	yes	yes
34	Set 4	*Unique_M50_hs0.10_15.5deg*	50	15.5	0.25	2.11	no	yes	yes	yes	yes	yes
35	Set 4	*Unique_M50_hs0.20_15.5deg*	50	15.5	0.25	2.20	no	yes	yes	yes	yes	yes
36	Set 4	*Unique_M75_hs0.15_15.5deg*	75	15.5	0.25	2.07	no	yes	yes	yes	yes	yes
37	Set 4	*Unique_M100_hs0.20_15.5deg*	100	15.5	0.25	1.98	no	yes	yes	yes	yes	yes
38	Set 4	*Unique_M100bis_hs0.20_15.5deg*	100	15.5	0.25	2.01	no	yes	yes	yes	yes	yes
39	Set 4	*Unique_M125_hs0.20_15.5deg*	125	15.5	0.25	1.91	no	yes	yes	yes	yes	yes
40	Set 4	*Unique_M143_hs0.25_15.5deg*	143	15.5	0.25	2.02	no	yes	yes	yes	yes	yes
41	Set 5	*Unique_M120_27.8deg_no_wedge*	120	27.8	0.20	3.70	no	yes	yes	yes	yes	yes

(continued from previous page)

3.1 Landslide characteristics

The reproduced landslides are measured by means of the principles introduced in section 2.5.4.3.1. In this section landslide characteristics are summarized. The whole information is available at Appendix C .

3.1.1 Form and velocity

Thickness h_s and velocity v_s are measured in time at the impact point. At this point, the landslide has already experienced a portion of frictional effects and thus the landslide itself is stretched. The front is faster and thicker than the tail. However, the maximum thickness is not always located at front, but immediately after. Examples of a relatively faster and relatively slower slide measurement are reported respectively in Figure 3.1 and Figure 3.2.

Unique values of thickness h_s and velocity v_s at impact are necessary to define the landslide properties. Frontal, middle and tail values of thickness and velocity are given, as well as the averaged values, as in equations (2.30) and (2.31). In the present research mean values are selected to be representative of the landslide. The length l_s is evaluated using equation (2.32).

The mean values h_s and v_s are used in calculating Fr and $E_{s,kin}$.

The ranges of the main properties of the landslides are summarized in Table 3.2 while the full measurements are given in sub-appendix C.2.

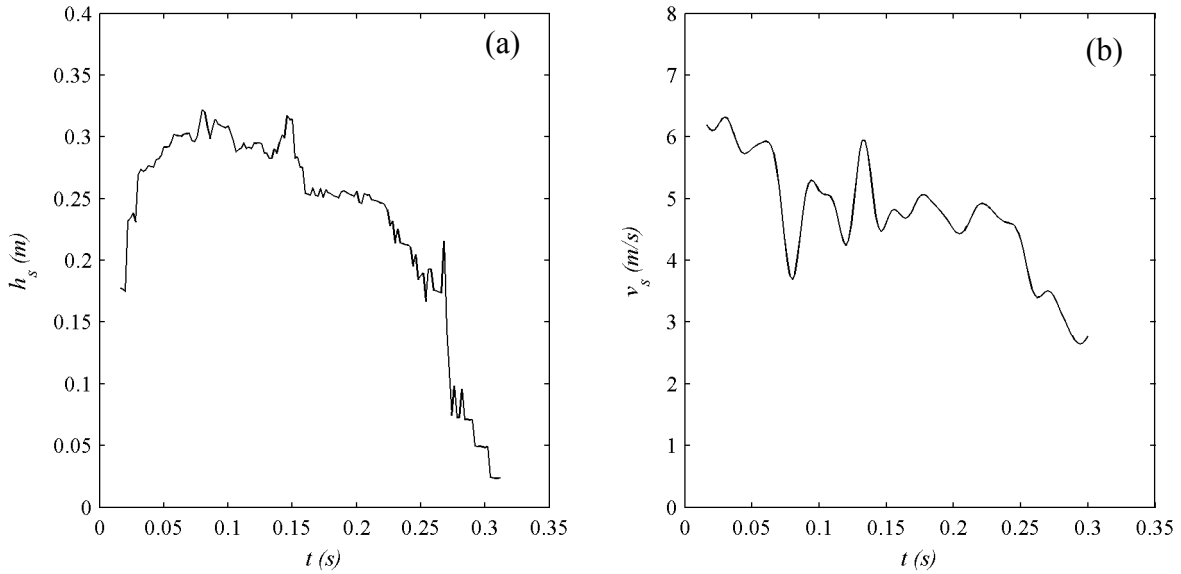

Figure 3.1. Time series of the granular material for experiment *Unique_M139.5_27.8deg* (*Fr* = 3.70): a) thickness; b) filtered velocity.

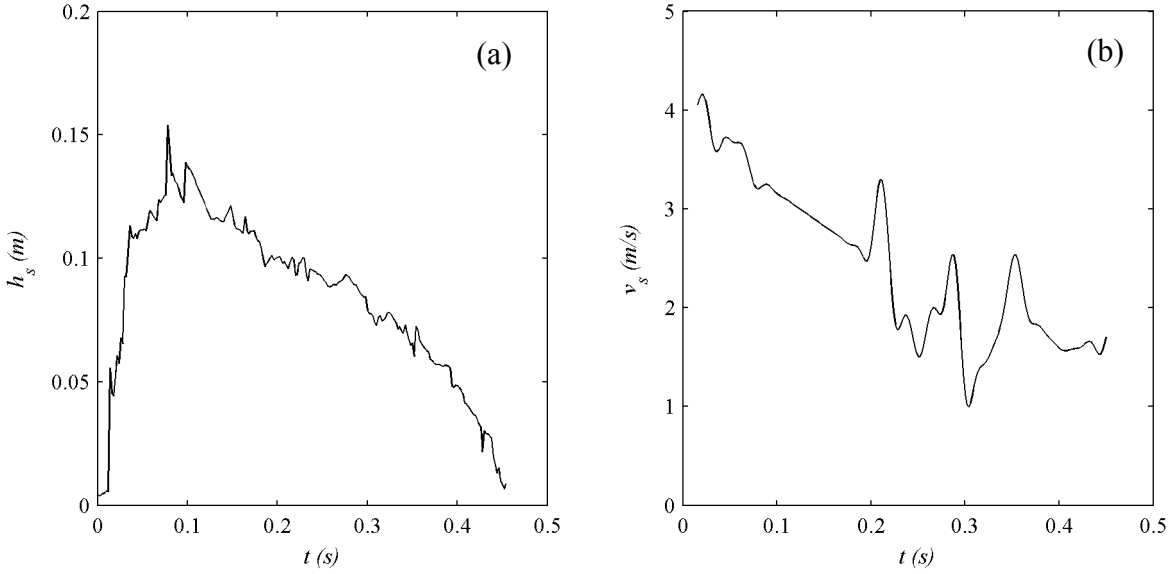

Figure 3.2. Time series of the granular material for experiment *Unique_M50_hs0.10_15.5deg* (*Fr* = 2.11): a) thickness; b) filtered velocity.

Table 3.2. Range of measured thickness, velocity and length of the landslides.

	$h_{s,front}$ (m)	h_s (m)	$v_{s,front}$ (m)	v_s (m/s)	l_s (m)
Maximum values	0.30	0.25	6.67	5.85	2.06
Minimum values	0.11	0.09	4.01	2.99	0.85

3.1.2 Energy

Several authors (i.e.: Kamphuis & Bowering, 1970; Huber, 1980; Fritz et al, 2004; Heller, 2008; Ataie-Ashtiani & Nik-Khah, 2008; Mohammed & Fritz, 2012), consider the kinetic energy at impact $E_{s,kin}$ when referring to landslide energy. Fritz et al (2004), Heller (2008) and Mohammed & Fritz (2012) use the front characteristics of the landslide. Here the averaged values of v_s are used, as they are thought to be more representative of the entire mass. Therefore, the results of energy conversion are expected to be lower when compared with the other authors: in the experiments being presented, the landslide energy computed with the average velocity is 28% lower than the energy computed with the front velocity.

In producing predictive empirical formulas (chapter 4) $E_{s,kin}$ is used as representative of the landslide.

However, in the numerical model presented in chapter 5, the underwater path the landslide has to travel after impact with water entails a residual $E_{s,pot}$. For instance, in the experimental results presented here, it can be seen that $E_{s,pot}$ is on average 20% of the total landslide energy E_s.

On this basis, the total energy of the landslide can be calculated as the sum of both its kinetic and potential energy at impact with the water basin, as follows:

$$E_s = E_{s,kin} + E_{s,pot} = \frac{1}{2} m_s v_s^2 + m'_s\, g z_{s,c} \tag{3.1}$$

In the previous equation, m'_s is the submerged sliding mass (see equation (2.14) in section 2.3.3), while $z_{s,c}$ is the height, referred to the bottom of the tank, of the centroid C of the landslides at impact with water (see equation (3.2) and Figure 3.3).

$$z_{s,c} = h_w + \frac{l_s}{2}\sin(\alpha) \tag{3.2}$$

In equation (3.2) it can be seen that $z_{s,c}$ is not referred to the centroid of the landslide lateral section, but to the middle point of the landslide bottom surface. The amount of potential energy associated with the supplementary height of the vertical coordinate of the centroid is found to be roughly 4% of E_s. Thus, it is disregarded for simplicity.

The experimental measurements of landslide energies are reported in Table 3.3 while the complete measurements are given in sub-appendix C.3.

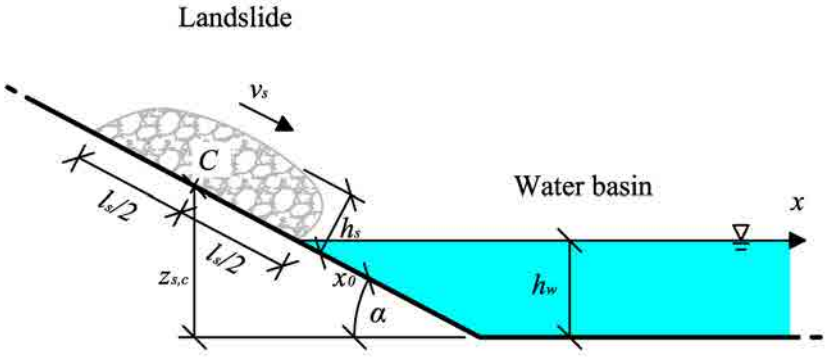

Figure 3.3. Sketch of landslide centroid position *C* at impact.

Table 3.3. Measured energies of landslides.

	Es,kin (J)	Es,pot (J)	Es (J)
Maximum values	2109.8	382.6	2476.1
Minimum values	271.9	121.4	393.3

3.1.3 Final deposit

The final deposits of the landslides were measured in order to take into account the deformations suffered. The turbidity of the water due to the presence of kaolin requires emptying

the wave tank to observe the landslide deposit. Therefore the measurement was not performed for those experiments that were conducted within the same day in order to avoid needing to empty and refill the water tank.

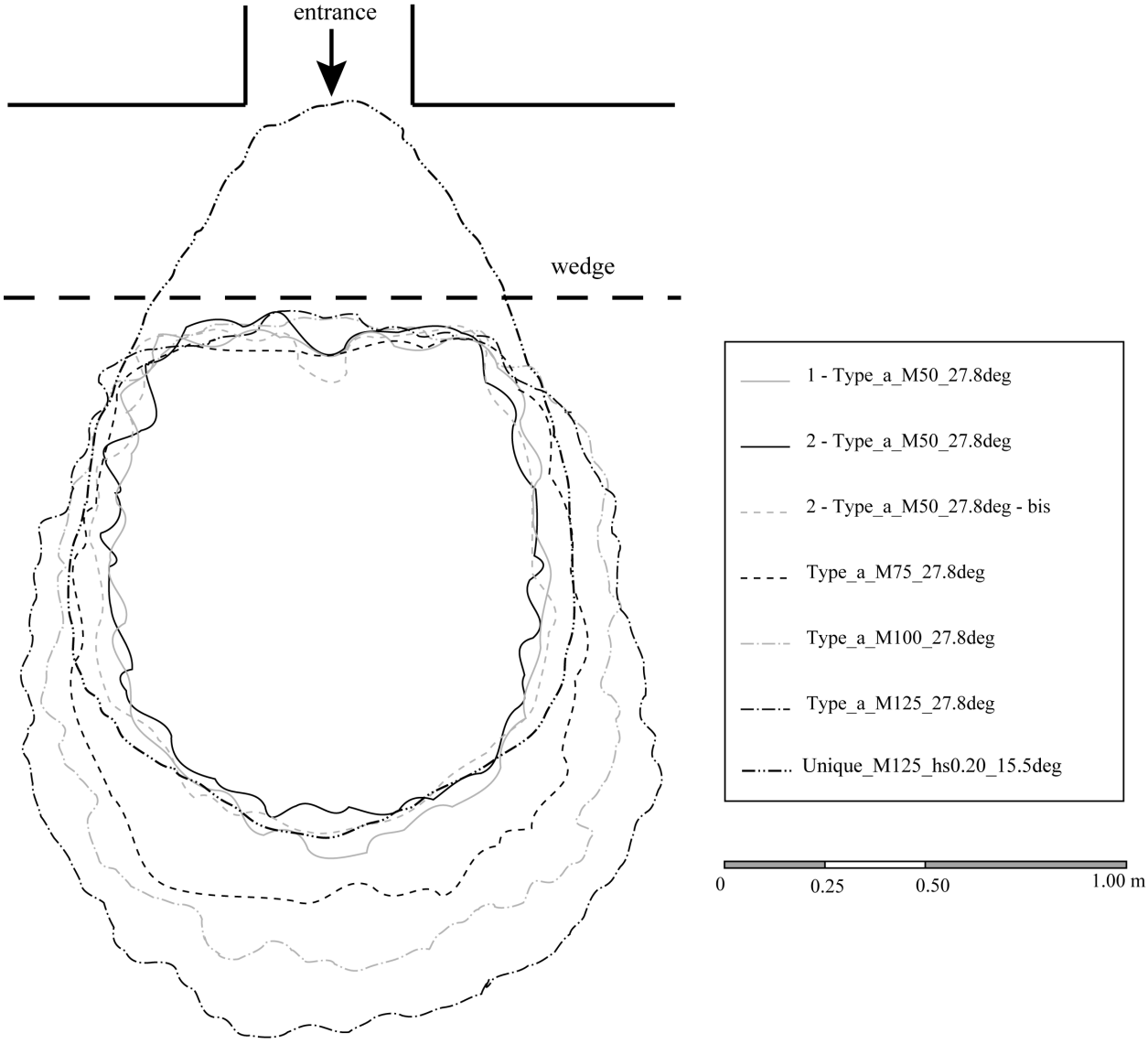

Figure 3.4. Qualitative contours of the final deposits obtained from aerial photos for some experiments.

The final deposit, having an elliptical form, was synthetically measured in its major axis a_d and minor axis b_d . In some cases, when the observation was possible, the distance from impact of the farthest grain was recorded. It can provide a measure of the water surface surfing or jumping by the particle that was observed by Mazzanti & De Blasio (2011).

Some contours obtained from orthogonal photos are reported in Figure 3.4. The observation shows that the experiments with lower angle experienced a particularly marked elongation in a_d due to the absence of the wedge and possibly also due to the increased momentum rate along the

main direction of propagation. The full available results are presented in sub-appendix C.4, while the maximum and minimum values are given in Table 3.4.

Table 3.4. Ranges of the final deposits measurements (*D* is the distance from impact of the farthest grain).

	a_d (m)	b_d (m)	D (m)
Maximum values	1.59	1.80	2.98
Minimum values	0.95	1.03	2.00

3.2 Wave characteristics

A qualitative sketch of the wave formation is given in Figure 3.5. The formed waves, being close to impact, are certainly in transition from highly non-linear wave (near field), to linear wave (far field). Unfortunately observation on far field was not possible in this work. Any efforts to theoretically reproduce the formed wave assuming linear, solitary or cnoidal wave have been useless. Thus only an experimental characterization of the formed waves has been used for this study.

The principal measurements of wave properties are here presented. The whole information is available in Appendix C and Appendix D . The wave celerity and amplitude as well as the first crest volume and potential energy are measured quasi-continuously in time and space from a Lagrangian point of view. For practical reasons, the length and the period between the first up-cross and second up-cross of the vertical water displacement are measured for some specific locations (probe-like) from a Lagrangian point of view.

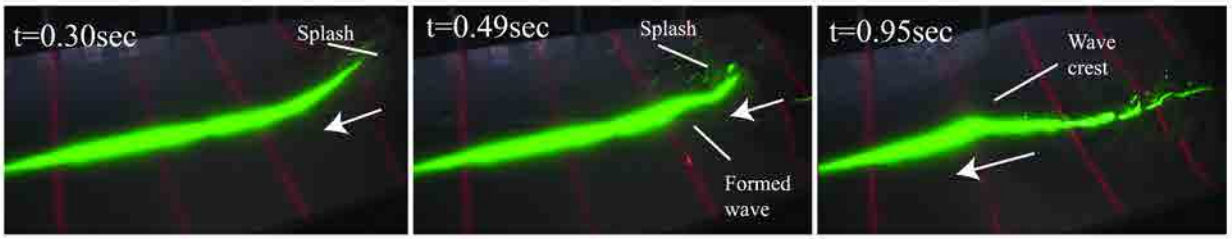

Figure 3.5. Sequence of wave formation and propagation (elapsed time from impact).

3.2.1 Spatial and time series

The wave profiles can be observed from a Lagrangian point of view, i.e. following the waves along the domain in space and time, or from an Eulerian point of view, i.e. measuring the waves in time at selected spots, as is the case for probes. In the present experimental configuration, both observations are possible.

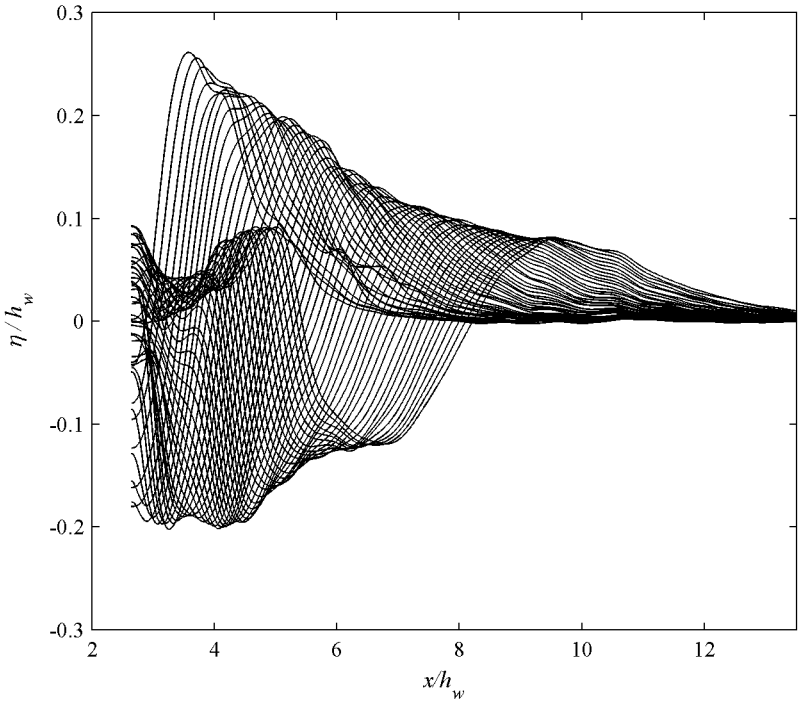

Figure 3.6. Wave profiles from a Lagrangian point of view for the experiment *Unique_M50_hs0.10_15.5deg*. The lines represent the water profiles along *x* for 50 time steps (Δt = 0.02 s).

In Figure 3.6 one can observe the wave profiles from a Lagrangian point of view, where the lines represent the water profiles along *x* for each time step. For instance the envelope curve corresponding to the maxima of Figure 3.6 represents the amplitude evolution of the first crest (see Figure 3.25).

In Figure 3.7 one can observe the wave profiles from an Eulerian point of view, where the lines represent the water profiles in *t* for selected *x* locations.

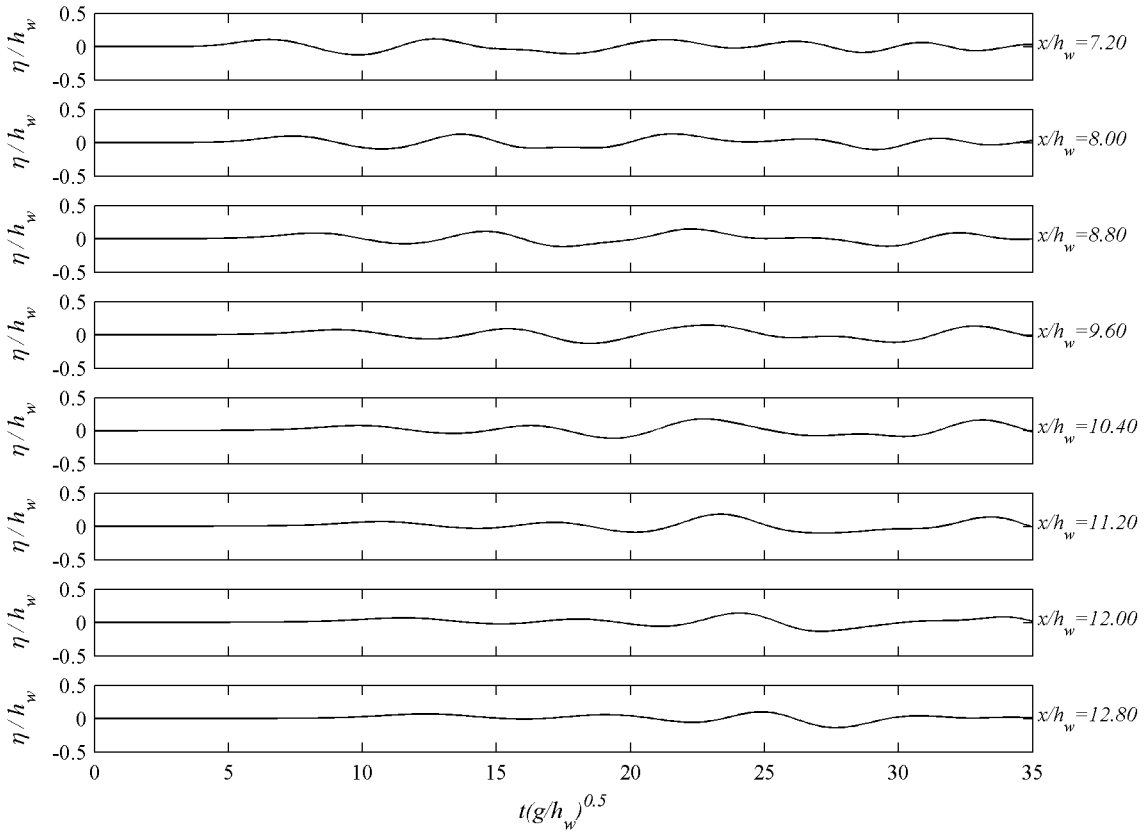

Figure 3.7. Wave time series from an Eulerian point of view. The lines represent the water profiles in *t* for 8 locations along the *x* (*Unique_M50_hs0.10_15.5deg*).

An interesting method to represent the wave profiles in space and time in a concise way is presented in Figure 3.8. Those figures are derived from 2D wave profiles (i.e. Figure 3.6) and can immediately provide much information at once, such as wave celerity, wave reflections (see also 3.2.2 and Figure 3.9) and the observation of other unexpected wave structures.

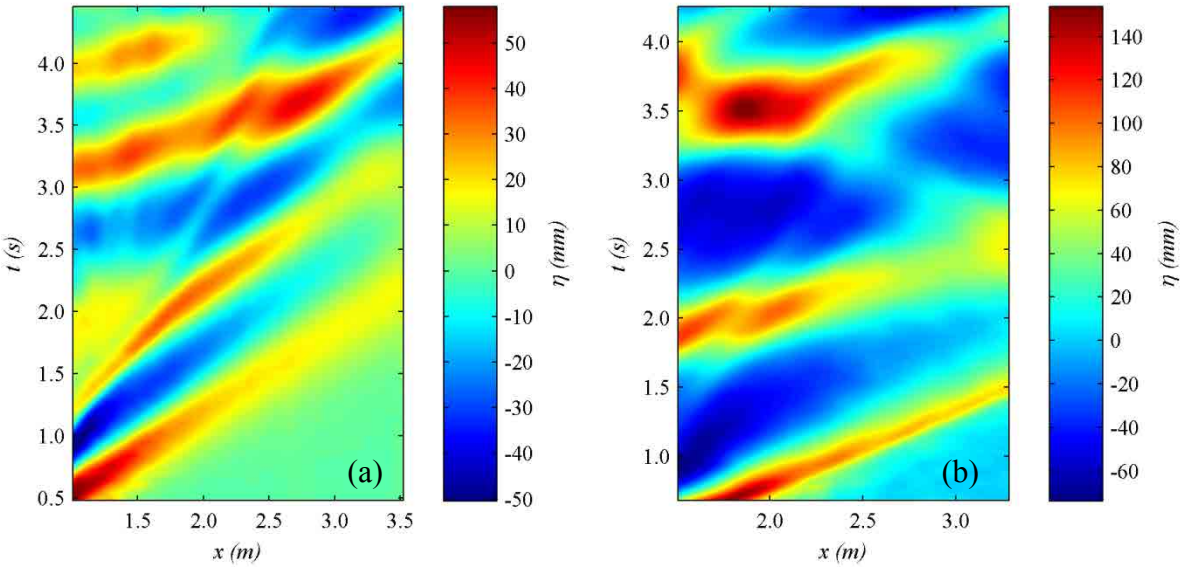

Figure 3.8. Experiment plots of the water surface evolution at the center line of the tank described in time and space: a) *Unique_M50_hs0.10_15.5deg*; b) *Unique_M139.5_27.8deg*.

3.2.2 Wave reflections analysis

The reflections are of two types:

- Frontal reflection: the waves reach the end wall of the tank and are reflected back symmetrically with respect to the frontal wall (Figure 3.10).
- Lateral reflection: the waves reach the lateral walls of the tank and are reflected symmetrically with respect to the lateral wall (Figure 3.12)

The beginning of the reflections can be assessed (see also section 2.4) when a certain water vertical displacement η_{ref}, having a fixed percentage p of the wave amplitude a, reaches the wall. The value of p is fixed, thanks to available observations.

$$\eta_{ref} = pa \tag{3.3}$$

3.2.2.1 Frontal reflections

For a certain location G on the main wave direction (green laser line), having a distance x_G from the impact point (see Figure 3.10), the time of the frontal reflection's arrival $t_{front,ref}$ may be evaluated with the follow equation:

$$t_{front,ref} = t_{ini,front,0.15a} + \frac{2d}{c} = t_{ini,front,0.15a} + \frac{2(L - x_G)}{\sqrt{gh_w}} \tag{3.4}$$

where, observing Figure 3.10, d is the distance between the point G and the wall, $c = \sqrt{gh_w}$ is the celerity of linear shallow water waves, $t_{ini,front,0.15a}$ is the time that the front of the first wave takes

to reach location *G*. The necessity of guessing a travel velocity as *c* is due to the fact that the reflected wave is already - and ideally - out of the observation boundaries. Thus, no data about the water profile is obviously known. It was observed that the celerity of shallow water waves is more appropriate to describe the propagation of a reflected wave. This can be proved by looking at Figure 3.9, where the guessed frontal reflected peak is marked over time-space plots, matching with locally higher water level. Consequently, propagation of the last known water profile is calculated, using the celerity *c*.

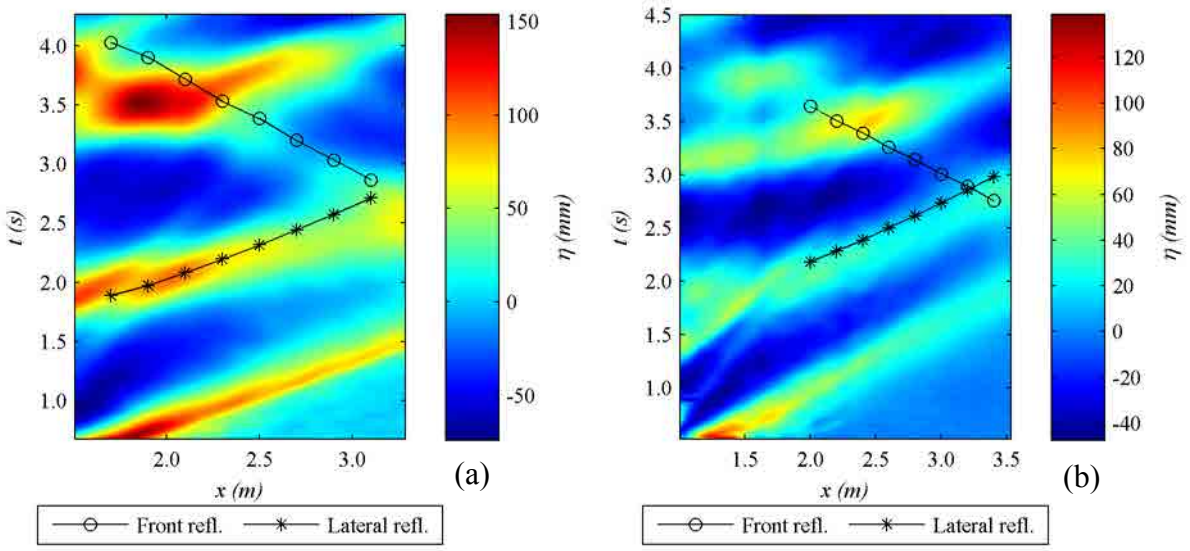

Figure 3.9. Plots of the water surface evolution at the center line of the tank described in time and space (distance from impact) for two experiments: a) *Unique_M139.5_27.8deg*; b) *Unique_M143_hs0.25_15.5deg*. The guessed first peak reflections are evaluated and reported at some distances from the impact.

The time $t_{ini,front,0.15a}$ is defined as the time that a water vertical displacement $\eta_{ref,front} = p_{front} a = 0.15a$ arrives at location *G*. The value p_{front} was established observing the comparison of the time series for a fixed location between experiments carried on in the GITS facility (the present study) and in GT facility (Mohammed, 2010). Being the GT tank much larger than the GITS one, the waves in the GT experiments are influenced by reflections much later than in the GITS ones. This means that a detachment point between the two time series can be observed. For instance, Figure 3.11 shows the detachment point for a case comparison between two similar experiments. Belonging to two different facilities, the water surface and time are rescaled to make the two series comparable. The detachment point arrives when

$\eta_{ref,front} = 0.15a$. Other comparisons between comparable experiments yield similar conclusions. Thus, the value of p_{front} is set conservatively at 0.15.

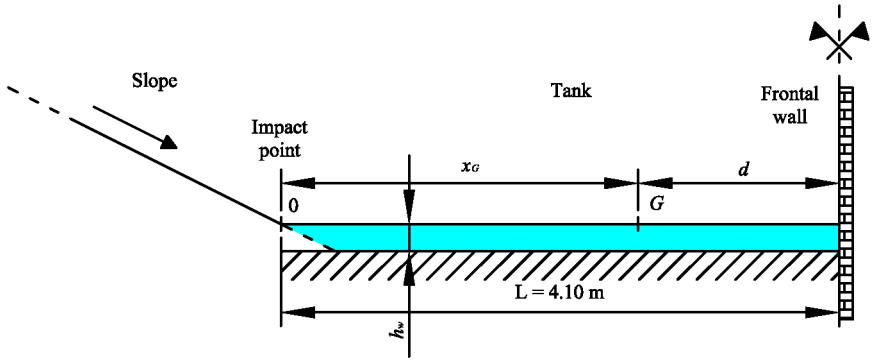

Figure 3.10. Schema of frontal reflection: Lateral view

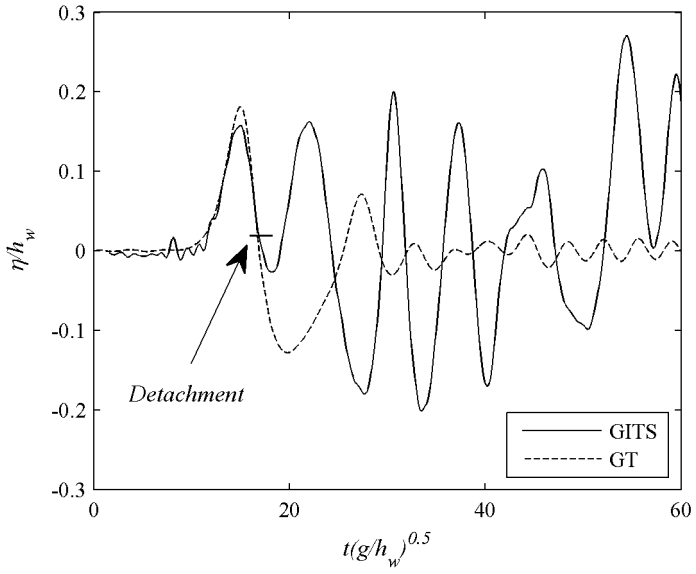

Figure 3.11. Wave time series comparison at x_G/h_w = 18 for a GITS experiment (*Unique_M50_27.8deg*), and a GT experiment from Mohammed (2010) (experiment 4th, h_w =0.30m).

3.2.2.2 Lateral reflections of circular wave front

It was observed that the shape of the wave front is elliptical, as described in the following chapter. However, at first instance, in evaluating the lateral reflection the wave front can be considered as circular. This theoretical assumption permits to simplify the representation of lateral reflection.

Further analysis of the elliptical wave front will be addressed at section 3.2.2.3.

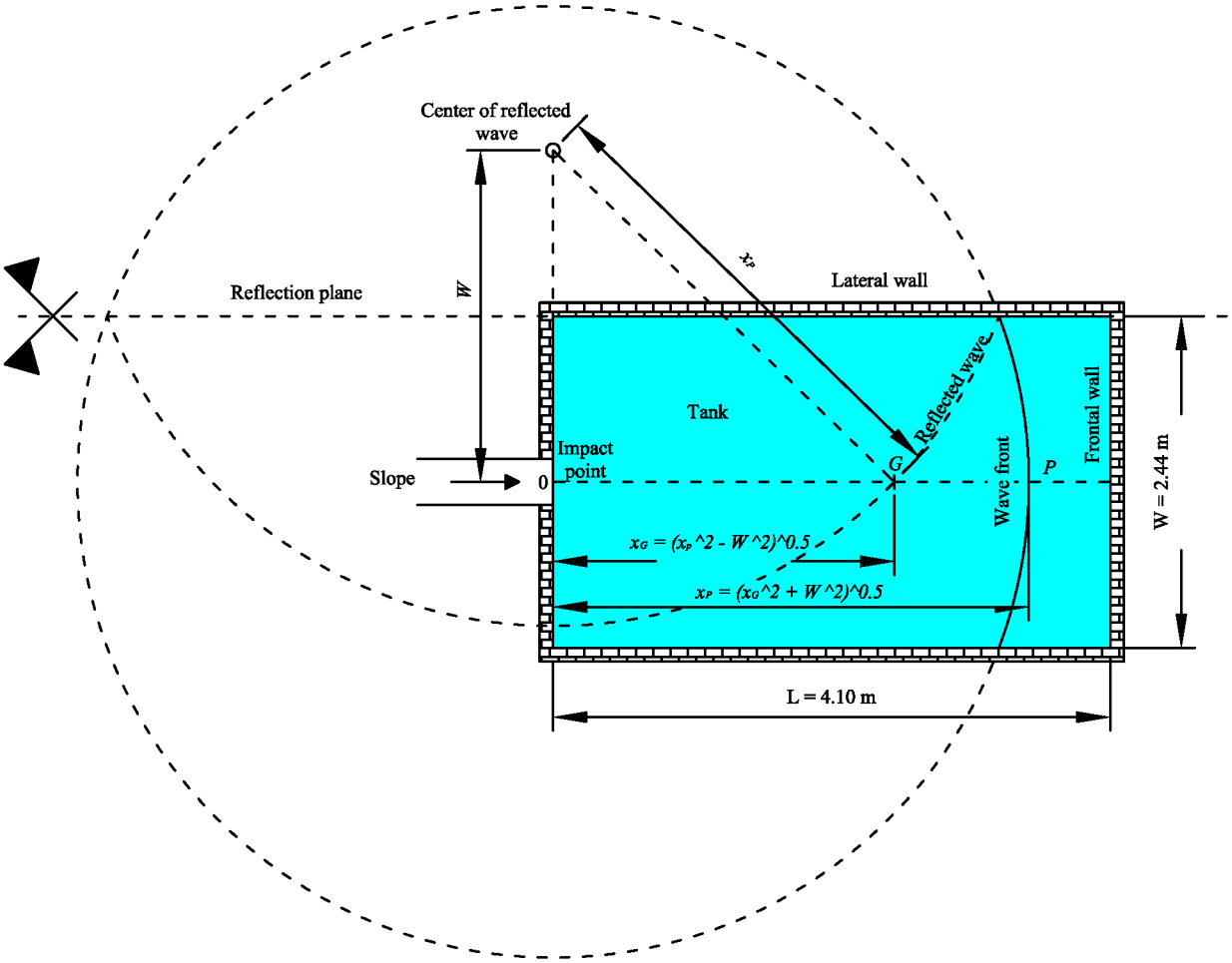

Figure 3.12. Schema of lateral reflection for a circular wave front: Aerial view.

Considering a certain location G on the main wave direction (green laser line) having a distance x_G from the impact point, the lateral reflection arrives in G when the wave front is at a certain point P having a distance x_P from the impact point (see Figure 3.12). For points close to impact, records of water profile are available, being inside the water tank. Thus the measure of the reflection is immediate and given when $\eta_{ref,lateral} = p_{lateral} a = 0.50a$. Once the location of P is outside the observation boundary, the same guessing is done as for the frontal reflection. But this time the celerity of a solitary wave $c_{sol} = \sqrt{g(h_w + a)}$ is used as propagation velocity of the water profile.

Using merely geometry as in Figure 3.12, the distances x_P is described as:

$$x_P = \sqrt{x_G{}^2 + W^2} \tag{3.5}$$

where W is the width of the water tank.

Two examples of assessing reflections for two different runs are given in Figure 3.13 and Figure 3.14.

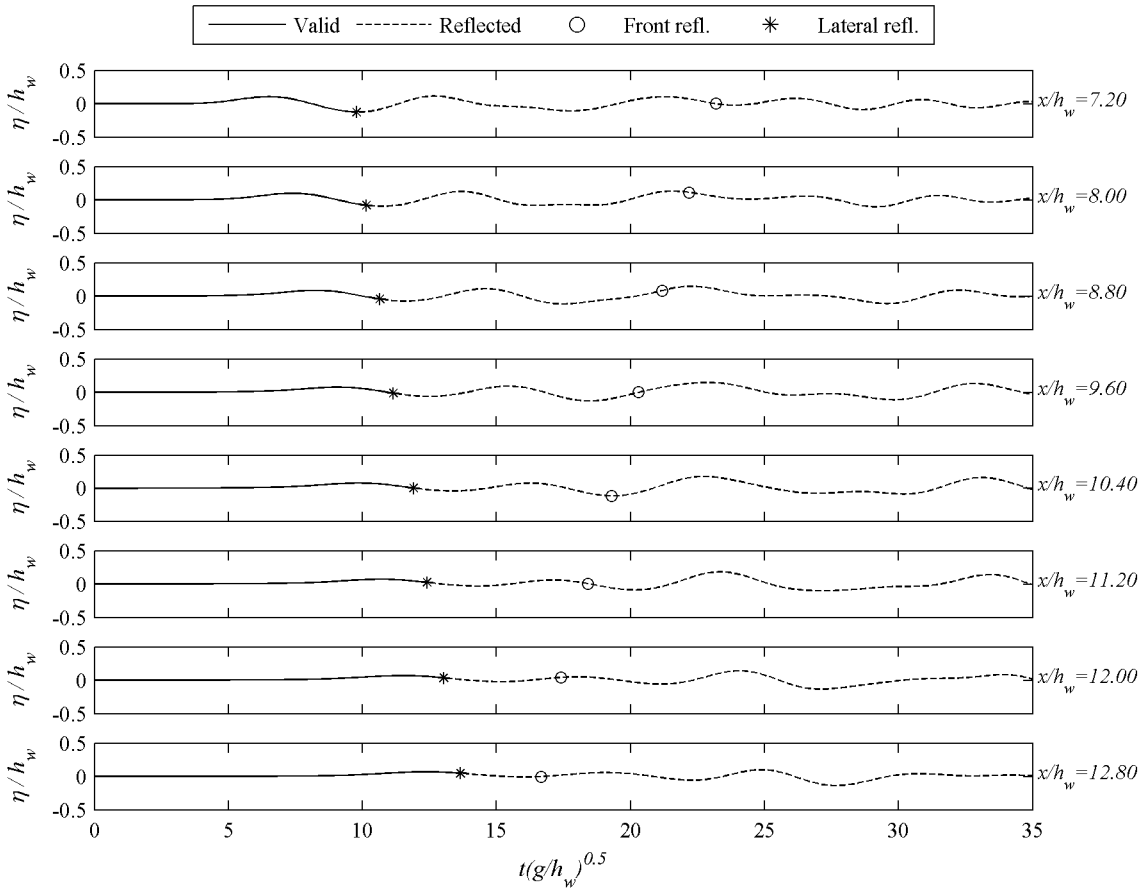

Figure 3.13. Time series and beginning of reflections at centerline by means of circular front wave after applying the thresholds *p* at different x/h_w locations for the run *Unique_M50_hs0.10_15.5deg*, having a *Fr* = 2.11.

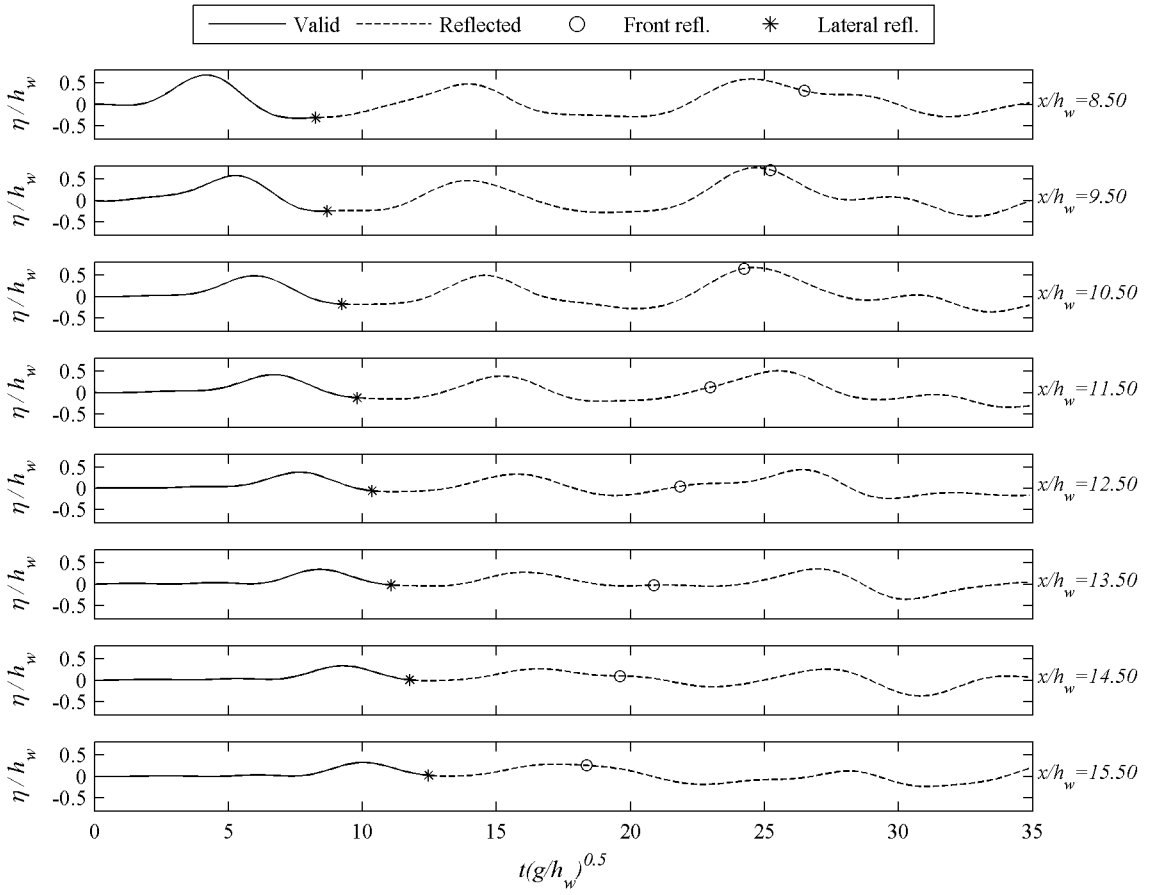

Figure 3.14.Time series and beginning of reflections at centreline by means of circular front wave, after applying the thresholds *p* at different x/h_w for the run *Unique_M139.5_27.8deg* having *Fr* = 3.70.

3.2.2.3 Elliptical wave front

After the observation of the radial propagation of the wave front, an elliptical shape was recognized. A proof of the inaccuracy of the circular wave front representation is given by Figure 3.15 and Figure 3.16. Those figures show how the frontal reflection is correctly located, as expected, but the estimated arrival of lateral reflections is clearly earlier than the actual arrival (see for comparison Figure 3.18, Figure 3.19 and Figure 3.20).

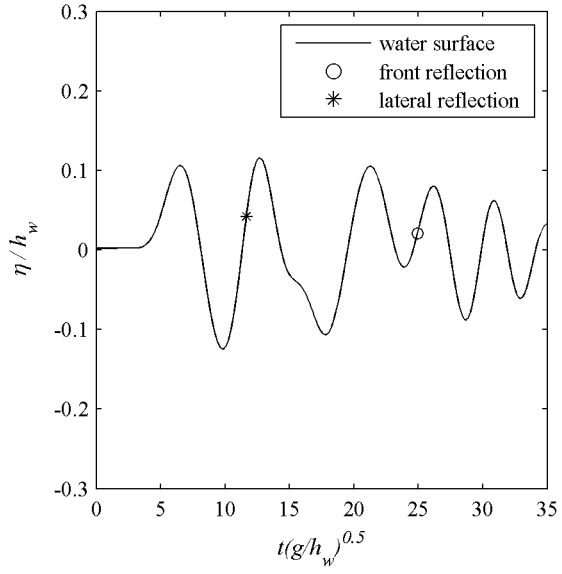

Figure 3.15. Water surface displacement at x/h_w = 7.2 for the run *Unique_M50_hs0.10_15.5deg*, having a *Fr* = 2.11: wave time series at the centerline of the tank and estimated peak reflections by means of circular wave front.

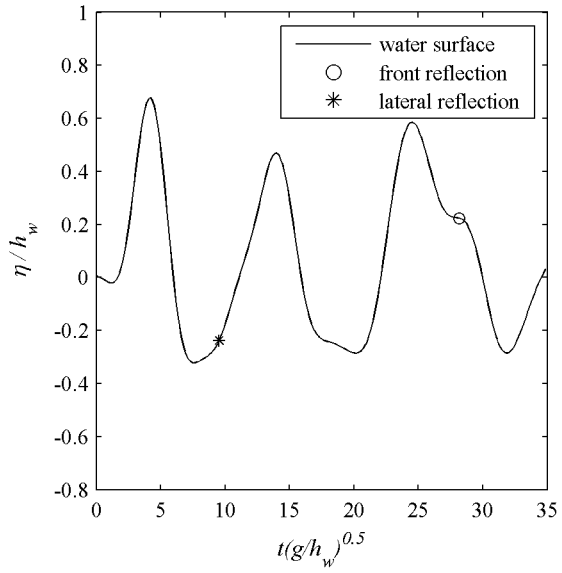

Figure 3.16. Water surface displacement at x/h_w = 8.5 for the run *Unique_M139.5_27.8deg* having *Fr* = 3.70: wave time series at the centerline of the tank and estimated pea reflections by means of circular wave front.

The assumption of an elliptical shape can be justified by the fact that the main inertia of the sliding material is in the main direction (θ = 0). Thus, the velocity of wave propagation can be expected to be higher along the main direction then in the other radial directions. The observation of the available transversal sections of measurement (red lasers) provides, when possible, some interesting data on the elliptical shape.

The elliptical shape was found to be similar for every run in the explored ranges of landslide velocity and angle of impact. Evidence of this statement can be found in the following chapter, analyzing two different key experiment configurations.

The classical equation of the ellipse in Cartesian reference is:

$$\frac{x^2}{a_e^{\,2}} + \frac{y^2}{b_e^{\,2}} = 1 \tag{3.6}$$

where a_e and b_e are respectively the major and minor semi-axes of an ellipse centered on the axes' origin (see Figure 3.17). The focus distances f from the center are given by

$$f = \sqrt{a_e^{\,2} - b_e^{\,2}} \tag{3.7}$$

and the eccentricity of the ellipse is given by

$$e = f / a_e \tag{3.8}$$

When $e = 0$ and thus $f = 0$ and $a_e = b_e$, the ellipse degenerates into a circle of radius $r = a_e = b_e$.

When $e = 1$ and thus $f = a_e$ and $b_e = 0$, the ellipse degenerates into a segment of longitude $2a_e$.

The eccentricity e and alternatively the ratio

$$n = \frac{b_e}{a_e} \tag{3.9}$$

give an idea of the difference from the associated semi-circle having $r = a_e$ and a semi-circumference $p_1 = \pi r$.

Ramanujan (1914) gives an approximated solution to the semi-circumference p_2 of an ellipse having an error of approximation, which was "obtained empirically", of the order of $\boldsymbol{h^8}$:

$$p_2 \approx \frac{\pi}{2}\left(3\left(a_e + b_e\right) - \sqrt{10a_e b_e + 3\left(a_e^{\,2} + b_e^{\,2}\right)}\right) \tag{3.10}$$

If $r = a_e$ and thus $b_e = na_e = nr$, equation (3.10) can be rewritten as

$$p_2 \approx \frac{\pi}{2} r\left(3\left(1+n\right) - \sqrt{10n + 3\left(1+n^2\right)}\right) \tag{3.11}$$

From the observed experiment, an average value of $n = 0.72$ is found, thus the ratio between the circumferences of the circle with $r = a_e$ and the ellipse with $n = 0.72$ can be obtained as:

$$\frac{p_1}{p_2} = \frac{\pi r}{0.866\pi r} = 1.155 \tag{3.12}$$

The ratio in equation (3.12) suggests that the estimated circular wave front assumed above has a perimeter 15.5% longer than the observed elliptical wave front.

The ellipse can be expected to change in shape farther in the field, until probably degenerating into a circle, which was observed by many researchers. This behavior can be expected far from the perturbation, where linear, sinusoidal, long waves are to be expected. Those waves travel with a celerity which depends only on the water depth. However, no significant change was observed inside our tank, due to the limited distance of propagation from impact measured. The eccentricity of the wave front is an interesting feature to be included in the evaluation of lateral reflection (which is expected to arrive later) and in the calculation of total wave energy.

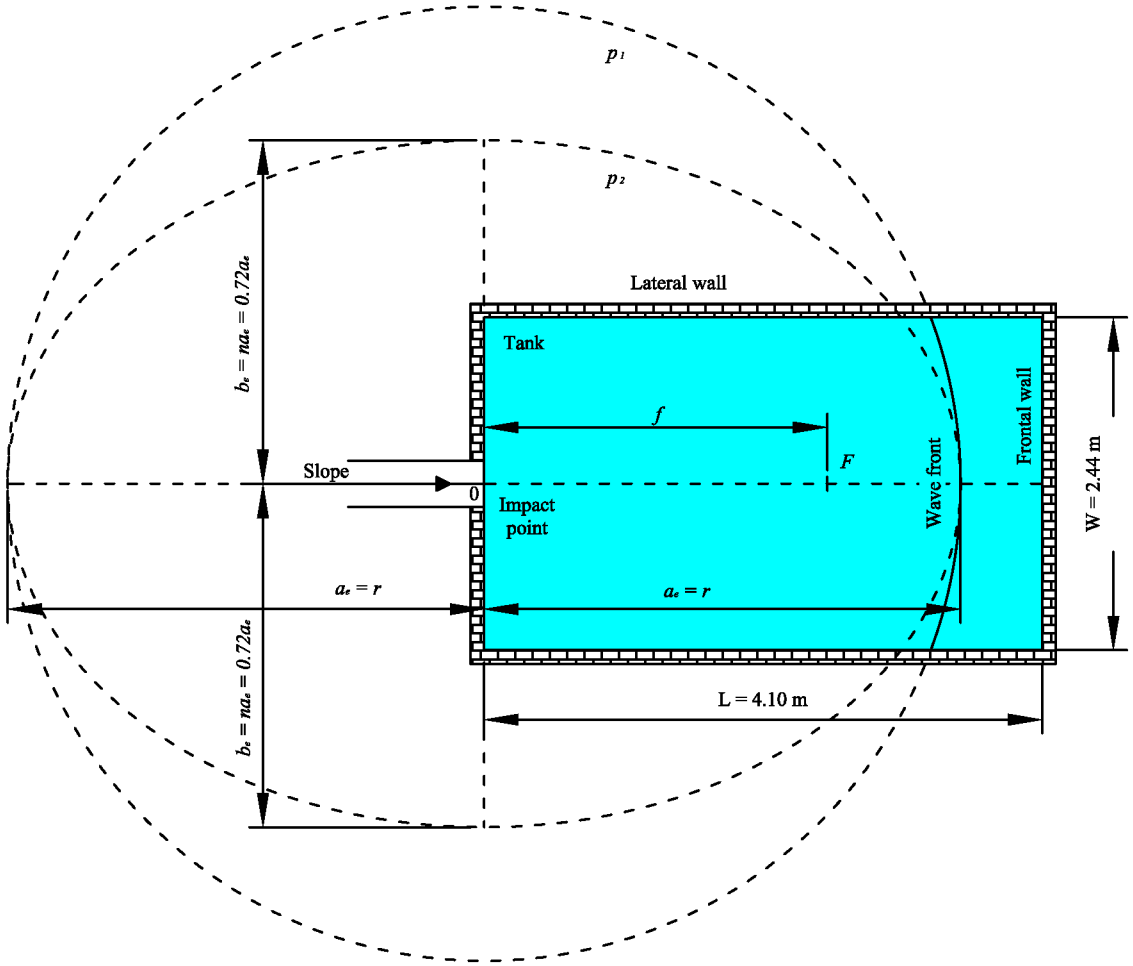

Figure 3.17. Comparison between circular and elliptical wave fronts in the experimental water tank.

3.2.2.4 Lateral reflections of elliptical wave

Using the concepts introduced in the previous chapter, it is immediate to state that the lateral velocity is n = 0.72 times slower than the main velocity along the main direction. Thus a correction of n is introduced in the calculation of lateral reflection achieved using the symmetries

of a circle. With this method, it is possible to estimate the time taken by the lateral reflection to arrive back to the longitudinal centerline of the tank.

Proofs of this behavior can be found observing the run *Unique_M139.5_27.8deg* having Fr = 3.70. According to Figure 3.18 the first peak arrives at a distance from impact of x/h_w = 8.5 after $t(g/h_w)^{0.5}$ = 4.202. At the same transversal section (x/h_w = 8.5), the first laterally reflected wave peak arrives back at the center line of the tank after $t(g/h_w)^{0.5}$ = 13.17, as shown in Figure 3.19. This observed time perfectly matches the time of lateral reflection estimated by means of an elliptical wave front form, as reported in Figure 3.18.

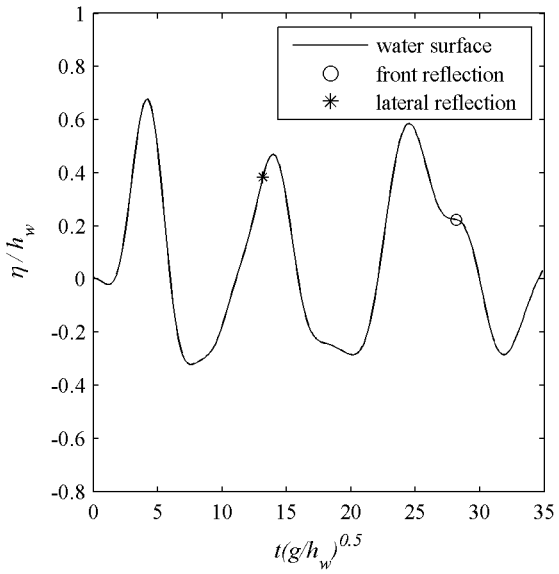

Figure 3.18. Water surface displacement at x/h_w = 8.5 for the run *Unique_M139.5_27.8deg* having Fr = 3.70: wave time series at the center line of the tank and estimated peak reflections by means of elliptical wave front of n = 0.72.

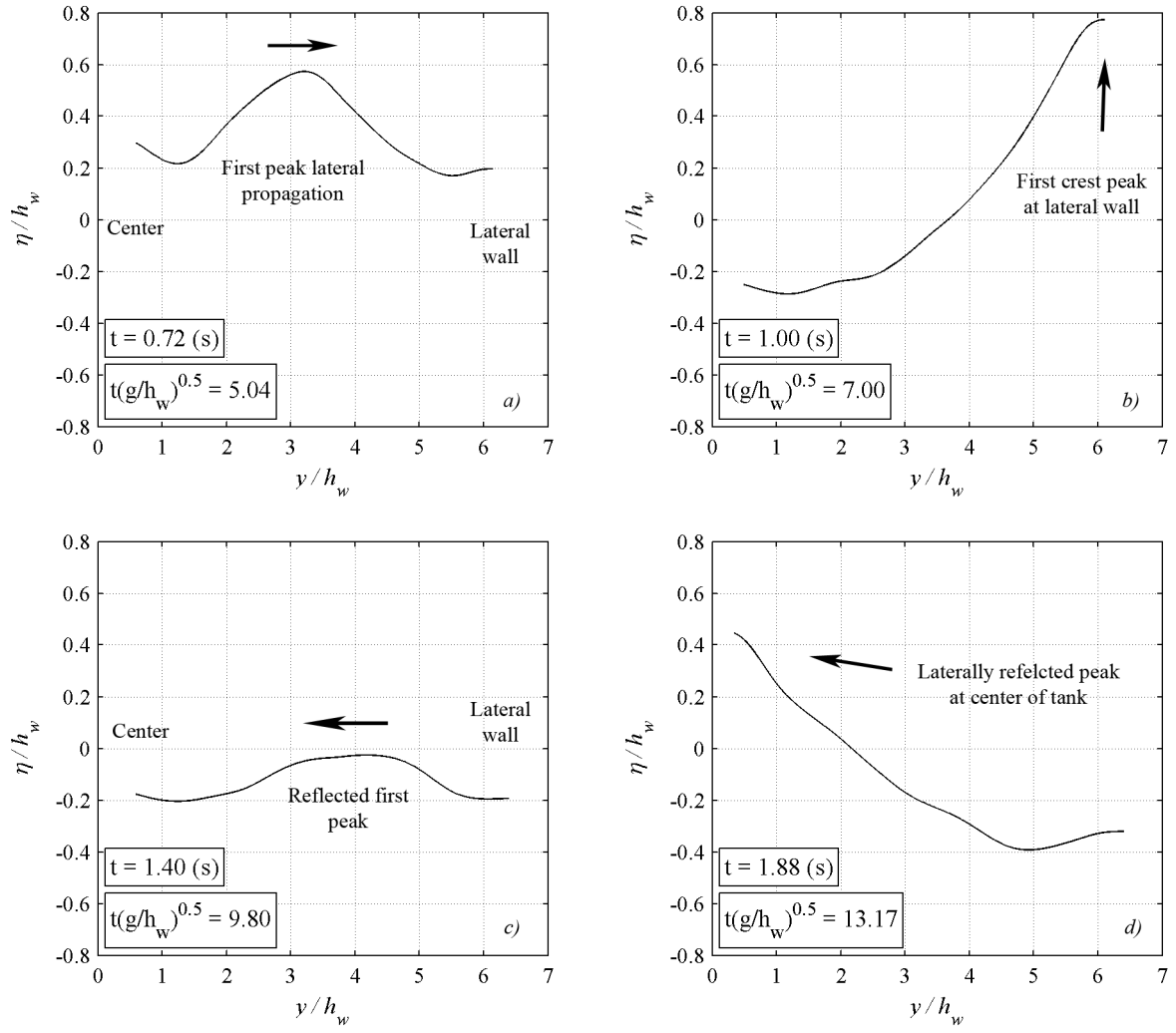

Figure 3.19.Run *Unique_M139.5_27.8deg* having *Fr* = 3.70. Sequence of propagation and reflection behavior of the first wave crest along the transversal section at a distance from impact of x/h_w = 8.5: a) lateral propagation of first peak; b) maximum run-up of the first peak at lateral wall; c) the peak is reflected back toward the center line of the tank; d) the reflected peak reaches the center line of the tank.

Similar results were found for the run *Unique_M50_hs0.10_15.5deg* having m = 50 kg, α = 15.5°, Fr = 2.11 and h_w = 0.25 m, at a distance from impact of x/h_w = 7.2. For experiments having a slope of α = 15.5°, the elliptical form was found to be n = 0.78, due to the lower velocity of impact. The application of an elliptical form ratio n = 0.78, confirms the expected behavior of the lateral reflection's peak arrival, as can be observed in Figure 3.20.

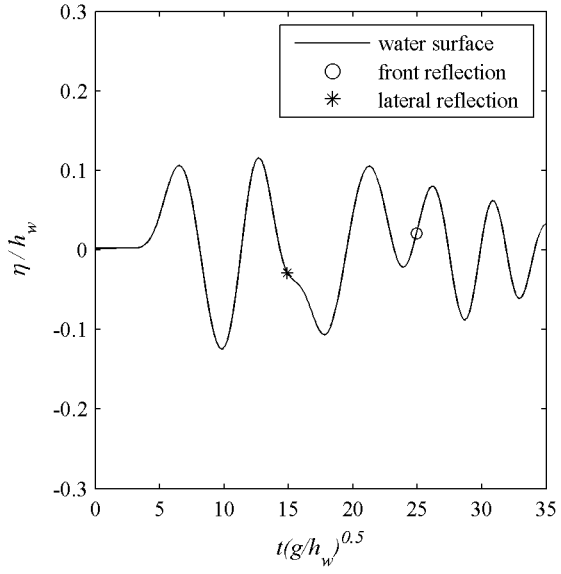

Figure 3.20. Water surface displacement at x/h_w = 7.2 for the run *Unique_M50_hs0.10_15.5deg*, having a *Fr* = 2.11: wave time series at the center line of the tank and estimated peak reflections by means of elliptical wave front of *n* = 0.78.

In Figure 3.21 and Figure 3.22 the reflected peaks are highlighted for the two mentioned runs: it can be seen that the first wave's laterally reflected peak overlaps mainly after, or at least at, the second wave crest. This observation is confirmed by analyzing the transversal measurement, where at the same location the first wave lateral reflection's peak arrives at the centerline simultaneously with the second wave peak. Thus, it is reasonable to state that the first crest and first trough signals are certainly clean.

A threshold of p_{front} = 0.15 is chosen due to reasons previously explained and p_{lat} = 0.50 is chosen observing that the influence of the lateral reflection is lower than the front reflection. The result of the application of those thresholds can be observed in Figure 3.23 and Figure 3.24.

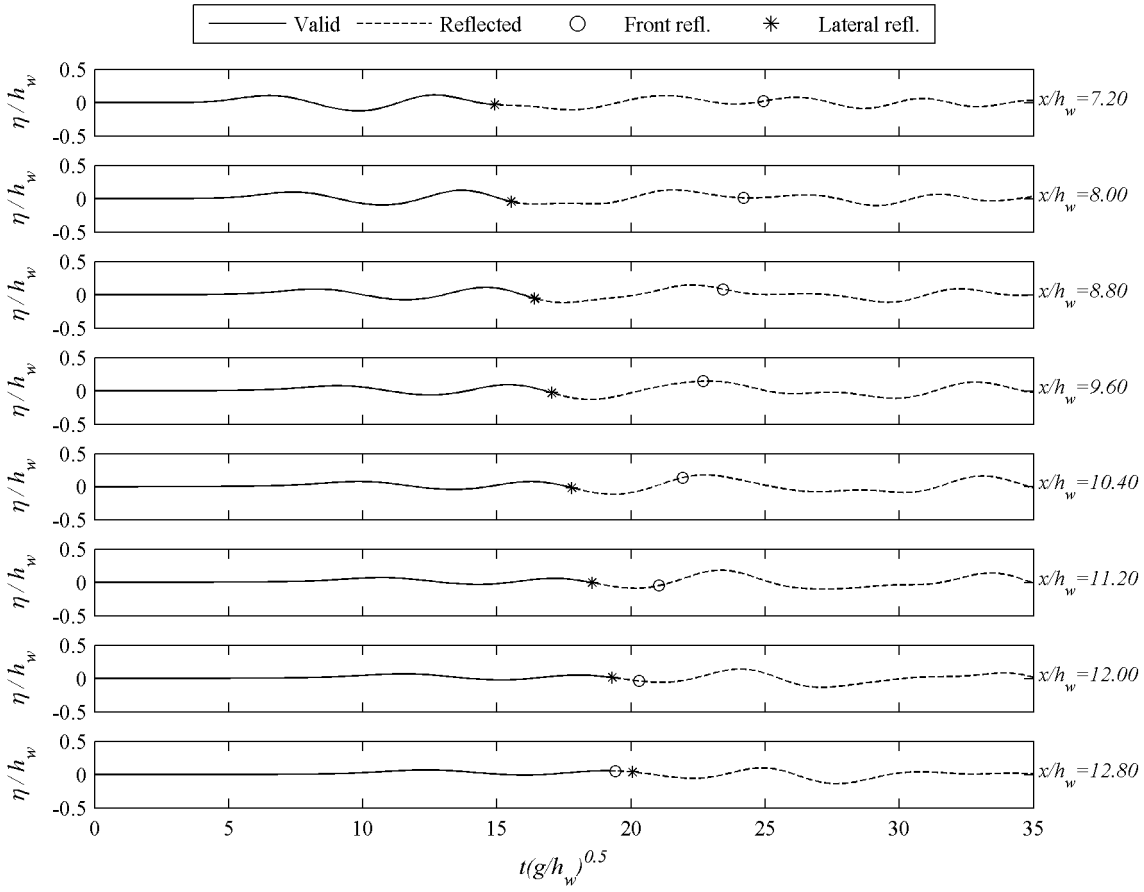

Figure 3.21. Time series at different x/h_w locations the run *Unique_M50_hs0.10_15.5deg*, having a Fr = 2.11. The points represent the peaks of the wave peaks reflected back to the centerline of the tank by means of an elliptical front.

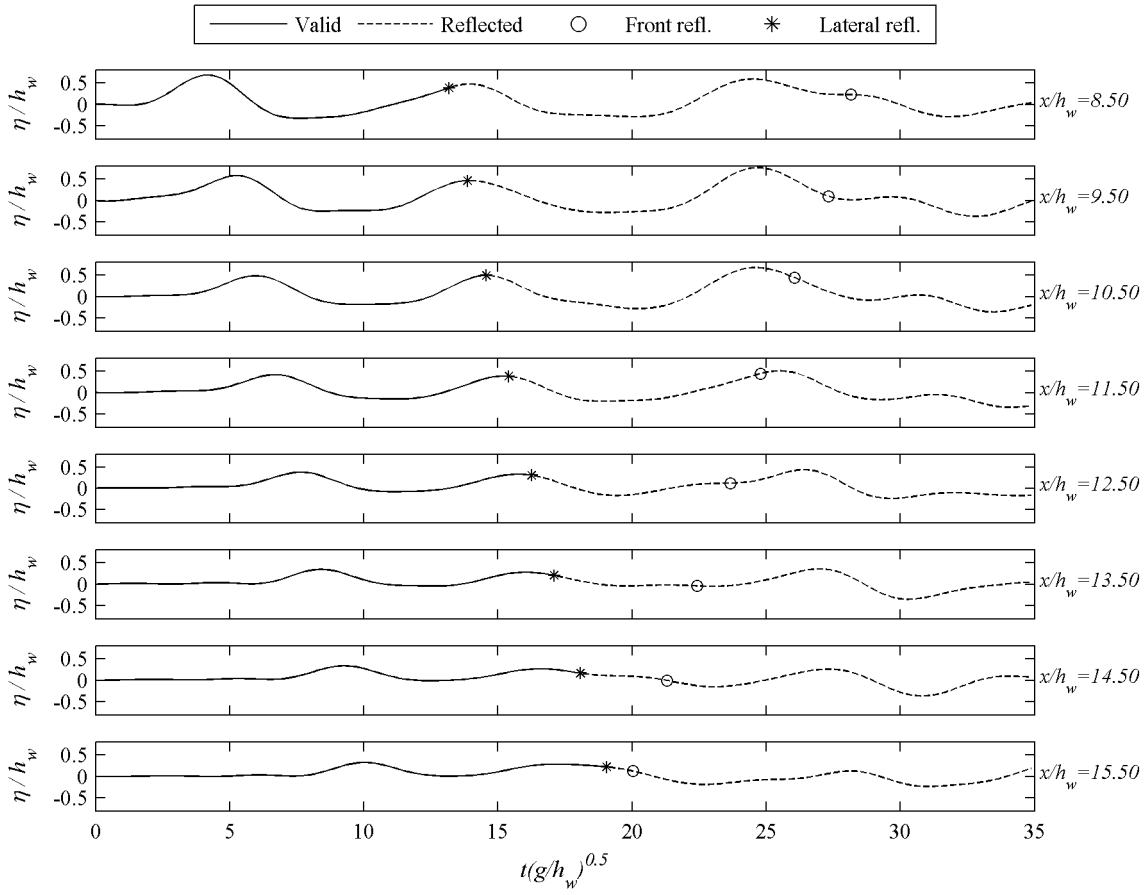

Figure 3.22. Time series at different x/h_w locations for the run *Unique_M139.5_27.8deg* having $Fr = 3.70$. The points represent the peaks of the wave peaks reflected back to the centerline of the tank by means of an elliptical front.

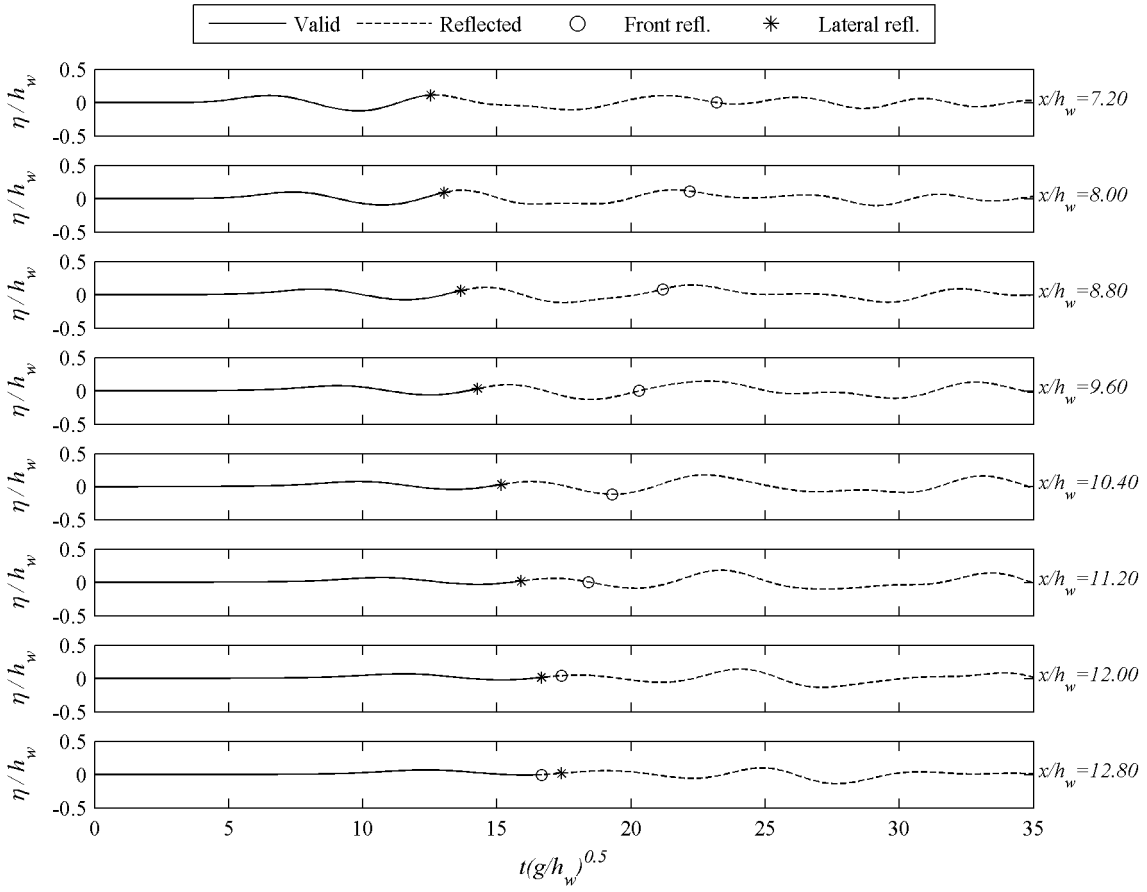

Figure 3.23. Time series at different x/h_w locations for the run *Unique_M50_hs0.10_15.5deg*, having a Fr = 2.11. The points represent the estimated beginning of reflected wave influences back to the centerline of the tank by means of an elliptical front.

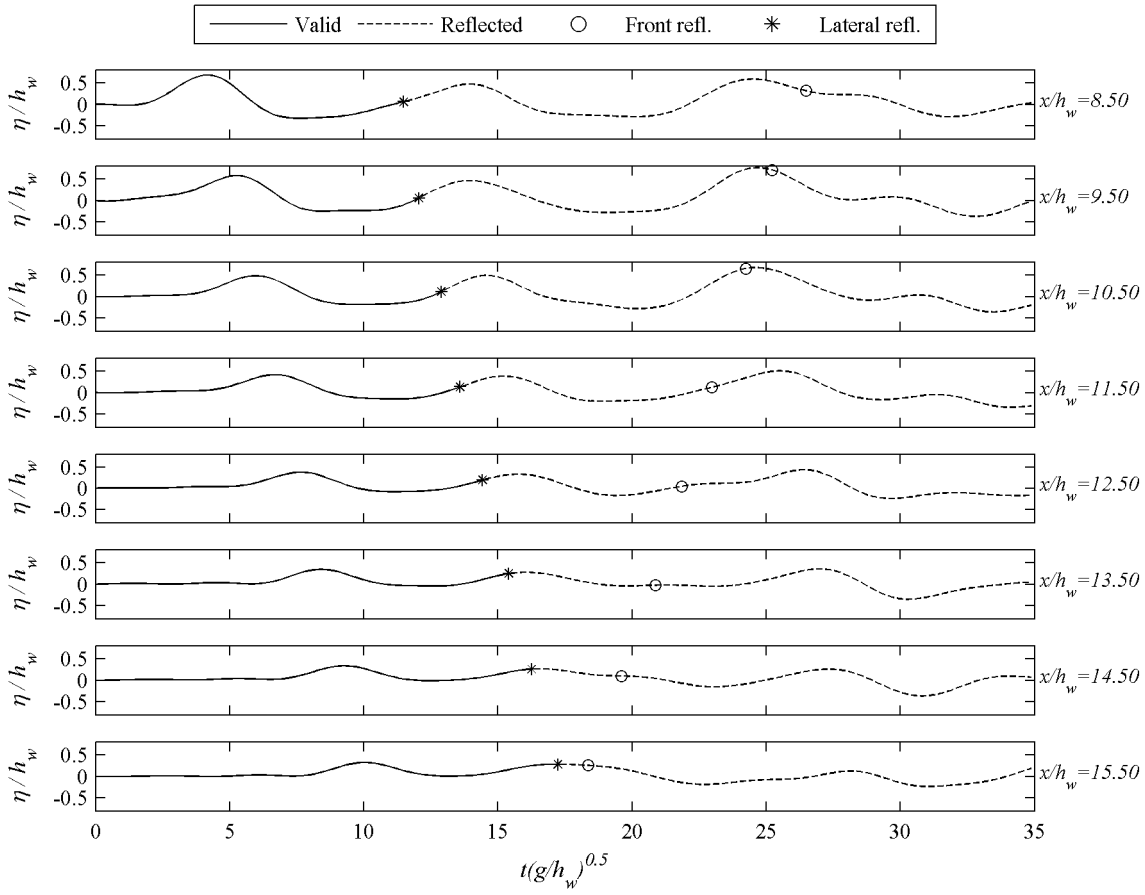

Figure 3.24. Time series at different x/h_w locations for the run *Unique_M139.5_27.8deg* having Fr = 3.70. The points represent the estimated beginning of reflected wave influences back to the centerline of the tank by means of an elliptical front.

3.2.3 Amplitude

The first wave crest amplitude is measured considering the envelope curve of the maxima of the first wave crest propagating along x and t. The decrease in amplitude was approximated by dimensionless exponential functions that can describe properly the amplitude decay in space and time. In section 4.6 the fitting dimensionless exponential functions of amplitude decay are presented and analyzed.

Figure 3.25 displays the first wave amplitude evolution in space (Figure 3.25a) and time (Figure 3.25b) for all the analyzed runs. The whole measurements of wave amplitude decay, together with the coefficients of the fitting dimensionless exponential functions, are given in sub-appendix C.5.

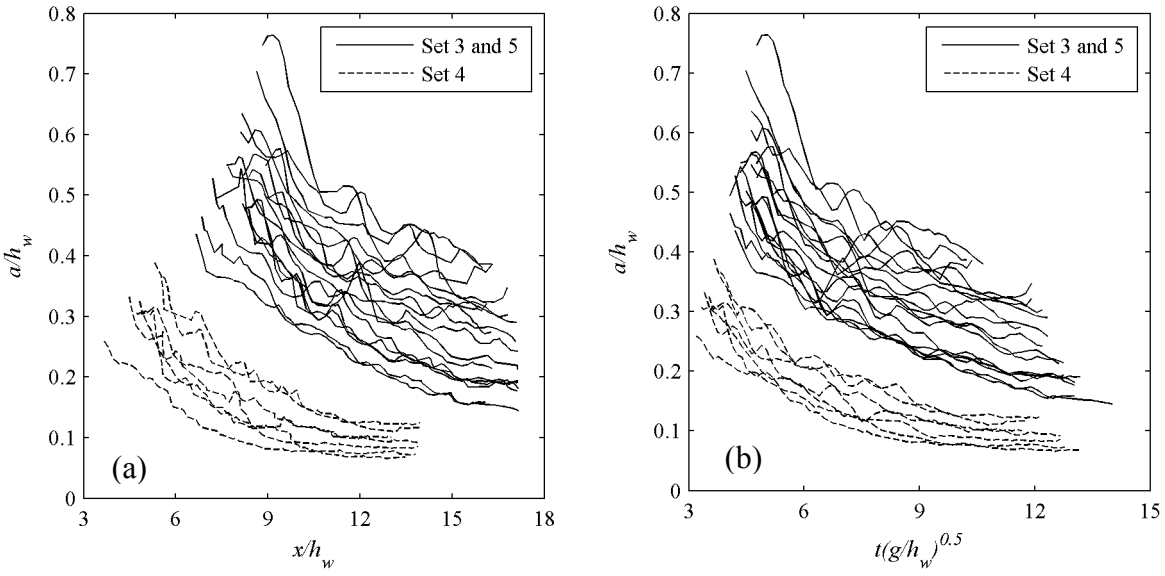

Figure 3.25. First crest amplitude in space (a) and time (b) for all the analyzed experiments.

The measured amplitudes of waves fall in the range $a/h_w = [0.05; 0.76]$. As a reference value, the upper limit is close to the breaking limit for solitary waves introduced by M'Cowan (1894): a_{sol}/h_w = 0.78. The reverse process that permits the wave to pass from a breaking to a non-breaking condition is not clear. On this basis, we might be in a breaking condition in some cases, at least close to impact. A breaking wave includes an added dissipation as well as air entrainment and detrainment processes. However it was not possible to observe these behaviors due to the condition of darkness required by the experiments.

3.2.4 Celerity

The celerity of the first wave peak, v_w , was measured along the main direction x to observe its spatial and temporal variation. Some concerns rose when observing high discontinuities in $v_w(x)$ and $v_w(t)$ due to peak position identification. This drawback is discussed in section 2.6.3 (see Figure 2.32). Finally, it was decided to average v_w along x or t to get a unique value. The wave celerity seems to be constant along the observed distance as confirmed, for instance, by the excellent linear fit in Figure 2.32b. The ranges, mean values and standard deviations of results are reported in Table 3.5. In this table it is possible to observe the relation between v_w, the linear shallow water wave celerity $c = \sqrt{gh_w}$ and the celerity of a solitary c_{sol} wave as equation (1.1). $c_{sol}(x,t)$ is calculated point by point with the available amplitude and averaged to get an unique value.

Also, the range of correlation coefficients of the linear fitting (equation (3.13)) similar to that in Figure 2.32b is reported in Table 3.5

$$x = v_w t + x_0 \tag{3.13}$$

Table 3.5. Ranges of first peaks celerity and ratio with the linear shallow water wave celerity and solitary wave celerity. R^2 is the correlation coefficient of the linear fitting similar to that in Figure 2.32b.

	v_w (m/s)	R^2 (-)	c (m/s)	v_w / c (-)	c_{sol} (m/s)	v_w / c_{sol} (-)
Mean values	1.56	0.996	1.45	1.08	1.64	0.95
Maximum values	1.91	0.999	1.57	1.36	1.72	1.12
Minimum values	1.38	0.989	1.40	0.98	1.57	0.88
Standard deviation	0.14	0.002	0.08	0.11	0.05	0.06

The observed celerity exceeds the celerity of linear shallow water waves by 8% on average and by 38% at most. This means that the celerity of the tsunami is higher than the one approximated by the shallow water theory. The standard deviation of the ratio v_w/c is 0.11.

The observed celerity is lower than the celerity of solitary waves by 5% in average. This means that the celerity of the tsunami is lower than the one approximated by the solitary wave theory. The standard deviation of the ratio v_w/c_{sol} is 0.06. Thus, for our observation both approximations work well.

Complete measurements and correlation coefficients are given in sub-appendix C.6.

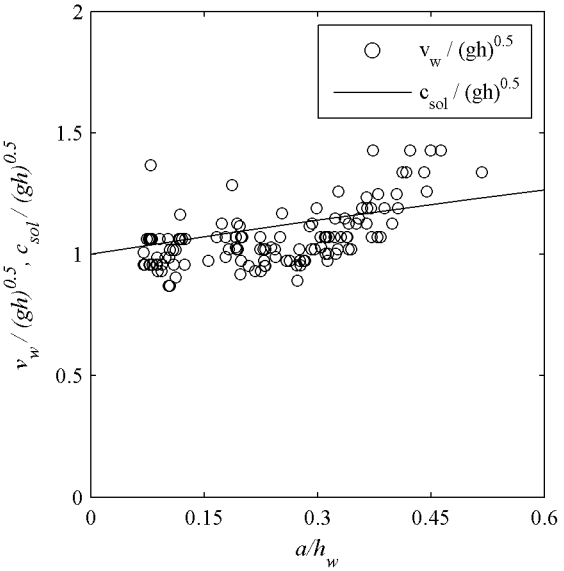

Figure 3.26. First peak celerity measured between selected spots (probe-like) for all the analyzed experiments.

A relationship between the wave amplitude and the first peak celerity for some selected locations can be observed in Figure 3.26. Here the velocity is calculated between selected spots, in a probe-like view.

3.2.5 Length and period

Length l and period T of the first wave from first up-cross to second up-cross are reported here respectively in Figure 3.27a and Figure 3.27b. The length and the period of a wave were measured in a probe-like configuration, where the measurement of the water surface displacement is available in time. It was not possible to measure l and T through measurements quasi continuous in space due to the limited window of observation.

The results of Figure 3.27a and Figure 3.27b are reported here for the sake of completeness. However they are partially compromised by reflections (see section 3.2.2). The length and the period start to be corrupted by reflections after a certain point in the wave tank. The start of corruption of the signals pertaining to l and T changes from an experiment to another. It was not possible to find a rule suitable to recognize the limits of observation for l and T.

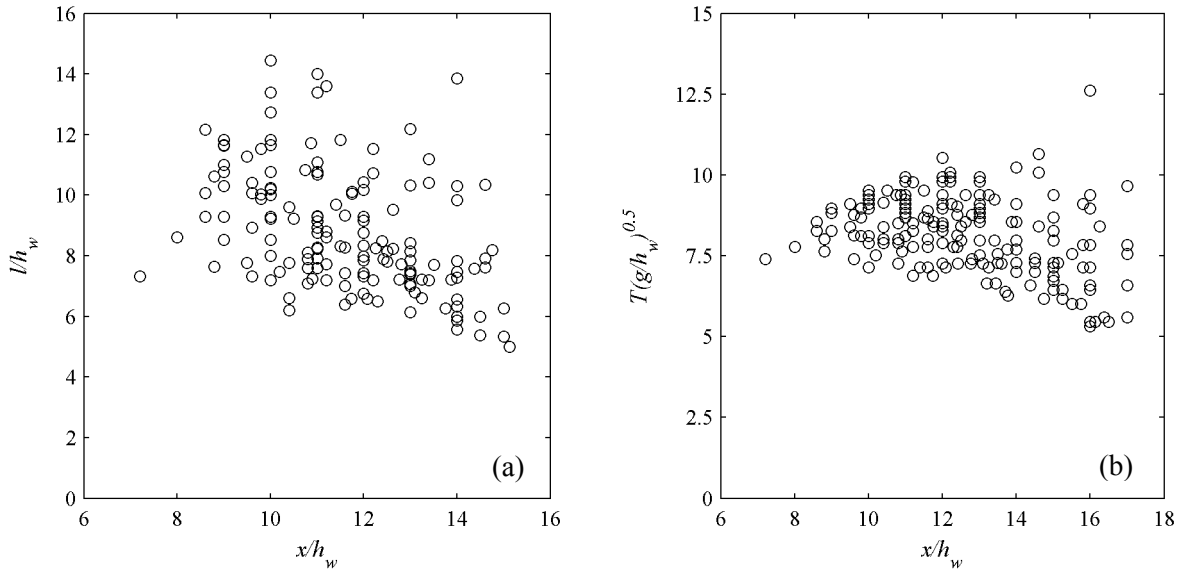

Figure 3.27. Length (a) and period (b) of the recorded first waves from first up-crossing point to second up-crossing point for all the analyzed experiments.

3.2.6 Volume of first crest

The volume of the first crests V_w is recorded for every experiment along distance and time. The wave volume is calculated as the integral of the first wave crest between P_1 and P_2 as

explained in section 2.5.4.3.2, Figure 2.26. The integral of the first wave crest semicircle having a constant vertical displacement η along the front is defined as:

$$V_w = \int_{x=P_1}^{x=P_2} (\pi x \eta)\, dx \tag{3.14}$$

In order to establish the exact position of the wave source and the wave elliptical form (as explained in section 3.2.2.3), two corrections were introduced. The first attempts to position the source of the wave at the centroid of the landslide front (see Figure 3.3) at impact with water *x'*, correcting the *x* as follow:

$$x' = x - \frac{h_{s,front}}{2} \sin^{-1}(\alpha) \tag{3.15}$$

This shifting is significant close to the wave source, but loses weight as the crest moves farther away.

The second correction attempts to reproduce the wave elliptical form through the introduction of a factor of shape correction *n* (see section 3.2.2.3). Therefore the resulting integral is:

$$V_w = n \int_{x=P_1}^{x=P_2} (\pi x' \eta)\, dx \tag{3.16}$$

The reference of the position of V_w still remains the distance from the intersection wedge-water level *x*.

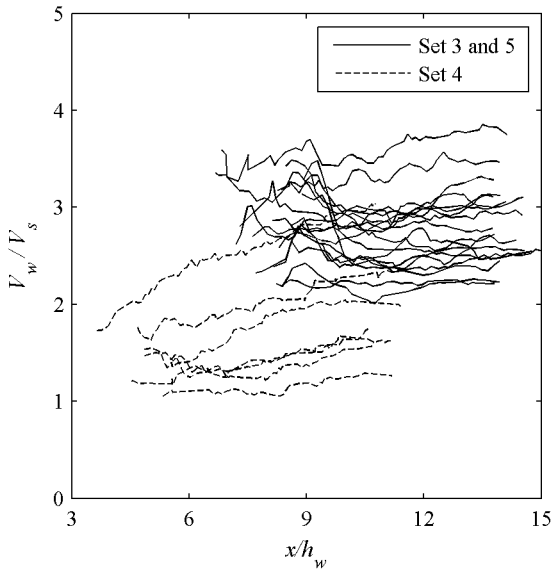

Figure 3.28. Evolution of the wave volume along the distance from impact for all the analyzed experiments.

Figure 3.28 displays the volume's evolution along the distance for all the experiments. Except close to impact, where the wave is still forming and the volume is increasing, the mentioned

volume stays almost constant along the wave propagation. This interesting result confirms that the leading wave does not lose volume in favor of the following waves. The results that prove this behavior are listed in Table 3.6 while the whole data are collated in sub-appendix C.7.

Table 3.6. Ranges of average and standard deviation of the wave volume along the distance

	V_w / V_s average	V_w / V_s STD
Mean values	2.47	0.14
Maximum values	3.61	0.37
Minimum values	1.16	0.02
STD	0.64	-

3.2.7 Energy of first crest

The landslide energy transfers to the water provoking at first a crater, then a large splash and finally the wave train. During this transfer, a large amount of energy is dissipated through friction between the landslide and the slope by means of basal friction, through turbulence dissipations due to the high Reynolds number involved, through the splash effect and through air entrainment and detrainment. These dissipations and the energy transfer are explained in chapter 5.

Immediately after the crater and the splash are extinguished, it is possible to take a first measurement of the leading wave's characteristics. At this point, called x_{max} and at time t_{max} (see chapter 4), the formed wave is found to be "suspended" at its highest amplitude and it retains mainly potential energy. After this instant, the wave starts to propagate and progressively the potential energy converts into kinetic energy. At the same time that the wave loses potential energy, it also loses amplitude. Close to formation, waves are non-linear. But sufficiently far from the generation point the waves stabilize (Kamphuis and Bowering, 1970) and begin assuming a linear behavior (LeMeauthe, 1996).

In our experiment, only the leading wave energy was evaluated, because reflection effects influence further measurements. However it was demonstrated that the leading wave of the wave train contains more than 90% of the total wave train energy (Law and Brebner, 1968). Thus only a minor amount of energy passes from the leading wave to the wave train. This behavior is partially confirmed by the steadiness of the wave volume along the x (see the previous section).

In section 2.2 it was explained how a negligible amount of energy is dissipated by wave damping due to interaction with boundaries.

Generally, the potential energy per unit width $dE_{w,pot}$ of a wave or a train of waves can be assessed as (Rayleigh, 1877; Lamb, 1932; Ippen, 1966):

$$dE_{w,pot}(x) = \frac{1}{2} b \rho_w g \int_{x_1}^{x_2} \eta^2 dx \tag{3.17}$$

where b is the unitary width of the wave front, x_1 and x_2 are respectively the starting and ending point of energy integration, and η is the water elevation with respect to the still water depth.

Theoretically, to measure the kinetic energy of a gravity wave the velocity field of the wave volume is needed. In effect, the kinetic energy per unit width $dE_{w,kin}$ of a wave or a train of waves is:

$$dE_{w,kin}(x,z) = \frac{1}{2} b \rho_w \int_{x_1}^{x_2} \int_{-h_w}^{\eta} \left({v_x}^2 + {v_z}^2 \right) dz dx \tag{3.18}$$

Some authors (i.e.: Fritz, 2002; Heller, 2008) took advantage of PIV to evaluate $E_{w,kin}$ but only close to impact.

Unfortunately, in the present study the measurement is done only on the water surface, not having adequate data on the velocity field of the wave volume.

It is also true that $E_{w,kin} = E_{w,pot} + E_\sigma$, where E_σ is the surface energy due to surface tension. In case of gravity waves $E_\sigma \approx 0$ and thus, assuming this equipartition of energy, the total energy can be calculated as:

$$E_w = E_{w,pot} + E_{w,kin} = 2E_{w,pot} \tag{3.19}$$

The error made using the equipartition of energy can be taken into account as an underestimation of around 11%, when compared with numerical computations (Williams, 1985 in Fritz et al., 2004).

In order to partially avoid such possible underestimation, in this thesis the total energy of waves E_w close to impact (at first measurement) was considered as merely potential energy, and that farther from impact (at last available measurement) was considered by equipartition of potential and kinetic energy.

Equipartition and energy conservation are confirmed by the measurement done in the tank where:

$$E_w \approx E_{w,pot}(x_{max}) \approx 2E_{w,pot}(x_{fin}) \tag{3.20}$$

Based upon the above assumptions, it was concluded that the measurement of $E_{w,pot}(x)$ is of primary importance to understand the energy conversion during the impact and the wave energy transport along the distance from impact.

The equation (3.17) is valuated having available the wave profile measurements along the space traveled, which is the case of the present study. All the researchers previously mentioned

in the state-of-the-art section, employing measurements of water displacement at certain spots (probe-like), use the definition of potential energy in time. They assume that the waves propagate with constant celerity c. The celerity variation of wave translation was found to rise by 30% both in 2D and 3D experiments. Thus, the assumption of constant celerity c leads to an uncertainty in energy estimation of ± 15% (Mohammed & Fritz, 2012).

The potential energy $E_{w,pot}$ of the semicircular first wave crest having a constant vertical displacement η along the front is defined as follow:

$$E_{w,pot}(x) = \frac{1}{2}\rho_w g \int_{x=P_1}^{x=P_2} \left(\eta^2 x\right) dx \tag{3.21}$$

Similarly to the measurement of the wave volume V_w , the correction on distance of wave source as equation (3.15) and the elliptical front shape correction n are applied as follow:

$$E_{w,pot}(x) = n\frac{1}{2}\rho_w g \int_{x=P_1}^{x=P_2} \left(\eta^2 x'\right) dx \tag{3.22}$$

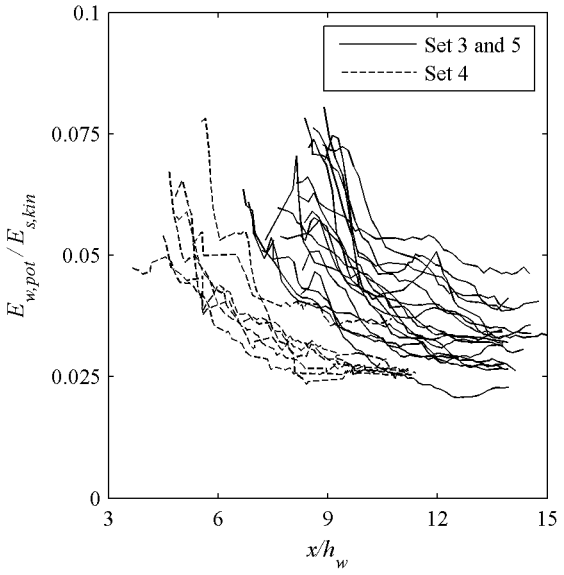

Figure 3.29. Evolution of the wave potential energy along the distance from impact for all the analyzed experiments.

The results of equation (3.22) calculated along x for every experiment is reported in dimensionless form in Figure 3.29. In this figure it is possible to appreciate the trend of the wave potential energy decay in favor of the wave kinetic energy. In effect, in Table 3.7 it is possible to appreciate the ranges of the wave energies, the energy conversion between landslide and wave as well as the total energy conservation of the first wave crest. The ratio $E_{w,pot}(x_{max})$ / $E_{w,pot}(x_{fin})$ is on average 2.05 for all the experiments.

The whole data for each experiment is collated in sub-section C.8.

Table 3.7. Ranges of energies of the first crest and energy conversion between landslides and waves.

	$E_{w,pot}(x_{max})$ (J)	$E_{w,pot}(x_{max})$ / $E_{s,kin}$	$E_{w,pot}(x_{fin})$ (J)	$E_{w,pot}(x_{max})$ / $E_{w,pot}(x_{fin})$
Mean values	64.55	0.064	33.22	2.05
Maximum values	138.50	0.081	76.07	2.55
Minimum values	13.51	0.047	7.10	1.43
Standard deviation	33.85	0.010	20.24	0.26

3.3 Comparison with previous authors

It was possible to compare the experimental results of this thesis with some previous authors' predictors introduced in the state-of-the-art (section 1.3). In particular, two different studies were selected: Heller & Hager (2010) and Mohammed & Fritz (2012). The first one is obtained by 2D and the second by 3D wave propagation experiments. The reasons for the choice of these two studies are that both use granular landslides and provide predictors for wave amplitude. The other authors either use rigid blocks as wave generators or provide only predictors related to wave height. Thus they are not taken into consideration for comparison purposes, on the basis that in the present study only the first wave amplitude is considered. To properly compare results, the front thickness and velocity of landslides are taken into account, in accordance with Heller & Hager (2010) and Mohammed & Fritz (2012).). However, in the present study thickness and velocity of the landslide centroids are used, for predictors in chapter 4, and for the model in chapter 5, as explained in section 3.1.

The comparison with the predictors of Heller & Hager (2010) shows that the experimental results are considerably overestimated in both the maximum wave amplitude (Figure 3.30a) and the wave amplitude along the distance (Figure 3.30b). This fact evidences that the 2D simulations, by concentrating the formed wave and its energy in a straight channel, produce higher waves amplitudes than in 3D simulation, where the wave front can expand laterally. This behavior has been observed also by Panizzo et al. (2005) (see Figure 1.15) and Mohammed & Fritz (2012).

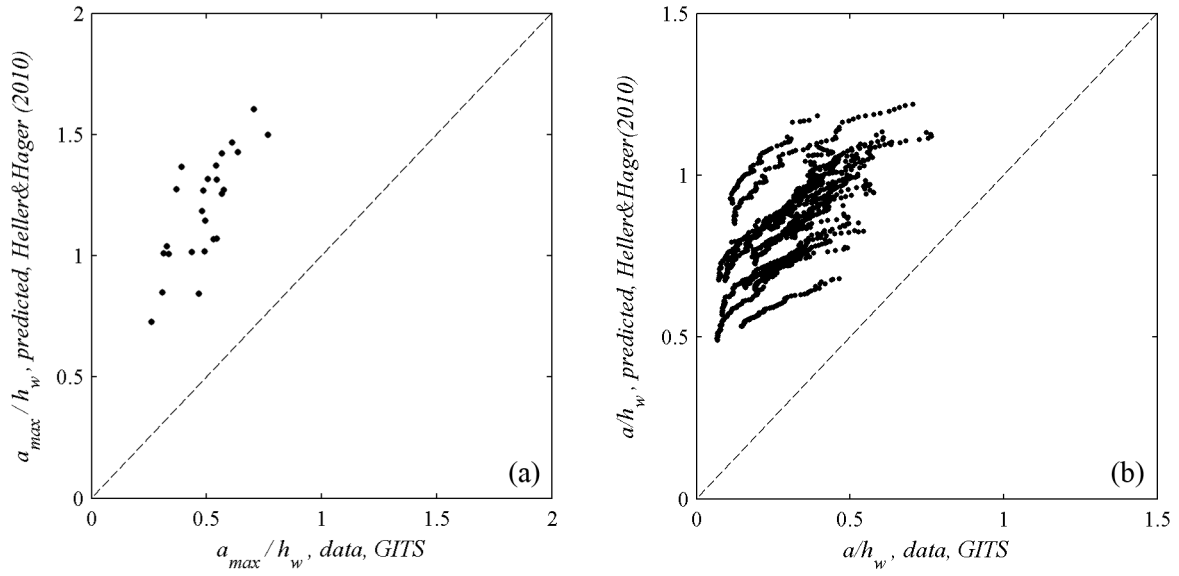

Figure 3.30. Comparison between the GITS data (the present study) and the predictive formulas of Heller & Hager (2010): a) maximum amplitude predicted with equation (1.9); b) amplitude along the distance predicted with equation (1.11).

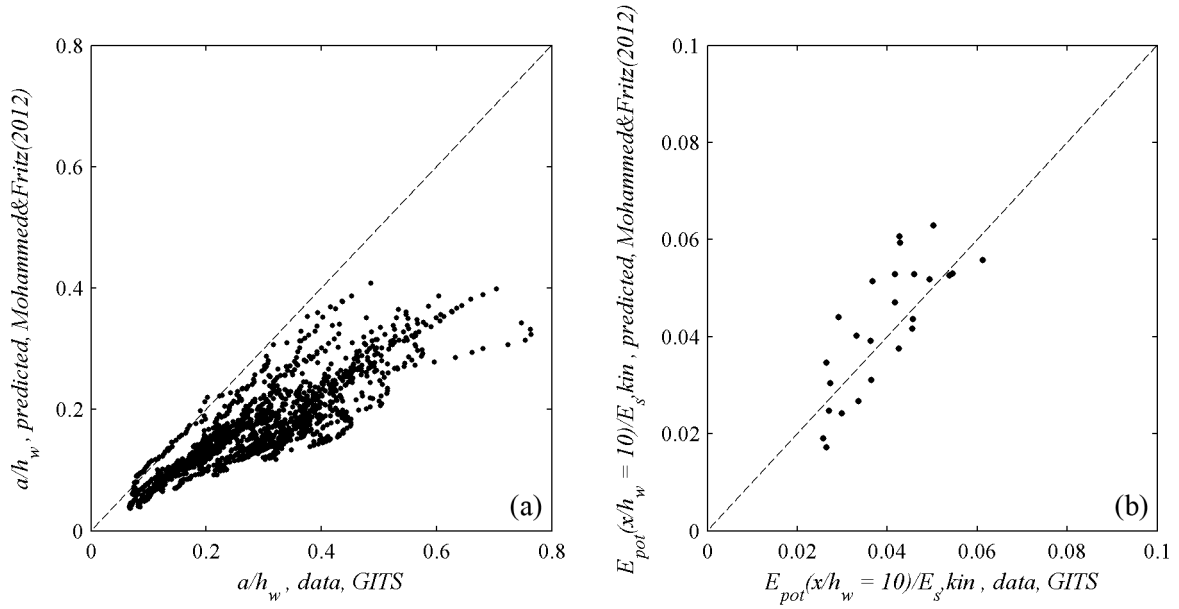

Figure 3.31. Comparison between the GITS data (the present study) and the predictive formulas of Mohammed & Fritz (2012): b) maximum amplitude predicted with equation (1.13); a) amplitude along the distance predicted with equation (1.16).

The comparison with the predictors of Mohammed & Fritz (2012) shows a better performance with respect to our experiments: data and predictions converge to zero for wave amplitude (Figure 3.31a). However the prediction of Mohammed & Fritz (2012) diverges for higher values, underestimating the measured *a* by a factor of circa 1.75. Higher amplitudes are positioned

closer to impact or are originated by higher landslide energy. Our wave generator obviously differs from that used to define the formula of Mohammed & Fritz (2012). The measured amplitudes of waves are in the range $a/h_w = [0.05; 0.76]$.

Therefore, their formula may not properly match our results for higher values of *a,* given that their range of validity is roughly from 0 to 0.38.

On the contrary, with respect to the first crest wave energy at a fixed distance $x/h_w = 10$, the predictor of equation (1.16) fits quite well the data of the present experiments (see Figure 3.31b).

Chapter 4: Empirical predictors of waves

4.1 Introduction

With the aim of predicting the

- maximum wave amplitude a_{max},
- maximum wave location x_{max},
- maximum wave time t_{max},
- wave amplitude decay in space $a(x)$,
- wave amplitude decay in time $a(t)$,
- energy conversion between landslide and water waves $\varepsilon_{s,kin}$ and
- characteristics of the final landslide deposit

different empirical relationships are introduced here by means of multivariable non-linear regressions. These relationships link the landslide features at impact with the waves being formed and the characteristics of the landslide final deposit. The analyses are based on the experimental results introduced in chapter 3. An *ad-hoc* methodology for the optimization framework is presented. The resulting predictors are proved case by case. Moreover the predictors are applied on two past events where available data permits their validation.

4.2 Methodology

The empirical formulas are designed using a multilevel approach: equations with different complexity are formulated in order to enhance usability on the basis of available data.

An *ad-hoc* nomenclature is introduced here to identify the parameters to be fitted, in agreement with the following form:

$$k_{\zeta_3}^{(\zeta_1,\zeta_2)} \tag{4.1}$$

where ζ_1 is the variable to be estimated, ζ_2 is the order of the formula, explained hereafter, and ζ_3 is the number of the parameter.

All formulas are determined using a common concept: to maximize the correlation between measured and estimated quantities.

Taking as an example the formula of equation (4.2), the fitting parameters $k_1^{(a_{max},1)}$ and $k_2^{(a_{max},1)}$ can be adequately optimized to maximize the correlation R^2 between measured and estimated

a_{max}. The task of optimization can be qualitatively seen in the plot of Figure 4.1 where a minimum value of $1-R^2$ for certain values of $k_1^{(a_{max},1)}$ and $k_2^{(a_{max},1)}$ is intuitively visible.

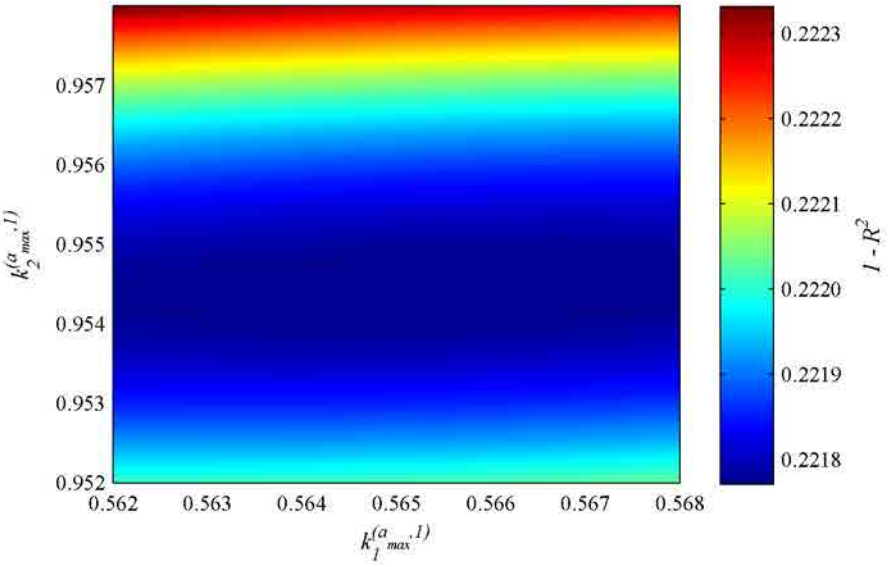

Figure 4.1. Values of $1-R^2$ between measured and estimated a_{max} for a set of parameters of equation (4.2).

To find the optimum values of parameters $k_1^{(a_{max},1)}$ and $k_2^{(a_{max},1)}$ (also known as "best-fitting parameters") that maximize the correlation R^2 between measured and estimated a_{max}, the *Nelder-Mead simplex direct search* algorithm is used. This algorithm (Lagarias et al. 1998), implemented in Matlab®, consists of an unconstrained nonlinear optimization which needs initial values and may give local solutions. Thus, the choice of initial values is important.

The result of the maximization of R^2 for the formula of equation (4.2) can be observed in section 4.3.1.

The methodology described above was applied to all empirical relationships of this chapter.

Considering n as the number of fitting parameters to be optimized, the empirical formulas proposed use the nomenclature of orders $\zeta_2 = n-1$ (i.e.: a zero order formula is made of $n = 1$ parameter, a first order formula is made of $n = 2$ parameters, etc…).

When $n > 2$ parameters need to be calibrated, the optimizing methodology used is the same of $n = 2$ but applied on a n-dimensional space.

4.3 Maximum wave amplitude

The maximum wave amplitude a_{max} of a landslide tsunami wave crest is of primary importance in evaluating the hazard of this phenomenon. The idea is to evaluate a_{max} and subsequently assess the wave amplitude decay, starting from the magnitude of the predicted maximum value (see section 4.6).

In our experiments a_{max} occurs close to impact, and as soon as the splash is exhausted. Therefore, it is also important to assess the distance from impact x_{max} where a_{max} occurs (see section 4.4) and the time from impact t_{max} when a_{max} occurs (see section 4.5).

Only the amplitude of the leading wave is analyzed, as it is considered to be the highest.

In this section, three different relationships are presented in order of complexity from a 1st order equation to a 3rd order equation.

4.3.1 1st order formula

The first model proposed in equation (4.2) provides evidence that h_s plays an important role on the magnitude of the formed wave's a_{max} .

$$\frac{a_{max}}{h_w} = k_1^{(a_{max},1)} \left(\frac{h_s}{h_w} \right)^{k_2^{(a_{max},1)}} \tag{4.2}$$

The optimization of the two parameters yields values of $k_1^{(a_{max},1)} = 5.64 \cdot 10^{-1}$, $k_2^{(a_{max},1)} = 9.56 \cdot 10^{-1}$, with a correlation coefficient between measured data and estimated values of $R^2 = 0.778$ and a mean squared error $MSE = 0.004$ (see Figure 4.2).

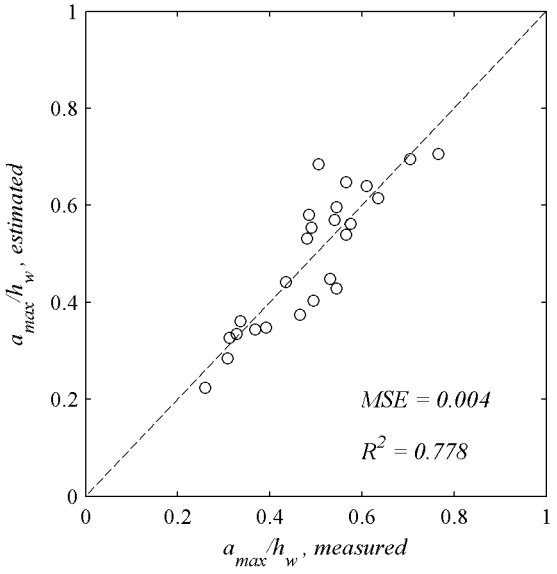

Figure 4.2. Correlation between measured dimensionless a_{max} and estimated dimensionless a_{max} using the optimized equation (4.2)

4.3.2 2nd order formula

The thickness of the sliding material has a certain importance in estimating a_{max}, but the fitting can be improved by the incorporation of other parameters. Thus the landslide kinetic energy at impact $E_{s,kin}/E_{w,hydrostatic}$ is introduced in equation (4.3), $E_{s,kin}$ having intrinsically the mass m_s and velocity v_s of the landslide and $E_{w,hydrostatic}$ the length l_s of the landslide.

$$\frac{a_{max}}{h_w} = k_1^{(a_{max},2)} \left(\frac{h_s}{h_w} \right)^{k_2^{(a_{max},2)}} \left(\frac{E_{s,kin}}{E_{w,hydrostatic}} \right)^{k_3^{(a_{max},2)}} \tag{4.3}$$

The optimization of equation (4.3) yields values of $k_1^{(a_{max},2)} = 2.88 \cdot 10^{-1}$, $k_2^{(a_{max},2)} = 3.89 \cdot 10^{-1}$, $k_3^{(a_{max},2)} = 2.54 \cdot 10^{-1}$, with a correlation coefficient between measured data and estimated values of $R^2 = 0.861$ and a $MSE = 0.003$ (see Figure 4.3).

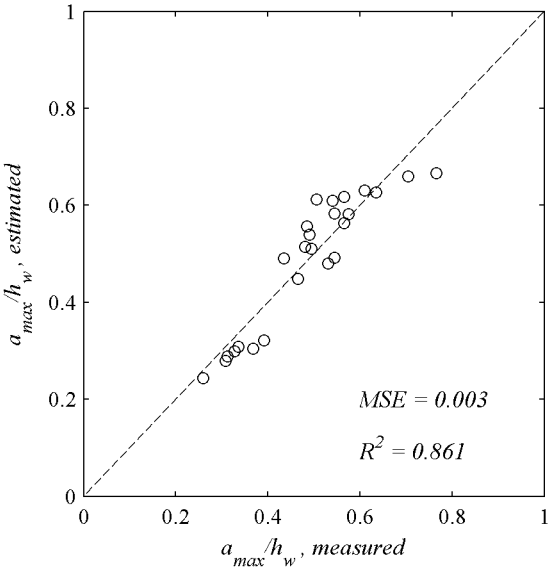

Figure 4.3. Correlation between measured dimensionless a_{max} and estimated dimensionless a_{max} using the optimized equation (4.3)

With the aim to compare directly a_{max} versus h_s, the parameter $k_2^{(a_{max},2)}$ can be conveniently taken as $k_2^{(a_{max},2)}$ = 1.0. Thus, subject to this condition, the optimization of equation (4.3) yields values of $k_1^{(a_{max},2)} = 4.78 \cdot 10^{-1}$, $k_2^{(a_{max},2)} = 1.0$, $k_3^{(a_{max},2)} = 6.66 \cdot 10^{-2}$, with a correlation coefficient between measured data and estimated values of $R^2 = 0.790$ and a $MSE = 0.005$ (see Figure 4.4).

With those values the equation (4.3) can be rewritten as:

$$\frac{a_{max}}{h_s} = 4.78 \cdot 10^{-1} \left(\frac{E_{s,kin}}{E_{w,hydrostatic}} \right)^{6.66 \cdot 10^{-2}} \tag{4.4}$$

The equation (4.4) describes the ratio between the formed leading wave maximum amplitude and the landslide average thickness with an MSE = 0.009 when reapplied to experimental data.

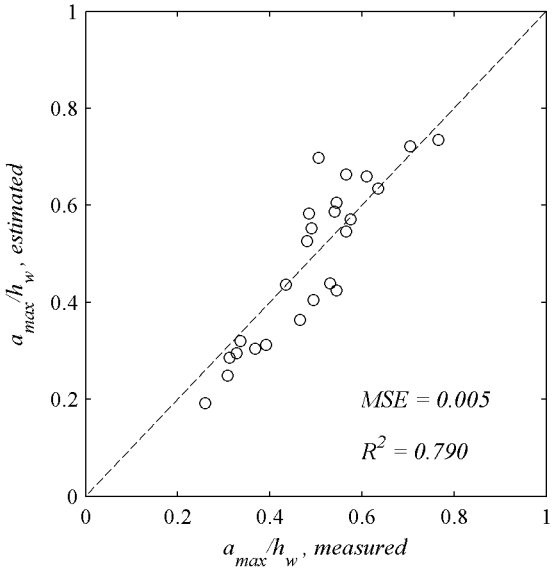

Figure 4.4. Correlation between measured dimensionless a_{max} and estimated dimensionless a_{max} using the optimized equation (4.3) with $k_2^{(a_{max},2)} = 1.0$.

4.3.3 3rd order formula

In the empirical formula of equation (4.3) $E_{s,kin}$ contains the velocity v_s of the landslide and $E_{w,hydrostatic}$ the length l_s of the landslide. In order to separate all the involved landslide parameters, the 3rd order empirical formula of equation (4.5) is introduced below.

$$\frac{a_{max}}{h_w} = k_1^{(a_{max},3)} \left(\frac{h_s}{h_w}\right)^{k_2^{(a_{max},3)}} \left(\frac{l_s}{h_w}\right)^{k_3^{(a_{max},3)}} \left(\frac{v_s}{\sqrt{g h_w}}\right)^{k_4^{(a_{max},3)}} \tag{4.5}$$

In equation (4.5) the values of the optimized fitting parameters are $k_1^{(a_{max},3)} = 1.18 \cdot 10^{-1}$, $k_2^{(a_{max},3)} = 4.59 \cdot 10^{-1}$, $k_3^{(a_{max},3)} = 4.63 \cdot 10^{-1}$ and $k_4^{(a_{max},3)} = 5.54 \cdot 10^{-1}$, with a correlation coefficient between measured data and estimated values of $R^2 = 0.924$ and a $MSE = 0.001$ (see Figure 4.5).

Equation (4.5) explains that the three landslide parameters h_s, l_s and v_s have a similar weight.

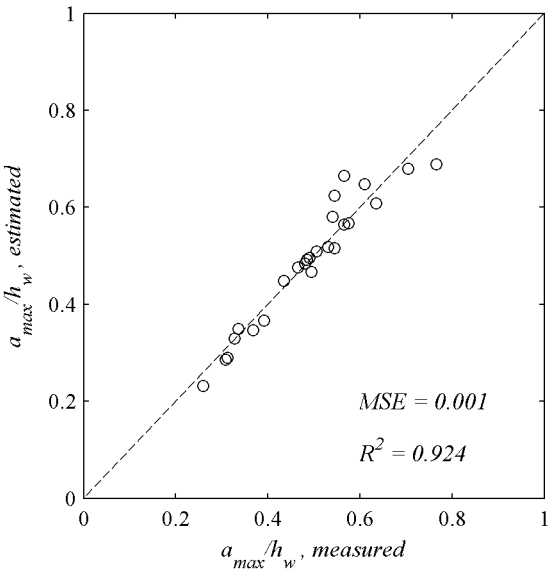

Figure 4.5. Correlation between measured dimensionless a_{max} and estimated dimensionless a_{max} using the optimized equation (4.5)

4.4 Maximum first crest amplitude's location

The location x_{max}, along the main direction, where the maximum wave amplitude a_{max} occurs, is estimated here by means of different empirical formulas. The importance of finding x_{max} lies in the reason that this location is the starting point of wave propagation, after formation is concluded. Thus, x_{max} is considered to be the starting point of the wave amplitude decay formulas along the main direction x (see section 4.6).

4.4.1 1st order formula

Following the form of equation (4.2), the first order formula to estimate x_{max} is defined in equation (4.6).

$$\frac{x_{max}}{h_w} = k_1^{(x_{max},1)} \left(\frac{h_s}{h_w} \right)^{k_2^{(x_{max},1)}} \tag{4.6}$$

The optimization of the two parameters yields values of $k_1^{(x_{max},1)} = 8.31$, $k_2^{(x_{max},1)} = 8.57 \cdot 10^{-1}$, with a correlation coefficient between measured data and estimated values of $R^2 = 0.765$ and a $MSE = 0.815$ (see Figure 4.6).

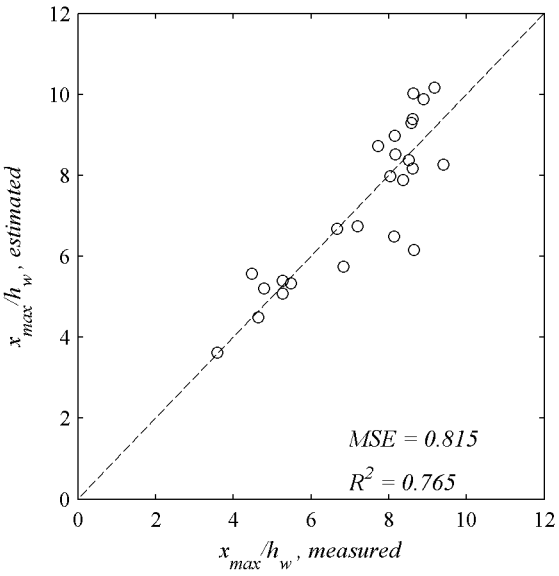

Figure 4.6. Correlation between measured dimensionless x_{max} and estimated dimensionless x_{max} using the optimized equation (4.6)

4.4.2 2nd order formula

Following the form of equation (4.3), the second order formula to estimate x_{max} is defined in equation (4.7).

$$\frac{x_{max}}{h_w} = k_1^{(x_{max},2)} \left(\frac{h_s}{h_w} \right)^{k_2^{(x_{max},2)}} \left(\frac{E_{s,kin}}{E_{w,hydrostatic}} \right)^{k_3^{(x_{max},2)}} \tag{4.7}$$

The optimization of equation (4.7) yields values of $k_1^{(x_{max},2)} = 3.97$, $k_2^{(x_{max},2)} = 1.98 \cdot 10^{-1}$, $k_3^{(x_{max},2)} = 2.77 \cdot 10^{-1}$, with a correlation coefficient between measured data and estimated values of $R^2 = 0.904$ and $MSE = 0.815$ (see Figure 4.7).

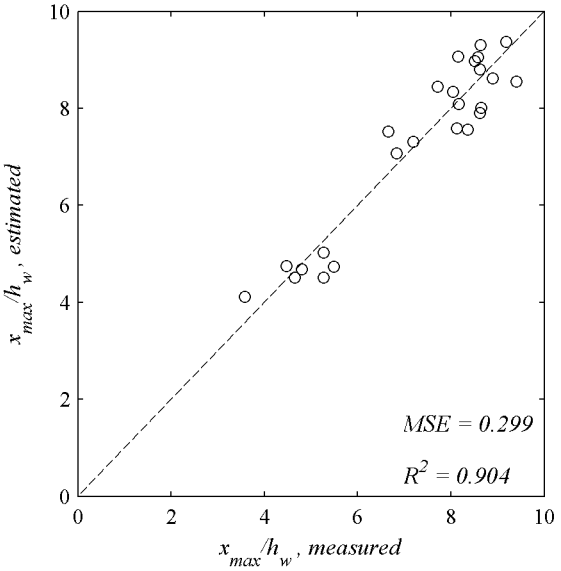

Figure 4.7. Correlation between measured dimensionless x_{max} and estimated dimensionless x_{max} using the optimized equation (4.7)

4.5 Maximum first crest amplitude's time

The elapsed time t_{max} , when the maximum wave amplitude a_{max} occurs, is estimated here by means of different empirical formulas. The importance of finding t_{max} lies in the reason that this is the initial time of wave propagation, after formation is concluded. Thus, t_{max} is considered as the zero time of the wave amplitude decay formulas in time along the main direction x (see section 4.6).

4.5.1 1st order formula

Following the form of equation (4.2), the first order formula to estimate t_{max} is defined in equation (4.8).

$$t_{max}\sqrt{g/h_w} = k_1^{(t_{max},1)}\left(\frac{h_s}{h_w}\right)^{k_2^{(t_{max},1)}} \tag{4.8}$$

The optimization of the two parameters yields values of $k_1^{(t_{max},1)} = 4.70$, $k_2^{(t_{max},1)} = 5.09\cdot10^{-1}$, with a correlation coefficient between measured data and estimated values of $R^2 = 0.701$ and a *MSE*=0.136 (see Figure 4.8).

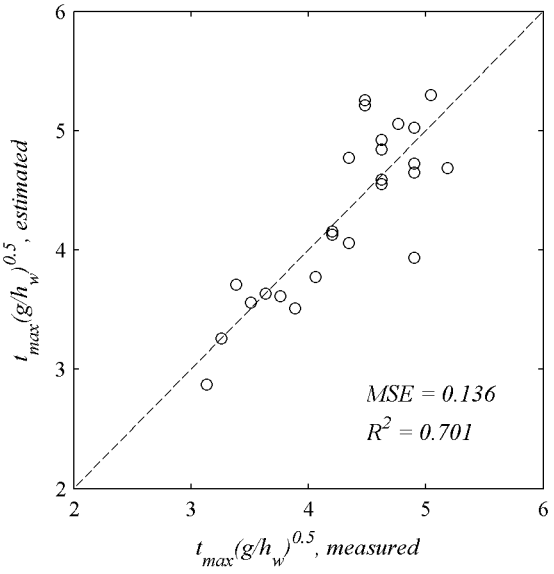

Figure 4.8. Correlation between measured dimensionless t_{max} and estimated dimensionless t_{max} using the optimized equation (4.8)

4.5.2 2nd order formula

Following the form of equation (4.3), the second order formula to estimate t_{max} is defined in equation (4.9).

$$t_{max}\sqrt{g/h_w} = k_1^{(t_{max},2)}\left(\frac{h_s}{h_w}\right)^{k_2^{(t_{max},2)}}\left(\frac{E_{s,kin}}{E_{w,hydrostatic}}\right)^{k_3^{(t_{max},2)}} \tag{4.9}$$

The optimization of equation (4.9) yields values of $k_1^{(t_{max},2)} = 3.03$, $k_2^{(t_{max},2)} = 9.95\cdot10^{-2}$, $k_3^{(t_{max},2)} = 1.64\cdot10^{-1}$, with a correlation coefficient between measured data and estimated values of $R^2 = 0.84$ and $MSE = 0.064$ (see Figure 4.9).

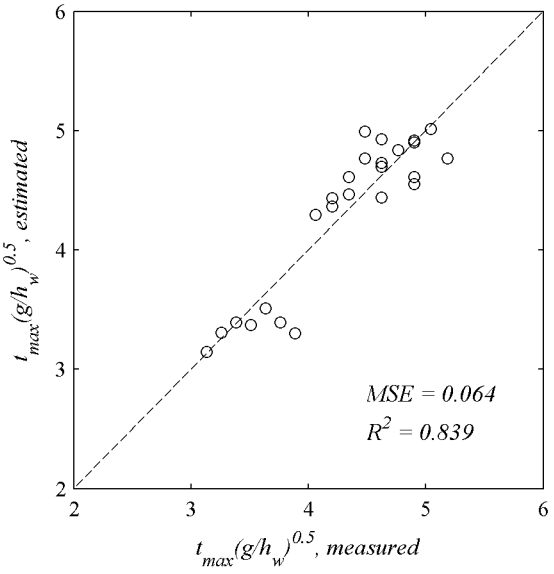

Figure 4.9. Correlation between measured dimensionless t_{max} and estimated dimensionless t_{max} using the optimized equation (4.9)

4.6 Wave propagation in space and time

The decrease in amplitude was approximated by dimensionless exponential functions that can properly describe the amplitude decay in space and time along the main direction *x*.

The fitting dimensionless exponential function in space has the following form:

$$\frac{a\left(x/h_w\right)}{h_w} = k_1^{(a(x))} e^{\left(k_2^{(a(x))} x/h_w\right)} \tag{4.10}$$

where $k_1^{(a(x))}$ represents the constant initial value of the amplitude and $k_2^{(a(x))} < 0$ represents the constant exponential decay along *x*.

The fitting dimensionless exponential function in time has the following form:

$$\frac{a\left(t\sqrt{g/h_w}\right)}{h_w} = k_1^{(a(t))} e^{\left(k_2^{(a(t))} t\sqrt{g/h_w}\right)} \tag{4.11}$$

where $k_1^{(a(t))}$ represents the constant initial value of the amplitude and $k_2^{(a(t))} < 0$ represents the constant exponential decay along *t*.

All the mentioned constants depend on the waves generation mechanism and thus on the landslide characteristics. In this sense, $k_1^{(a(x))}$ and $k_1^{(a(t))}$ correspond to the maximum wave amplitude a_{max}. The maximum wave is given in different places (x_{max}) and time (t_{max}), depending on the wave generation. Therefore, a correction on the initial distance and initial time needs to be done as follows:

$$x' = x - x_{max} \tag{4.12}$$

$$t' = t - t_{max} \tag{4.13}$$

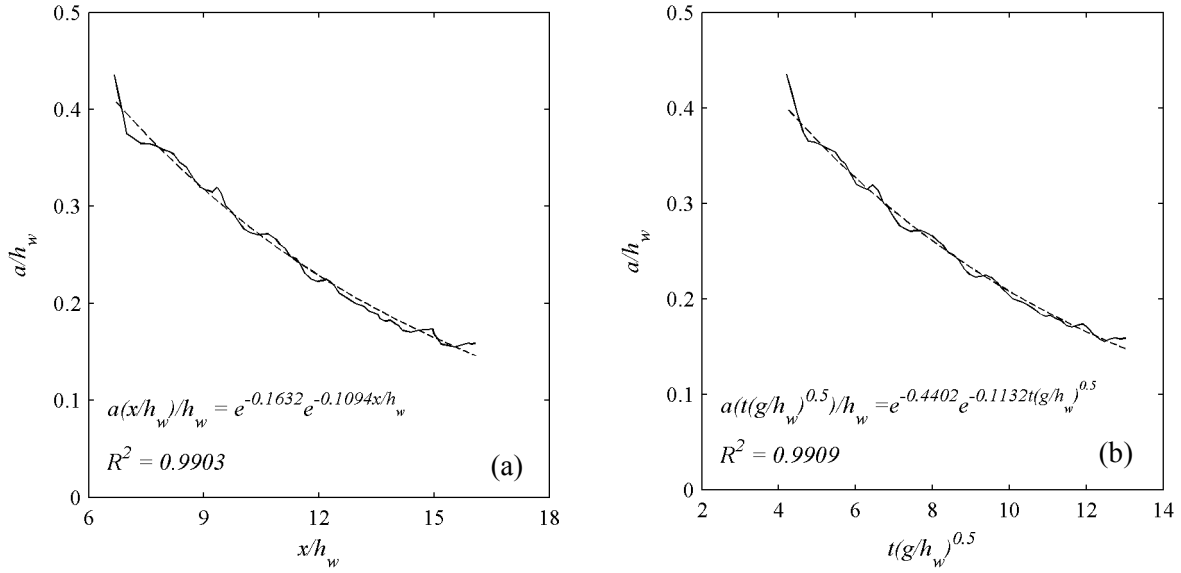

Figure 4.10. Data and exponential fitting of the dimensionless first wave amplitude in space (a) and time (b) for the run *Unique_M50_27.8deg*. Fitting equations and regression coefficients are reported within the figures.

Regarding the decay of waves in space and time, mean values are used after analyzing the propagation of each wave profiles for all the runs. An example of this analysis for one experiment is given in Figure 4.10. All values of wave decay are reported in sub-appendix C.5.

The mean values are $k_2^{(a(x))} = -0.102$ and $k_2^{(a(t))} = -0.108$.

Upon these bases, the formulas (4.10) and (4.11) become respectively as follows:

$$a\left(x/h_w\right) = a_{max}e^{\left(-0.102(x-x_{max})/h_w\right)} \tag{4.14}$$

$$a\left(t\sqrt{g/h_w}\right) = a_{max}e^{\left(-0.108(t-t_{max})\sqrt{g/h_w}\right)} \tag{4.15}$$

where a_{max} is given by any equation shown in section 4.3, x_{max}/h_w is given by any equation shown in section 4.4 and $t_{max}\sqrt{g/h_w}$ is given by any equation shown in section 4.5.

If equations (4.5) for a_{max} and (4.7) for x_{max} are used, the reapplication on experimental data of equation (4.14) yields a correlation coefficient between measured data and estimated values of $R^2 = 0.842$ and an $MSE = 0.003$ (see Figure 4.11a).

Similarly, if equations (4.5) for a_{max} and (4.9) for t_{max} are used, the reapplication on experimental data of equation (4.15) yields a correlation coefficient between measured data and estimated values of $R^2 = 0.865$ and a $MSE = 0.002$ (see Figure 4.11b).

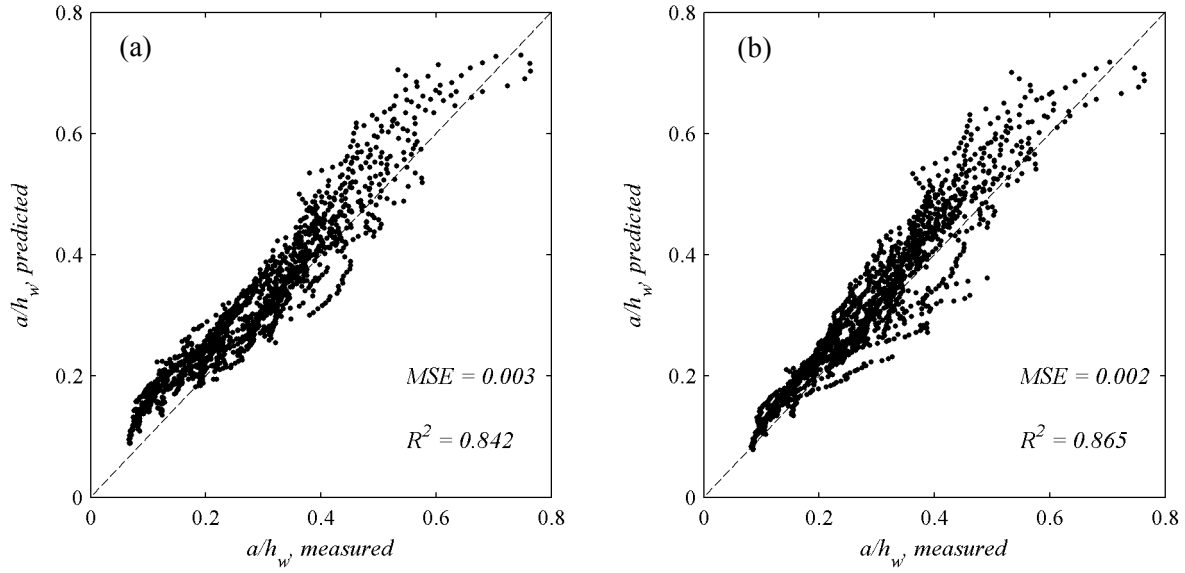

Figure 4.11. Comparison between the measured amplitudes and the amplitudes predicted by: (a) the formula of amplitude decay in space (equation (4.14)); (b) the formula of amplitude decay in time (equation (4.15)). MSE is the means squared error.

4.7 Energy transfer from landslide to water body

It was found essential to evaluate the efficiency of energy conversion $\varepsilon_{s,kin}$ from the kinetic energy of the landslide upon impact ($E_{s,kin}$) to the total energy of the formed leading wave E_w:

$$\varepsilon_{s,kin} = \frac{E_w}{E_{s,kin}} \tag{4.16}$$

E_w is calculated trough the equation (3.22) in section 3.2.7. In the presented experiments $\varepsilon_{s,kin}$ ranges from $4.70 \cdot 10^{-2}$ to $8.10 \cdot 10^{-2}$.

Thanks to the presented experimental results, E_w can be related to $E_{s,kin}$ by means of empirical relationships.

4.7.1 2nd order formula

For the purpose of taking into account the influence of the landslide shape, the two landslide parameters h_s and l_s are introduced here. Equation (4.17) is converted from a third order to a second order formula merging h_s and l_s below the same fitting parameter exponent. Moreover, the parameter $k_3^{(E_w,2)}$ is conveniently taken $k_3^{(E_w,2)} = 1.0$ to directly obtain the efficiency of energy conversion.

$$\frac{E_w}{E_{w,hydrostatic}} = k_1^{(E_w,2)} \left(\frac{h_s}{l_s}\right)^{k_2^{(E_w,2)}} \left(\frac{E_{s,kin}}{E_{w,hydrostatic}}\right)^{k_3^{(E_w,2)}} \tag{4.17}$$

The optimization of equation (4.17) gives as result $k_1^{(E_w,2)} = 1.40 \cdot 10^{-1}$, $k_2^{(E_w,2)} = 4.17 \cdot 10^{-1}$, with a correlation coefficient between measured data and estimated values of $R^2 = 0.934$ and a $MSE = 0.015$ (see Figure 4.12).

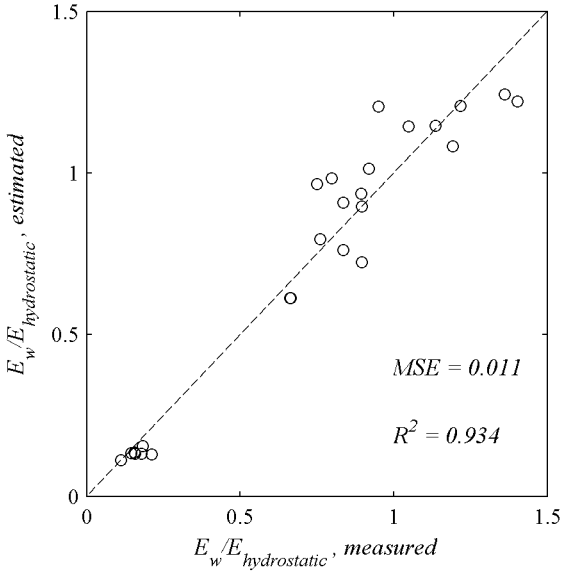

Figure 4.12. Correlation between measured dimensionless E_w and estimated dimensionless E_w using equation (4.17).

Reworking equation (4.17) and inserting the encountered parameters' values yields the following formula of efficiency:

$$\varepsilon_{s,kin} = \frac{E_w}{E_{s,kin}} = 1.40 \cdot 10^{-1} \left(\frac{h_s}{l_s}\right)^{4.17 \cdot 10^{-1}} \tag{4.18}$$

The reapplication of equation (4.18) to our data yields a MSE = 10^{-4}.

4.8 Final deposit

The length of the final deposit is important in estimating the runout distance of the landslide. Moreover, the width of the deposit records the final granular mass deformation. The model of energy transfer in chapter 5 requires as input the characteristics of the final deposit. In the real world, the final deposit measurements are data available only through the analysis of similar past events. In chapter 1 it was argued that the frequency of landslide tsunamis events is low. Thus, the number of measurements of final deposit is undoubtedly limited.

The final deposit characteristics found in the experiments were presented in section 3.1.3. The deposit has an elliptical form.

With the aim to evaluate the relationships existing between the landslide features at impact and the major axis of deposit a_d , the predictor of equation (4.19) is introduced.

$$\frac{a_d}{h_w} = \alpha^{k_1^{(a_d,3)}} \left(\frac{h_s}{h_w}\right)^{k_2^{(a_d,3)}} \left(\frac{l_s}{h_w}\right)^{k_3^{(a_d,3)}} \left(\frac{v_s}{\sqrt{gh_w}}\right)^{k_4^{(a_d,3)}} \tag{4.19}$$

The parameters being optimized are $k_1^{(a_d,3)} = -4.07 \cdot 10^{-1}$, $k_1^{(a_d,3)} = 4.85 \cdot 10^{-1}$, $k_1^{(a_d,3)} = 8.66 \cdot 10^{-1}$, $k_1^{(a_d,3)} = 3.14 \cdot 10^{-1}$. The sliding slope α is in radians. The formula in equation (4.19) is compared with the measured data, yielding an $R^2 = 0.693$ and an $MSE = 0.016$ (see Figure 4.13).

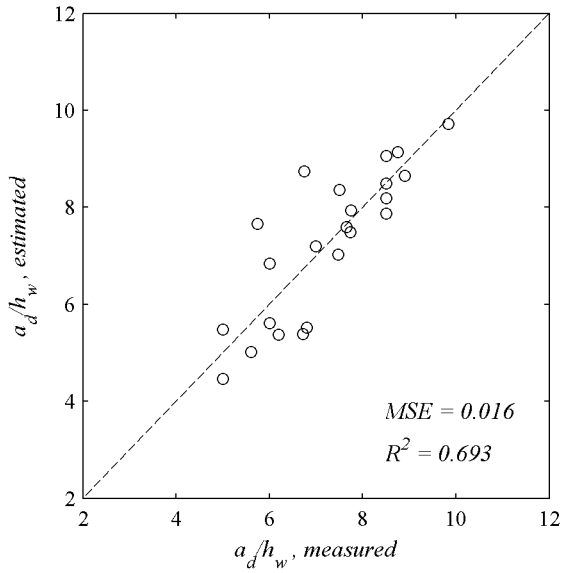

Figure 4.13. Correlation between measured dimensionless a_d and estimated dimensionless a_d using equation (4.19).

The estimation of the area of deposit $A_d = \pi a_d b_d$ permits to determine the basal friction that the deposit experiences, and to indirectly measure the minor axis b_d.

The relationship between landslide features at impact and A_d is given in equation (4.20).

$$\frac{A_d}{h_w^{\,2}} = \alpha^{k_1^{(A_d,3)}} \left(\frac{h_s}{h_w}\right)^{k_2^{(A_d,3)}} \left(\frac{l_s}{h_w}\right)^{k_3^{(A_d,3)}} \left(\frac{v_s}{\sqrt{gh_w}}\right)^{k_4^{(A_d,3)}} \tag{4.20}$$

The parameter being optimized are $k_1^{(a_d,3)} = -1.09$, $k_1^{(a_d,3)} = 9.14 \cdot 10^{-1}$, $k_1^{(a_d,3)} = 1.69$, $k_1^{(a_d,3)} = 1.28$. The sliding slope α is in radians. The formula in equation (4.20) is compared with the measured data, yielding an $R^2 = 0.803$ and an $MSE = 0.062$ (see Figure 4.14).

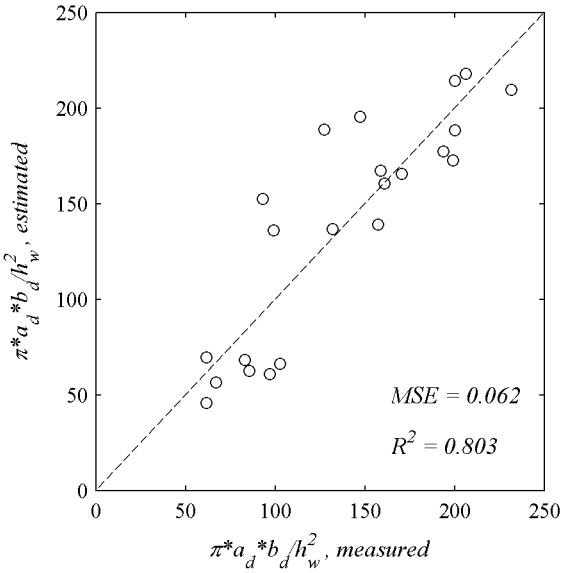

Figure 4.14. Correlation between measured dimensionless A_d and estimated dimensionless A_d using equation (4.20).

4.9 Application on historical events

In the previous sections the empirical predictive formulas were introduced and validated with the experimental data. The next step is to test the formulas on real events to evaluate their predictive capability and their usability. Therefore, two examples of past events are selected for their important features and are analyzed hereinafter.

It is clear that a real event entails complex terrain morphology and geomorphology. Thus, for a detailed analysis, scaled physical models or 3D numerical models should be employed. However, we believe that simplified empirical formulas can be an important tool for a rapid estimation of the potential effects of landslide tsunamis.

4.9.1 Vajont Dam, 1963

The event of the Vajont Dam, which is described in section 1.1.1, is analyzed in detail here in order to apply the predictors defined in this chapter. It is a point of fact that the Vajont event concerns a partially submerged landslide, thus it is different from the landslide initial configuration investigated in this thesis. However, the results encountered are still worthy of interest and are submitted hereafter.

On the 9th of October 1963 a landslide of limestone (ρ = 2700 kg/m^3) with an estimated volume of 270x10^6 m^3 and a front width of 2 km was mobilized and entered into the reservoir. At the time of impact the lake had an average depth of 200 m. The maximum velocity the landslide reached at impact has been estimated in about 30 m/s (Hendron & Patton, 1987; Pinyol & Alonso, 2010). The thickness of the landslide can be estimated in 250 m from the geological profiles before and after the event where the rupture surface is visible (Figure 4.15). The same value of thickness is reported in Genevois & Ghirotti (2005).

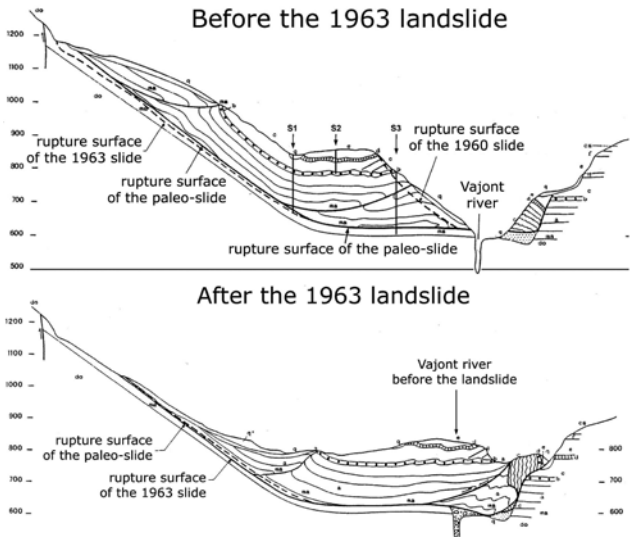

Figure 4.15. Geological sections of the Vajont valley before and after event. (Panizzo et al. 2005 after Semenza, 2001).

The run-up on the opposite flank (close to the town of Casso) was recorded as 210 m by Semenza (2001). The flank has an average slope of 22.5°.

Based on the above assumptions, the calculation of the first wave amplitude was performed using equation (4.3), giving an amplitude of 60 m. The transformation from amplitude to the run-up *Ru* has been done using the following formula of Synolakis (1987):

$$\frac{Ru}{h_w} = 2.831\sqrt{\cot\gamma}\left(\frac{a_{sol}}{h_w}\right)^{5/4} \tag{4.21}$$

valid for the run-up of a solitary wave along an impermeable flank with slope γ. The equation (4.21) with $a_{sol} = a_{max}$ = 60 m, h_w = 200 m and γ = 22.5° gives a Ru_{max} = 200 m which is quite close to the value observed by Semenza (2001).

The slight underestimation of Ru_{max} can be attributed to the fact that the wave that hit the north flank was still in its formation and thus in the splash zone, where the observed amplitudes

are certainly higher. Indeed the computed x_{max} through equation (4.7) shows that the maximum wave amplitude would has been formed at a horizontal distance of about 940 m from impact, while the actual distance travelled was around 600 m. The estimated elapsed time from landslide impact to formed wave impact with shoreline is 15 s.

In Table 4.1 displays a summary of data and results of this application framework where t_{max} is given separately because no validation is available.

Table 4.1. Summary of data and results of the Vajont Dam event of 1963 after applying the predictors of equations (4.3), (4.7) and (4.9).

Data						
V_s (Mm^3)	hs (m)	w_s (m)	v_s (m/s)	h_w (m)	γ (°)	Ru (m)
270	250	2000	30	200	22.5	210
Results						
a_{max} (m)	x_{max} (m)	Ru_{max} (m)		t_{max} (s)		
60	940	200		15		

4.9.2 Lake Chehalis, 2007

The second event analyzed is the one of Lake Chehalis, of 2007. The case was previously described in section 1.1.1.

Following the observations of Brideau et al. (2012), Roberts et al (2013) and Lawrence et al. (2013), the landslide had a volume of $3x10^6$ m^3 , a mean thickness of 40 m and a width of 210 m. On the day of the event the lake had a depth of 175 m. The landslide velocity was estimated having a maximum value of 60 m/s by Wang et al. (2015). The maximum run up of 38 m was observed on the flank of the lake opposite to the landslide, where the lake width is 700 m (see Figure 1.7). The flank where the 38 m run-up was observed has a slope of approximatively 28.5°. This slope is obtained from Google Earth© (map of 2010, Figure 4.16).

On the basis of the above data, the calculation of the first wave amplitude was performed using the equation (4.5), resulting in a max amplitude of 18 m at a distance x_{max} of 500 m and at a time t_{max} from impact of 11 s. It should be noted that x_{max} was calculated with equation (4.7) and t_{max} with equation (4.9). The transformation from amplitude to run-up was performed with equation (4.21), giving a Ru_{max} of 39 m. This value is acceptably close to the maximum observed run-up.

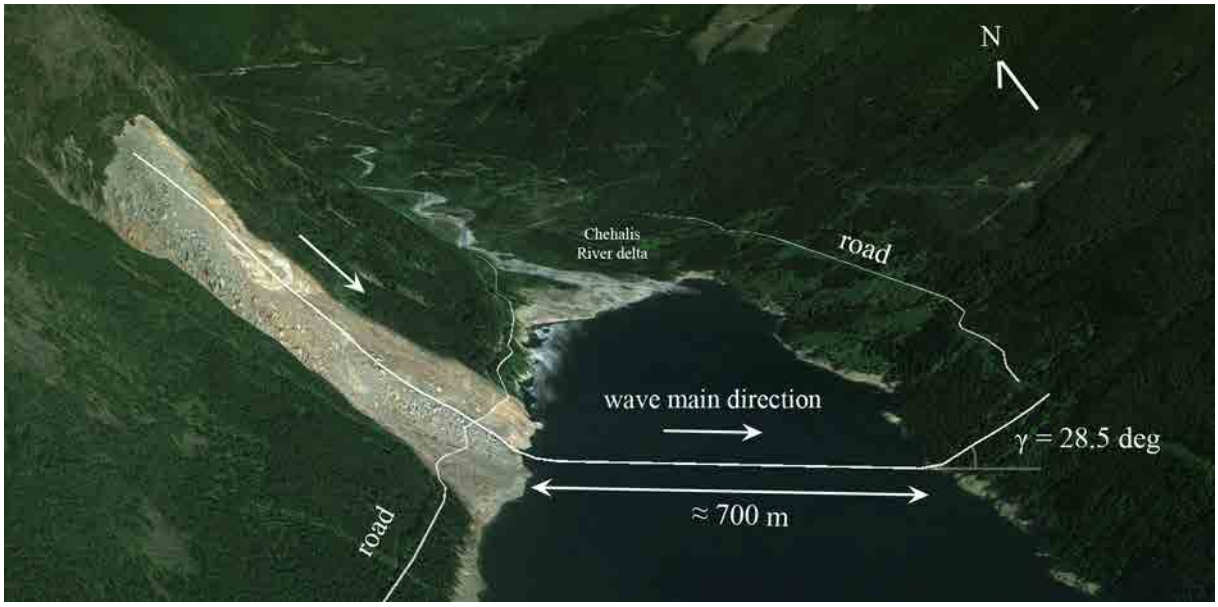

Figure 4.16. Sketch of the Lake Chehalis event of 2007. Oblique photo taken from Google Earth (image of 2010, accessed in 2015).

Table 4.2. Summary of data and results of the Lake Chehalis event of 2007 after applying the predictors of equations (4.5), (4.7) and (4.9).

Data								
V_s (Mm^3)	hs (m)	w_s (m)	v_s (m/s)	h_w (m)	γ (°)	Ru (m)		
3	40	210	60	175	28.5	38		
Results								
a_{max} (m)	x_{max} (m)	t_{max} (s)	Ru_{max} (m)	a (x=700m) (m)	Ru_{700m} (m)	t_{hit} (s)	a (t=15.6s) (m)	$Ru_{15.6s}$ (m)
18	500	11	39	16	34	15.6	16	34

Being the distance from landslide impact to opposite lake shorelines about x = 700 m, an attempt was performed to evaluate the wave amplitude, taking into account the amplitude decay. The distance x is calculated along the landslide axial direction (see Figure 4.16). Equation (4.14) was used to evaluate $a(x$=700 m) employing the computed a_{max}=18 m and x_{max}=500 m. The resulted amplitude is $a(x$=700 m)=16 m. This amplitude is introduced into the run-up formula of (4.21) giving a Ru_{700m} of 34 m. This value is again very close to the values observed around the area hit by the wave along the landslide axial direction: similar values of Ru can be observed in Figure 1.7.

An attempt was performed to measure the wave run-up using the wave decay in time. In section 3.2.4 it was shown that the celerity of the leading wave crest is similar to that of the associated solitary wave, once the wave is formed. Using this approximation it is possible to

estimate the time that the leading wave crest takes from the position and instant of its maximum amplitude (x_{max} = 500m and t_{max} = 11s) to hit the opposite shoreline. Finally the formula to estimate the total elapsed time of shoreline's hit is the follow:

$$t_{hit} = t_{max} + \frac{700 - x_{max}}{c_{sol}} = t_{max} + \frac{700 - x_{max}}{\sqrt{g \cdot (h_w + a_{\max})}} = 11 + \frac{700 - 500}{\sqrt{9.81 \cdot (175 + 18)}} = 15.6s \qquad (4.22)$$

With this estimation of time the equation (4.15) was used to evaluate $a(t$=15.6s) employing the computed a_{max}=18 m and t_{max}=11 s. The resulted amplitude is $a(t$=15.6s)=16 m. This amplitude is introduced into the run-up formula of (4.21) giving a $Ru_{15.6s}$ of 34 m. This value is the same of that evaluated with the formula of wave decay in space and it is again very close to the observed run-up.

Table 4.1 displays a summary of data and results from this calculation.

4.10 Conclusions

Different empirical predictors were presented in this chapter for the purpose of estimating the identified variables. A summary of all predictive formulas is presented in Table 4.3.

In estimating the maximum wave amplitude a_{max}, three different dimensionless empirical relationships were presented in equations (4.2), (4.3) and (4.5). The evaluation of a_{max} is important as it is a fundamental magnitude for the assessment of the maximum hazard posed by landslide tsunamis. Moreover a_{max}, together with x_{max} and t_{max}, is the first step to calculate wave propagation along the main direction x within the water body.

The 1st order formula (equation (4.2)), estimates a_{max} simply trough the landslide's average thickness. In the 2nd order formula (equation (4.3)) the ratio is introduced between landslide kinetic energy $E_{s,kin}$ and the opposed basin hydrostatic energy $E_{w,hydrostatic}$. This permits to enhance considerably the quality of the estimating formula. The ratio $E_{s,kin}/E_{w,hydrostatic}$ is a good parameter for estimating a_{max}: in fact, it involves several landslide parameters at once (m_s, v_s, w_s and l_s). The 3rd order formula of equation (4.5), was set up in order to separately account the contribution of the three main selected landslide parameters: h_s, l_s, v_s. The three parameters have a similar weight in estimating a_{max}. Moreover the equation (4.5) leads to a good correlation (R^2 = 0. 924) between measured and estimated a_{max}.

As explained earlier, this study analyzes exclusively the amplitude of the leading wave crest, as it is considered to be the highest. Detailed discussions on the highest wave were reported by different authors: Noda (1970) observed the leading wave as the largest while Kamphuis & Bowering (1972), Fritz (2002), Zweifel et al. (2006) and Heller (2008) concludes that generally

the leading wave can be considered the highest wave, and it is not so in few cases only. Heller (2008), for instance, affirms that within about 5% of the effected runs the secondary wave crest was higher than the primary wave crest. These runs were the ones having a low landslide energy. For those reasons, we can conclude that the assessment of the leading wave as being the wave with the highest magnitude is appropriate.

Table 4.3. Dimensionless predictive empirical formulas

Estimated variable	Predictive formula	R^2
a_{max}	$a_{max}/h_w = 5.64\cdot10^{-1}\cdot\left(h_s/h_w\right)^{9.56\cdot10^{-1}}$	0.778
	$a_{max}/h_s = 4.78\cdot10^{-1}\left(E_{s,kin}/E_{w,hydrostatic}\right)^{6.66\cdot10^{-2}}$	0.790
	$a_{max}/h_w = 2.88\cdot10^{-1}\cdot\left(h_s/h_w\right)^{3.89\cdot10^{-1}}\cdot\left(E_{s,kin}/E_{w,hydrostatic}\right)^{2.54\cdot10^{-1}}$	0.861
	$a_{max}/h_w = 1.18\cdot10^{-1}\cdot\left(h_s/h_w\right)^{4.59\cdot10^{-1}}\cdot\left(l_s/h_w\right)^{4.63\cdot10^{-1}}\cdot\left(v_s/\sqrt{gh_w}\right)^{5.54\cdot10^{-1}}$	0.924
x_{max}	$x_{max}/h_w = 8.31\cdot\left(h_s/h_w\right)^{8.57\cdot10^{-1}}$	0.765
	$x_{max}/h_w = 3.97\cdot\left(h_s/h_w\right)^{1.98\cdot10^{-1}}\cdot\left(E_{s,kin}/E_{w,hydrostatic}\right)^{2.79\cdot10^{-1}}$	0.904
t_{max}	$t_{max}\sqrt{g/h_w} = 4.70\cdot\left(h_s/h_w\right)^{5.09\cdot10^{-1}}$	0.701
	$t_{max}\sqrt{g/h_w} = 3.03\cdot\left(h_s/h_w\right)^{9.95\cdot10^{-2}}\cdot\left(E_{s,kin}/E_{w,hydrostatic}\right)^{1.64\cdot10^{-1}}$	0.839
$a(x)$	$a\left(x/h_w\right) = a_{max}\cdot e^{\left(-0.102\left(x-x_{max}\right)/h_w\right)}$	0.842
$a(t)$	$a\left(t\sqrt{g/h_w}\right) = a_{max}\cdot e^{\left(-0.108\left(t-t_{max}\right)\sqrt{g/h_w}\right)}$	0.865
$\varepsilon_{s,kin}$	$\varepsilon_{s,kin} = E_w/E_{s,kin} = 1.40\cdot10^{-1}\left(h_s/l_s\right)^{4.17\cdot10^{-1}}$	0.934
a_d	$a_d/h_w = \alpha^{-4.07\cdot10^{-1}}\cdot\left(h_s/h_w\right)^{4.85\cdot10^{-1}}\cdot\left(l_s/h_w\right)^{8.66\cdot10^{-1}}\cdot\left(v_s/\sqrt{gh_w}\right)^{3.14\cdot10^{-1}}$	0.693
A_d	$A_d/h_w{}^2 = \alpha^{-1.09}\cdot\left(h_s/h_w\right)^{9.14\cdot10^{-1}}\cdot\left(l_s/h_w\right)^{1.69}\cdot\left(v_s/\sqrt{gh_w}\right)^{1.28}$	0.803

The location (x_{max}) and the time (t_{max}) where and when the maximum wave amplitude occurs depend on the landslide parameters. A more energetic landslide produces an a_{max} farther and later, when compared with a less energetic landslide. Those results are reflected in equations from (4.6) to (4.9). x_{max} is considered the initial distance from impact where wave amplitude starts to decay in space. Similarly, t_{max} is considered the initial elapsed time from impact when wave amplitude starts to decay in time. Thus, x_{max} and t_{max} are introduced in the amplitude decay formulas.

The predictors of wave amplitude decay along x and in t are designed to have an initial maximum amplitude a_{max} which depends on wave generation. a_{max} should be calculated with one of the proposed formulas. The initial point x of decay is shifted based on a proposed formula of x_{max} while the initial time t of decay is shifted based on a proposed formula of t_{max}.

Observing equation (4.14) the dimensionless coefficient of amplitude decay in space is equal to -0.102. While observing equation (4.15) the dimensionless coefficient of amplitude decay in time is equal to -0.108. In particular a characteristic of exponential decay in time is the time required for the amplitude to fall to 1/2 of its initial value. This time is called "half-life", and is denoted by the symbol $t_{1/2}$. The dimensionless half-life may be written in terms of the constant decay as:

$$t_{1/2} = \frac{\ln(2)}{-k_2^{(a(t))}} \tag{4.23}$$

Being in our experiments $-k_2^{(a(t))} = 0.108$ in average, the average dimensionless half-time is

$$t_{1/2} = \frac{\ln(2)}{0.108} = 6.42 \tag{4.24}$$

This result highlights the high decay that the wave experiences. In our experiment, in those runs where the h_w = 0.2m the wave decays by 1/2 after less than 1s. For a hypothetical case where h_w = 100m the half-life should be $t_{1/2} \approx$20s.

An empirical formula has been presented to predict the influence of the landslide energy and shape on energy conversion. The selected landslide dimensionless parameters are:

- the ratio between landslide kinetic energy $E_{s,kin}$ and $E_{w,hydrostatic}$
- the ratio between the landslide average thickness h_s and length at impact l_s .

Equation (4.18) explains that, increasing the ratio between landslide thickness and length at constant landslide load and velocity, the energy conversion efficiency increases.

Many authors have described the efficiency of energy conversion $\varepsilon_{s,kin}$. Kamphuis & Bowering (1970) (2D block landslides) found a $\varepsilon_{s,kin}$ between 0.1 and 0.5, Huber (1980) (2D and 3D block landslides) from 0.01 to 0.4, Fritz et al (2004) and Heller (2008) (2D granular landslides) from 0.02 to 0.3 and Ataie-Ashtiani & Nik-Khah (2008) (2D block and granular landslides) from 0.05 to 0.5. All mentioned studies affirm that: when increasing the angle of impact or increasing the landslide weight or increasing the landslide Froude number, the efficiency decreases.

In the presented experiments $\varepsilon_{s,kin}$ was found to range from 0.047 to 0.081, while in Mohammed & Fritz (2012), also addressing 3D granular landslides, from 0.004 to 0.040.

It is interesting to observe that: (1) 3D experiments carried out with granular material experience a lower efficiency of conversion compared with 2D experiments; (2) 3D experiments carried out with granular material, experience a lower efficiency of conversion, compared with 3D experiments carried out with solid blocks. The lower efficiency can be seen as the result of the unconfined boundaries along the three directions in the zone of impact: (1) the energy transfers trough 3 directions and it is not confined along a channel; (2) the granular material can deform along the three directions and, especially, it can expand horizontally, thus decreasing the front surface, and therefore reducing drag.

The final deposit predictors were introduced for the purpose of providing tools to estimate landslide deformations, which are not data commonly found, except in past events analysis. Several authors focus on final granular landslide deformation in reproducing landslide tsunamis. Fritz (2002) analyzes experimentally the granular landslide deformation in 2D, estimating its runout. Mohammed (2010) however, analyzes experimentally the granular landslide deformation in 3D. Particularly Mohammed (2010) scanned the final deposit in 3D in detail. However the lateral expansion was not scanned because of the limited size of the scanner. Here, the lateral expansion is measured, even if the experimental tests were carried out with a fixed w_s.

One can observe that in both equations (4.19) and (4.20) the impact angle α is introduced. The impact angle is deemed an important parameter for the final form of the deposit. The lower the angle, the longer and wider the final deposit.

The empirical predictors are then applied to two historical events: the Vajont Dam (1963, Italy) and the Lake Chehalis (2007, Canada). Those applications are presented in order to demonstrate the capability and the usability of the empirical formulas as tools for the prediction of landslide tsunamis' potential hazard. In the case of Vajont, a wave run-up of 200 m was estimated against the observed run-up of 210 m. In the case of Lake Chehalis the run-up was estimated in 39 m, while the observed run-up rose to 38 m. Both estimations are satisfactory.

Therefore it can be concluded that the defined empirical predictors, having been successfully tested both on the data measured experimentally and on real events, are capable of predicting the hazard associated with tsunamis generated by landslides whenever predictions on landslides characteristics are available.

Chapter 5: Energy transfer from landslide to water body: a simplified numerical model

5.1 Introduction

In the case of landslide tsunamis it is deemed important to understand the process of energy transfer between landslide and water body. The energy conversion process is described in section 4.7 by means of empirical relationships between E_s and $E_{w,pot,ini}$, similarly to what reported by other previous authors. Basal friction and turbulence are recognized as the main factors of energy loss, but, in the case of sub-aerial landslides generating tsunamis, only few authors (i.e. Walder et al., 2003) investigate the mechanisms involved. Especially in 3D experiments, where 3D deformations of granular material are verified, a lack of research was found on energy conversion.

In this chapter we introduce a simplified 1D forward Euler model including 3D landslide deformations. The model intends to evaluate energy losses and energy transfer between landslide and water body during the evolution of landslide tsunami events.

Granular mass movements can experience a certain basal entrainment of erodible bed material that can increase the final volume of sedimentation. Moreover, the presence of erodible bed material can increase or decrease the mobility of the mass movement (Egashira et al., 2001; Medina et al., 2008; Mangeney et al., 2010; Iverson, 2012; Crosta et al., 2015). However, in the present study a fixed bottom is used for simplicity, simulating a landslide moving over bedrock. Thus, the amount of sediment mass is conserved unaltered.

Five important behaviors influencing the energy conversion are recognized in landslide generated wave occurrence:

1. basal friction of landslide in its sub-aerial and underwater motion
2. 3D landslide deformation due to its granular feature and its interaction between bedrock and water body
3. energy dissipation due to friction at landslide-water boundary
4. splash effects, due to the surface tension breaking
5. air entrainment at impact, where energy can be lost due to air compressibility

LeMehaute & Wang (1996) and Walder et al. (2003) refer to those dissipative processes as difficult to analyze and incorporate in numerical models. Thus, they are either disregarded or incorporated into other dissipative processes as a "black box". Being unquantified in this work as well as in literature, one can say that splash effect and air entrainment can be hypothetically disregarded and that the dissipations considered by this method are restricted to basal friction and friction at landslide-water boundary.

In conclusion, through the method presented in this chapter, the author attempts to explain the first three behaviours in the aforementioned list, while the fourth and fifth are not addressed and require further investigation.

In order to examine the first and second behaviour it is necessary to evaluate the basal friction angle $\varphi_{s\text{-}b}$ as well as the drag coefficient C_d.

In particular, the drag coefficient C_d of a landslide is a fundamental value when dealing with numerical simulations of landslide tsunamis. C_d defines the reaction forces (drag forces) that the water exercises on the landslide and thus it measures the amount of energy transferred to the water body. For granular landslides which deform along the three directions, C_d is not commonly found in literature due to its complexity (Mazzanti & Bozzano, 2009), and it is often addressed to the C_d of block slides or to the order unity (Grilli and Watts, 2005).

For the purpose of researching the energy transfer involved in the described process, in this chapter the author attempts to give explicitly values for C_d and $\varphi_{s\text{-}b}$ for 3D deformable landslides.

Moreover, the effects of friction at the landslide-water boundary will be explored, being here assimilated to turbulent dissipation. In measuring this phenomenon a time of contact $t_{contact}$ between granular material and water must be introduced. Similarly, other authors (i.e.: Walder et al., 2003; Panizzo et al., 2005) consider the time of landslide underwater motion as a parameter important for the evaluation of the unknown processes taking place during wave formation. Unfortunately, this time is not easily obtained by empirical formulations or numerical models. Therefore, $t_{contact}$ is treated separately here as a computational option.

Applications of the experimental dataset of this study will be presented in sections 5.3.

5.2 Methodology

A new coordinate $\underset{\sim}{x}$ is defined along the path of propagation from the landslide basal centre of mass at impact $\underset{\sim}{x}_0$, through the underwater slope and finally along the tank bottom (see Figure 5.1a and Figure 5.1b).

Once the sliding box stops and the flaps open, the material starts to slide along the slope, till it reaches the horizontal bottom of the water tank and stops in $\underset{\sim}{x}_{stop}$, forming the final deposit. Following similar methods used in landslides and debris-flows (i.e.: Hungr et al., 2005), $\underset{\sim}{x}_{stop}$ is placed on the horizontal center of mass of the deposit. The distance from $\underset{\sim}{x}_0$ to $\underset{\sim}{x}_{stop}$ is known as run-out distance.

Going through the path, the initial energy, acquired by the slide due to the acceleration of the box, is largely dissipated by means of basal Coulomb friction. The residual, energy is transferred to the water by momentum. Drag forces and friction continue to act while the slide's velocity decreases till the stop. Only a part of the equivalent "energy of drag" is transferred to the wave train. The energy conversion from drag to the wave train is difficult to determine: it involves turbulence at the solid-liquid boundary as well as other dissipative processes that have been disregarded at first instance.

When the sliding material enters the water body, a huge crater is formed and the splash is created (Fritz et al., 2003). Thus, only a partial contact occurs between the two phases. Once the crater collapses, the water comes back in contact with the granular material and turbulent friction between the two phases is produced.

On this basis, one can say that the time of contact is a portion of the time t_{stop} when the landslide stops. The difficulty in assessing the initial time of contact between water and landslide ($t_{contact}$) is here a major obstacle. The evaluation of the total energy dissipated by turbulence E_t is highly sensitive to $t_{contact}$ because E_t depends on $\rho_w v_s^3$ (see equation (5.9)). Undoubtedly, experimental observations of landslide underwater motion would be necessary to assess $t_{contact}$ and t_{stop}, and thus to correctly evaluate the turbulence. Unfortunately, those data are not available in our experiments. Furthermore, $t_{contact}$ is not easily measurable either in real events or in experiments. Thus, the evaluation of turbulence dissipation, entailing high uncertainty, is calculated indirectly as the difference between the evaluated energy of drag and the measured energy of wave (see Figure 5.3 and equations (5.1) and (5.2)).

However, an attempt at measuring $t_{contact}$ is discussed in section 5.2.3.

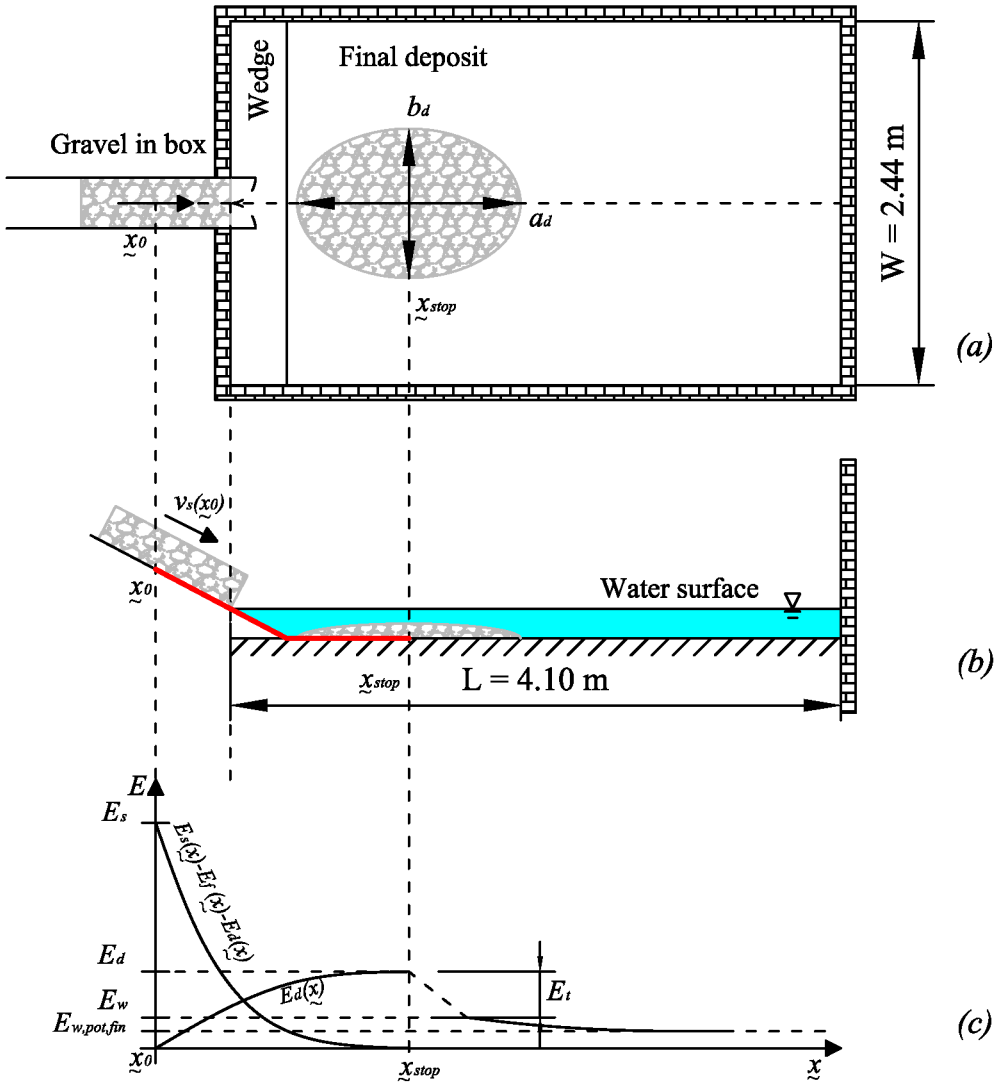

Figure 5.1. Sketch of the experiment and associated energy conversion for the presented model in presence of wedge: (a) aerial view; (b) lateral view (walked path marked in red); (c) qualitative energies evolution along the run-out distance (for the quantitative energy plot see Figure 5.14).

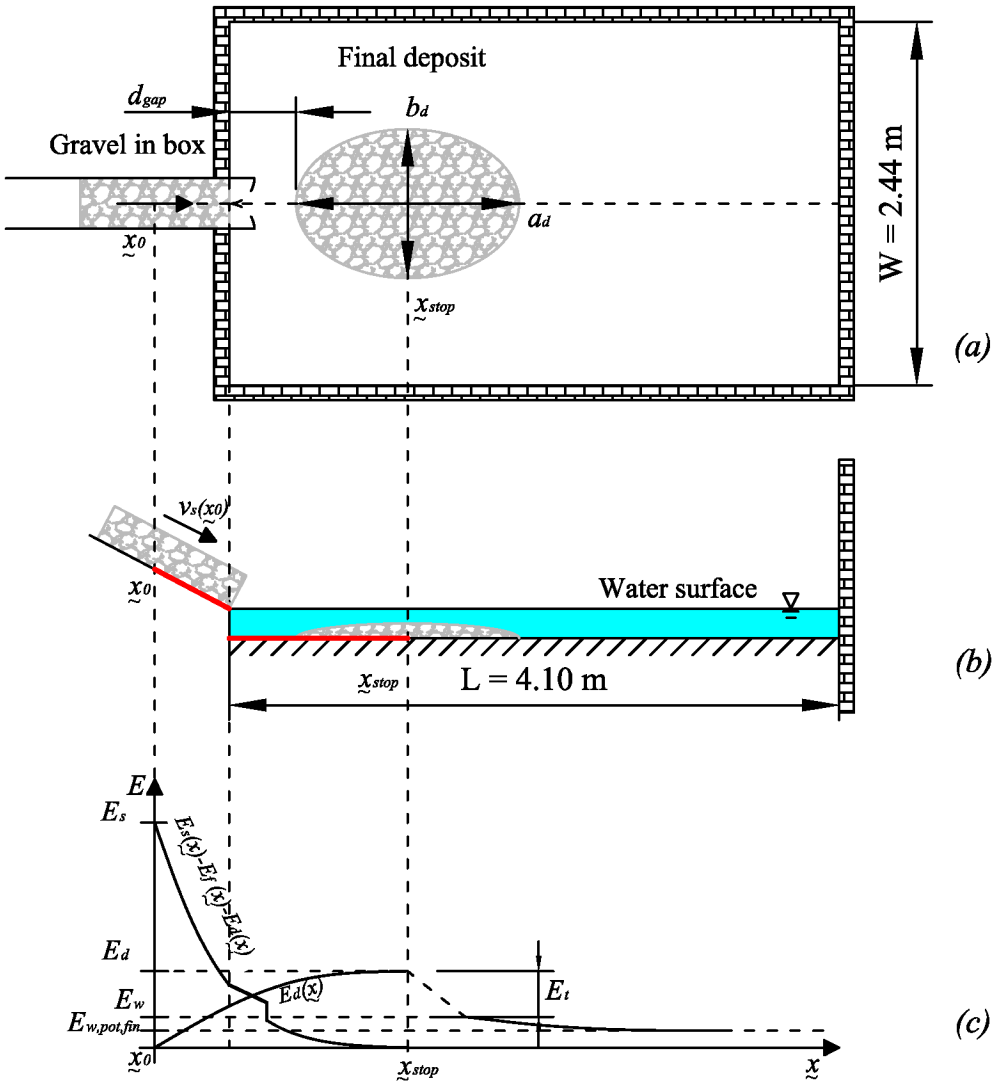

Figure 5.2. Sketch of the experiment and associated energy conversion for the presented model in absence of wedge: (a) aerial view; (b) lateral view (walked path marked in red); (c) qualitative energies evolution along the run-out distance (for the quantitative energy plot see Figure 5.16 and Figure 5.18).

Following to the previous considerations, the energy balance of the landslides tsunami process may be described by the follow equations

$$E_s - E_f - E_d = 0 \tag{5.1}$$

$$E_d = E_w + E_t \tag{5.2}$$

where E_s is the initial total energy of the slide at the impact point x_0 with the water basin, E_f is the total dissipated energy by means of basal friction, E_d is the total energy of drag transferred to the water body and E_w is the total energy of the wave train. E_s and E_w are measured in the presented experiments (see respectively section 3.1.2 and 3.2.7). E_f and E_d are evaluated trough

the presented methodology. The energy of turbulence is thus evaluated as the difference between the evaluated E_d and the measured E_w.

The energy transfer is synthetically explained in the flow charts of Figure 5.3 and Figure 5.4 and in the sketch of Figure 5.1c. The conversion ratios ε are presented in the results of the methodology (see section 5.3).

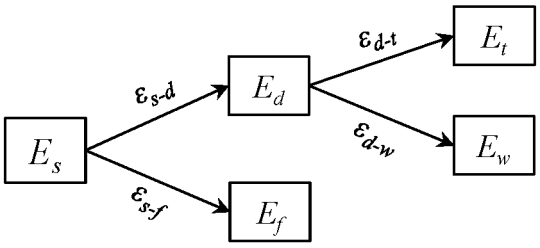

Figure 5.3. Flow chart of energy conversion for landslide tsunamis, following the implemented methodology. ε are the ratios of conversion between the different energies.

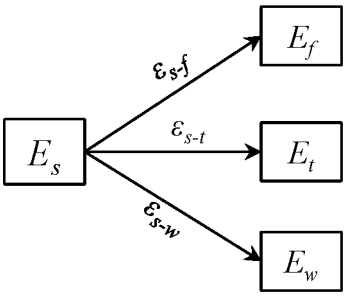

Figure 5.4. Rearranged flow chart of the implemented methodology as a generalization of the flow chart in Figure 5.3. ε are the ratios of conversion between the different energies.

Being presented in equation (3.1), E_s can be evaluated as the sum of kinetic energy $E_{s,kin}$ and the potential energy $E_{s,pot}$ as follow:

$$E_s = E_{s,kin} + E_{s,pot} = \frac{1}{2} m_s v_s^2 + m'_s \, g z_{s,c} \tag{5.3}$$

The Coulomb shear-stress in a given point is described by the following law:

$$\tau(\underset{\sim}{x}) = \rho'_{s,bulk,sat} g h_s(\underset{\sim}{x}) \tan \varphi_{s-b} \tag{5.4}$$

where $\varphi_{s\text{-}b}$ is the internal friction angle between granular material and bottom, $\rho'_{s,bulk,sat}$ is the submerged density of the bulk material and $h_s(\underset{\sim}{x})$ is the landslide thickness evolution along the travel distance. During the penetration and sedimentation into the water basin, the landslide changes in shape, reducing its thickness and increasing its basal area, as the volume remain

conserved. Here the evolution of landslide thickness is considered linear from the measured mean thickness at the exit of the box $h_s\left(\underset{\sim}{x}_0\right)$ till the final mean thickness of the deposit $h_s\left(\underset{\sim}{x}_{stop}\right)$.

The associated Coulomb force F_c can be calculated as:

$$F_c(\underset{\sim}{x}) = \tau(\underset{\sim}{x}) s_{basal}(\underset{\sim}{x}) \tag{5.5}$$

where $s_{basal}\left(\underset{\sim}{x}\right)$ is the evolution of the basal area of the landslide, assumed to be linear, from the initial basal area at impact $s_{basal}\left(\underset{\sim}{x}_0\right) = w_s l_s$ to the elliptical area of final deposit $s_{basal}\left(\underset{\sim}{x}_{stop}\right) = \pi a_d b_d / 4$.

The dissipated energy by means of basal friction can be calculated as:

$$E_f = \int_{\underset{\sim}{x}_o}^{\underset{\sim}{x}_{stop}} F_c(\underset{\sim}{x}) d\underset{\sim}{x} \tag{5.6}$$

The drag force may be evaluated as:

$$F_d(\underset{\sim}{x}) = \frac{1}{2} C_d \rho'_{s,bulk,sat}\, s_{front}(\underset{\sim}{x}) v_s^2(\underset{\sim}{x}) \tag{5.7}$$

where C_d is the drag coefficient that here includes both skin and form effects, $s_{front}\left(\underset{\sim}{x}\right)$ is the landslide frontal area linearly changing from $s_{front}(\underset{\sim}{x}_0) = w_s h_s(\underset{\sim}{x}_0)$ to $s_{front}(\underset{\sim}{x}_{stop}) = b_d h_s(\underset{\sim}{x}_{stop})$ and $v_s\left(\underset{\sim}{x}\right)$ is the velocity along the distance.

In gathering together results of experiments belonging to different datasets, the presence or absence of the wedge at the box exit has created a major obstacle. Being the granular material deformable, in presence of the wedge, the transition between the box and the bottom of the tank can be considered smooth enough to exclude additional losses in landslide energy.

In Figure 5.1a and Figure 5.1b it is possible to observe the configuration of the experiments in presence of the wedge.

In absence of the wedge the transition between the bottom of the box and the bottom of the tank (see Figure 5.2a and Figure 5.2b) forces the landslide to jump. During the jump the landslide loses contact with the bottom, and thus it is not subjected to basal friction but only to drag forces (neglecting turbulences that are introduced at a later stage in the calculation). The jump is thus simulated as a parabolic fall of a mass subjected to drag through the water. The mass has an initial angle given by the detachment slope α and a known detachment velocity decomposed in horizontal and vertical directions.

Once the landslide lands on the flat bottom of the tank a certain amount of its momentum is lost through the sudden change of direction. The calculation of the residual velocity after impact

is achieved assuming that the landslide only has the horizontal component of velocity prior to impact. This means an additional and instantaneous energy dissipation by impact (see Figure 5.2c).

Because of the jump in the absence of wedge, an additional set of data is needed: the deposit does not rest at the foot of the wedge, but at a certain horizontal distance d_{jump} from the detachment point. It is important to highlight that d_{jump} is a distance calculated in the aftermath of the experiments and does not correspond to the length of the jump, which is calculated trough the previously presented methodology. It is possible to observe the configuration of the experiments in the absence of wedge in Figure 5.2.

$v_s\left(\underset{\sim}{x}\right)$ is iteratively calculated step by step till the stop, considering the Coulomb and drag resistive forces and the impact with the bottom of the tank in case of the absence of wedge. Once v_s = 0, the flow - and thus the calculation - stops, giving the run-out distance $\underset{\sim}{x}_{stop}$ and the stopping time t_{stop}. This method is also known as a "stopping method" (see section 5.2.2).

C_d is dependent mainly on the shape of the object penetrating into the fluid. A value of C_d for the granular landslide is evaluated trough an optimization framework in section 5.2.2.

From equation (5.7) the energy of drag E_d can be calculated by integrating F_d along $\underset{\sim}{x}$ as follows:

$$E_d = \int_{\underset{\sim}{x}_0}^{\underset{\sim}{x}_{stop}} F_d(\underset{\sim}{x}) d\underset{\sim}{x} \tag{5.8}$$

The gap between E_d and $E_{w,ini}$ (see Figure 5.1c and Figure 5.2c) is explained here by turbulent frictional effects at the boundary between gravel and water. The power of this turbulence P_t is given by:

$$P_t(t) = \rho_w v_s^{\,3}(t) A(t) \tag{5.9}$$

where *A(t)* is the evolution in time of the area of contact between gravel and water. Integrating the equation (5.9) in time gives the turbulence energy dissipated E_t as follows:

$$E_t = \int_{t_{contact}}^{t_{stop}} P_t(t) dt \tag{5.10}$$

where $t_{contact}$ is the time of beginning of contact between granular material and water (see section 5.2.3).

5.2.1 Experimental dataset

The experiments used to optimize and evaluate the present model are chosen based on their making available the following data:

- landslide geometry and velocity at impact
- final deposit geometry
- produced wave energy

The experimental dataset used in this work has been introduced in Table 3.1 (chapter 3). Within the 41 experiments performed, 23 are selected to carry out the present model. The experiments are specified in Table 5.1.

Results of 20 experiments are used to optimize the needed parameters, reserving 3 experiments (13% of the used dataset) for the validation. Thus a pool of 20 + 3 experiments is used to validate the presented model. Finally, the model was applied on the 3 reserved experiments. For the purpose of covering the different features of the dataset, the 3 experiments have been chosen as follows: 1 for α = 27.7° and in presence of wedge, 1 for α = 15.5° and in absence of wedge, 1 for α = 27.8° and in absence of wedge.

The 3 experiments reserved for the validation are: 1) *Unique_M100_27.8deg*; 2) *Unique_M100_hs0.15_15.5deg*; 3) *Unique_M120_27.8deg_no_wedge*.

Table 5.1. Experimental dataset used for the optimization, validation and reapplication (in bold) of the presented model.

#	# set	Name	*m (kg)*	*α (°)*	h_w *(m)*	*Fr*	Wedge	Optimization dataset	Validation dataset	Reapplication dataset
1	Set 1	Type_a_M50_27.8deg	50	27.8	0.20	3.38	yes	yes	yes	
2	Set 1	Type_a_M50_27.8deg	50	27.8	0.16	4.02	yes	yes	yes	
3	Set 1	Type_a_M75_27.8deg	75	27.8	0.19	3.94	yes	yes	yes	
4	Set 1	Type_a_M100_27.8deg	100	27.8	0.19	3.95	yes	yes	yes	
5	Set 1	Type_a_M125_27.8deg	125	27.8	0.19	4.05	yes	yes	yes	
6	Set 1	Type_a_M140_27.8deg	140	27.8	0.18	4.10	yes	yes	yes	
7	Set 1	Type_a_M110_27.8deg	110	27.8	0.20	4.17	yes	yes	yes	
18	Set 3	Unique_M75_27.8deg	75	27.8	0.20	3.61	yes	yes	yes	
19	**Set 3**	**Unique_M100_27.8deg**	**100**	**27.8**	**0.20**	**3.65**	**yes**	**no**	**yes**	✓
22	Set 3	Unique_M125_27.8deg	125	27.8	0.20	3.66	yes	yes	yes	
24	Set 3	Unique_M136_27.8deg	136	27.8	0.20	3.69	yes	yes	yes	
25	Set 3	Unique_M139.5_27.8deg	139.5	27.8	0.20	3.70	yes	yes	yes	
26	Set 3	Unique_M50_hs0.10_27.8deg	50	27.8	0.20	4.12	yes	yes	yes	
32	Set 3	Unique_M75_hs0.20_27.8deg	75	27.8	0.20	4.03	yes	yes	yes	
33	Set 3	Unique_M75_hs0.25_27.8deg	75	27.8	0.20	3.38	yes	yes	yes	
34	Set 4	Unique_M50_hs0.10_15.5deg	50	15.5	0.25	2.11	no	yes	yes	
35	Set 4	Unique_M50_hs0.20_15.5deg	50	15.5	0.25	2.20	no	yes	yes	
36	Set 4	Unique_M75_hs0.15_15.5deg	75	15.5	0.25	2.07	no	yes	yes	
37	**Set 4**	**Unique_M100_hs0.20_15.5deg**	**100**	**15.5**	**0.25**	**1.98**	**no**	**no**	**yes**	✓
38	Set 4	Unique_M100bis_hs0.20_15.5deg	100	15.5	0.25	2.01	no	yes	yes	
39	Set 4	Unique_M125_hs0.20_15.5deg	125	15.5	0.25	1.91	no	yes	yes	
40	Set 4	Unique_M143_hs0.25_15.5deg	143	15.5	0.25	2.02	no	yes	yes	
41	**Set 5**	**Unique_M120_27.8deg_no_wedge**	**120**	**27.8**	**0.20**	**3.70**	**no**	**no**	**yes**	✓

5.2.2 Optimization of the landslide basal friction angle and drag coefficient

In predicting or back-analyzing real events, the available data are usually scarce. Thus, it was decided to design a simplified model capable to work with as few data as possible.

This methodology needs two parameters to be calibrated, in order to fulfill the total distance x_{stop} of landslide mobility from initiation to deposition using a stopping method. The two designated parameters are the basal friction angle $\varphi_{s\text{-}b}$ and the coefficient of drag C_d.

The choice of $\varphi_{s\text{-}b}$ and C_d affects (1) on the run-out distance (stopping method) and (2) the energy transferred to the water body (drag energy of landslide versus first crest wave energy). However, $\varphi_{s\text{-}b}$ plays a role mainly on the run-out distance, while the energy transferred to the water body is mainly dependent on C_d.

To find the optimum set of parameters, leading to the lowest sum of quadratic relative errors in the run-out distance, a calibration set of 20 experiments is chosen, saving 3 experiments for the validation and reapplication (see Table 5.1).

The sum of quadratic relative errors Δ in the run-out distance is defined as follow:

$$\Delta = \sum \delta^2 = \sum_i \left(\frac{x_{stop,measured,i} - x_{stop,estimated,i}}{x_{stop,measured,i}} \right)^2 \tag{5.11}$$

where i identifies the i-th experiment.

Δ is evaluated for different values of $\varphi_{s\text{-}b}$ and C_d , showing the presence of a minimum (Figure 5.5). Thus a more rigorous minimum was sought through the Nelder-Mead simplex direct search algorithm, similar to that used in the empirical relationships (see section 4.2).

Optimum values of $\varphi_{s\text{-}b}$ = 24.89° and C_d = 1.26 were found. This remarkable result shows that, under the simplifying assumption of 3D landslide linear deformations, it is possible to find a unique drag coefficient for different wave generator configuration.

Data on the landslide time of stop is not available in our experiments, thus the optimization is merely performed using the run-out distance.

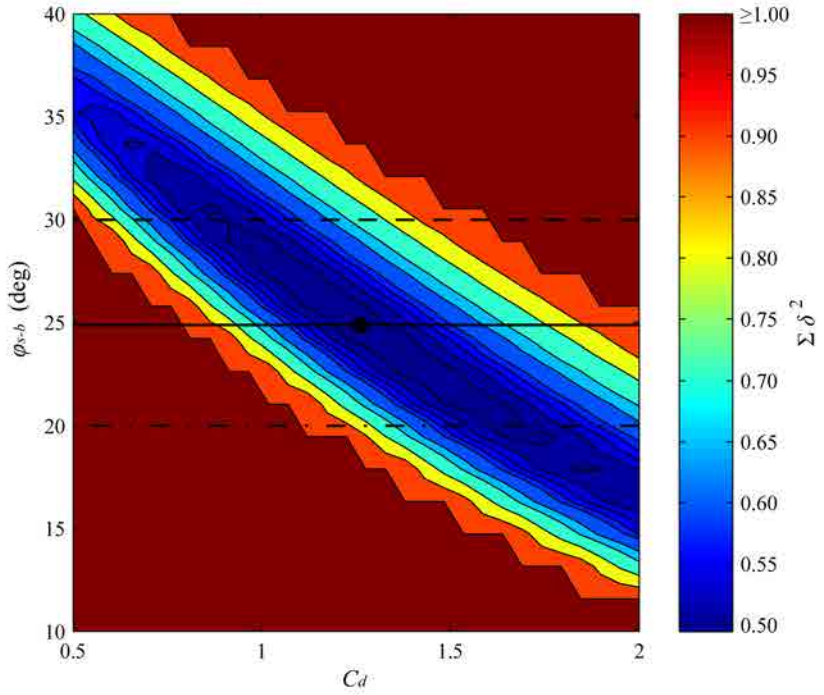

Figure 5.5. Graphical coarse search of optimum values of $\varphi_{s\text{-}b}$ and C_d. The values of the sum of the quadratic relative errors $\sum \delta^2$ are calculated for 600 points in the plotted domain and classified in ranges for plotting purposes. Moreover, a threshold of $\sum \delta^2 = 1.0$ is chosen. The point represents the found optimum values $\varphi_{s\text{-}b}$=24.86° and C_d = 1.26, corresponding to the minimum $\sum \delta^2$. The horizontal solid, dashed and dash-dot lines represent the lines for selected $\varphi_{s\text{-}b}$ drawn in Figure 5.19.

5.2.3 Optimization of time of contact between landslide and water

In this section, an attempt is made to find a common value of the time of contact between landslide and water for every experiment. The time of contact $t_{contact}$ is used to evaluate the dissipation due to turbulent friction between water and granular material, as in equation (5.10). It was speculated in equation (5.2) that the dissipated energy E_t may be evaluated as the difference between E_d and the measured E_w. Taking the equation (5.10), it is possible to observe that E_t depend on $t_{contact}$. Therefore, a common value of $t_{contact}$ may exists that can minimize the following sum of quadratic relative differences Δ_t :

$$\Delta_t = \sum_i \left(\frac{\left(\int_{t_{contact,i}}^{t_{stop,i}} P_{t,i}(t)\,dt \right) - \left(E_{d,i} - E_{w,i} \right)}{\left(E_{d,i} - E_{w,i} \right)} \right)^2 \tag{5.12}$$

where i identifies the i-th experiment.

Varying $t_{contact}$, a minimum value of Δ_t was searched through the Nelder-Mead simplex direct search algorithm, similar to that used in the empirical relationships (see section 4.2) and in finding the optimum values of $\varphi_{s\text{-}b}$ and C_d (see section 5.2.2).

The dimensionless time of contact found is thus the following:

$$t_{contact} / t_{stop} = 0.76 \tag{5.13}$$

5.3 Results

Following the approach explained in section 5.2.1, the methodology is applied here, using the optimized $\varphi_{s\text{-}b}$ and C_d, to the entire dataset of 23 experiments. The methodology is thus validated on the dataset and then reapplied on the three selected experiments not included in the optimization framework. The results are illustrated hereinafter.

The first purpose is to validate the run-out distance. This result is shown in Figure 5.6, where measured and estimated dimensionless $\tilde{x}_{stop}$ are correlated. A correlation coefficient between measured data and estimated values of $R^2 = 0.661$, a mean relative error of 2% and a maximum relative error of 30% are found.

R^2 can be seen as having a relatively low value. The center of mass of the final deposit is supposed equivalent to the measured geometrical center of the ellipse. But the observed final deposits had a non-symmetrical form at least longitudinally (see Figure 3.4) and this assumption can introduce an inaccuracy estimating $\tilde{x}_{stop}$. However the value of R^2 exhibits a certain correlation and the low mean relative error gives optimism for the analyses that follow.

In relating the energy of landslide at impact to the generated energy of drag, a simple linear regression with zero intercept gives an excellent result. In Figure 5.7 the aforementioned relationship can be appreciated between the dimensionless E_s and E_d , giving a correlation coefficient $R^2 = 0.967$. Through this result it can be obtained the efficiency of conversion $\varepsilon_{s\text{-}d}$ between E_s and E_d:

$$\varepsilon_{s-d} = E_d / E_s = 0.479 \tag{5.14}$$

Thus, it can be concluded that about 48% of the landslide energy is converted into the equivalent energy of drag.

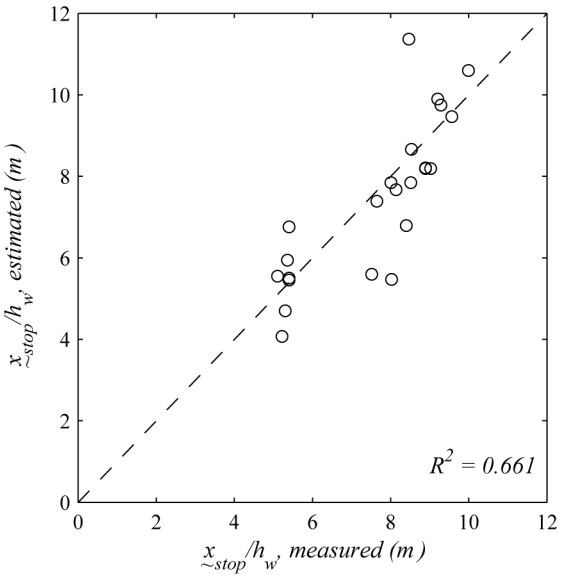

Figure 5.6. Validation of the run-out distance $x_{\sim stop}$.

A similar result is found for the relation between the energy of waves and the energy of drag. In Figure 5.8 the relationship can be appreciated between the dimensionless E_w and E_d, giving a correlation coefficient R^2 = 0.936. Through this result it can be obtained the efficiency of conversion $\varepsilon_{d\text{-}w}$ between E_w and E_d:

$$\varepsilon_{d-w} = E_w / E_d = 1/8.556 = 0.117 \tag{5.15}$$

Therefore, it can be concluded that about 12% of the drag energy is converted into wave energy.

Taking into account the experimental dataset chosen, a zero order regression between E_s and E_w, is performed and presented in Figure 5.9. The relationship between the dimensionless E_s and E_w, gives a correlation coefficient R^2 = 0.938. Through this result it can be obtained the efficiency of conversion $\varepsilon_{s\text{-}w}$ between E_s and E_w:

$$\varepsilon_{s-w} = E_w / E_s = 0.055 \tag{5.16}$$

It can be deduced that about 6% of the total landslide's energy at impact is converted into the wave energy.

Finally, the rates of energy conversions are reported in the flow charts of Figure 5.10 and Figure 5.11.

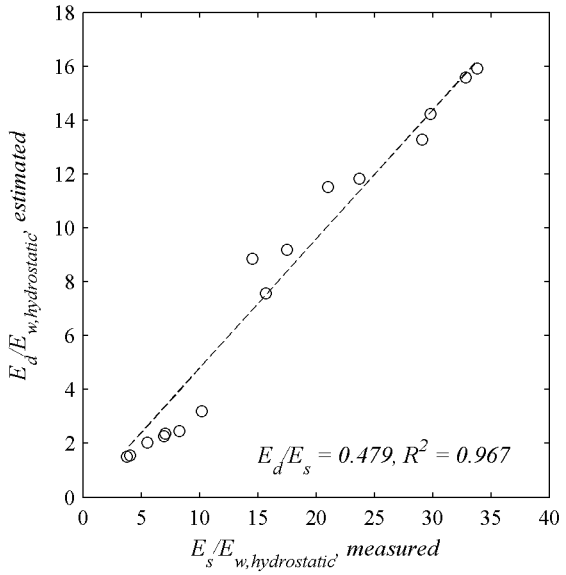

Figure 5.7. Resulting relationship between E_s and E_d: around 48% of the total landslide energy is converted to drag energy.

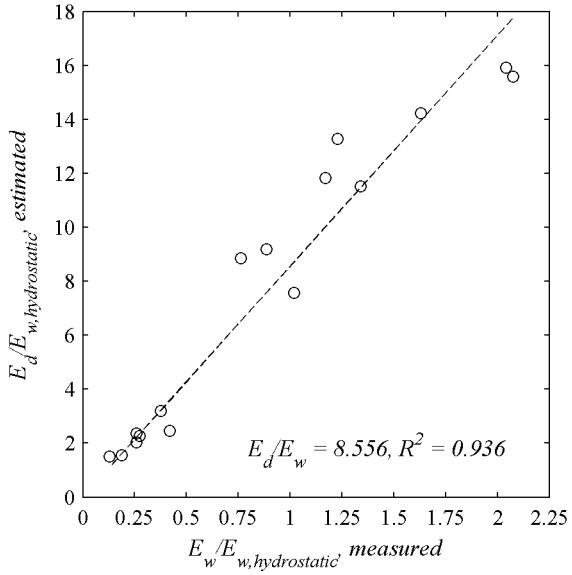

Figure 5.8. Resulting relationship between E_w and E_d: around 12% of the total drag energy is converted to wave energy.

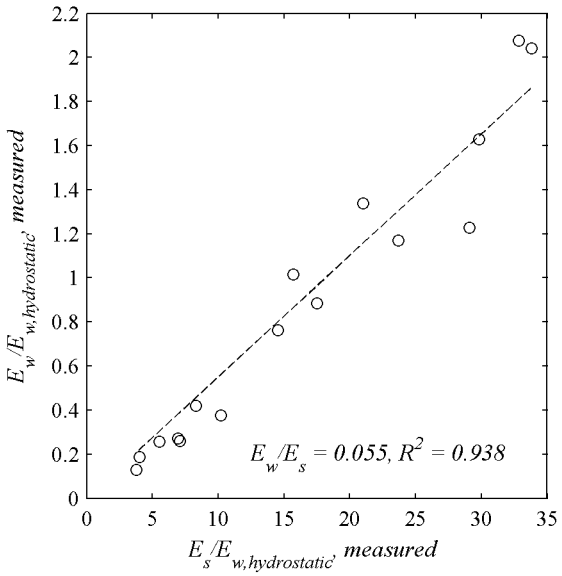

Figure 5.9. Resulting relationship between E_s and E_w: around 6% of the total landslide energy is converted to wave energy. This is an empirical result similar to that in section 4.7, but for the partial dataset of Table 5.1.

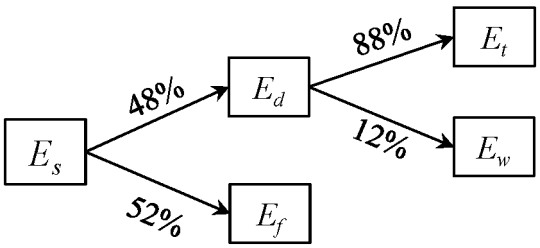

Figure 5.10. Flow chart of the energy conversion resulting from the presented methodology (rounded values percent).

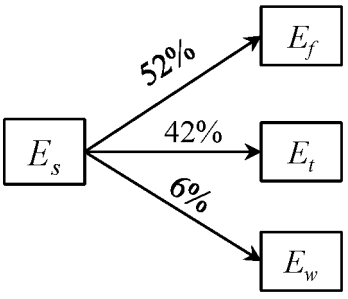

Figure 5.11. Rearranged flow chart of the energy conversion resulting from the presented methodology (rounded values percent).

Concerning the time of stop, applying the result found in section 5.2.3, a poor regression coefficient (R^2 = 0.293) is found between the difference E_d - E_w and the evaluated E_t (Figure 5.12). This result is intended to be qualitative due to the lack of experimental data on t_{stop}.

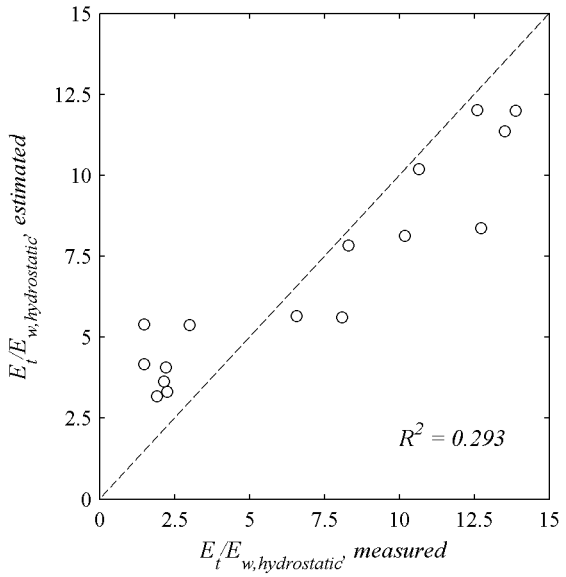

Figure 5.12. Validation of the dissipation by turbulences, applying the time of contact between landslide and water, found in section 5.2.3.

After a first validation, the methodology is applied to the three aforementioned experiments. At first instance the method is deemed satisfactory if it is capable of correctly predicting the run-out distance. If this fact occurs, therefore the model is able to describe in detail the behavior of the energy transmission in tsunami generation. The results of the run-out estimation for the reapplication dataset are given in Table 5.2 and described here below.

Table 5.2. Run-out estimation results for the reapplication dataset

Run	$x_{stop,measured}/h_w$	$x_{stop,estimated}/h_w$	$x_{stop,estimated}/x_{stop,measured}$
Unique_M100_27.8deg	8.52	7.85	0.92
Unique_M100_hs0.20_15.5deg	5.10	5.55	1.09
Unique_M120_27.8deg_no_wedge	8.00	7.91	0.99

In reapplying the methodology on the experiment *Unique_M100_27.8deg*, one can observe that the transition between wedge and tank bottom is relatively smooth, thanks to the deformable nature of the granular mass. In Figure 5.13 the landslide's *Fr* can be observed along the path of

landslide propagation. The landslide experiences resistance to motion due to basal friction and drag. The landslide rapidly decreases its velocity on the flat bottom till it stops.

In this case $\tilde{x}_{stop,measured}/h_w = 8.52$ and $\tilde{x}_{stop,estimated}/h_w = 7.85$. Thus the ratio between estimated and measured run-out distance is $\tilde{x}_{stop,estimated}/\tilde{x}_{stop,measured} = 0.92$. The difference of 8% in run-out prediction is satisfactory.

The evolution of energies along the run-out is given in Figure 5.14. In this case around 50% of energy is dissipated by friction and the other 50% is attributed to drag.

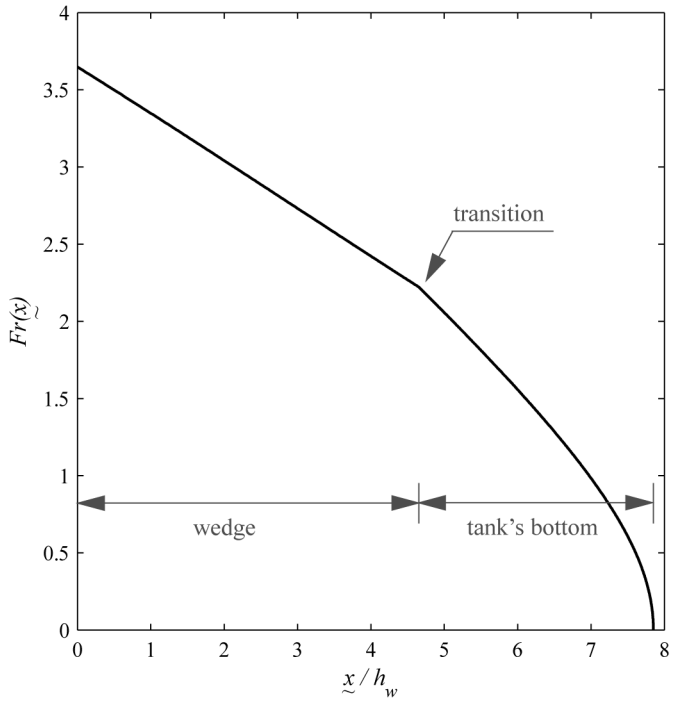

Figure 5.13. Result of landslide *Fr* along the run-out distance for the run *Unique_M100_27.8deg*.

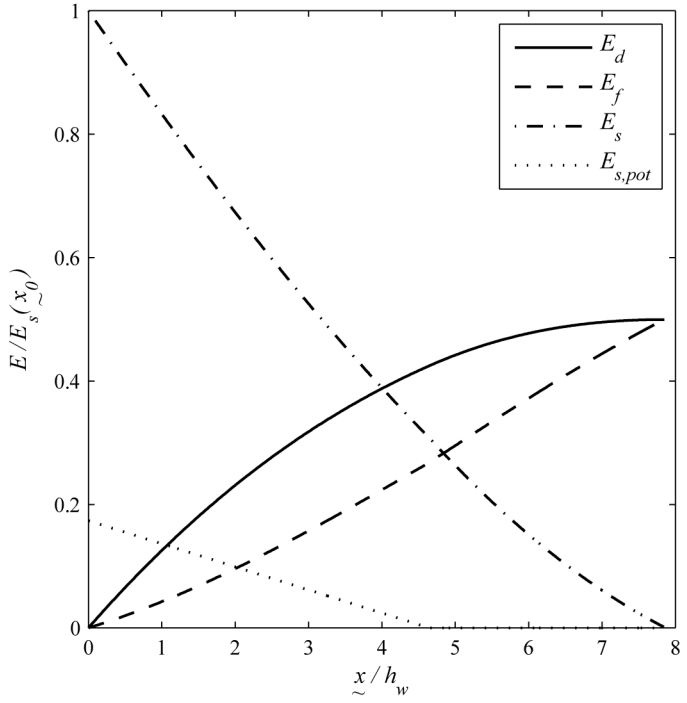

Figure 5.14. Resulting dimensionless conversion of energy for the run *Unique_M100_27.8deg*.

In case of the absence of wedge, the behavior increases in complexity. Observing the result for the experiment *Unique_M100_hs0.20_15.5deg* in Figure 5.15, sharp discontinuities can be recognized in the landslide *Fr* evolution along the run-out distance. The first discontinuity appears at the box exit, where the landslide detaches from the slope at $\tilde{x}/h_w \approx 2$. After this point the parabolic jump accelerates the mass, as the material is not subject to Coulomb friction and drag only partially resists the motion. At the landing point, around $\tilde{x}/h_w \approx 3.75$, a certain amount of energy is lost through impact. The velocity, as introduced in section 5.2, is assumed conserved only in the horizontal direction, while the velocity along the vertical direction is cancelled. Thus the *Fr* suddenly decreases. After this point the effect of Coulomb friction appears again, while drag never ceased acting. These behaviors are reflected on the energies evolution that can be observed in Figure 5.16.

In this case $\tilde{x}_{stop,measured}/h_w = 5.10$ and $\tilde{x}_{stop,estimated}/h_w = 5.55$. Thus, the ratio between estimated and measured run-out distance is $\tilde{x}_{stop,estimated}/\tilde{x}_{stop,measured} = 1.09$. The difference of 9% in the run-out prediction is satisfactory.

Reflecting the absence of the wedge, similar results were obtained for the run *Unique_M120_27.8deg_no_wedge*. Figure 5.17 and Figure 5.18 demonstrate this statement. The

only difference is that a resulting positive acceleration during the parabolic trajectory does not occur because of the stronger drag acting against the mass. In this case the landslide has a higher velocity compared to the previous case. Thus, being $E_d\left(\underset{\sim}{x}\right) \propto v_s^{\,2}\left(\underset{\sim}{x}\right)$ (see equation (5.7)), the resistance exercised by the drag strongly counteracts the gravitational acceleration.

In the last two experiments, the effect of the jump entails an additional energy loss through ground impact. However, in the graphics shown it can be observed how this last energy loss is partially replaced by the energy excess due to the absence of Coulomb friction during the jump.

For the run *Unique_M120_27.8deg_no_wedge* $\underset{\sim}{x}_{stop,measured}/h_w = 8.00$ and $\underset{\sim}{x}_{stop,estimated}/h_w = 7.91$. Thus, the ratio between estimated and measured run-out distance is $\underset{\sim}{x}_{stop,estimated}/\underset{\sim}{x}_{stop,measured} = 0.99$. The difference of 1% in run-out prediction is certainly satisfactory.

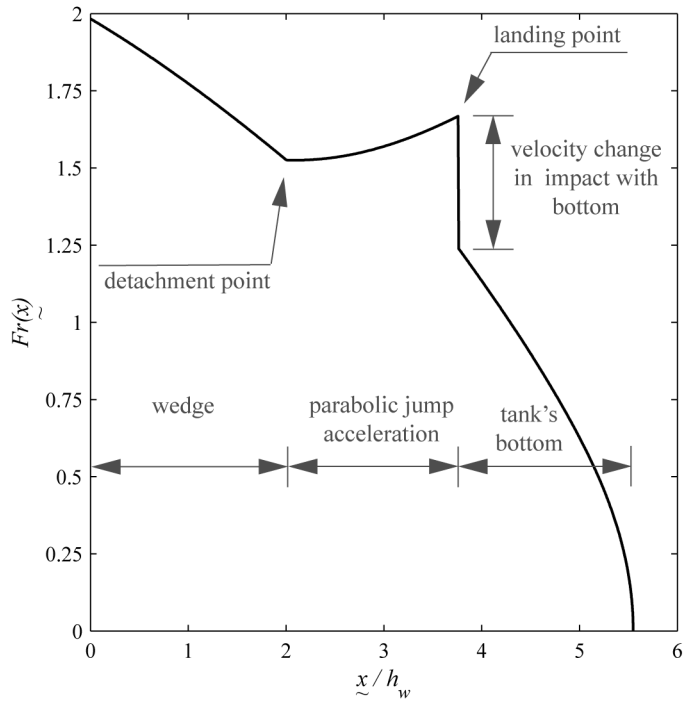

Figure 5.15. Result of landslide *Fr* along the run-out distance for the run *Unique_M100_hs0.20_15.5deg*.

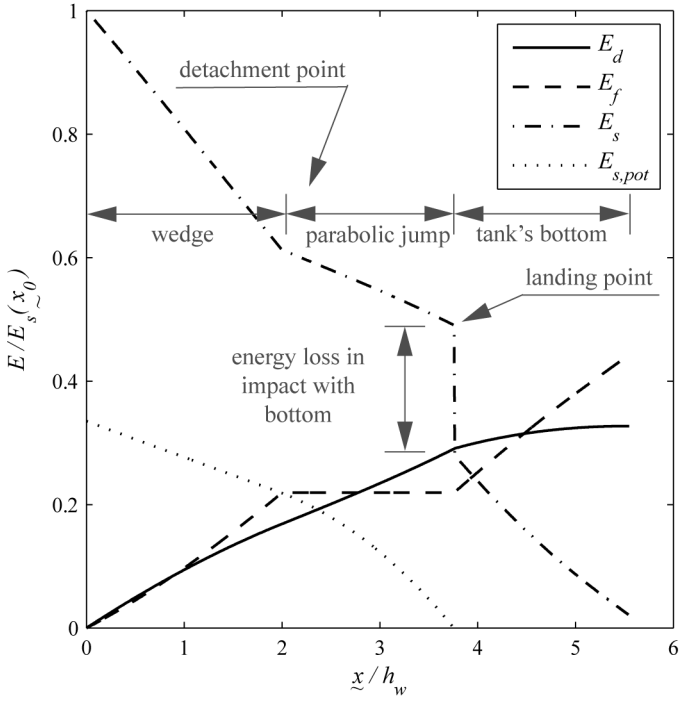

Figure 5.16. Resulting dimensionless conversion of energy for the run *Unique_M100_hs0.20_15.5deg*.

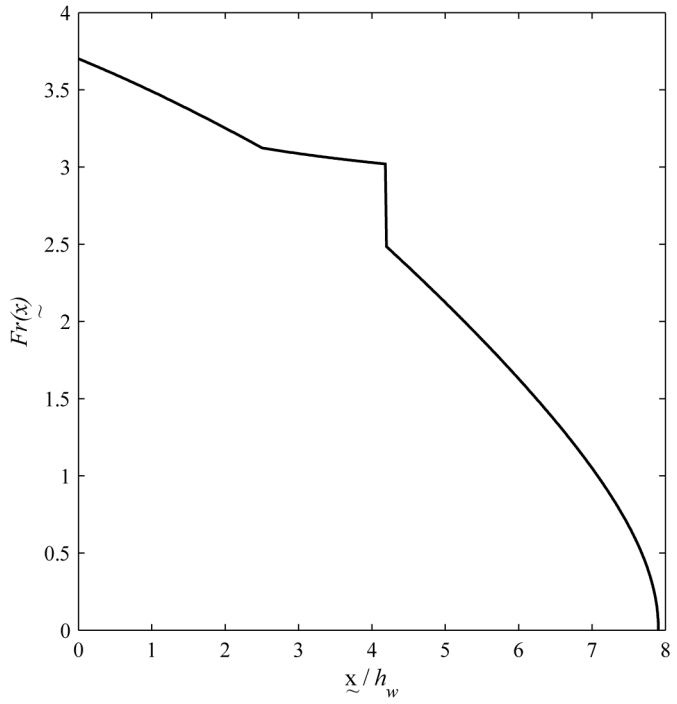

Figure 5.17. Result of landslide *Fr* along the run-out distance for the run *Unique_M120_27.8deg_no_wedge.* The evolution is found to be similar to the one in Figure 5.15.

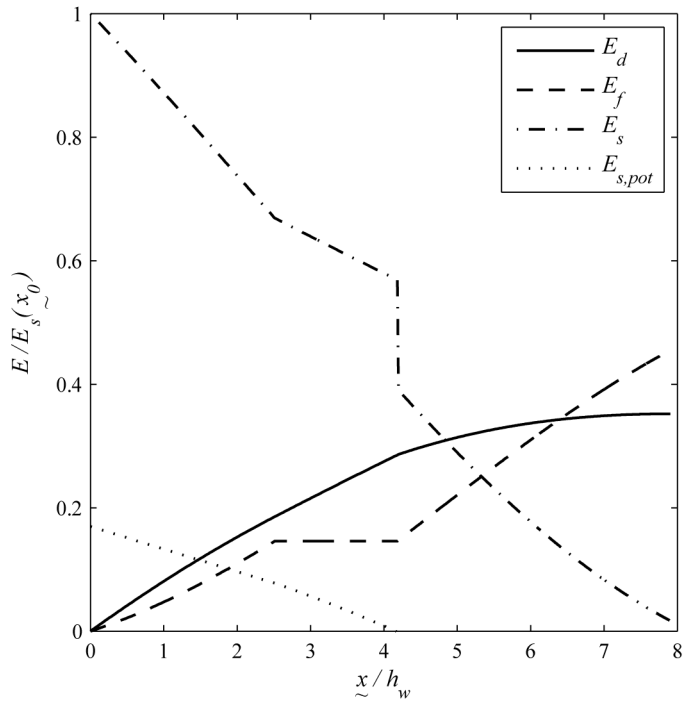

Figure 5.18. Resulting dimensionless conversion of energy for the run *Unique_M120_27.8deg_no_wedge*. The evolution is found to be similar to the one in Figure 5.16.

5.4 Conclusions

In the present chapter a simplified 1D forward Euler model including linear 3D landslides deformations is introduced. The model, under simplifying hypotheses and after an adequate optimization of parameters, is able to evaluate the energy losses and energy transfer between landslide and water body during the landslide tsunami process. The optimized parameters are the basal friction angle $\varphi_{s\text{-}b} = 24.89°$ and the drag coefficient $C_d = 1.26$.

Similar values of C_d to that found in this study were proposed by previous authors for landslides simulated by rigid blocks in their underwater motion: Watts (1998) gives experimentally a $C_d = 1.65$ for squared sliding blocks; Grilli et al. (2002) give $C_d = 1.53$ in numerical 2D simulations; Enet and Grilli (2007) found experimentally a $C_d = 0.36$ for an ellipsoidal rigid sliding block; Di Risio et al. (2009) found experimentally a $C_d = 0.403$ for an ellipsoidal rigid sliding block.

Other authors preferred to give the value implicitly, clustered empirically with other coefficients (i.e.: Walder et al., 2003).

Similar approaches to that presented in this chapter, were used in assessing the run-out of snow avalanches (Perla et al., 1980), landslides (Hungr et al., 2005), debris flows (Hurlimann et

al., 2008; Bregoli et al., 2011) that follow a granular fluid flow rheology of Voellmy (1955). This approach is a two parameter mass point model and is described by the following formula after Rickenmann (2005):

$$\frac{1}{2}\frac{dv_s^{\,2}}{d\tilde{x}} = g\left(\sin\alpha - \mu_m \cos\alpha\right) - \frac{v^2}{\xi} \tag{5.17}$$

μ_m is the sliding friction coefficient, ξ is the turbulence coefficient, also called "mass to drag ratio". Thus μ_m entails basal frictional forces while ξ implicitly contain drag forces. In the case of granular landslides provoking tsunamis Mazzanti & Bozzano (2009) introduce the methodology of equation (5.17), guessing sets of values of μ_m and ξ with back analysis. However their purpose was to evaluate the run-out distance. Hence they have not proposed explicit values of C_d and $\varphi_{s\text{-}b}$.

Thus, the result of the presented method is a step forward in this topic, given that separate explicit values of C_d and $\varphi_{s\text{-}b}$ are provided and are suitable to evaluate the energy transfer from landslide to water body. This achievement shows that, under the simplifying assumption of 3D landslide linear deformations, it is possible to define a unique drag coefficient. The result is of additional interest when considering that the experiment manifold used for the optimization of the two parameters is heterogenic in its configuration (presence or absence of wedge).

The value of C_d found is thought to be constant for the experienced landslide velocities. This can be justified by the fact that in underwater landslide motion, for values of $Re^* >> 1$, C_d is essentially constant, as demonstrated by Watts (1998).

The method is highly sensitive to the basal friction angle $\varphi_{s\text{-}b}$ as expected. Thus $\varphi_{s\text{-}b}$ needs to be evaluated carefully. In Figure 5.19 it can be seen that a change of 15% in $\varphi_{s\text{-}b}$ corresponds to a 30% change in C_d . This change leads to a variation of 25% in the evaluation of E_d after the application of the method.

For the experiments of the present work $\varphi_{s\text{-}b} = 30°$ in dry condition (see section 2.3.3), but the calibration shows a value of $\varphi_{s\text{-}b} = 24.86°$ (see Figure 5.5). The presence of water may be the reason of the reduction in $\varphi_{s\text{-}b}$: the material has been penetrating into the water and may already be in a partially saturated condition. Moreover, a reason for the reduction in $\varphi_{s\text{-}b}$ can be found in the lower roughness of the steel bottom of the sliding box, where the gravel is initially placed. Steiner (2006) roughly estimated $\varphi_{s\text{-}b} = 24.7°$ between gravel and the same steel bottom of the present study.

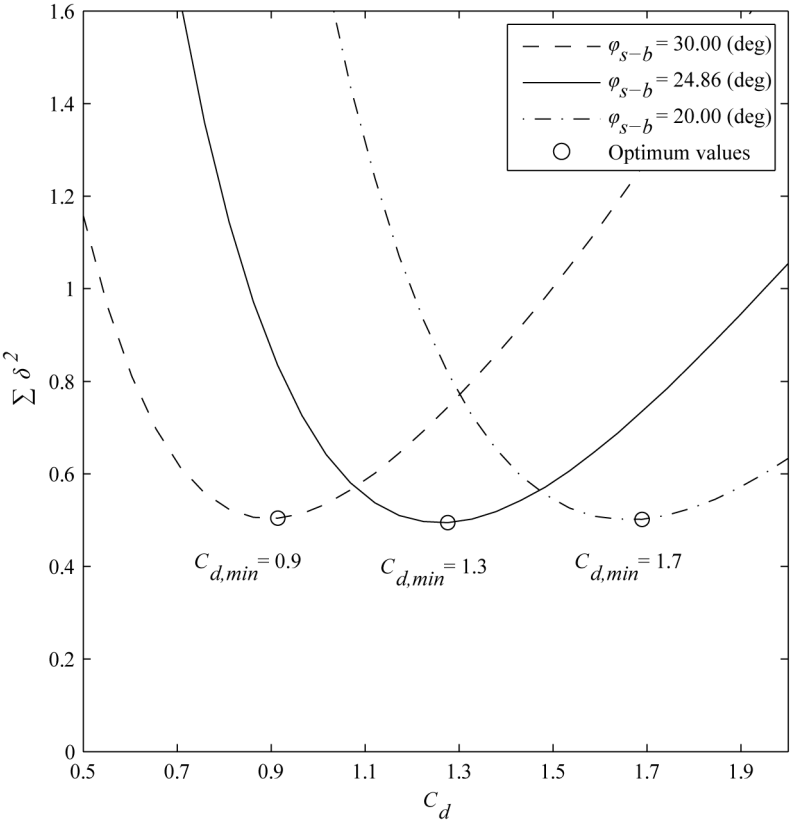

Figure 5.19. Optimum values of C_d for selected basal friction angles using a coarse method of graphical optimization. Solid, dashed and dash-dot lines are in agreement with the lines drawn in Figure 5.5.

An attempt at finding a mean optimum time of contact between water and sediments was carried out with the aim of evaluating the dissipation by turbulence. The average contact time found relating to the time of stop is $t_{contact}/t_{stop} = 0.76$. The validation shows a poor regression with the data (see Figure 5.12). This value should receive more investigation and should be correlated with measurements of t_{stop}, not available here.

The validation of the methodology shows that the run-out distance is correctly reproduced, entailing a regression of R^2 = 0.661 and a mean relative error of 2% between measured and estimated $\underset{\sim}{x}_{stop}$ (Figure 5.6).

R^2 has a relatively low value. In principle $\underset{\sim}{x}_{stop}$ is related to the center of mass and the run-out distance depends also on the final deformation of the granular mass. As explained earlier the final deposit is here assumed synthetically as an ellipse. Therefore the center of mass is supposed equivalent to the measured geometrical center of the ellipse. But the observed final deposits had a non-symmetrical form at least longitudinally (see Figure 3.4) and this assumption can

introduce an inaccuracy estimating $\underset{\sim}{x}_{stop}$. A detailed scan of the final deposit morphology could improve the results but, at the same time, add complexity to the model. Nevertheless the value of R^2 exhibits a certain correlation and the low mean relative error gives optimism concerning the quality of the analyses. Especially in the 3 cases of reapplication, the error in run-out evaluation is less than 9% (Table 5.2).

Concerning the estimation of the drag energy, Figure 5.7 shows an excellent relation between measured E_s and evaluated E_d (R^2 = 0.967). Moreover, Figure 5.8 shows that the wave energy and the drag energy have a good linear relationship (R^2 = 0.936).

Finally, the energy conversions in landslide tsunami generation have been accounted through the presented method as follows: of the total landside energy, about 52% is dissipated through Coulomb basal friction, about 42% is dissipated through other dissipative processes (mainly turbulence) and the other 6% is transferred to the waves being formed.

Splash and air entrainment losses were considered of smaller scale with respect to turbulence losses, and therefore disregarded. On the contrary, turbulence is potentially a greater source of energy loss, as it depends on v_s^3.

The aforementioned conversion rates are of primary interest, as they were not detailed in the past by other authors. However A similar conclusion, but for a sliding block, was detailed by Walder et al. (2003):

"It thus appears that submerged block-landslide motion is resisted primarily by frictional forces and only to a minor degree by hydrodynamic drag."

Our model confirms the importance of frictional forces and hydrodynamic drag for 3D deformable granular landslides and, additionally, quantifies the amount of energy conversions (see Figure 5.10 and Figure 5.11). It comes out that frictional forces and drag forces have a similar weight on energy transfer.

It is necessary to point out that here all sets of experiments (in presence or absence of wedge) are collected together. In the absence of wedge there is an additional energy loss related to the impact of the mass on the tank bottom. This loss is partially counteracted by the temporary absence of the Coulomb friction during the jump.

Therefore to correctly reproduce the energy rates of conversion it is necessary to correctly reproduce the morphology of the path $\underset{\sim}{x}$ of landslide propagation.

The goodness of the aforementioned rates of conversion is proved by the high correlation coefficients. Moreover, the existence of optimum C_d and $\varphi_{s\text{-}b}$ gives confidence that the model can

be applied. Eventually, the physics involved is correctly reproduced as confirmed by the reapplication of the method on the three designated experiments.

Therefore, it can be concluded that, under simplifying assumptions, the presented methodology is capable of describing energy conversion during the process of tsunamis generated by landslides.

The next important step should be the validation with experimental data produced by other similar laboratories as well as with data extracted from real events. This task is left to future studies. However, as of the time of concluding this thesis, complete experimental results of other investigations involving 3D deformable granular landslides has not been found.

Chapter 6: Conclusions and outlook

With the objective of studying the phenomena of tsunamis generated by granular landslides, a new experimental set-up was constructed in the fluvial-morphodynamics laboratory of the GITS team within the Hydraulic, Coastal and Environmental Engineering Department of the UPC (Barcelona, Spain).

The experimental device was created to devote specific attention to reproducing what had been identified as the main issues needing to be addressed: three-dimensional granular landslide deformation and three-dimensional wave propagation. Those features were scarcely addressed by previous researches.

It was found necessary to force the landslide to acquire a high velocity in order to fill gaps in previous researches and to achieve similarity with events occurring in nature. A high landslide velocity certainly avoids scale effects entailing high *Re* numbers.

The experimental device was defined, based upon these premises. It consists in a wheeled steel box sliding along a steep slope flume. The box is suddenly stopped and it then releases the granular material into a rectangular wave tank of 4.10x2.45 m.

The covered ranges of the main governing parameters are:

- still water depth: $0.16\ \text{m} \leq h_w \leq 0.25\ \text{m}$,
- angle of landslide impact: $\alpha = 15.5, 27.5°$,
- landslide velocity at impact: $1.9 \leq Fr_{average} \leq 4.2$ or $2.6 \leq Fr_{front} \leq 4.8$,
- landslide mass weight: $50 \leq m \leq 143\ \text{kg}$,
- landslide thickness: $0.4 \leq h_s/h_w \leq 1.3$,
- landslide length : $4.2 \leq l_s/h_w \leq 8.4$

Only a landslide width of $w_s = 0.34\ \text{m}$ is investigated.

A new measuring system was set up to observe the mass movement and the wave propagation at high resolution. It is based upon an extensive use of imagery processing.

The images are captured trough an array of different video cameras. Due to the high velocity of the simulated landslide, a high-speed video camera, able to shoot up to 1000 frames per second, is focused upon the exit of the sliding box. The camera records the evolution of the granular material along a center line drawn by a laser sheet.

A number of laser sheets project lines on the water surface. The water has been previously loaded with a small amount of kaolin that colors the fluid in white, reflecting the lasers at water surface. Three high-definition video cameras focus on the water tank, recording from different points of view the produced water displacement at the laser sheets.

Through a calibration process employing a mathematical-geometrical transformation algorithm created *ad-hoc* by the GITS team, the metrical measurement along each laser line is achieved.

The measurement tools entail a maximum global measurement uncertainty of 15%.

The measurement of the produced waves are given continuously in time (Eulerian) and space (Lagrangian) to avoid the classic spot measures given by probes, thus noticeably increasing the frequency and number of experimental data made available.

A total number of 41 experiments was carried out. The results of 25 experiments are employed in defining empirical predictors (chapter 4) and in defining the model of energy transfer from landslide to water body (chapter 5). The other 16 experiments were conducted with a configuration that did not permit the simultaneous observation of landslide and wave evolution, and thus they are disregarded in the analysis of results. However, because they include the observation of landslide evolution, 7 experiments of those 16 were used for the model described in chapter 5. The remaining 9 experiments are merely used for descriptive purposes.

Thanks to the gathered data it was possible to observe the different features of the studied phenomenon.

Once the box flaps open at the end of the channel, the granular mass suddenly starts to stretch due to the basal friction with the wedge. At impact with water the granular mass suffers additional deformations due to the hydrodynamic drag resistance and turbulence at water-solid boundaries. These last two effects were not witnessed due to the absence of underwater observations during the landslide propagation. Finally the granular mass deposits on the tank bottom. The form of the final deposit is quasi-elliptical due to the longitudinal and lateral expansions that the granular mass suffered.

The leading wave crest's volume and energy are practically conserved during the wave propagation. The celerity of the first crest is comparable with the celerity of solitary waves as observed by previous authors.

The celerity of the first wave of a tsunami is certainly the most important feature concerning the early warning and the evacuation of population. But in order to evaluate the potential hazard it is also necessary to define the intensity of the possible event.

Therefore, for the purpose of predicting the effect of landslide tsunamis, a number of empirical predictors are defined through a multivariable regression approach. The empirical formulas give the predictions for the following tsunami's leading wave crest characteristics:

- maximum amplitude,
- location of maximum amplitude,
- time of maximum amplitude,
- amplitude decay in space and time,
- energy conversion.

Moreover, it has been proposed formulas describing the landslide deformation.

The evolution of the first crest amplitude shows that after its maximum condition, given at a certain location and time by the generation features, the amplitude starts to rapidly decay exponentially along the propagation following the rule $a(x)/h_w \propto e^{-0.1x/h_w}$. A similar conclusion can be drawn for the first crest propagation in time. In particular a characteristic of exponential decay in time is the time required for the amplitude to fall to 1/2 of its initial value. This time, denoted as $t_{1/2}$, is called "half-life". In the present application $t_{1/2}$ depends on the depth of the water body. Thus, through the presented work it was possible to define the half-life of the first crest amplitude of the tsunami as $t_{1/2} = 6.42\left(g/h_w\right)^{-0.5}$ s. For instance, for a water body having a depth of 100 m, the crest amplitude is reduced to its half after 20 s.

All the empirical formulas were successfully tested on the experimental dataset. Moreover the predictive formulas are applied to two past events: the Vajont Dam (Italy, 1963) and the Lake Chehalis (Canada, 2007). The analysis of the first event shows a predicted run-up of 200 m versus the observed run-up of 210 m. The analysis of the second event produces a predicted maximum run-up of 39 m, while the one observed was documented as 38 m.

Thus, it was demonstrated that the predictive tools defined here are able to quantify the potential hazard posed by landslide generated tsunamis, and that they can be useful in risk-assessment frameworks.

With the aim of investigating the energy losses and energy conversions during landslide impact with the water body, a simplified 1D forward Euler model is introduced, including linear 3D landslides deformations. The model, under simplifying hypotheses and after an adequate optimization of parameters, is capable of evaluating the rates of loss in the energy transfer between landslide and water body during the landslide tsunami process. The optimized parameters are the basal friction angle $\varphi_{s\text{-}b} = 24.89°$ and the drag coefficient $C_d = 1.26$.

Similar work was carried out by previous authors, but their studies concern the use of rigid blocks. Thus, in this sense, the effort produced in this thesis adds a piece of knowledge in respect of the behavior of deformable granular landslides.

The validation of the methodology shows that the run-out distance of the landslide is correctly reproduced. Particularly in the 3 cases of reapplication, the error in run-out evaluation is less than 9%.

Finally, the energy conversions in landslide tsunami generation were calculated through the presented method as follows: of the total landside energy, about 52% is dissipated by Coulomb basal friction, about 42% is dissipated by other dissipative processes (mainly turbulence) and the other 6% is transferred to the waves being formed.

Splash and air entrainment losses were considered of smaller scale with respect to turbulence losses, and therefore disregarded. On the contrary, turbulence is potentially a great source of energy loss, as it depends on v_s^3.

An attempt at finding a mean optimum time of contact between water and sediments was carried out, with the aim of evaluating the dissipation by turbulence. The average contact time related to the time of stop that was found is $t_{contact}/t_{stop} = 0.76$. The validation shows a poor regression with the data. This value should need more investigations and should be associated with underwater measurements of t_{stop}, not available here.

The model defined here confirms the importance of frictional forces and hydrodynamic drag for 3D deformable granular landslides and, additionally, quantifies the amount of energy conversions. It emerges that frictional forces and drag forces have a similar weight on energy transfer.

It is important to remark that to correctly reproduce the energy rates of conversion, it is necessary to correctly reproduce the morphology of the path of landslide propagation. Thus, the results of energy conversion exposed here are representative of certain specific morphology configurations. However, the model can be synthetically adapted to any path morphology.

Therefore, it can be concluded that, under simplifying assumptions, the presented methodology is capable of describing the energy conversion during the process of tsunamis generated by landslides.

The next important step should be the validation with experimental data produced by other similar laboratories and on the basis of data extracted from real events. This task is left to future studies. However, as of the time of concluding this thesis, complete experimental results of other investigations involving 3D deforming granular landslides has not been found.

The studies contained in this thesis certainly present some limitations.

In evaluating the experimental results, only the main wave direction of propagation (axial to the landslide motion) is analyzed.

In evaluating the volume and the energy of the first crest, a constant wave amplitude of the wave front was considered. Some authors propose an amplitude attenuation along the radial direction β proportional to the cosβ. However, because of the lack of observation, no radial attenuation has been considered here. Further observation should be devoted to this behavior.

The lateral wave expansion needs more data to be analyzed. However, in some cases it was possible to evaluate the wave lateral expansion, noting that the wave front has a semi-elliptical form. This was fundamental in analyzing the lateral reflections and thus the clean part of the wave signal. The results indicate that practically only the signal relative to the first crest is clean, while the rest is partially compromised by lateral and frontal wave reflection. For these reasons the evaluation of the first wave height, trough, length and period are not analyzed because they are thought to be compromised by reflections. To avoid this problem, a larger wave tank should have been employed. However, it was observed by several researchers that the first crest is certainly the most important and destructive in the case of tsunamis provoked by subaerial landslides.

Therefore, it can be concluded that the tools proposed in this thesis are certainly suitable for the assessment of hazards related to the phenomenon object of this study.

The presented work entails an interesting outlook. Some recommendations for related future studies are proffered hereafter, in order to improve the understanding of tsunamis generated by subaerial granular landslides.

The set-up is undoubtedly able to cover wider ranges of parameters than the ones investigated in this thesis. Therefore, widening those ranges should be investigated in future studies.

One of the main limitations of the set-up was recognized in the narrow wave tank. Moving the landslide generator to a wider and longer tank should be recommended in order to improve considerably upon this research: a wider tank should diminish lateral reflection problems and permit the observation of lateral wave propagation; a longer tank would permit the analysis of longer wave profiles.

Similarly, in order to evaluate the amplitude decay in the far field, a longer tank should be used.

The underwater observation of landslide motion is suggested, as it is of primary interest in analyzing the granular landslide deformations. Particularly the time of underwater motion should

help the understanding of the energy losses due to turbulence. Moreover, it can improve the evaluation of time of stop and landslide run-out distance.

A detailed scan of the final deposit morphology could improve the observation of the final deformation of the landslide. It could be of help in defining the position of the real center of mass of the deposit, which is significant in evaluating the landslide run-out.

An important feature of a landslide tsunami is its capability to create large run-ups on the flanks of the water body. This behavior is the main responsible of the devastation along the shorelines and it is of primary importance when referring to the potential hazard of the tsunami itself. Some formulas of transformation from wave crest to wave run-up exist in literature concerning certain wave types. Those formulas were used to define the run-up within the present work. However a dedicated study associating landslide-generated waves with the possible run-up along inclined flanks is suggested as an improvement of the present study.

Two frameworks are recommended concerning the application of the presented experimental results. The first refers to the application of the proposed numerical model to other experimental set-ups, in order to evaluate the capability of capturing the energy transfer during the landslide tsunami process. The second concerns the use of an advanced numerical model to reproduce the experimental results of this thesis. As an example, OpenFOAM could be a suitable model that, under the necessary assumptions, should be capable of reproducing the described behavior.

Bibliography

Abdel-Aziz, Y. & Karara, H. (1971), 'Direct linear transformation into object space coordinates in close-range photogrammetry, in Proc. Symp. Close-Range Photogrammetry', *Urbana-Champaign* pp. 1–18.

Ataie-Ashtiani, B. & Nik-Khah, A. (2008), 'Impulsive waves caused by subaerial landslides', *Environmental Fluid Mechanics* **8**(3), 263–280. http://dx.doi.org/10.1007/s10652-008-9074-7

Bateman, A., Granados, A., Medina, V., Velasco, D. & Nalesso, M. (2006), Experimental procedure to obtain 2D time-space high-speed water surfaces, *in* 'Proceedings of the International Conference on Fluvial Hydraulics, River Flow', pp. 1879–1888.

Bellotti, G., Di Risio, M. & De Girolamo, P. (2009), 'Feasibility of tsunami early warning systems for small volcanic islands', *Nat. Hazards Earth Syst. Sci* **9**, 1911–1919.

Bonaccorso, A., Calvari, S., Garfi, G., Lodato, L. & Patane, D. (2003), 'Dynamics of the december 2002 flank failure and tsunami at Stromboli Volcano inferred by volcanological and geophysical observations', *Geophys. Res. Lett* **30**(18), 1941.

Boussinesq, J. (1872), 'Théorie des ondes et des remous que se propagent le long d'un canal rectangulaire horizontal, en communiquant au liquide contenu dans ce canal des vitesses sensiblement pareilles de la surface au fond', *J. Math. Pures Appl.* **17**, 55–108.

Bregoli, F. (2008), Messa a punto di un' apparecchiatura sperimentale e prove preliminari per lo studio della morfodinamica di alvei in ghiaia, Master's thesis, Università degli Studi di Firenze.

Bregoli, F., Bateman, A., Medina, V., Ciervo, F., Hürlimann, M. & Chevalier, G. (2011), Development of preliminary assessment tools to evaluate debris flow hazard, *in* D. L. H. Rinaldo Genevois & A. Prestininzi, eds, '5th International Conference on Debris-Flow Hazards Mitigation, Mechanics, Prediction and Assessment', pp. 835–844.

Bregoli, F., Medina, V., Chevalier, G., Hürlimann, M. & Bateman, A. (2014), 'Debris-flow susceptibility assessment at regional scale: Validation on an alpine environment', *Landslides* pp. 1–18. http://dx.doi.org/10.1007/s10346-014-0493-x

Brideau, M.-A. & Stead, D. (2012), 'Evaluating kinematic controls on planar translational slope failure mechanisms using three-dimensional distinct element modelling', *Geotechnical and Geological Engineering* **30**(4), 991–1011.

Brideau, M.-A., Sturzenegger, M., Stead, D., Jaboyedoff, M., Lawrence, M., Roberts, N. J., Ward, B. C., Millard, T. H. & Clague, J. J. (2012), 'Stability analysis of the 2007 Chehalis lake

landslide based on long-range terrestrial photogrammetry and airborne LiDAR data', *Landslides* **9**(1), 75–91.

Buckingham, E. (1914), 'On physically similar systems; illustrations of the use of dimensional equations', *Physical Review* **4**(4), 345–376.

Butterworth, S. (1930), 'On the theory of filter amplifiers', *Experimental wireless and wireless engineer* **7**(6), 536–541.

Capone, T. (2010), SPH numerical modelling of impulse water waves generated by landslides, PhD thesis, Hydraulic, Transportation and Roads Department of La Sapienza University of Rome.

Chevalier, G. (2012), Assessing debris-flow hazard focusing on statistical morpho-fluvial susceptibility models and magnitude-frequency relationships. Application to the Central-Eastern Pyrenees, PhD thesis, BarcelonaTech.

Coussot, P. & Meunier, M. (1996), 'Recognition, classification and mechanical description of debris flows', *Earth Science Reviews* **40**, 209–227.

Crosta, G., De Caro, M., Volpi, G., De Blasio, F., Imposimato, S. & Roddeman, D. (2015), Propagation and erosion of a fast moving granular mass, *in* G. Lollino, D. Giordan, G. B. Crosta, J. Corominas, R. Azzam, J. Wasowski & N. Sciarra, eds, 'Engineering Geology for Society and Territory - Volume 2', Springer International Publishing, pp. 1677–1681. http://dx.doi.org/10.1007/978-3-319-09057-3_298

Crosta, G., Imposimato, S. & Roddeman, D. (2015), 'Landslide spreading, impulse water waves and modelling of the Vajont rockslide', *Rock Mechanics and Rock Engineering* pp. 1–24. http://dx.doi.org/10.1007/s00603-015-0769-z

Cruden, D. M. (1991), 'A simple definition of a landslide', *Bulletin of Engineering Geology and the Environment* **43**(1), 27–29.

Dean, R. & Dalrymple, R. (1991), *Water wave mechanics for scientists and engineers*, Vol. 2.

Dennis, J. E. & Schnabel, R. B. (1996), *Numerical methods for unconstrained optimization and nonlinear equations*, Vol. 16, Siam.

Di Risio, M., Bellotti, G., Panizzo, A. & De Girolamo, P. (2009), 'Three-dimensional experiments on landslide generated waves at a sloping coast', *Coastal Engineering* **56**(5-6), 659–671.

do Carvalho, R. F. & Antunes do Carmo, J. (2007), 'Landslides into reservoirs and their impacts on banks', *Environmental Fluid Mechanics* **7**(6), 481–493. http://dx.doi.org/10.1007/s10652-007-9039-2

Egashira, S., Honda, N. & Itoh, T. (2001), 'Experimental study on the entrainment of bed material into debris flow', *Physics and Chemistry of the Earth, Part C: Solar, Terrestrial, Planetary Science* **26**, 645–650.

Enet, F. & Grilli, S. T. (2007), 'Experimental study of tsunami generation by three-dimensional rigid underwater landslides', *Journal of Waterway, Port, Coastal, and Ocean Engineering* **133**(6), 442–454.

Fell, R., Corominas, J., Bonnard, C., Cascini, L., Leroi, E. & Savage, W. Z. (2008), 'Guidelines for landslide susceptibility, hazard and risk zoning for land use planning', *Engineering Geology* **102**, 85 – 98. Landslide Susceptibility, Hazard and Risk Zoning for Land Use Planning. http://www.sciencedirect.com/science/article/pii/S0013795208001762

Fritz, H. (2002), Initial phase of landslide generated impulse waves, PhD thesis, ETH Zurich.

Fritz, H. (2009), 'Landslide tsunami generator experiments', *Internal Document, Research Laboratory at the Oregon State University (USA)* .

Fritz, H., Hager, W. & Minor, H. (2004), 'Near field characteristics of landslide generated impulse waves', *Journal of waterway, port, coastal, and ocean engineering* **130**, 287.

Fritz, H., Hager, W. & Minor, H.-E. (2003), 'Landslide generated impulse waves. 2. hydrodynamic impact craters', *Experiments in Fluids* **35**(6), 520–532. http://dx.doi.org/10.1007/s00348-003-0660-7

Fritz, H. M. (2001), 'Lituya Bay case rockslide impact and wave run-up', *Science of Tsunami Hazards* **19**(1), 3–22.

Genevois, R. & Ghirotti, M. (2005), 'The 1963 Vaiont landslide', *Giornale di Geologia Applicata* **1**, 41–52.

Grilli, S. T., Vogelmann, S. & Watts, P. (2002), 'Development of a 3d numerical wave tank for modeling tsunami generation by underwater landslides', *Engineering Analysis with Boundary Elements* **26**(4), 301–313.

Grilli, S. T. & Watts, P. (2005), 'Tsunami generation by submarine mass failure. i: Modeling, experimental validation, and sensitivity analyses', *Journal of Waterway, Port, Coastal, and Ocean Engineering* **131**(6), 283–297. http://dx.doi.org/10.1061/(ASCE)0733-950X(2005)131:6(283)

Grimstad, E. (2005), The Loen rock slide - an analysis of the stability, *in* Senneset, Flaate & Larsen, eds, 'Landslides and Avalanches: ICFL 2005 Norway'.

Guevara, A. (2007), Study of the protection measures against local scour at bridge piers, Master's thesis, Technical University of Catalonia (BarcelonaTech).

Harbitz, C., Glimsdal, S., Løvholt, F., Kveldsvik, V., Pedersen, G. & Jensen, A. (2014), 'Rockslide tsunamis in complex fjords: From an unstable rock slope at åkerneset to tsunami risk in western Norway', *Coastal Engineering* **88**, 101–122.

Heller, V. (2008), Landslide generated impulse waves: Prediction of near field characteristics, PhD thesis, ETH Zurich.

Heller, V. (2011), 'Scale effects in physical hydraulic engineering models', *Journal of Hydraulic Research* **49**(3), 293–306. http://dx.doi.org/10.1080/00221686.2011.578914

Heller, V. & Hager, W. (2010), 'Impulse product parameter in landslide generated impulse waves', *Journal of Waterway, Port, Coastal, and Ocean Engineering* **145**, 155.

Hendron, A. J. & Patton, F. D. (1987), 'The Vaiont slide—a geotechnical analysis based on new geologic observations of the failure surface', *Engineering Geology* **24**(1), 475–491.

Hermanns, R. L., L'Heureux, J.-S. & Blikra, L. H. (2013), Landslide triggered tsunami, displacement wave, *in* P. Bobrowsky, ed., 'Encyclopedia of Natural Hazards', Encyclopedia of Earth Sciences Series, Springer Netherlands, pp. 611–615. http://dx.doi.org/10.1007/978-1-4020-4399-4_95

Hermanns, R. L., Oppikofer, T., Roberts, N. J. & Sandøy, G. (2014), Catalogue of historical displacement waves and landslide-triggered tsunamis in norway, *in* 'Engineering Geology for Society and Territory-Volume 4', Springer, pp. 63–66.

Huang, B., Yin, Y., Liu, G., Wang, S., Chen, X. & Huo, Z. (2012), 'Analysis of waves generated by Gongjiafang landslide in Wu Gorge, three Gorges reservoir, on November 23, 2008', *Landslides* **9**(3), 395–405. http://dx.doi.org/10.1007/s10346-012-0331-y

Huang, B., Yueping, Y., Xiaoting, C., Guangning, L., Sichang, W. & Zhibing, J. (2013), 'Experimental modeling of tsunamis generated by subaerial landslides: two case studies of the Three Gorges Reservoir, China', *Environmental Earth Sciences* pp. 1–13. http://dx.doi.org/10.1007/s12665-013-2765-5

Huber, A. (1980), Schwallwellen in seen als folge von bergsturzen, *in* D. Vischer, ed., 'Versuchsanstalt fur Wasserbau, Hydrologie und Glaziologie', number 47 *in* 'VAW Mitteilung', ETH, Zurich.

Huber, A., H. W. (1997), Forecasting impulse waves in reservoirs., *in* 'C31:993-1005. Florence, Italy. Commission International des Grands Barrages: Paris.'.

Hungr, O., Corominas, J., Eberhardt, E. et al. (2005), 'Estimating landslide motion mechanism, travel distance and velocity', *Landslide Risk Management* pp. 99–128.

Hungr, O., Evans, S., Bovis, M. & Hutchinson, J. (2001), 'A review of the classification of landslides of the flow type', *Environmental and Engineering Geoscience* **7**(3), 221.

Hürlimann, M., Rickenmann, D., Medina, V. & Bateman, A. (2008), 'Evaluation of approaches to calculate debris-flow parameters for hazard assessment', *Engineering Geology* **102**(3-4), 152–163.

Ippen, A. T. (1966), Estuary and coastal hydrodynamics, *in* 'Engineering Society monographs', McGraw-Hill Book Company New York.

Iverson, R. (1997), 'The physics of debris flows', *Rev. Geophys.* **35**, 245–296.

Iverson, R. M. (2012), 'Elementary theory of bed-sediment entrainment by debris flows and avalanches', *Journal of Geophysical Research: Earth Surface (2003–2012)* **117**(F3).

Johnson, R. (1997), *A modern introduction to the mathematical theory of water waves*, Vol. 19, Cambridge University Press.

Kamphuis, J. & Bowering, R. (1970), Impulse waves generated by landslides, Vol. 1.

Keulegan, G. H. (1948), 'Gradual damping of solitary waves', *J. Res. Natl. Bur. Stand* **40**(6), 487–498.

Lagarias, J. C., Reeds, J. A., Wright, M. H. & Wright, P. E. (1998), 'Convergence Properties of the Nelder–Mead Simplex Method in Low Dimensions', *SIAM Journal on Optimization* **9**(1), 112–147. http://dx.doi.org/10.1137/S1052623496303470

Laitone, E. V. (1960), 'The second approximation to cnoidal and solitary waves', *Journal of Fluid Mechanics* **9**(03), 430–444. http://dx.doi.org/10.1017/S0022112060001201

Lamb, H. (1932), *Hydrodynamics*, Cambridge University Press, Cambridge.

Law, L. & Brebner, A. (1968), On water waves generated by landslides, *in* 'Proceedings of the Third Australasian Conference on Hydraulics and Fluid Mechanics', pp. 155–159.

Lawrence, M. S., Roberts, N. J. & Clague, J. J. (2013), The 2007 Chehalis Lake landslide, British Columbia: A landslide-generated surge wave (tsunami) with implications for dam safety, *in* 'Geo-Montreal'.

LeMehaute, B. & Wang, S. (1996), *Water waves generated by underwater explosion*, Advanced Series on Ocean Engineering, World Scientific, Singapore.

Mader, C. (1999), 'Modeling the 1958 Lituya Bay mega-tsunami', *Science of Tsunami Hazards* **17(2)**(5), 57–67.

Mangeney, A., Roche, O., Hungr, O., Mangold, N., Faccanoni, G. & Lucas, A. (2010), 'Erosion and mobility in granular collapse over sloping beds', *Journal of Geophysical Research: Earth Surface* **115**(F3). F03040. http://dx.doi.org/10.1029/2009JF001462

Maramai, A., Graziani, L. & Tinti, S. (2005), 'Tsunamis in the Aeolian Islands (southern Italy): a review', *Marine Geology* **215**, 11 – 21. http://www.sciencedirect.com/science/article/pii/S0025322704003226

Mazzanti, P. & Bozzano, F. (2009), 'An equivalent fluid/equivalent medium approach for the numerical simulation of coastal landslides propagation: theory and case studies', *Natural Hazards and Earth System Science* **9**(6), 1941–1952. http://www.nat-hazards-earth-syst-sci.net/9/1941/2009/

Mazzanti, P. & De Blasio, F. V. (2011), 'The dynamics of coastal landslides: insights from laboratory experiments and theoretical analyses', *Bulletin of Engineering Geology and the Environment* **70**(3), 411–422.

M'Cowan, J. (1893), 'On the highest wave of permanent type', *Proceedings of the Edinburgh Mathematical Society* **12**, 112–112. http://journals.cambridge.org/article_S0013091500001747

Medina, V., Hürlimann, M. & Bateman, A. (2008), 'Application of FLATModel, a 2D finite volume code, to debris flows in the northeastern part of the Iberian Peninsula', *Landslides* **5**(1), 127–142. http://dx.doi.org/10.1007/s10346-007-0102-3

Miller, D. (1960), 'Giant waves in Lituya Bay, Alaska', *Geological Survey Professional Paper* **354**.

Miyamoto, K. (2010), 'Numerical Simulation of Landslide Movement and Unzen-Mayuyama Disdaster in 1792, Japan', *J. of Disaster Research* **Vol.5 No.3**, 280–287.

Mohammed, F. (2010), Physical modeling of tsunamis generated by three-dimensional deformable granular landslides, PhD thesis, Georgia Institute of Technology.

Mohammed, F. & Fritz, H. M. (2012), 'Physical modeling of tsunamis generated by three-dimensional deformable granular landslides', *Journal of Geophysical Research: Oceans* **117**(C11), C11015. http://dx.doi.org/10.1029/2011JC007850

Moré, J. J., Garbow, B. S. & Hillstrom, K. E. (1980), User guide for minpack-1, Technical report, Argonne National Laboratory Report ANL-80-74, Argonne, Ill.

Morlotti, E. (2010), Funzione del bosco nella fase di arresto dei debris flow, PhD thesis, Università degli studi di Milano.

Noda, E. (1970), 'Water waves generated by landslides', *Journal of the Waterways, Harbors and Coastal Engineering Division* **96**(4), 835–855.

Novak, P., Guinot, V., Jeffrey, A. & Reeve, D. E. (2010), *Hydraulic Modelling–An Introduction: Principles, Methods and Applications*, CRC Press.

Panizzo, A. (2004), Physical and numerical modelling of subaerial landslide generated waves, PhD thesis, L'Aquila University.

Panizzo, A., De Girolamo, P., Di Risio, M., Maistri, A. & Petaccia, A. (2005), 'Great landslide events in italian artificial reservoirs', *Natural Hazards and Earth System Science* **5**(5), 733–740.

Panizzo, A., De Girolamo, P. & Petaccia, A. (2005), 'Forecasting impulse waves generated by subaerial landslides', *J. Geophys. Res* **110**(C12025), C12025.

Pastor, M., Herreros, I., Merodo, J. F., Mira, P., Haddad, B., Quecedo, M., González, E., Alvarez-Cedrón, C. & Drempetic, V. (2009), 'Modelling of fast catastrophic landslides and impulse waves induced by them in fjords, lakes and reservoirs', *Engineering Geology* **109**(1), 124–134.

Perla, R., Cheng, T. & McClung, D. M. (1980), 'A two-parameter model of snow-avalanche motion', *Journal of Glaciology* **26**, 197–207.

Quecedo, M., Pastor, M. & Herreros, M. (2004), 'Numerical modelling of impulse wave generated by fast landslides', *International journal for numerical methods in engineering* **59**(12), 1633–1656.

Ramanujan, S. (1914), 'Modular equations and approximations to π', *Quarterly Journal of Mathematics* **XLV**, 350 – 372.

Rayleigh, L. (1877), 'On progressive waves', *Proc. London Math. Soc.* **9**, 21–26.

Roberts, N. J., McKillop, R. J., Lawrence, M. S., Psutka, J. F., Clague, J. J., Brideau, M.-A. & Ward, B. C. (2013), Impacts of the 2007 landslide-generated tsunami in Chehalis Lake, Canada, *in* 'Landslide science and practice', Springer, pp. 133–140.

Roberts, N., McKillop, R., Hermanns, R., Clague, J. & Oppikofer, T. (2014), Preliminary global catalogue of displacement waves from subaerial landslides, *in* K. Sassa, P. Canuti & Y. Yin, eds, 'Landslide Science for a Safer Geoenvironment', Springer International Publishing, pp. 687–692. http://dx.doi.org/10.1007/978-3-319-04996-0_104

Saelevik, G., Jensen, A. & Pedersen, G. (2009), 'Experimental investigation of impact generated tsunami; related to a potential rock slide, Western Norway', *Coastal Engineering* **56**(9), 897 – 906. http://www.sciencedirect.com/science/article/pii/S0378383909000581

Sainz, A. & Herrero, M. (1999), 'Estabilidad de laderas y riesgo de deslizamientos e inundación en el embalse de yesa', *Geological internal report of the University of Zaragoza* .

Saltelli, A., Ratto, M., Andres, T., Campolongo, F., Cariboni, J., Gatelli, D., Saisana, M. & Tarantola, S. (2008), *Global Sensitivity Analysis: The Primer*, Wiley. http://books.google.es/books?id=wAssmt2vumgC

Scott-Russell, J. (1837), Experimental researches into the laws of certain hydrodynamical phenomena, *in* 'Edin. Roy Soc Trans XIV, 1840, 47-109, plus Plates I and III.'.

Scott-Russell, J. (1844), Report on waves, *in* 'Proc. Roy. Soc. Edinburgh', Vol. 319.

Semenza, E. (2001), *La storia del Vajont raccontata dal geologo che ha scoperto la frana*, Tecomproject.

Serrano-Pacheco, A., Murillo, J. & Garcá-Navarro, P. (2009), 'A finite volume method for the simulation of the waves generated by landslides', *Journal of hydrology* **373**(3), 273–289.

Slingerland, R. & Voight, B. (1979), *Rockslides and avalanches. Developments in geotechnical engineering*, Elsevier, Amsterdam, chapter Occurrences, properties and predictive models of landslide-generated impulse waves., pp. 2:317–397.

Slingerland, R. & Voight, B. (1982), 'Evaluating hazard of landslide-induced water waves', *Journal of the Waterway Port Coastal and Ocean Division* **108**(4), 504–512.

Steiner, F. (2006), Experimental study on granular debris flows, Master's thesis, ETH-Zurich.

Synolakis, C. E. (1987), 'The runup of solitary waves', *Journal of Fluid Mechanics* **185**, 523–545.

Taylor, J. R. (1997), *An introduction to error analysis: the study of uncertainties in physical measurements*, University science books.

Tsai, R. (1987), 'A versatile camera calibration technique for high-accuracy 3d machine vision metrology using off-the-shelf tv cameras and lenses', *Robotics and Automation, IEEE Journal of* **3**(4), 323–344.

Voellmy, A. (1955), 'Über die zerstörungskraft von lawinen', *Schweizerische Bauzeitung* **73**, 212–285.

Walder, J. S., Watts, P., Sorensen, O. E. & Janssen, K. (2003), 'Tsunamis generated by subaerial mass flows', *Journal of Geophysical Research: Solid Earth* **108**(B5). http://dx.doi.org/10.1029/2001JB000707

Wang, J., Ward, S. N. & Xiao, L. (2015), 'Numerical simulation of the December 4, 2007 landslide-generated tsunami in Chehalis Lake, Canada', *Geophysical Journal International* **201**(1), 372–376. http://gji.oxfordjournals.org/content/201/1/372.abstract

Ward, S. & Day, S. (2001), 'Cumbre Vieja volcano—potential collapse and tsunami at La Palma, Canary Islands', *Geophys. Res. Lett* **28**(17), 3397–3400.

Ward, S. N. (2001), 'Landslide tsunami', *Journal of Geophysical Research: Solid Earth* **106**(B6), 11201–11215. http://dx.doi.org/10.1029/2000JB900450

Watt, S. F., Pyle, D. M., Naranjo, J. A. & Mather, T. A. (2009), 'Landslide and tsunami hazard at Yate volcano, Chile as an example of edifice destruction on strike-slip fault zones', *Bulletin of volcanology* **71**(5), 559–574.

Watt, S., Talling, P., Vardy, M., Heller, V., HÃ¼hnerbach, V., Urlaub, M., Sarkar, S., Masson, D., Henstock, T., Minshull, T., Paulatto, M., Friant, A. L., Lebas, E., Berndt, C., Crutchley, G., Karstens, J., Stinton, A. & Maeno, F. (2012), 'Combinations of volcanic-flank and seafloor-sediment failure offshore montserrat, and their implications for tsunami generation', *Earth and Planetary Science Letters* **319-320**(0), 228 – 240. http://www.sciencedirect.com/science/article/pii/S0012821X11006893

Watts, P. (1998), 'Wavemaker curves for tsunamis generated by underwater landslides', *Journal of Waterway, Port, Coastal, and Ocean Engineering* **124**(3), 127–137. http://dx.doi.org/10.1061/(ASCE)0733-950X(1998)124:3(127)

Waythomas, C. F., Watts, P. & Walder, J. S. (2006), 'Numerical simulation of tsunami generation by cold volcanic mass flows at Augustine Volcano, Alaska', *Natural Hazards and Earth System Science* **6**(5), 671–685. http://www.nat-hazards-earth-syst-sci.net/6/671/2006/

Wiegel, R., Noda, E., Kuba, E., Gee, D. & Tornberg, G. (1970), 'Water waves generated by landslides in reservoirs', *Journal of the Waterways, Harbors and Coastal Engineering Division* **96**(2), 307–333.

Williams, J. M. (1985), *Tables of progressive gravity waves*, Pitman Boston.

Zhang, D., Wang, G., Yang, T., Zhang, M., Chen, S. & Zhang, F. (2013), 'Satellite remote sensing-based detection of the deformation of a reservoir bank slope in Laxiwa Hydropower Station, China', *Landslides* **10**(2), 231–238. http://dx.doi.org/10.1007/s10346-012-0378-9

Zhao, T., Utili, S. & Crosta, G. (2015), 'Rockslide and Impulse Wave Modelling in the Vajont Reservoir by DEM-CFD Analyses', *Rock Mechanics and Rock Engineering* pp. 1–20.

Zweifel, A., Hager, W., Minor, H. et al. (2006), 'Plane impulse waves in reservoirs', *Journal of waterway, port, coastal, and ocean engineering* **132**, 358.

Appendices

Appendix A

Technical drawings of the experimental set-up (see next pages):

1. Sliding box
2. Flume

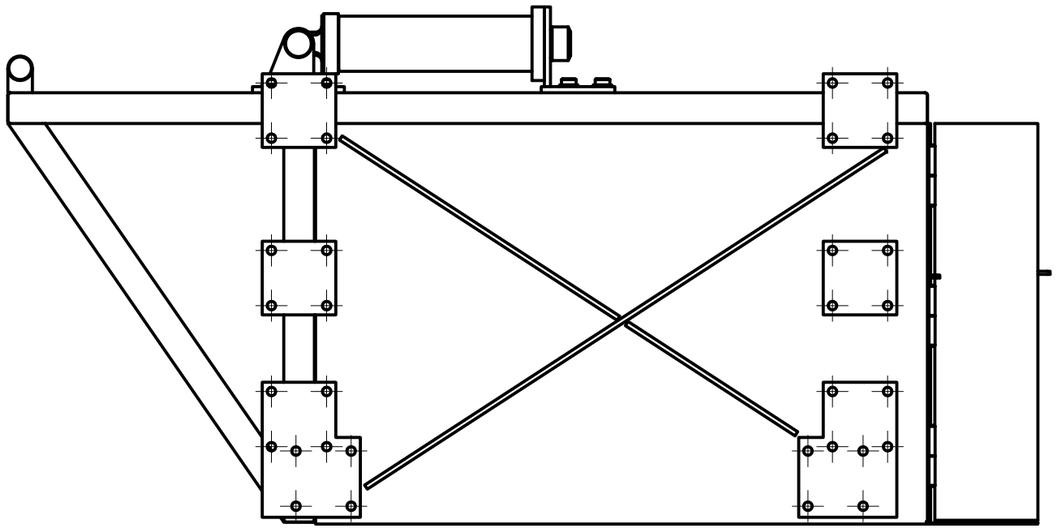

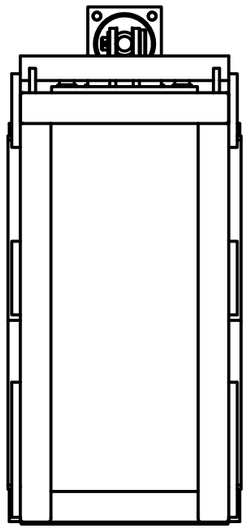

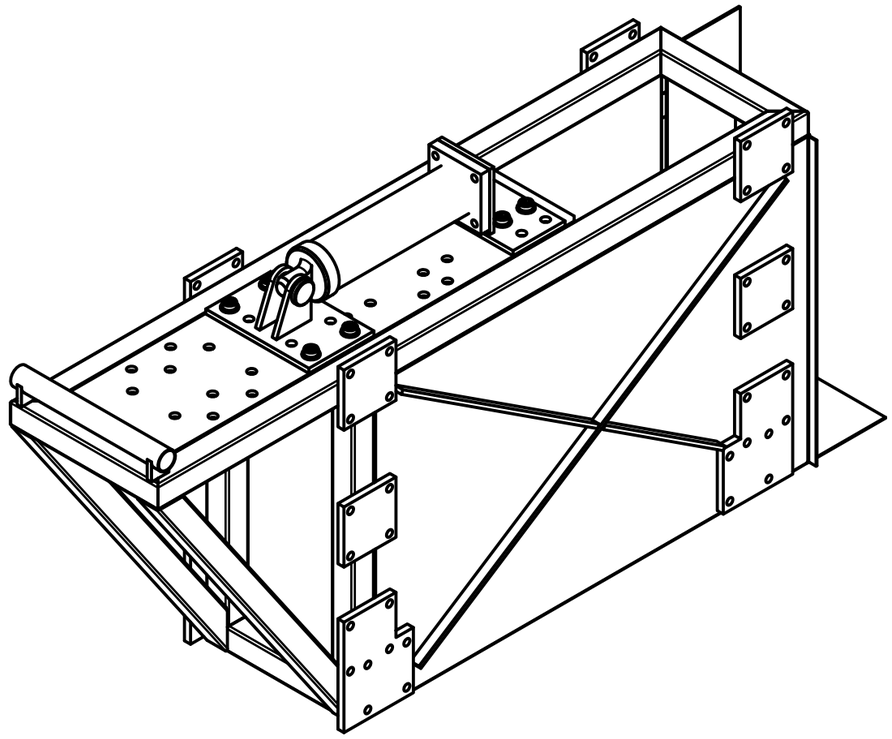

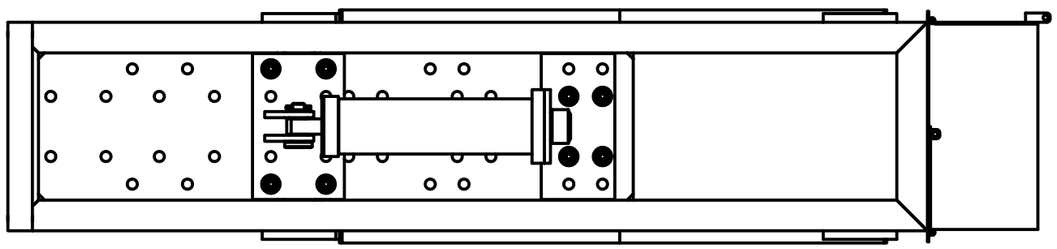

Drawing 1

Sliding box
Scale 1:10

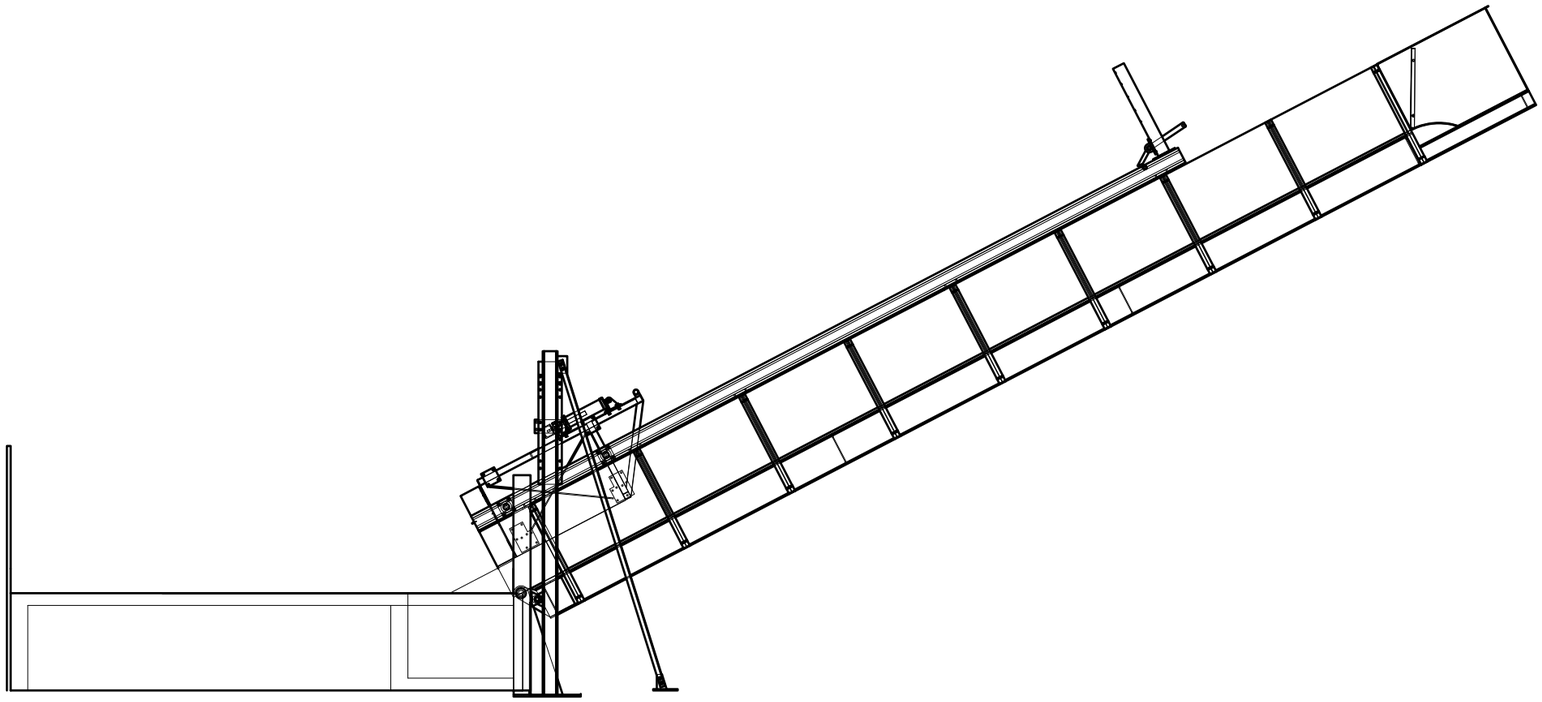

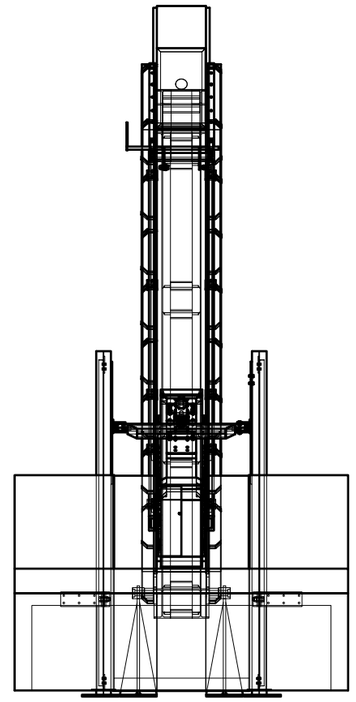

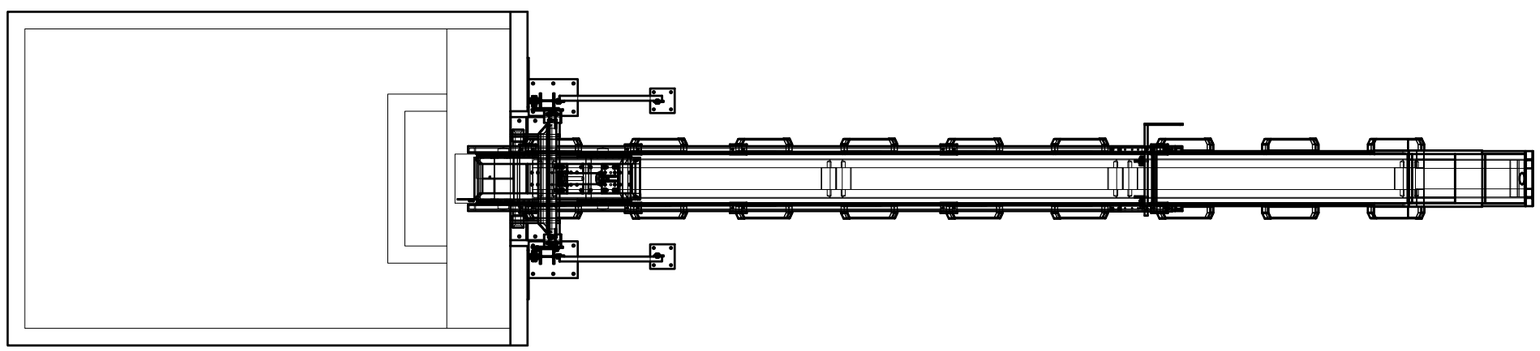

Drawing 2

Flume
Scale 1:50

Appendix B

Experimental data sheet (in Spanish)

Caracterización	
Fecha	
Numero secuencial exp.	
Nombre exp.	
Numero exp.	
Variables de experimento	
Peso material(kg)	
Altura material (Hs) (m)	
Largo material (Ls) (m)	
Largo material (Lb) (m)	
Ancho carro (W) (m)	
Altura agua (hw) (m)	
Gravado camera HV	
Obturador	
Velocidad (f/s)	
Lente	
Gravado camera HD Sony (b y c)	
Definicion (HD, FullHD)	
Velocidad (f/s)	
Gravado fotocamera Canon (a)	
Definicion (HD, FullHD)	
Velocidad (f/s)	
Tiempo obturador (sec)	
Obturador	
ISO	
Lente	
Laser verde	
Potencia	

Posiciones lasers	
Distancias	(cm)
D	
1	
1-2	
2-3	
3-4	
4-5	
5-6	
6	
tot	
Mancha final piedra	
a (m)	
b (m)	
dmax (m)	

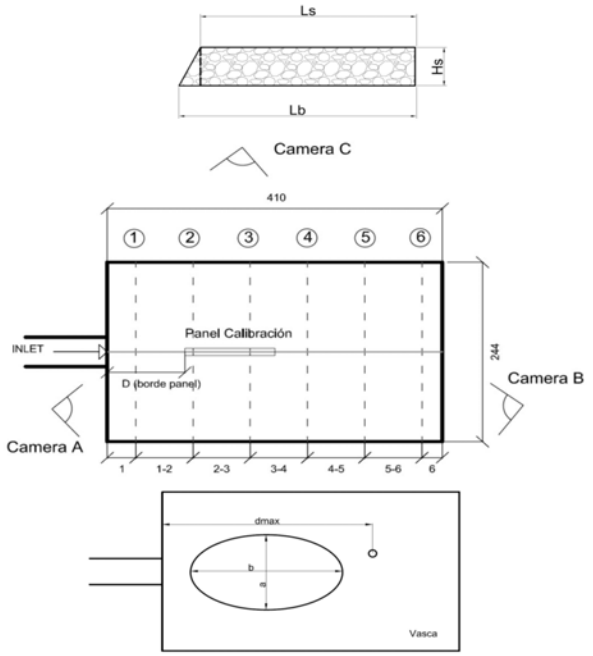

Observaciones

Appendix C

The present appendix contains the tables of the experimental results. ND means no data available.

C.1 Main features of experiments

#	# set	Name	m (kg)	α (°)	h_w (m)	h_s/h_w (-)	Fr (-)
1	Set 1	*Type_a_M50_27.8deg*	50	27.8	0.20	0.90	3.38
2	Set 1	*Type_a_M50_27.8deg*	50	27.8	0.16	0.54	4.02
3	Set 1	*Type_a_M75_27.8deg*	75	27.8	0.19	0.70	3.94
4	Set 1	*Type_a_M100_27.8deg*	100	27.8	0.19	0.79	3.95
5	Set 1	*Type_a_M125_27.8deg*	125	27.8	0.19	1.02	4.05
6	Set 1	*Type_a_M140_27.8deg*	140	27.8	0.18	1.19	4.10
7	Set 1	*Type_a_M110_27.8deg*	110	27.8	0.20	0.80	4.17
8	Set 1	*Type_a_M120_27.8deg*	120	27.8	0.20	0.85	3.84
9	Set 2	*Type_b_M50_27.8deg*	50	27.8	0.20	ND	ND
10	Set 2	*Type_b_M50_27.8deg*	50	27.8	0.16	ND	ND
11	Set 2	*Type_b_M75_27.8deg*	75	27.8	0.19	ND	ND
12	Set 2	*Type_b_M100_27.8deg*	100	27.8	0.19	ND	ND
13	Set 2	*Type_b_M125_27.8deg*	125	27.8	0.19	ND	ND
14	Set 2	*Type_b_M140_27.8deg*	140	27.8	0.18	ND	ND
15	Set 2	*Type_b_M110_27.8deg*	110	27.8	0.20	ND	ND
16	Set 2	*Type_b_M120_27.8deg*	120	27.8	0.20	ND	ND
17	Set 3	*Unique_M50_27.8deg*	50	27.8	0.20	0.78	3.86
18	Set 3	*Unique_M75_27.8deg*	75	27.8	0.20	0.98	3.61
19	Set 3	*Unique_M100_27.8deg*	100	27.8	0.20	1.00	3.65
20	Set 3	*Unique_M110_27.8deg*	110	27.8	0.20	1.12	3.64
21	Set 3	*Unique_M120_27.8deg*	120	27.8	0.20	1.21	3.70
22	Set 3	*Unique_M125_27.8deg*	125	27.8	0.20	1.22	3.66
23	Set 3	*Unique_M130_27.8deg*	130	27.8	0.20	1.14	3.68
24	Set 3	*Unique_M136_27.8deg*	136	27.8	0.20	1.25	3.69
25	Set 3	*Unique_M139.5_27.8deg*	139.5	27.8	0.20	1.26	3.70
26	Set 3	*Unique_M50_hs0.10_27.8deg*	50	27.8	0.20	0.65	4.12
27	Set 3	*Unique_M50_hs0.15_27.8deg*	50	27.8	0.20	0.98	3.86
28	Set 3	*Unique_M50_hs0.20_27.8deg*	50	27.8	0.20	0.94	3.69
29	Set 3	*Unique_M50_hs0.25_27.8deg*	50	27.8	0.20	1.03	3.83
30	Set 3	*Unique_M75_hs0.10_27.8deg*	75	27.8	0.20	0.75	3.85
31	Set 3	*Unique_M75_hs0.15_27.8deg*	75	27.8	0.20	0.71	3.95

#	# set	Name	m (kg)	α (°)	h_w (m)	h_s/h_w (-)	Fr (-)
32	Set 3	*Unique_M75_hs0.20_27.8deg*	75	27.8	0.20	0.99	4.03
33	Set 3	*Unique_M75_hs0.25_27.8deg*	75	27.8	0.20	1.23	3.38
34	Set 4	*Unique_M50_hs0.10_15.5deg*	50	15.5	0.25	0.38	2.11
35	Set 4	*Unique_M50_hs0.20_15.5deg*	50	15.5	0.25	0.56	2.20
36	Set 4	*Unique_M75_hs0.15_15.5deg*	75	15.5	0.25	0.49	2.07
37	Set 4	*Unique_M100_hs0.20_15.5deg*	100	15.5	0.25	0.58	1.98
38	Set 4	*Unique_M100bis_hs0.20_15.5deg*	100	15.5	0.25	0.63	2.01
39	Set 4	*Unique_M125_hs0.20_15.5deg*	125	15.5	0.25	0.60	1.91
40	Set 4	*Unique_M143_hs0.25_15.5deg*	143	15.5	0.25	0.60	2.02
41	Set 5	*Unique_M120_27.8deg_no_wedge*	120	27.8	0.20	1.01	3.70
		Maximum values	**143**	**27.8**	**0.25**	**1.26**	**4.89**
		Minimum values	**50**	**15.5**	**0.16**	**0.38**	**2.56**

C.2 Form and velocity of landslides

#	# set	Name	$h_{s,front}$ (m)	h_s (m)	$v_{s,front}$ (m)	v_s (m/s)	l_s (m)
1	Set 1	*Type_a_M50_27.8deg*	0.200	0.180	6.000	5.000	ND
2	Set 1	*Type_a_M50_27.8deg*	0.120	0.087	5.830	5.093	ND
3	Set 1	*Type_a_M75_27.8deg*	0.170	0.133	6.670	5.440	ND
4	Set 1	*Type_a_M100_27.8deg*	0.180	0.150	6.500	5.370	ND
5	Set 1	*Type_a_M125_27.8deg*	0.240	0.193	6.670	5.557	ND
6	Set 1	*Type_a_M140_27.8deg*	0.220	0.213	6.400	5.490	ND
7	Set 1	*Type_a_M110_27.8deg*	0.170	0.160	6.390	5.849	ND
8	Set 1	*Type_a_M120_27.8deg*	0.200	0.170	6.390	5.377	ND
17	Set 3	*Unique_M50_27.8deg*	0.170	0.155	6.000	5.410	0.917
18	Set 3	*Unique_M75_27.8deg*	0.184	0.157	5.560	5.060	1.339
19	Set 3	*Unique_M100_27.8deg*	0.196	0.191	6.129	5.110	1.308
20	Set 3	*Unique_M110_27.8deg*	0.221	0.212	5.970	5.100	1.470
21	Set 3	*Unique_M120_27.8deg*	0.254	0.231	6.020	5.181	1.517
22	Set 3	*Unique_M125_27.8deg*	0.253	0.219	6.000	5.130	1.339
23	Set 3	*Unique_M130_27.8deg*	0.246	0.228	6.290	5.160	1.460
24	Set 3	*Unique_M136_27.8deg*	0.304	0.249	6.200	5.170	1.480
25	Set 3	*Unique_M139.5_27.8deg*	0.272	0.253	5.980	5.180	1.500
26	Set 3	*Unique_M50_hs0.10_27.8deg*	0.111	0.130	5.888	5.775	1.148
27	Set 3	*Unique_M50_hs0.15_27.8deg*	0.190	0.196	5.707	5.407	0.902
28	Set 3	*Unique_M50_hs0.20_27.8deg*	0.229	0.188	6.266	5.172	0.940
29	Set 3	*Unique_M50_hs0.25_27.8deg*	0.267	0.206	6.338	5.366	0.849
30	Set 3	*Unique_M75_hs0.10_27.8deg*	0.168	0.150	5.836	5.387	1.285
31	Set 3	*Unique_M75_hs0.15_27.8deg*	0.199	0.141	5.836	5.530	1.068
32	Set 3	*Unique_M75_hs0.20_27.8deg*	0.235	0.199	6.121	5.648	1.124
33	Set 4	*Unique_M75_hs0.25_27.8deg*	0.281	0.245	5.839	4.739	0.896
34	Set 4	*Unique_M50_hs0.10_15.5deg*	0.113	0.095	4.010	3.298	1.153
35	Set 4	*Unique_M50_hs0.20_15.5deg*	0.203	0.141	4.510	3.452	1.198
36	Set 4	*Unique_M75_hs0.15_15.5deg*	0.130	0.122	4.100	3.248	1.436
37	Set 4	*Unique_M100_hs0.15_15.5deg*	0.178	0.145	4.200	3.106	1.735
38	Set 4	*Unique_M100bis_hs0.20_15.5deg*	0.181	0.157	4.007	3.148	1.800
39	Set 4	*Unique_M125_hs0.20_15.5deg*	0.220	0.149	4.610	2.992	1.974
40	Set 4	*Unique_M143_hs0.25_15.5deg*	0.256	0.151	4.510	3.161	2.059
41	Set 5	*Unique_M120_27.8deg_no_wedge*	0.246	0.202	5.849	5.184	1.291
		Maximum values	**0.30**	**0.25**	**6.67**	**5.85**	**2.06**
		Minimum values	**0.11**	**0.09**	**4.01**	**2.99**	**0.85**

C.3 Energy of landslides

#	# set	Name	$E_{s,kin}$ (J)	$E_{s,pot}$ (J)	E_s (J)
1	Set 1	*Type_a_M50_27.8deg*	625.0	137.1	762.1
2	Set 1	*Type_a_M50_27.8deg*	648.6	124.5	773.0
3	Set 1	*Type_a_M75_27.8deg*	1109.8	201.0	1310.7
4	Set 1	*Type_a_M100_27.8deg*	1441.8	267.9	1709.8
5	Set 1	*Type_a_M125_27.8deg*	1929.8	334.9	2264.7
6	Set 1	*Type_a_M140_27.8deg*	2109.8	366.2	2476.1
7	Set 1	*Type_a_M110_27.8deg*	1881.4	301.7	2183.1
8	Set 1	*Type_a_M120_27.8deg*	1734.5	329.1	2063.6
17	Set 3	*Unique_M50_27.8deg*	731.7	137.1	868.8
18	Set 3	*Unique_M75_27.8deg*	960.1	205.7	1165.8
19	Set 3	*Unique_M100_27.8deg*	1305.6	274.3	1579.9
20	Set 3	*Unique_M110_27.8deg*	1430.6	301.7	1732.2
21	Set 3	*Unique_M120_27.8deg*	1610.6	329.1	1939.7
22	Set 3	*Unique_M125_27.8deg*	1644.8	342.8	1987.6
23	Set 3	*Unique_M130_27.8deg*	1730.7	356.5	2087.2
24	Set 3	*Unique_M136_27.8deg*	1817.6	373.0	2190.6
25	Set 3	*Unique_M139.5_27.8deg*	1871.6	382.6	2254.2
26	Set 3	*Unique_M50_hs0.10_27.8deg*	833.9	137.1	971.0
27	Set 3	*Unique_M50_hs0.15_27.8deg*	730.9	137.1	868.0
28	Set 3	*Unique_M50_hs0.20_27.8deg*	668.8	137.1	806.0
29	Set 3	*Unique_M50_hs0.25_27.8deg*	719.8	137.1	857.0
30	Set 3	*Unique_M75_hs0.10_27.8deg*	1088.1	205.7	1293.8
31	Set 3	*Unique_M75_hs0.15_27.8deg*	1146.7	205.7	1352.4
32	Set 3	*Unique_M75_hs0.20_27.8deg*	1196.4	205.7	1402.1
33	Set 4	*Unique_M75_hs0.25_27.8deg*	842.0	205.7	1047.7
34	Set 4	*Unique_M50_hs0.10_15.5deg*	271.9	121.4	393.3
35	Set 4	*Unique_M50_hs0.20_15.5deg*	297.9	121.4	419.4
36	Set 4	*Unique_M75_hs0.15_15.5deg*	395.6	182.2	577.7
37	Set 4	*Unique_M100_hs0.15_15.5deg*	482.5	242.9	725.4
38	Set 4	*Unique_M100bis_hs0.20_15.5deg*	495.5	242.9	738.4
39	Set 4	*Unique_M125_hs0.20_15.5deg*	559.3	303.6	862.9
40	Set 4	*Unique_M143_hs0.25_15.5deg*	714.4	347.3	1061.7
41	Set 5	*Unique_M120_27.8deg_no_wedge*	1612.2	329.1	1941.4
		Maximum values	**2109.8**	**382.6**	**2476.1**
		Minimum values	**271.9**	**121.4**	**393.3**

C.4 Final deposit of landslides

#	# set	Name	a_d (m)	b_d (m)	D (m)
1	Set 1	*Type_a_M50_27.8deg*	1.30	1.15	2.08
2	Set 1	*Type_a_M50_27.8deg*	1.26	1.08	2.57
3	Set 1	*Type_a_M75_27.8deg*	1.45	1.30	2.18
4	Set 1	*Type_a_M100_27.8deg*	1.60	1.40	2.35
5	Set 1	*Type_a_M125_27.8deg*	1.71	1.59	2.48
6	Set 1	*Type_a_M140_27.8deg*	1.80	1.55	2.70
7	Set 1	*Type_a_M110_27.8deg*	1.53	1.32	2.98
8	Set 1	*Type_a_M120_27.8deg*	ND	ND	ND
17	Set 3	*Unique_M50_27.8deg*	ND	ND	ND
18	Set 3	*Unique_M75_27.8deg*	1.40	1.20	2.00
19	Set 3	*Unique_M100_27.8deg*	1.55	1.40	ND
20	Set 3	*Unique_M110_27.8deg*	ND	ND	ND
21	Set 3	*Unique_M120_27.8deg*	ND	ND	ND
22	Set 3	*Unique_M125_27.8deg*	1.70	1.50	2.30
23	Set 3	*Unique_M130_27.8deg*	ND	ND	ND
24	Set 3	*Unique_M136_27.8deg*	1.70	1.50	ND
25	Set 3	*Unique_M139.5_27.8deg*	1.75	1.50	2.35
26	Set 3	*Unique_M50_hs0.10_27.8deg*	1.20	1.05	ND
27	Set 3	*Unique_M50_hs0.15_27.8deg*	ND	ND	ND
28	Set 3	*Unique_M50_hs0.20_27.8deg*	ND	ND	ND
29	Set 3	*Unique_M50_hs0.25_27.8deg*	ND	ND	ND
30	Set 3	*Unique_M75_hs0.10_27.8deg*	ND	ND	ND
31	Set 3	*Unique_M75_hs0.15_27.8deg*	ND	ND	ND
32	Set 3	*Unique_M75_hs0.20_27.8deg*	1.50	1.25	ND
33	Set 4	*Unique_M75_hs0.25_27.8deg*	1.35	1.20	ND
34	Set 4	*Unique_M50_hs0.10_15.5deg*	1.25	0.98	ND
35	Set 4	*Unique_M50_hs0.20_15.5deg*	1.25	0.98	ND
36	Set 4	*Unique_M75_hs0.15_15.5deg*	1.40	0.95	ND
37	Set 4	*Unique_M100_hs0.15_15.5deg*	1.55	1.10	ND
38	Set 4	*Unique_M100bis_hs0.20_15.5deg*	1.50	1.10	ND
39	Set 4	*Unique_M125_hs0.20_15.5deg*	1.68	1.15	2.30
40	Set 4	*Unique_M143_hs0.25_15.5deg*	1.70	1.20	2.40
41	Set 5	*Unique_M120_27.8deg_no_wedge*	1.70	1.45	2.32
		Maximum values	**1.59**	**1.80**	**2.98**
		Minimum values	**0.95**	**1.03**	**2.00**

C.5 Amplitude of the first crests

Name	a_{max}/h_w	x_{max}/h_w	$t_{max}(g/h_w)^{0.5}$	$k_2^{(a(x))}$	R^2, $k_2^{(a(x))}$	$k_2^{(a(t))}$	R^2, $k_2^{(a(t))}$
	(-)	(-)	(-)	(-)	(-)	(-)	(-)
Unique_M50_27.8deg	0.436	6.660	4.202	-0.109	0.990	-0.113	0.991
Unique_M75_27.8deg	0.528	7.195	4.202	-0.087	0.955	-0.093	0.952
Unique_M100_27.8deg	0.564	8.040	4.622	-0.066	0.889	-0.073	0.854
Unique_M110_27.8deg	0.547	7.715	4.622	-0.064	0.937	-0.073	0.927
Unique_M120_27.8deg	0.567	8.615	4.762	-0.067	0.917	-0.073	0.891
Unique_M125_27.8deg	0.635	8.150	4.622	-0.055	0.944	-0.072	0.933
Unique_M130_27.8deg	0.608	8.575	4.902	-0.071	0.915	-0.083	0.885
Unique_M136_27.8deg	0.704	8.630	4.482	-0.071	0.818	-0.095	0.809
Unique_M139.5_27.8deg	0.764	9.180	5.043	-0.092	0.874	-0.126	0.871
Unique_M50_hs0.10_27.8deg	0.465	6.840	4.062	-0.113	0.984	-0.116	0.980
Unique_M50_hs0.15_27.8deg	0.492	8.620	4.902	-0.109	0.900	-0.111	0.893
Unique_M50_hs0.20_27.8deg	0.478	8.365	4.622	-0.106	0.970	-0.112	0.974
Unique_M50_hs0.25_27.8deg	0.486	8.170	4.342	-0.099	0.934	-0.096	0.908
Unique_M75_hs0.10_27.8deg	0.544	8.130	4.342	-0.094	0.969	-0.100	0.968
Unique_M75_hs0.15_27.8deg	0.493	8.645	4.902	-0.107	0.905	-0.109	0.895
Unique_M75_hs0.20_27.8deg	0.577	9.405	5.183	-0.091	0.907	-0.097	0.883
Unique_M75_hs0.25_27.8deg	0.503	8.890	4.482	-0.070	0.841	-0.076	0.841
Unique_M50_hs0.10_15.5deg	0.261	3.580	3.132	-0.142	0.907	-0.142	0.921
Unique_M50_hs0.20_15.5deg	0.310	5.268	3.884	-0.153	0.860	-0.154	0.885
Unique_M75_hs0.15_15.5deg	0.310	4.648	3.257	-0.149	0.889	-0.147	0.914
Unique_M100_hs0.15_15.5deg	0.329	4.796	3.508	-0.152	0.925	-0.154	0.936
Unique_M100bis_hs0.20_15.5deg	0.336	4.468	3.383	-0.133	0.946	-0.131	0.943
Unique_M125_hs0.20_15.5deg	0.369	5.484	3.759	-0.131	0.943	-0.130	0.946
Unique_M143_hs0.25_15.5deg	0.393	5.268	3.633	-0.147	0.947	-0.148	0.949
Unique_M120_27.8deg_no_wedge	0.542	8.510	4.902	-0.078	0.914	-0.087	0.881
Maximum values	**0.764**	**9.405**	**5.183**	**-0.055**	**0.990**	**-0.072**	**0.991**
Minimum values	**0.261**	**3.580**	**3.132**	**-0.153**	**0.818**	**-0.154**	**0.809**
Average values	**0.489**	**7.274**	**4.310**	**-0.102**	**0.919**	**-0.108**	**0.913**
STD	**0.126**	**1.732**	**0.591**	**0.031**	**0.043**	**0.027**	**0.045**

C.6 Celerity of the first crests

#	# set	Name	v_w (m/s)	R^2	c (m/s)	v_w / c (-)	c_{sol} (m/s)	v_w / c_{sol} (-)
17	Set 3	*Unique_M50_27.8deg*	1.45	0.998	1.40	1.03	1.57	0.92
18	Set 3	*Unique_M75_27.8deg*	1.48	0.997	1.40	1.06	1.61	0.92
19	Set 3	*Unique_M100_27.8deg*	1.57	0.996	1.40	1.12	1.65	0.95
20	Set 3	*Unique_M110_27.8deg*	1.60	0.995	1.40	1.14	1.65	0.97
21	Set 3	*Unique_M120_27.8deg*	1.53	0.996	1.40	1.09	1.65	0.93
22	Set 3	*Unique_M125_27.8deg*	1.84	0.996	1.40	1.31	1.71	1.08
23	Set 3	*Unique_M130_27.8deg*	1.64	0.996	1.40	1.17	1.67	0.98
24	Set 3	*Unique_M136_27.8deg*	1.89	0.989	1.40	1.35	1.69	1.12
25	Set 3	*Unique_M139.5_27.8deg*	1.91	0.996	1.40	1.36	1.72	1.11
26	Set 3	*Unique_M50_hs0.10_27.8deg*	1.44	0.999	1.40	1.03	1.57	0.92
27	Set 3	*Unique_M50_hs0.15_27.8deg*	1.42	0.998	1.40	1.02	1.58	0.90
28	Set 3	*Unique_M50_hs0.20_27.8deg*	1.47	0.998	1.40	1.05	1.58	0.93
29	Set 3	*Unique_M50_hs0.25_27.8deg*	1.38	0.997	1.40	0.98	1.58	0.88
30	Set 3	*Unique_M75_hs0.10_27.8deg*	1.48	0.997	1.40	1.05	1.62	0.91
31	Set 3	*Unique_M75_hs0.15_27.8deg*	1.43	0.998	1.40	1.02	1.58	0.90
32	Set 3	*Unique_M75_hs0.20_27.8deg*	1.52	0.997	1.40	1.09	1.63	0.93
33	Set 3	*Unique_M75_hs0.25_27.8deg*	1.51	0.994	1.40	1.08	1.61	0.94
34	Set 4	*Unique_M50_hs0.10_15.5deg*	1.56	0.998	1.57	0.99	1.66	0.94
35	Set 4	*Unique_M50_hs0.20_15.5deg*	1.55	0.996	1.57	0.99	1.66	0.93
36	Set 4	*Unique_M75_hs0.15_15.5deg*	1.53	0.997	1.57	0.98	1.67	0.91
37	Set 4	*Unique_M100_hs0.15_15.5deg*	1.57	0.995	1.57	1.00	1.69	0.93
38	Set 4	*Unique_M100bis_hs0.20_15.5deg*	1.54	0.997	1.57	0.99	1.68	0.92
39	Set 4	*Unique_M125_hs0.20_15.5deg*	1.56	0.996	1.57	1.00	1.71	0.91
40	Set 4	*Unique_M143_hs0.25_15.5deg*	1.56	0.992	1.57	1.00	1.71	0.91
41	Set 5	*Unique_M120_27.8deg_no_wedge*	1.58	0.995	1.40	1.13	1.64	0.97
		Mean values	**1.56**	**0.996**	**1.45**	**1.08**	**1.64**	**0.95**
		Maximum values	**1.91**	**0.999**	**1.57**	**1.36**	**1.72**	**1.12**
		Minimum values	**1.38**	**0.989**	**1.40**	**0.98**	**1.57**	**0.88**
		STD	**0.14**	**0.002**	**0.08**	**0.11**	**0.05**	**0.06**

C.7 Volume of the first crests

#	# set	Name	V_w / V_s average	V_w / V_s std
17	Set 3	*Unique_M50_27.8deg*	3.32	0.13
18	Set 3	*Unique_M75_27.8deg*	2.72	0.11
19	Set 3	*Unique_M100_27.8deg*	2.79	0.04
20	Set 3	*Unique_M110_27.8deg*	2.52	0.10
21	Set 3	*Unique_M120_27.8deg*	2.20	0.10
22	Set 3	*Unique_M125_27.8deg*	2.85	0.10
23	Set 3	*Unique_M130_27.8deg*	2.22	0.02
24	Set 3	*Unique_M136_27.8deg*	2.47	0.17
25	Set 3	*Unique_M139.5_27.8deg*	2.59	0.11
26	Set 3	*Unique_M50_hs0.10_27.8deg*	3.61	0.14
27	Set 3	*Unique_M50_hs0.15_27.8deg*	3.05	0.17
28	Set 3	*Unique_M50_hs0.20_27.8deg*	3.04	0.15
29	Set 3	*Unique_M50_hs0.25_27.8deg*	2.51	0.10
30	Set 3	*Unique_M75_hs0.10_27.8deg*	3.05	0.15
31	Set 3	*Unique_M75_hs0.15_27.8deg*	3.01	0.14
32	Set 3	*Unique_M75_hs0.20_27.8deg*	3.01	0.16
33	Set 3	*Unique_M75_hs0.25_27.8deg*	2.64	0.20
34	Set 4	*Unique_M50_hs0.10_15.5deg*	2.50	0.37
35	Set 4	*Unique_M50_hs0.20_15.5deg*	1.77	0.24
36	Set 4	*Unique_M75_hs0.15_15.5deg*	2.00	0.21
37	Set 4	*Unique_M100_hs0.15_15.5deg*	1.47	0.11
38	Set 4	*Unique_M100bis_hs0.20_15.5deg*	1.42	0.16
39	Set 4	*Unique_M125_hs0.20_15.5deg*	1.38	0.11
40	Set 4	*Unique_M143_hs0.25_15.5deg*	1.16	0.08
41	Set 5	*Unique_M120_27.8deg_no_wedge*	2.48	0.11
		Mean values	**2.47**	**0.14**
		Maximum values	**3.61**	**0.37**
		Minimum values	**1.16**	**0.02**
		STD	**0.64**	

C.8 Energy of the first crests

#	# set	Name	$E_{w,pot}(x_{max})$ (J)	$E_{w,pot}(x_{max})$ / $E_{s,kin}$	$E_{w,pot}(x_{fin})$ (J)	$E_{w,pot}(x_{max})$ / $E_{w,pot}(x_{fin})$
17	Set 3	*Unique_M50_27.8deg*	46.58	0.064	19.41	2.40
18	Set 3	*Unique_M75_27.8deg*	59.01	0.061	30.26	1.95
19	Set 3	*Unique_M100_27.8deg*	78.01	0.060	44.55	1.75
20	Set 3	*Unique_M110_27.8deg*	81.97	0.057	48.56	1.69
21	Set 3	*Unique_M120_27.8deg*	92.99	0.058	51.66	1.80
22	Set 3	*Unique_M125_27.8deg*	108.70	0.066	76.07	1.43
23	Set 3	*Unique_M130_27.8deg*	102.08	0.059	55.31	1.85
24	Set 3	*Unique_M136_27.8deg*	138.50	0.076	70.67	1.96
25	Set 3	*Unique_M139.5_27.8deg*	136.27	0.073	72.84	1.87
26	Set 3	*Unique_M50_hs0.10_27.8deg*	50.82	0.061	22.13	2.30
27	Set 3	*Unique_M50_hs0.15_27.8deg*	53.93	0.074	25.04	2.15
28	Set 3	*Unique_M50_hs0.20_27.8deg*	52.38	0.078	26.00	2.01
29	Set 3	*Unique_M50_hs0.25_27.8deg*	45.20	0.063	22.06	2.05
30	Set 3	*Unique_M75_hs0.10_27.8deg*	76.76	0.071	34.26	2.24
31	Set 3	*Unique_M75_hs0.15_27.8deg*	53.45	0.047	26.17	2.04
32	Set 3	*Unique_M75_hs0.20_27.8deg*	89.34	0.075	42.62	2.10
33	Set 3	*Unique_M75_hs0.25_27.8deg*	67.84	0.081	28.29	2.40
34	Set 4	*Unique_M50_hs0.10_15.5deg*	13.51	0.050	7.10	1.90
35	Set 4	*Unique_M50_hs0.20_15.5deg*	19.51	0.065	7.76	2.51
36	Set 4	*Unique_M75_hs0.15_15.5deg*	26.77	0.068	10.50	2.55
37	Set 4	*Unique_M100_hs0.15_15.5deg*	28.42	0.059	13.80	2.06
38	Set 4	*Unique_M100bis_hs0.20_15.5deg*	27.01	0.055	13.19	2.05
39	Set 4	*Unique_M125_hs0.20_15.5deg*	43.72	0.078	20.63	2.12
40	Set 4	*Unique_M143_hs0.25_15.5deg*	39.08	0.055	18.44	2.12
41	Set 5	*Unique_M120_27.8deg_no_wedge*	81.92	0.051	43.29	1.89
		Mean values	**64.55**	**0.064**	**33.22**	**2.05**
		Maximum values	**138.50**	**0.081**	**76.07**	**2.55**
		Minimum values	**13.51**	**0.047**	**7.10**	**1.43**
		STD	**33.85**	**0.010**	**20.24**	**0.26**

Appendix D

This appendix contains the graphics of all the 25 complete experiments. Each ISO A3 sheet corresponds to an experiment.

Unique_M50_27.8deg

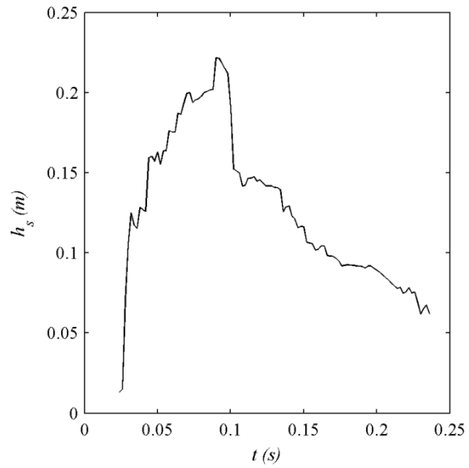

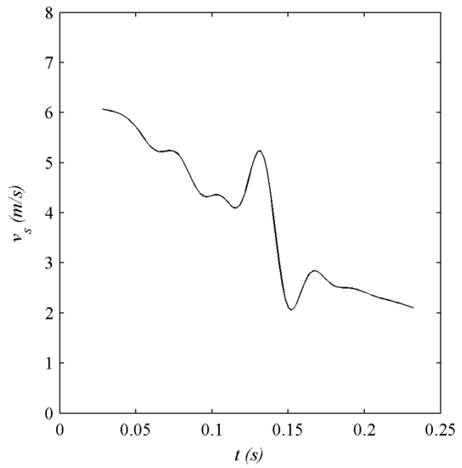

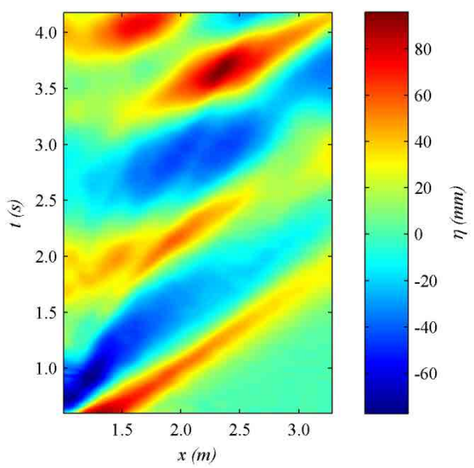

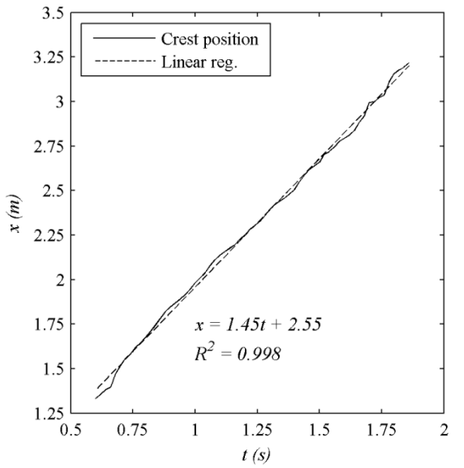

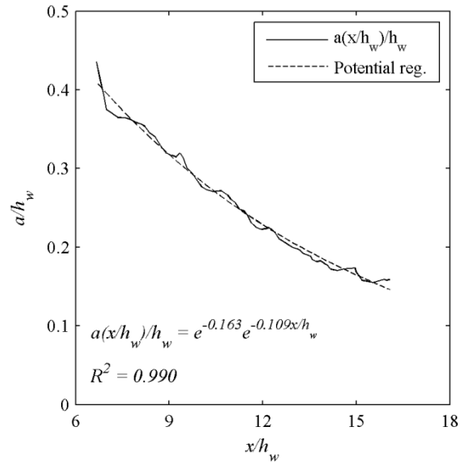

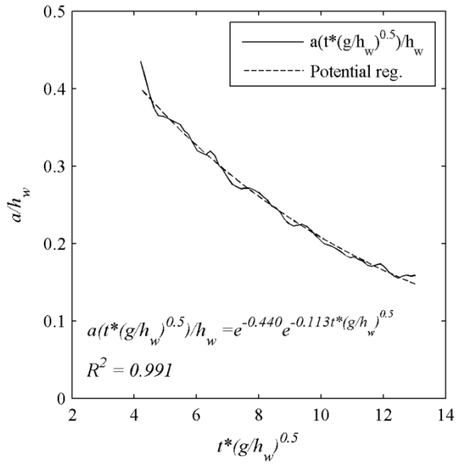

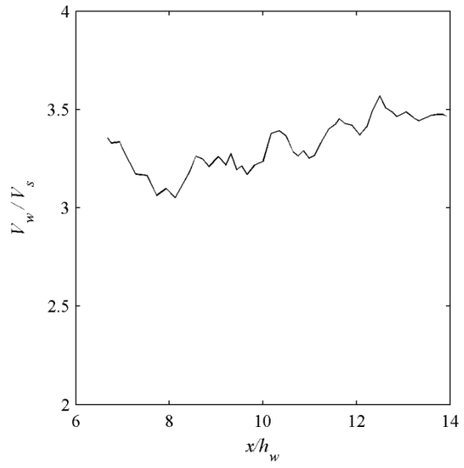

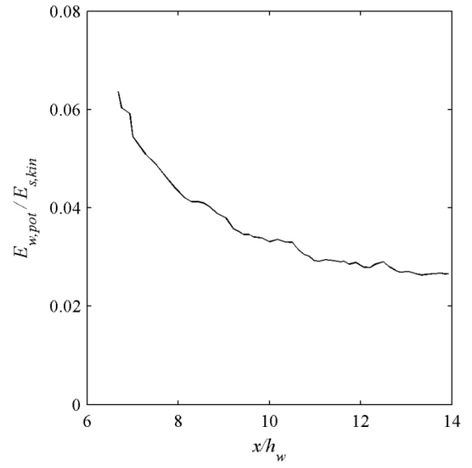

Name of Experiment	Camera HS					Cameras HD						Green Laser
	Shutter opening	Speed (f/s)	Exposition (ms)	Img. size (pixels)	Lens	Img. size	Speed (f/s)	Exposition (s)	Shutter opening	ISO	Lenses	Power (V)
Unique_M50_27.8deg	1.4F	500	2	800x800	Nikon50	A,C) HD (no full)	A,C) 50	C) 1/160, A) 1/120	A,C) 3.5F	C) 400, A) 800	A) Canon 18-55; C) Tamron 17-135	3/5

Red laser positions (m)								Landslide's parameters						Final deposit (m)			
1	1-2	2-3	3-4	4-5	5-6	6	Total	α (°)	m (kg)	$h_{s,ini}$ (m)	$l_{s,ini}$ (m)	w_s (m)	h_w (m)	a_d	b_d	D	$h_{s,fin}$
0.50	0.60	0.60	0.60	0.60	0.60	0.60	410	27.8	50	0.12	1	0.34	0.2	ND	ND	ND	ND

Observations

Camera HS and CameraC same calibration of *Unique_M75_27.8deg*

Unique_M75_27.8deg

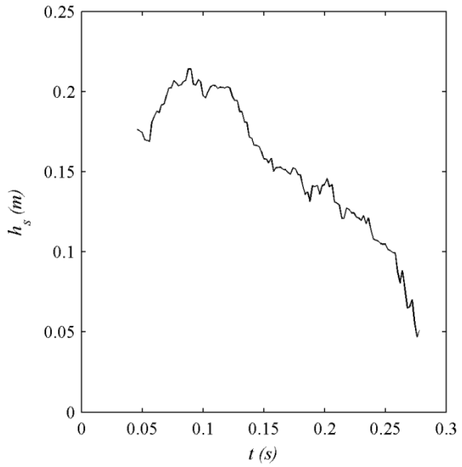

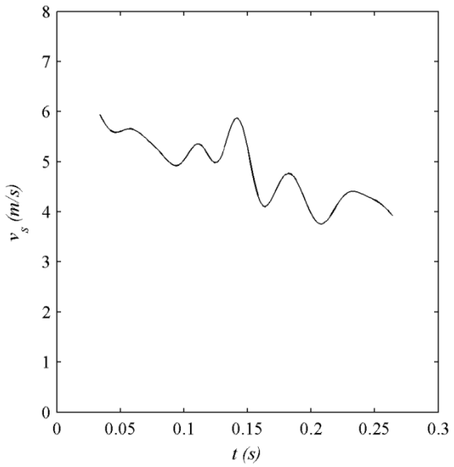

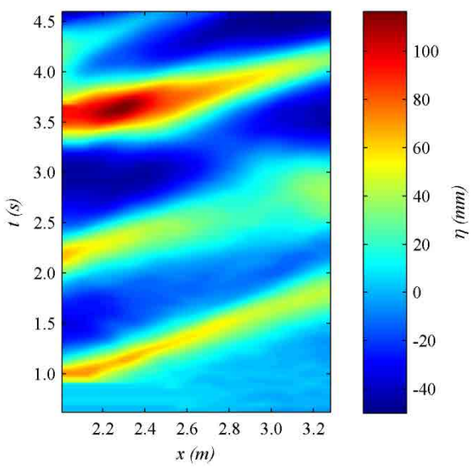

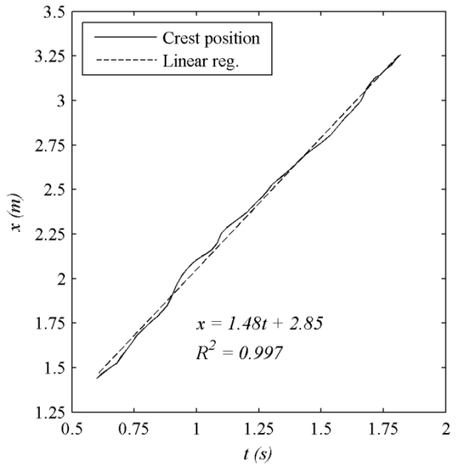

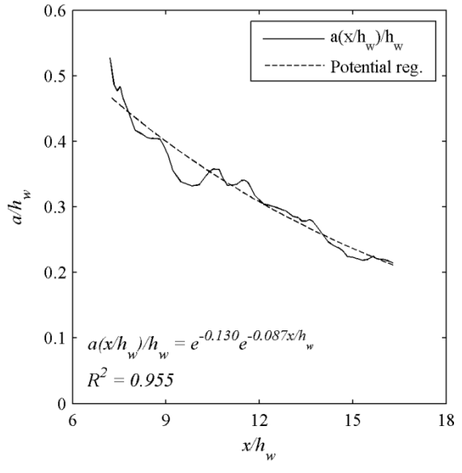

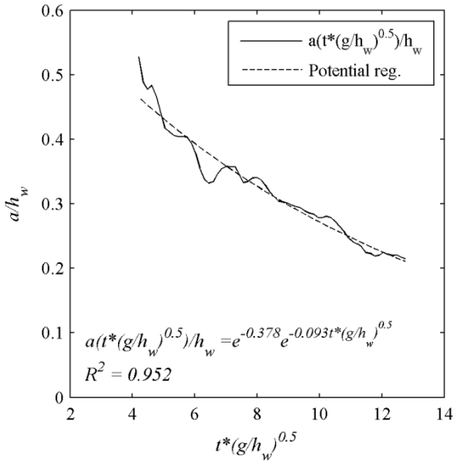

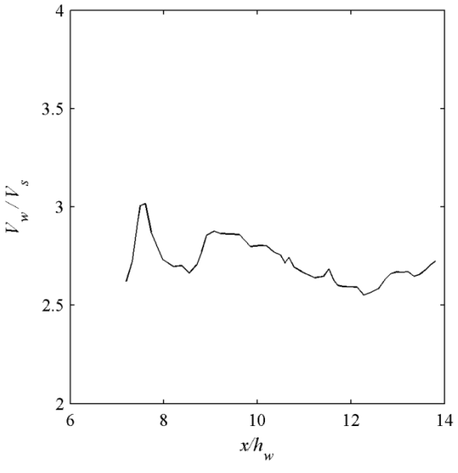

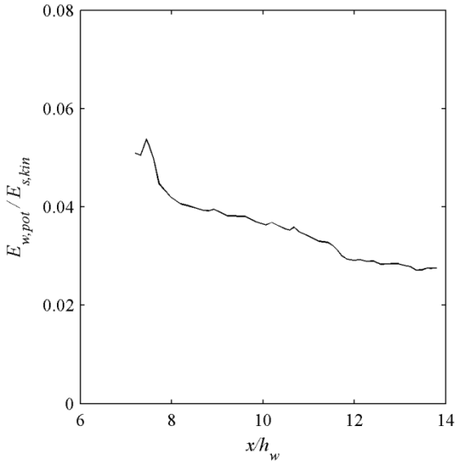

Name of Experiment	Camera HS					Cameras HD						Green Laser
	Shutter opening	Speed (f/s)	Exposition (ms)	Img. size (pixels)	Lens	Img. size	Speed (f/s)	Exposition (s)	Shutter opening	ISO	Lenses	Power (V)
Unique_M75_27.8deg	1.4F	500	2	800x800	Nikon50	A,C) HD (no full)	A,C) 50	C) 1/160, A) 1/120	A,C) 3.5F	C) 400, A) 800	A) Canon 18-55; C) Tamron 17-135	3/5

Red laser positions (m)								Landslide's parameters						Final deposit (m)			
1	1-2	2-3	3-4	4-5	5-6	6	Total	α (°)	m (kg)	$h_{s,ini}$ (m)	$l_{s,ini}$ (m)	w_s (m)	h_w (m)	a_d	b_d	D	$h_{s,fin}$
0.50	0.60	0.60	0.60	0.60	0.60	0.60	410	27.8	75	0.15	1	0.34	0.2	1.4	1.2	2.0	0.10

Observations

Calibrations of Camera HS and CameraC *ad-hoc* for this experiment. Panel of calibration positioned as the *Unique_M100_27.8deg*. CameraA is used to record red lasers. Red lasers calibration is done with the panel stuck to lateral wall: distance from wall and first points column is 10.3cm

Unique_M100_27.8deg

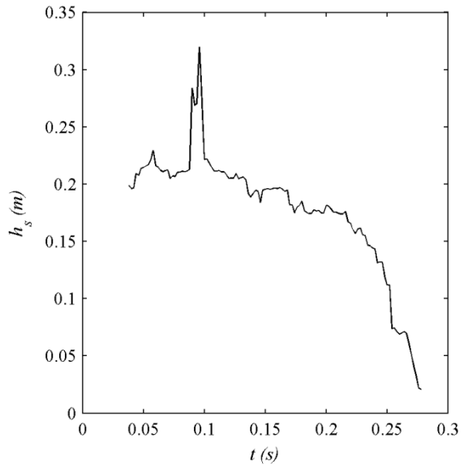

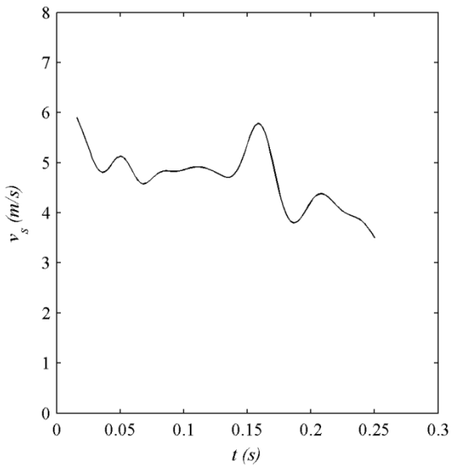

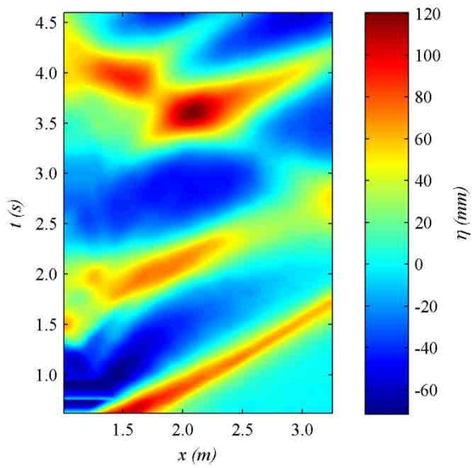

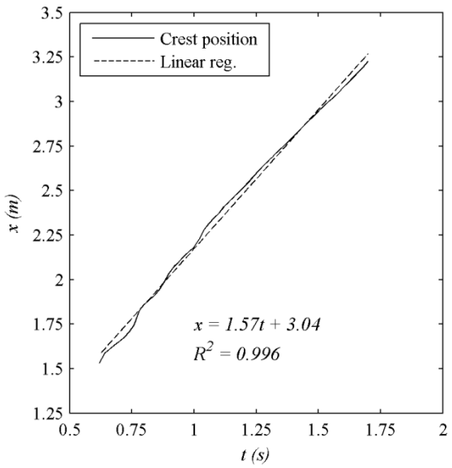

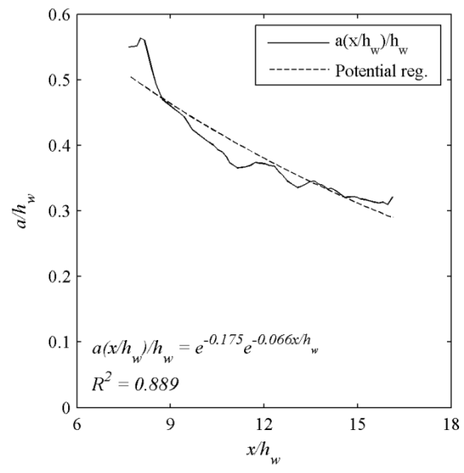

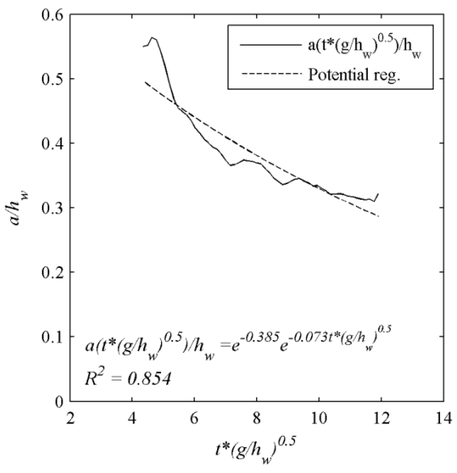

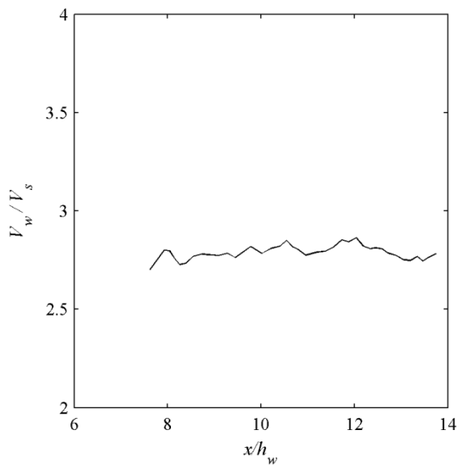

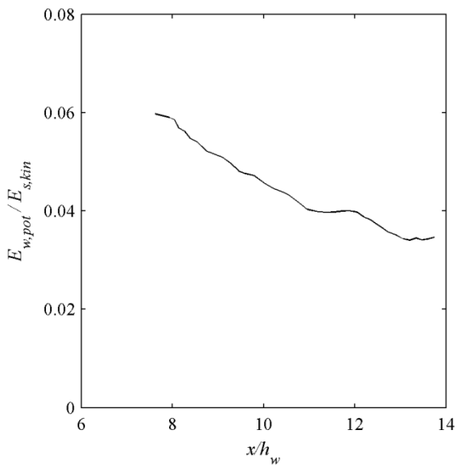

Name of Experiment	**Camera HS**					**Cameras HD**						**Green Laser**
	Shutter opening	**Speed (f/s)**	**Exposition (ms)**	**Img. size (pixels)**	**Lens**	**Img. size**	**Speed (f/s)**	**Exposition (s)**	**Shutter opening**	**ISO**	**Lenses**	**Power (V)**
Unique_M100_27.8deg	1.4F	500	2	800x800	Nikon50	C) HD (no full)	C) 50	C) 1/160	C) 3.5F	C) 400	A) Canon 18-55; C) Tamron 17-135	3/5

Red laser positions (m)								**Landslide's parameters**						**Final deposit (m)**			
1	**1-2**	**2-3**	**3-4**	**4-5**	**5-6**	**6**	**Total**	***α*** **(°)**	***m*** **(kg)**	$h_{s,ini}$ **(m)**	$l_{s,ini}$ **(m)**	w_s **(m)**	h_w **(m)**	a_d	b_d	***D***	$h_{s,fin}$
0.50	0.60	0.60	0.60	0.60	0.60	0.60	410	27.8	100	0.20	1	0.34	0.2	1.55	1.4	ND	0.10

Observations

Calibrations *ad-hoc* for this run. The HS camera calibration grid is posed with the center column over the marked point of the flume. The camera HD (C) is calibrated with the grid center column posed on the center of the tank (4.20/2 m). After erasing a coloumn to calibrate, the horizontal distance of the center of the grid to the intersection wedge/water is 1.93 m. The same calibration is used in *Unique_M136_27.8deg*.

Unique_M110_27.8deg

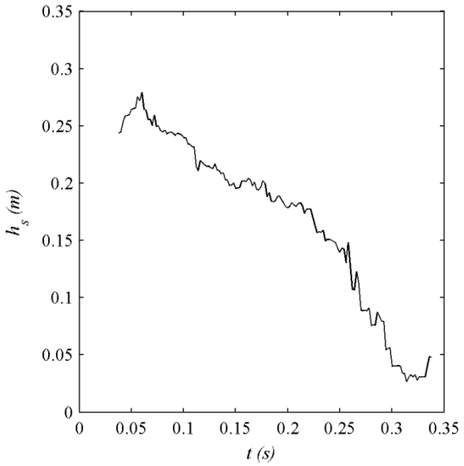

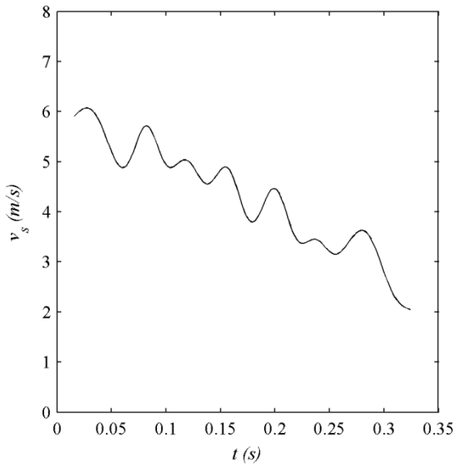

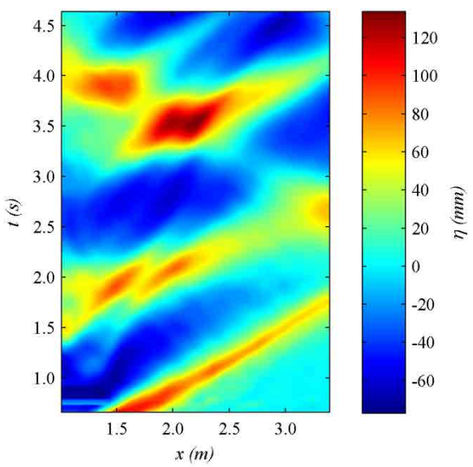

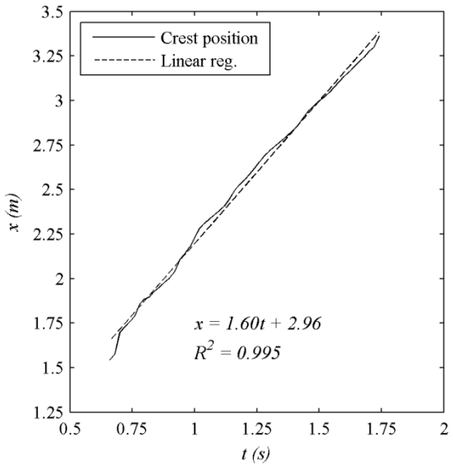

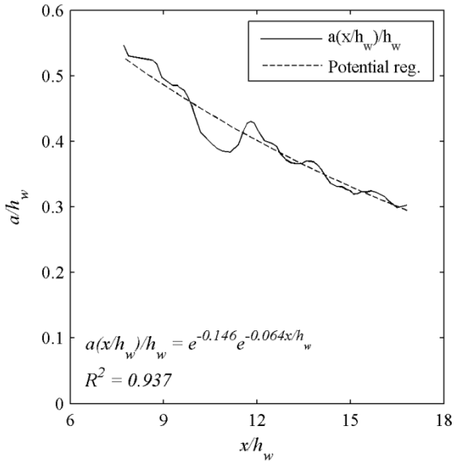

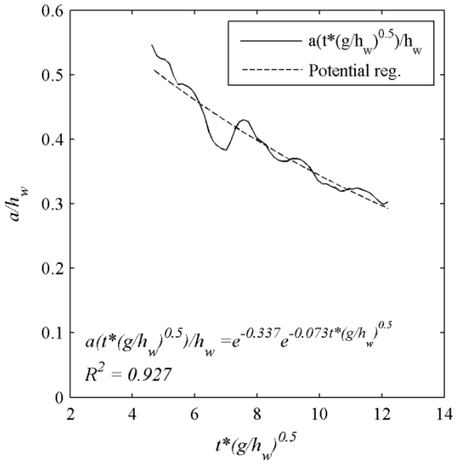

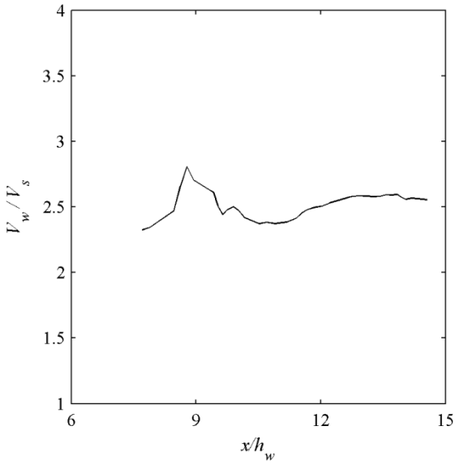

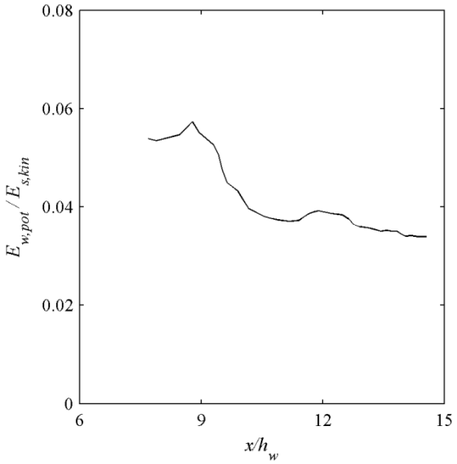

Name of Experiment	Camera HS					Cameras HD						Green Laser
	Shutter opening	Speed (f/s)	Exposition (ms)	Img. size (pixels)	Lens	Img. size	Speed (f/s)	Exposition (s)	Shutter opening	ISO	Lenses	Power (V)
Unique_M110_27.8deg	1.4F	500	2	800x800	Nikon50	B),C) HD; A) 720x576	B,C) 50, A) 25	C) 1/160	C) 4F	C) 400, B) 6400	A) Canon 18-55; C) Tamron 17-135	3/5

Red laser positions (m)								Landslide's parameters						Final deposit (m)			
1	1-2	2-3	3-4	4-5	5-6	6	Total	α (°)	m (kg)	$h_{s,ini}$ (m)	$l_{s,ini}$ (m)	w_s (m)	h_w (m)	a_d	b_d	D	$h_{s,fin}$
0.50	0.60	0.60	0.60	0.60	0.60	0.60	410	27.8	110	0.25	1	0.34	0.2	1.56	1.4	ND	0.12

Observations

Calibrations same of *Unique_M130_27.8deg*.

Unique_M120_27.8deg

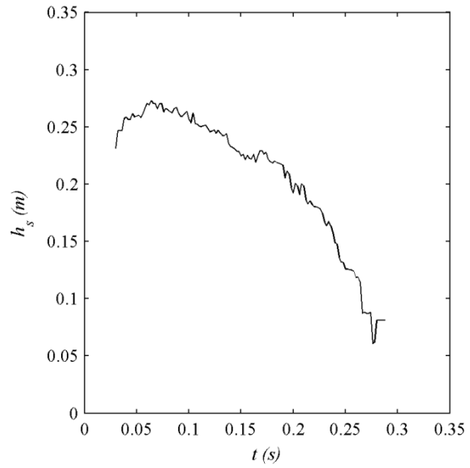

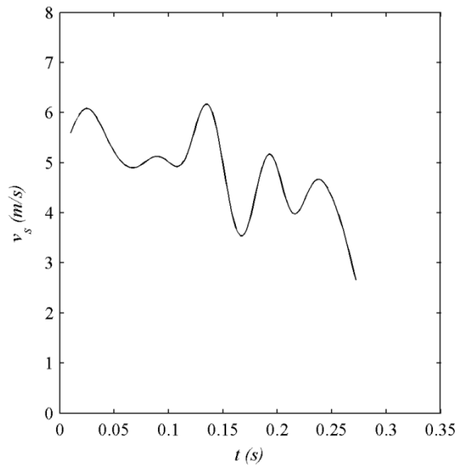

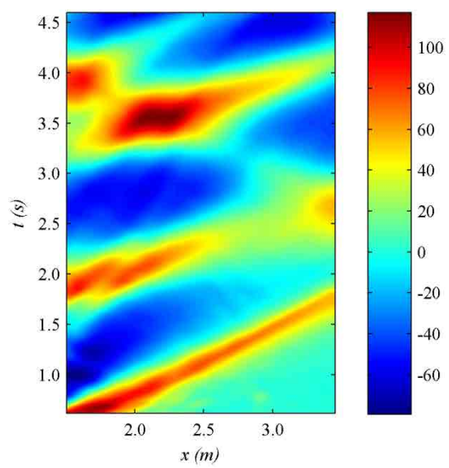

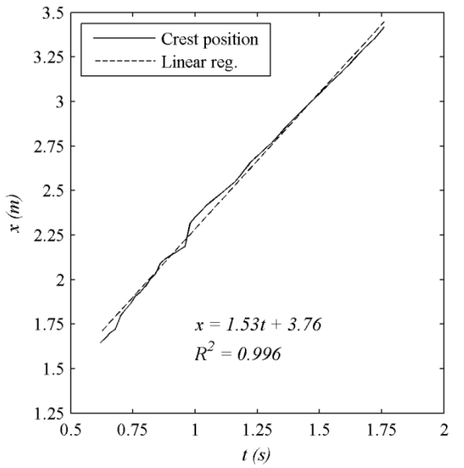

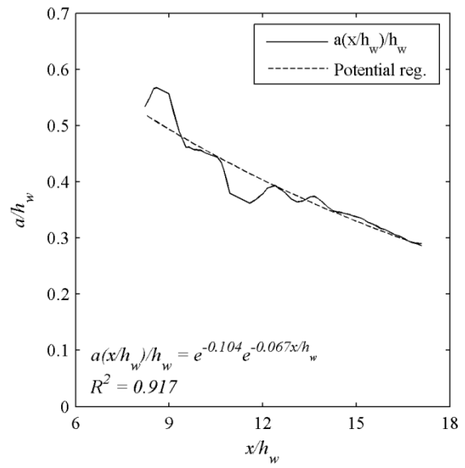

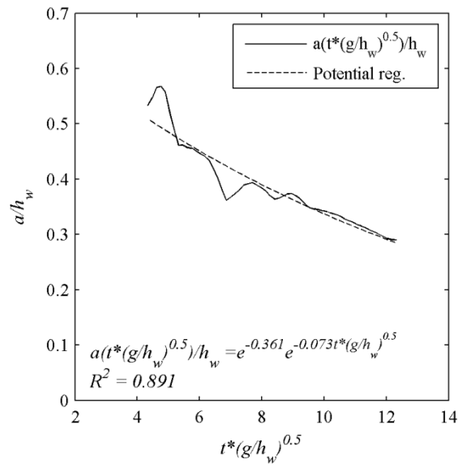

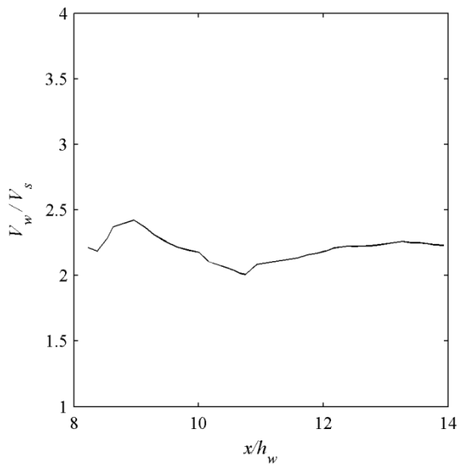

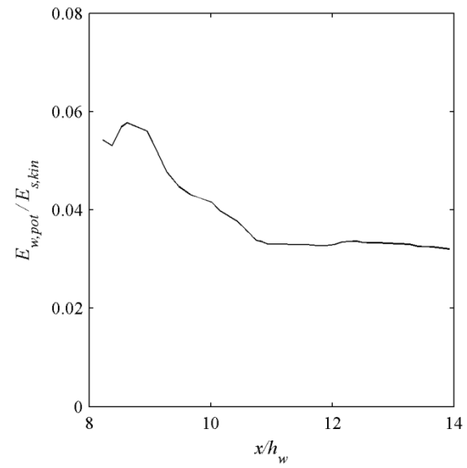

Name of Experiment	Camera HS					Cameras HD						Green Laser
	Shutter opening	Speed (f/s)	Exposition (ms)	Img. size (pixels)	Lens	Img. size	Speed (f/s)	Exposition (s)	Shutter opening	ISO	Lenses	Power (V)
Unique_M120_27.8deg	1.4F	500	2	800x800	Nikon50	C) HD	C) 50	C) 1/160	C) 4F	C) 400	C) Tamron 17-135	3/5

Red laser positions (m)								Landslide's parameters						Final deposit (m)			
1	1-2	2-3	3-4	4-5	5-6	6	Total	α (°)	m (kg)	$h_{s,ini}$ (m)	$l_{s,ini}$ (m)	w_s (m)	h_w (m)	a_d	b_d	D	$h_{s,fin}$
0.50	0.60	0.60	0.60	0.60	0.60	0.60	410	27.8	120	0.25	1	0.34	0.2	1.6	1.5	ND	0.12

Observations

Calibrations *ad-hoc*.

Unique_M125_27.8deg

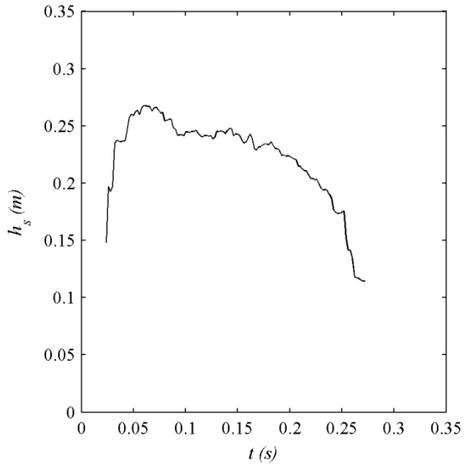

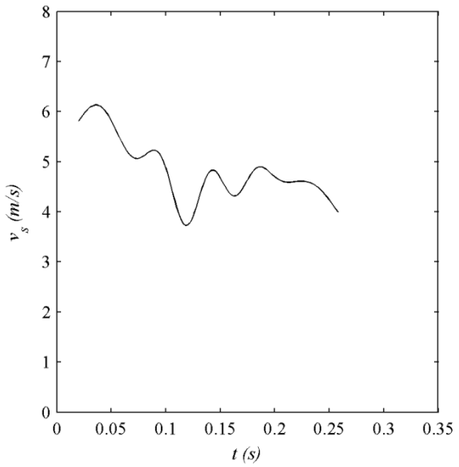

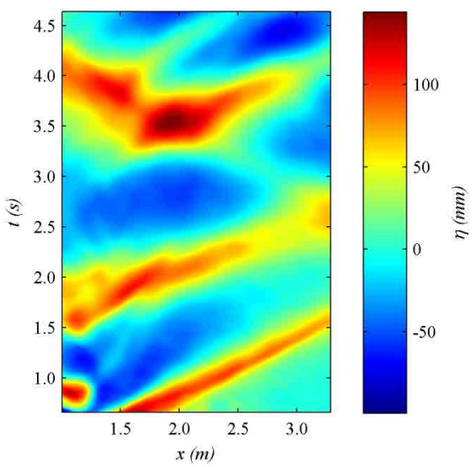

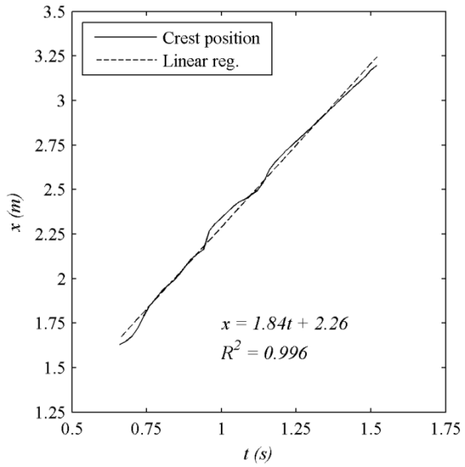

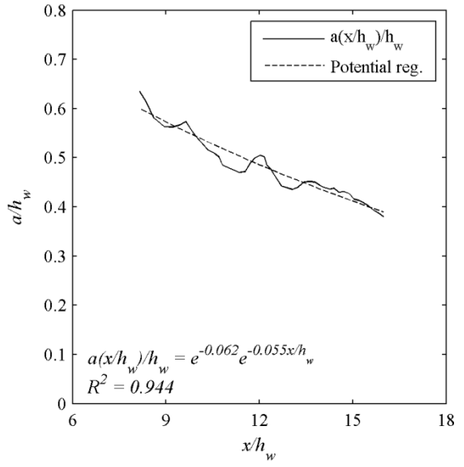

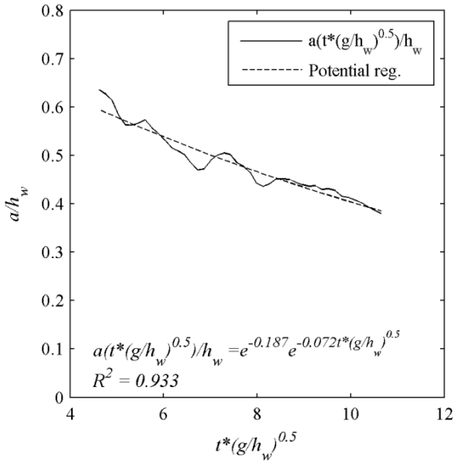

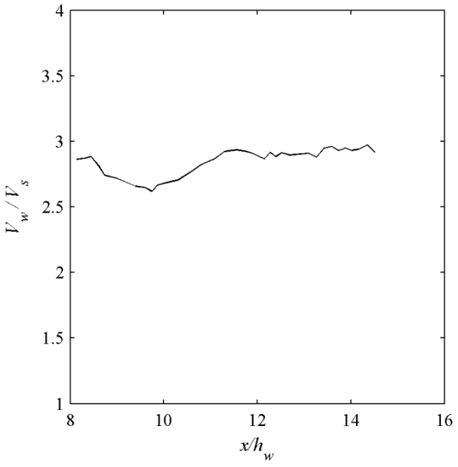

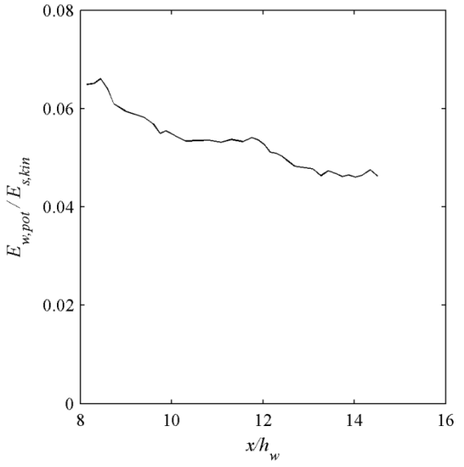

Name of Experiment	Camera HS					Cameras HD						Green Laser
	Shutter opening	Speed (f/s)	Exposition (ms)	Img. size (pixels)	Lens	Img. size	Speed (f/s)	Exposition (s)	Shutter opening	ISO	Lenses	Power (V)
Unique_M125_27.8deg	1.4F	500	2	800x800	Nikon50	C) HD	C) 50	C) 1/160	C) 4F	C) 400	C) Tamron 17-135	3/5

Red laser positions (m)								Landslide's parameters						Final deposit (m)			
1	1-2	2-3	3-4	4-5	5-6	6	Total	α (°)	m (kg)	$h_{s,ini}$ (m)	$l_{s,ini}$ (m)	w_s (m)	h_w (m)	a_d	b_d	D	$h_{s,fin}$
0.50	0.60	0.60	0.60	0.60	0.60	0.60	410	27.8	125	0.25	1	0.34	0.2	1.7	1.5	2.3	0.12

Observations

Calibrations same of *Unique_M75_27.8deg*

Unique_M130_27.8deg

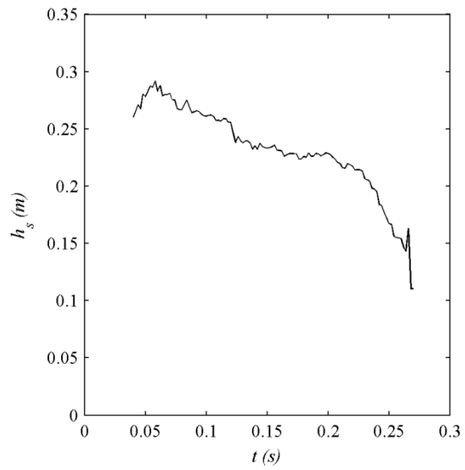

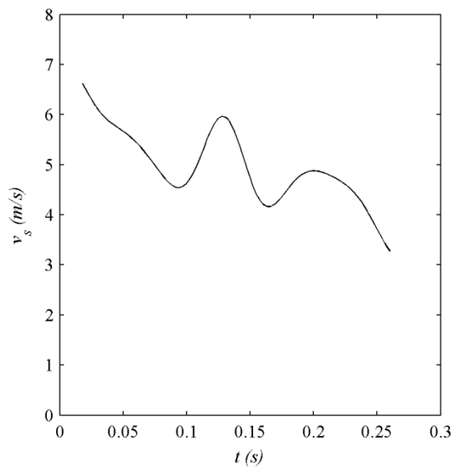

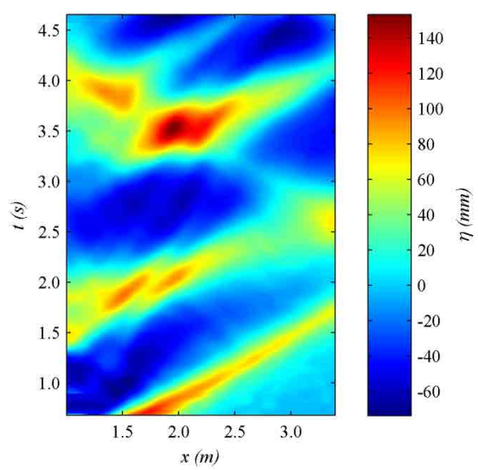

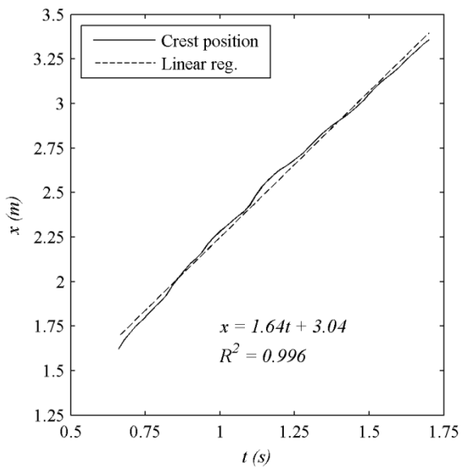

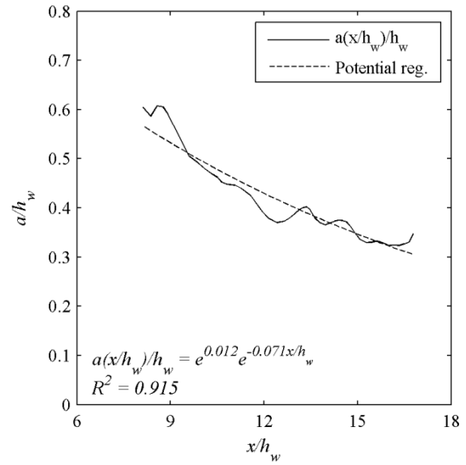

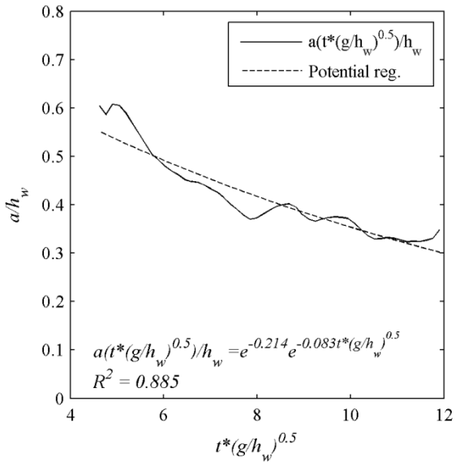

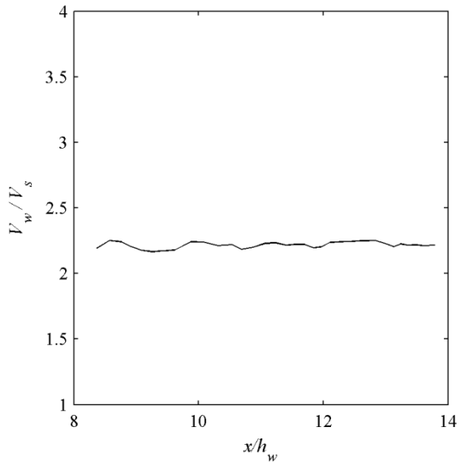

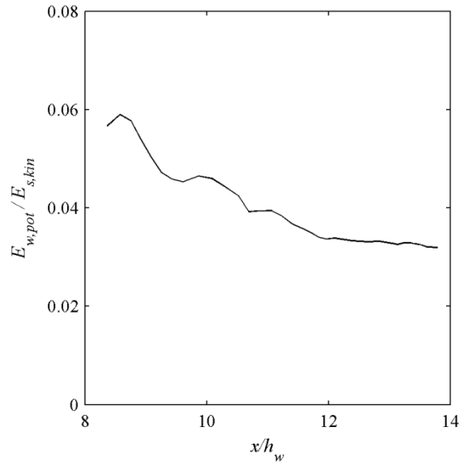

Name of Experiment	Camera HS					Cameras HD						Green Laser
	Shutter opening	Speed (f/s)	Exposition (ms)	Img. size (pixels)	Lens	Img. size	Speed (f/s)	Exposition (s)	Shutter opening	ISO	Lenses	Power (V)
Unique_M130_27.8deg	1.4F	500	2	800x800	Nikon50	C) HD	C) 50	C) 1/160	C) 4F	C) 400	C) Tamron 17-135	3/5

Red laser positions (m)								Landslide's parameters						Final deposit (m)			
1	1-2	2-3	3-4	4-5	5-6	6	Total	α (°)	m (kg)	$h_{s,ini}$ (m)	$l_{s,ini}$ (m)	w_s (m)	h_w (m)	a_d	b_d	D	$h_{s,fin}$
0.50	0.60	0.60	0.60	0.60	0.60	0.60	410	27.8	130	0.25	1	0.34	0.2	ND	ND	ND	ND

Observations

Calibrations *ad-hoc* for this run.

Unique_M136_27.8deg

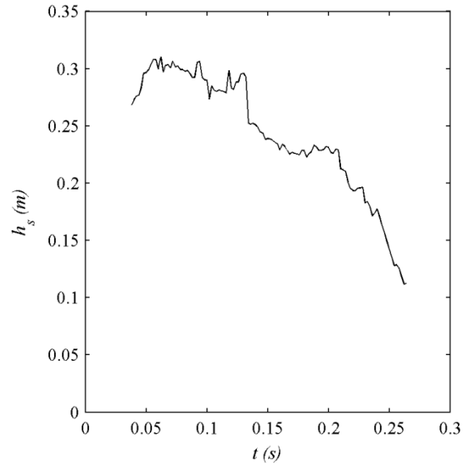

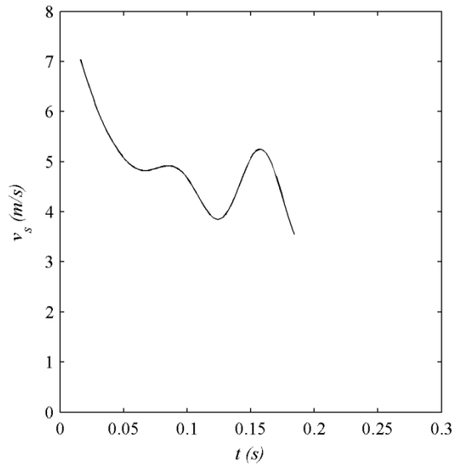

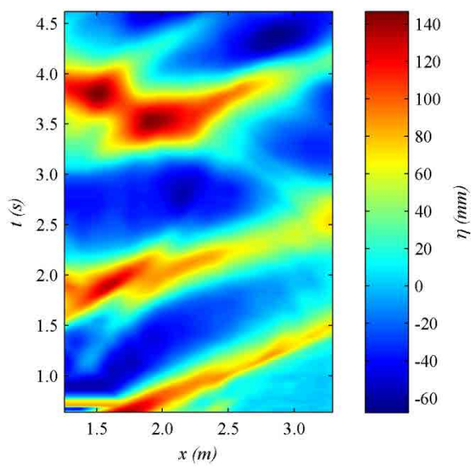

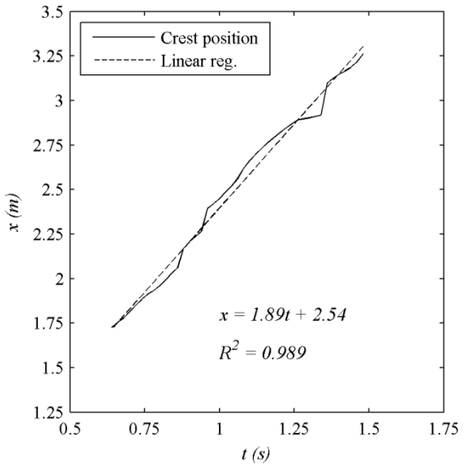

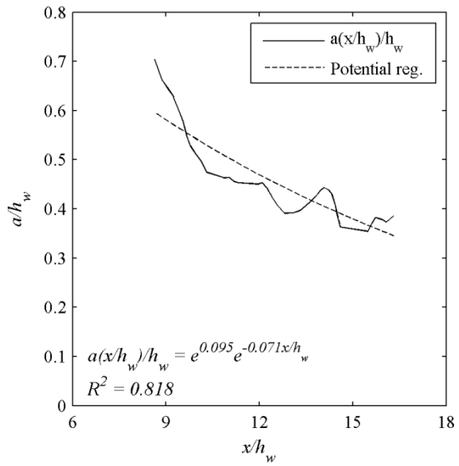

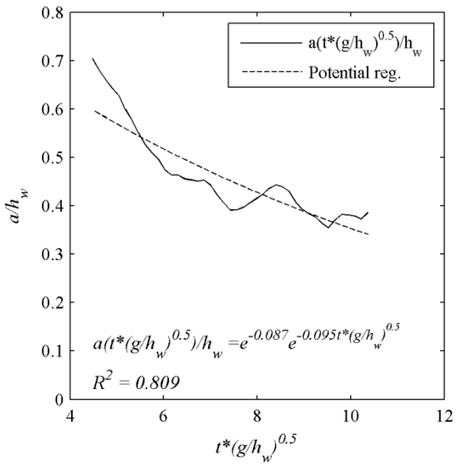

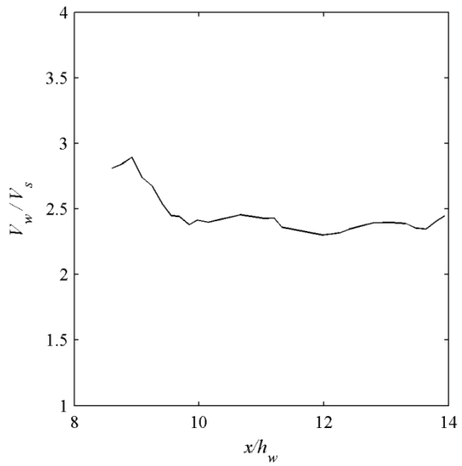

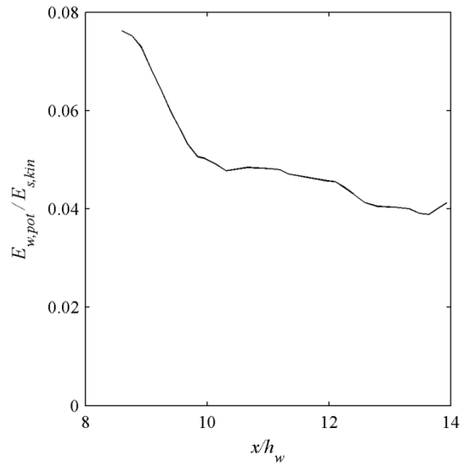

Name of Experiment	Camera HS					Cameras HD						Green Laser
	Shutter opening	Speed (f/s)	Exposition (ms)	Img. size (pixels)	Lens	Img. size	Speed (f/s)	Exposition (s)	Shutter opening	ISO	Lenses	Power (V)
Unique_M136_27.8deg	1.4F	500	2	800x800	Nikon50	C) HD	C) 50	C) 1/160	C) 4F	C) 800	C) Tamron 17-135	3/5

Red laser positions (m)								Landslide's parameters						Final deposit (m)			
1	1-2	2-3	3-4	4-5	5-6	6	Total	α (°)	m (kg)	$h_{s,ini}$ (m)	$l_{s,ini}$ (m)	w_s (m)	h_w (m)	a_d	b_d	D	$h_{s,fin}$
0.50	0.60	0.60	0.60	0.60	0.60	0.60	410	27.8	136	0.25	1	0.34	0.2	1.7	1.5	ND	0.10

Observations

First experiments with DragonLasers Green Laser. The calibr. grid of HS camera is settled with the center column over the marked point of intersection wedge/wáter. Camera HD is calibrated with the center of the panel (erasing the more left column) at the center of the tank (mark at 4.20/2m).The *x* distance from center of calibr. grid and intersection water/wedge is 1.93m. The image of calibration of HS cam is cropped at 800x800 pixels anchored at NW corner. While the sequence of images is cropped at 800x1024 anchored at NW corner (this was an error on setting AOI/ROI)

Unique_M139.5_27.8deg

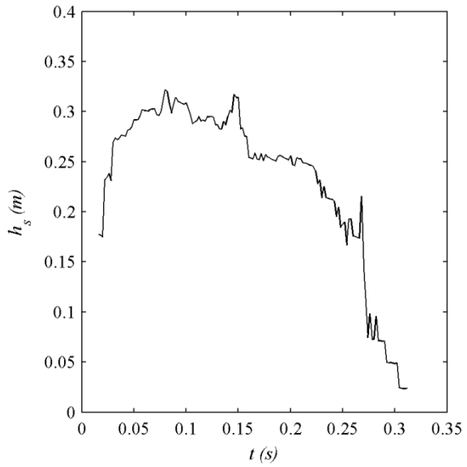

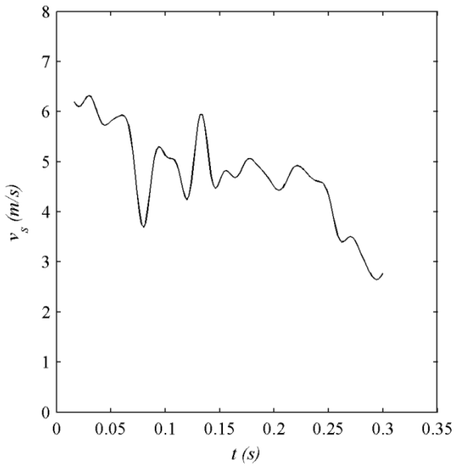

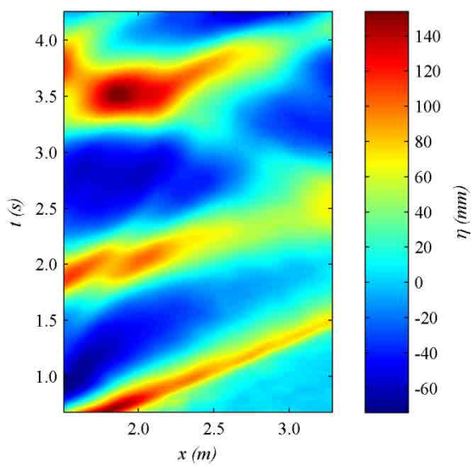

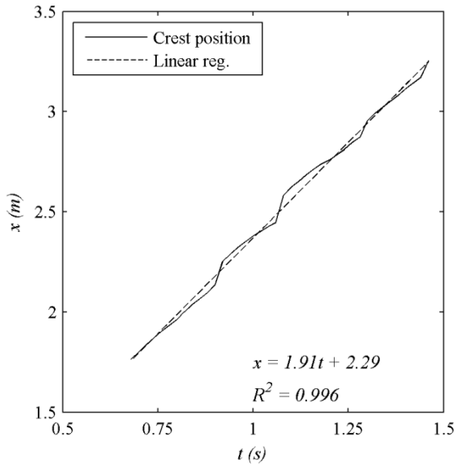

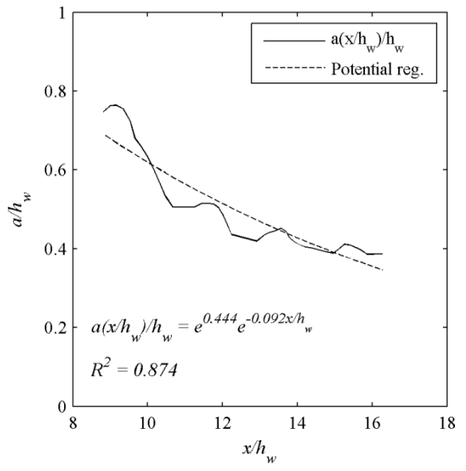

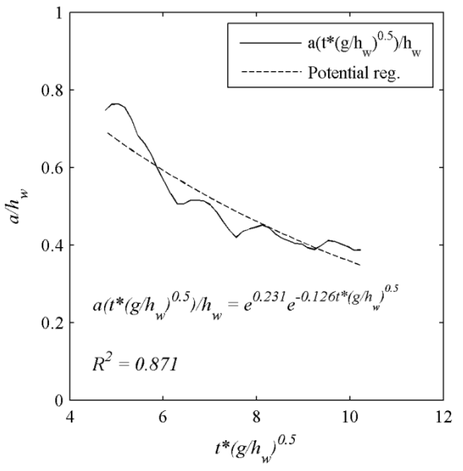

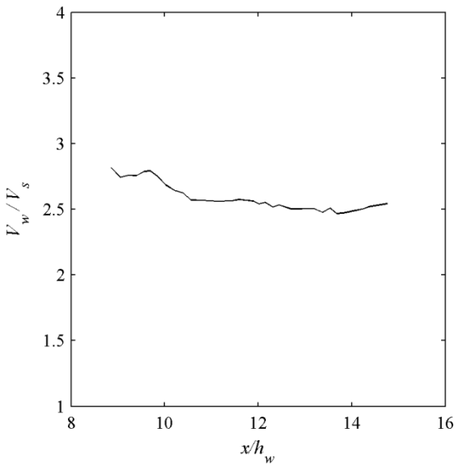

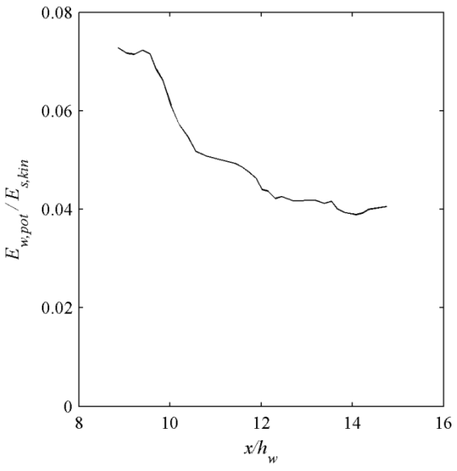

Name of Experiment	Camera HS					Cameras HD						Green Laser
	Shutter opening	Speed (f/s)	Exposition (ms)	Img. size (pixels)	Lens	Img. size	Speed (f/s)	Exposition (s)	Shutter opening	ISO	Lenses	Power (V)
Unique_M139.5_27.8deg	1.4F	500	2	800x800	Nikon50	A,C) HD (no full)	A,C) 50	C) 1/160, A) 1/120	A,C) 3.5F	C) 400, A) 800	A) Canon 18-55; C) Tamron 17-135	3/5

Red laser positions (m)								Landslide's parameters						Final deposit (m)			
1	1-2	2-3	3-4	4-5	5-6	6	Total	α (°)	m (kg)	$h_{s,ini}$ (m)	$l_{s,ini}$ (m)	w_s (m)	h_w (m)	a_d	b_d	D	$h_{s,fin}$
0.50	0.60	0.60	0.60	0.60	0.60	0.60	410	27.8	139.5	0.25	1	0.34	0.2	1.70	1.50	2.30	0.10

Observations

Camera HS and CameraC same calibration of *Unique_M75_27.8deg*. CameraA is used to record red lasers. Red lasers calibration is done with the panel stuck to lateral wall: distance from wall and first points column is 10.3cm

Unique_M50_hs0.10_27.8deg

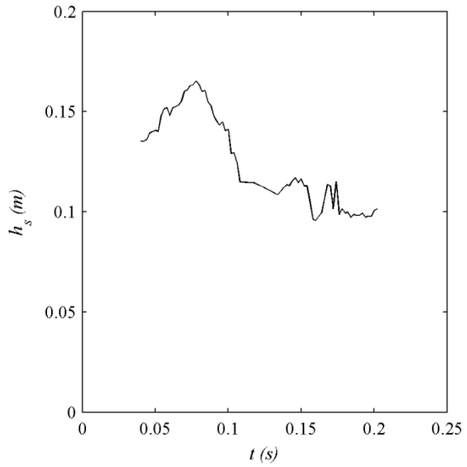

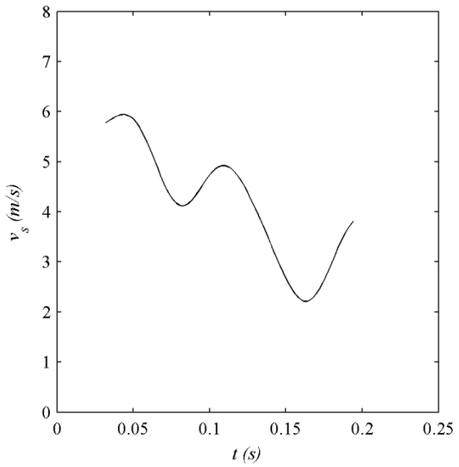

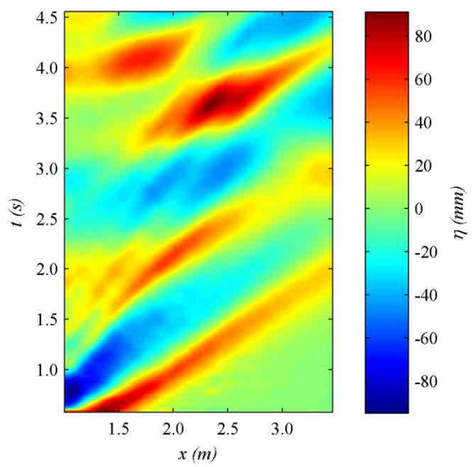

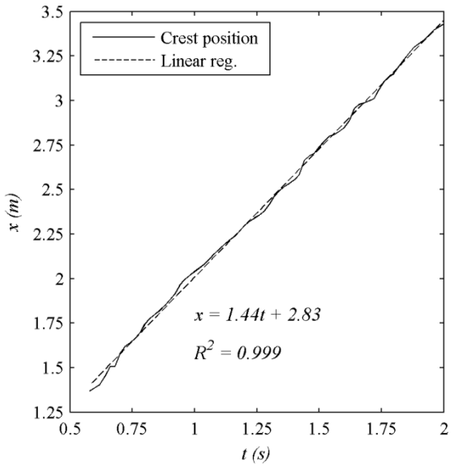

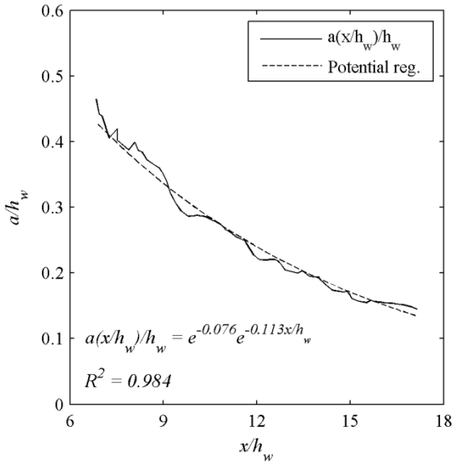

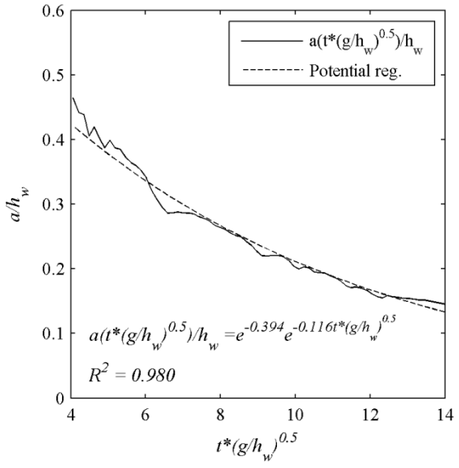

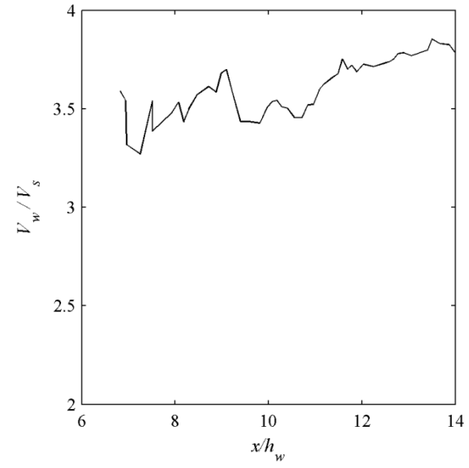

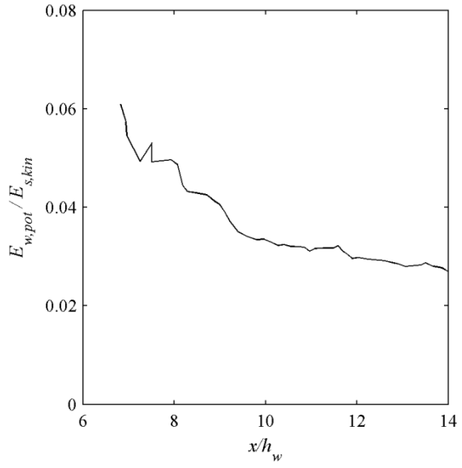

Name of Experiment	Camera HS					Cameras HD						Green Laser
	Shutter opening	Speed (f/s)	Exposition (ms)	Img. size (pixels)	Lens	Img. size	Speed (f/s)	Exposition (s)	Shutter opening	ISO	Lenses	Power (V)
Unique_M50_hs0.10_27.8deg	1.4F	500	2	800x800	Nikon50	C) HD	C) 50	C) 1/160	C) 4F	C) 400	C) Tamron 17-135	3/5

Red laser positions (m)								Landslide's parameters						Final deposit (m)			
1	1-2	2-3	3-4	4-5	5-6	6	Total	α (°)	m (kg)	$h_{s,ini}$ (m)	$l_{s,ini}$ (m)	w_s (m)	h_w (m)	a_d	b_d	D	$h_{s,fin}$
0.50	0.60	0.60	0.60	0.60	0.60	0.60	410	27.8	50	0.12	0.85	0.34	0.2	1.2	1.05	ND	0.10

Observations

Calibration of HS is *ad-hoc* for this run. Calibration HD same as *Unique_M120_27.8deg*.

Unique_M50_hs0.15_27.8deg

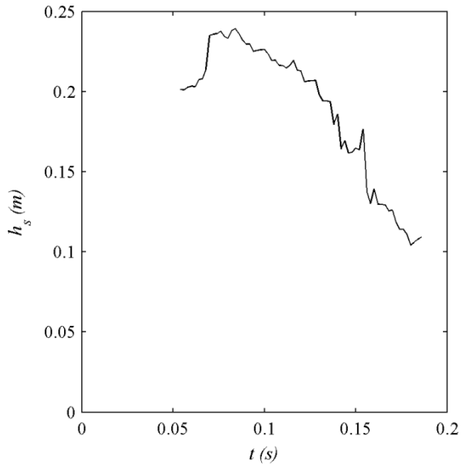

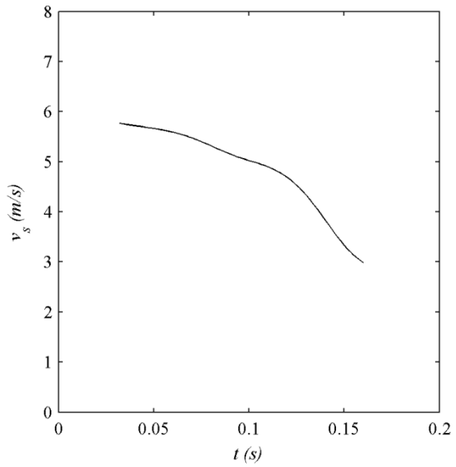

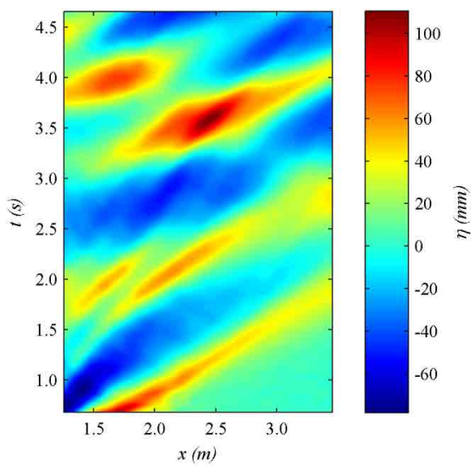

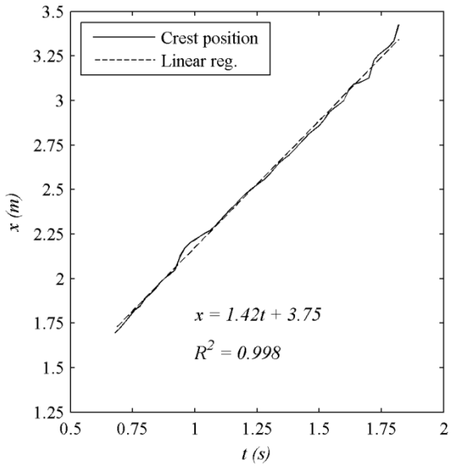

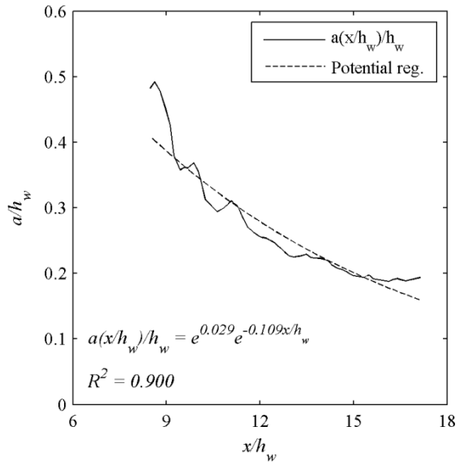

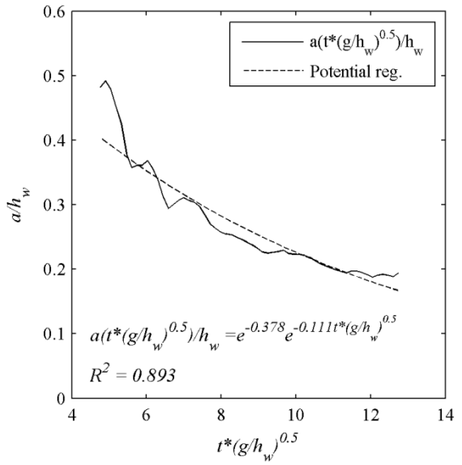

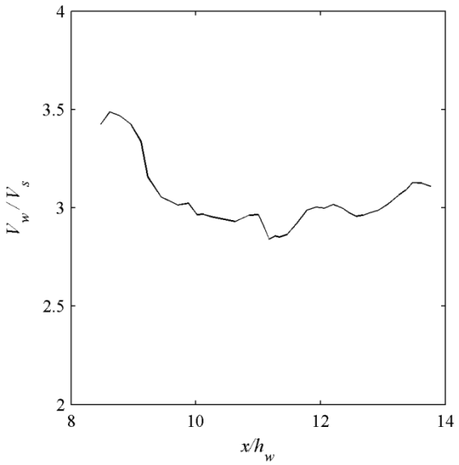

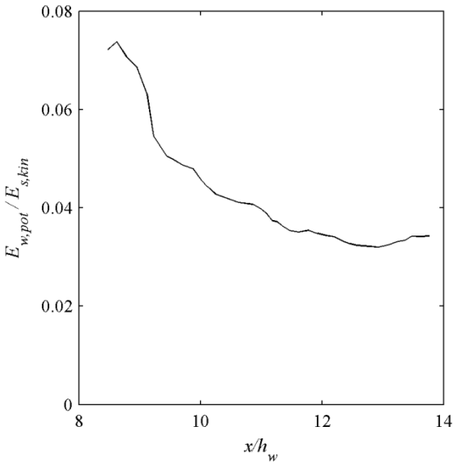

Name of Experiment	**Camera HS**					**Cameras HD**						**Green Laser**
	Shutter opening	**Speed (f/s)**	**Exposition (ms)**	**Img. size (pixels)**	**Lens**	**Img. size**	**Speed (f/s)**	**Exposition (s)**	**Shutter opening**	**ISO**	**Lenses**	**Power (V)**
Unique_M50_hs0.15_27.8deg	1.4F	500	2	800x800	Nikon50	C) HD	C) 50	C) 1/160	C) 4F	C) 400	C) Tamron 17-135	3/5

Red laser positions (m)								**Landslide's parameters**						**Final deposit (m)**			
1	**1-2**	**2-3**	**3-4**	**4-5**	**5-6**	**6**	**Total**	***α*** **(°)**	***m*** **(kg)**	$h_{s,ini}$ **(m)**	$l_{s,ini}$ **(m)**	w_s **(m)**	h_w **(m)**	a_d	b_d	***D***	$h_{s,fin}$
0.50	0.60	0.60	0.60	0.60	0.60	0.60	410	27.8	50	0.12	0.55	0.34	0.2	ND	ND	ND	ND

Observations

Calibration of HS is *ad-hoc* for this run. Calibration HD same as *Unique_M120_27.8deg*.

Unique_M50_hs0.20_27.8deg

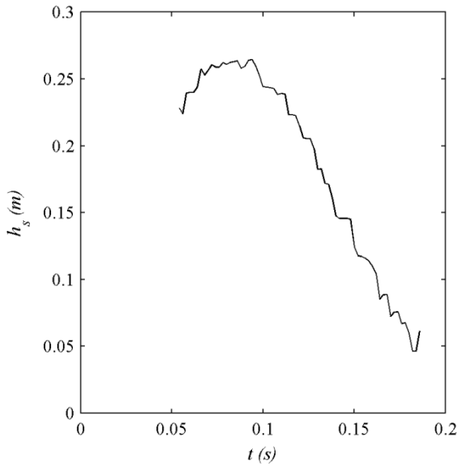

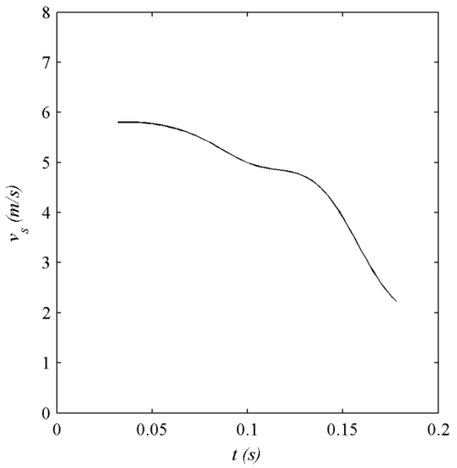

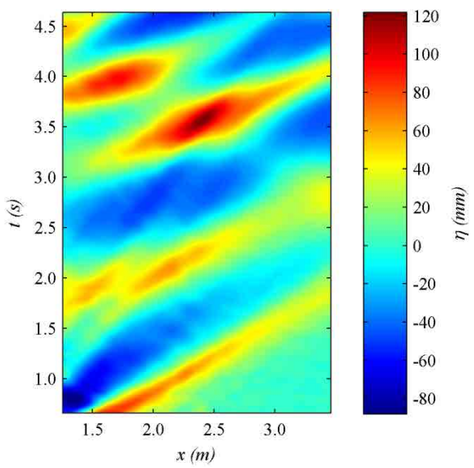

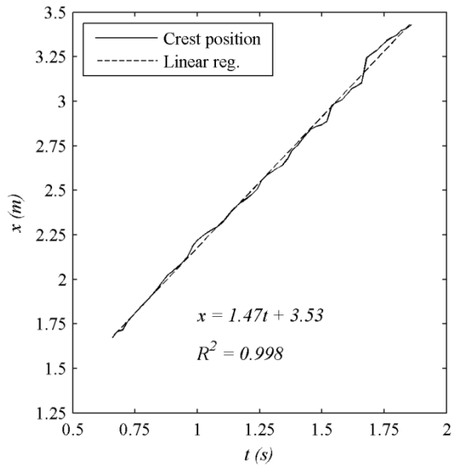

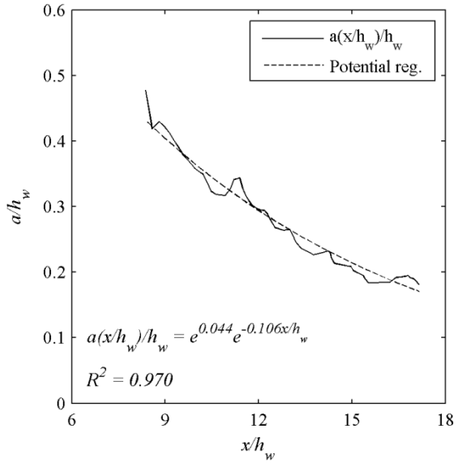

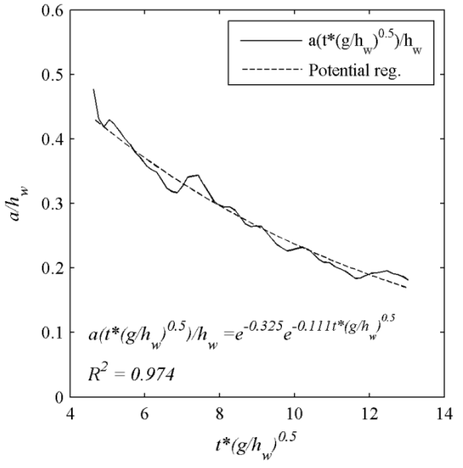

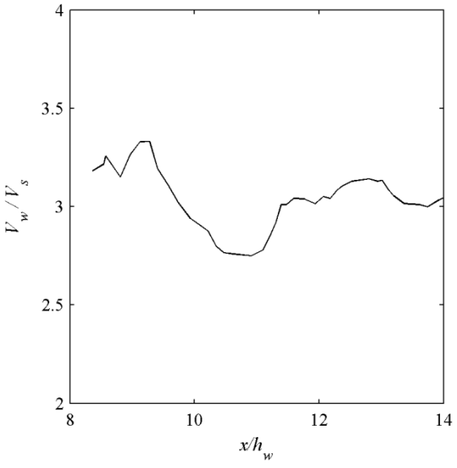

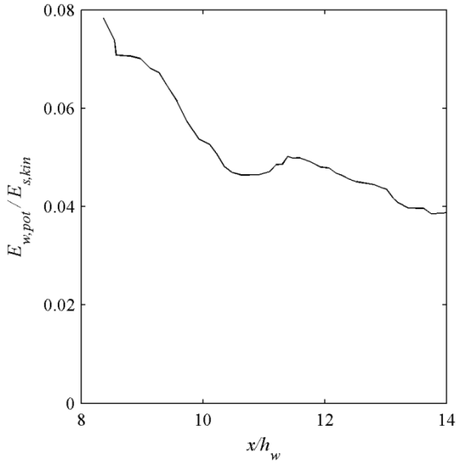

Name of Experiment	Camera HS					Cameras HD						Green Laser
	Shutter opening	Speed (f/s)	Exposition (ms)	Img. size (pixels)	Lens	Img. size	Speed (f/s)	Exposition (s)	Shutter opening	ISO	Lenses	Power (V)
Unique_M50_hs0.20_27.8deg	1.4F	500	2	800x800	Nikon50	C) HD	C) 50	C) 1/160	C) 4F	C) 400	C) Tamron 17-135	3/5

Red laser positions (m)								Landslide's parameters						Final deposit (m)			
1	1-2	2-3	3-4	4-5	5-6	6	Total	α (°)	m (kg)	$h_{s,ini}$ (m)	$l_{s,ini}$ (m)	w_s (m)	h_w (m)	a_d	b_d	D	$h_{s,fin}$
0.50	0.60	0.60	0.60	0.60	0.60	0.60	410	27.8	50	0.20	0.50	0.34	0.2	ND	ND	ND	ND

Observations

Calibration of HS same as *Unique_M50_hs0.15_27.8deg*. Calibration HD same as *Unique_M120_27.8deg*.

Unique_M50_hs0.25_27.8deg

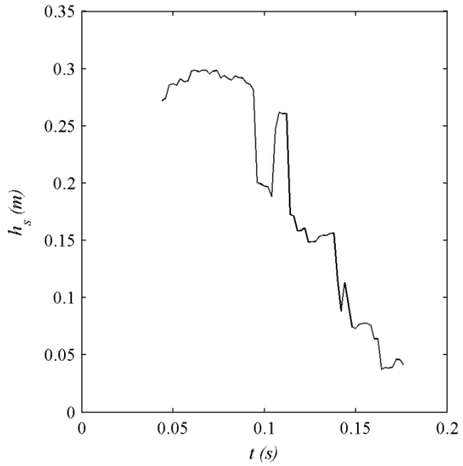

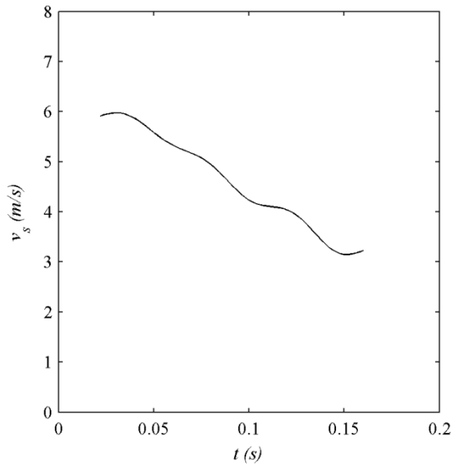

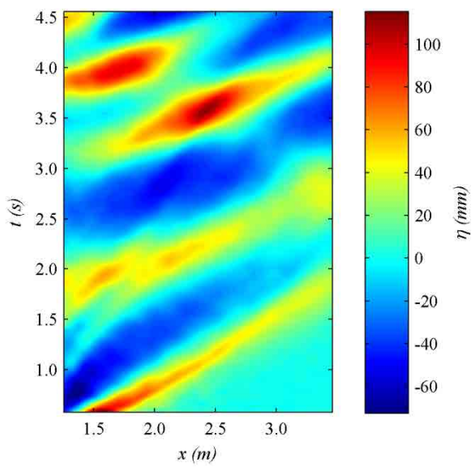

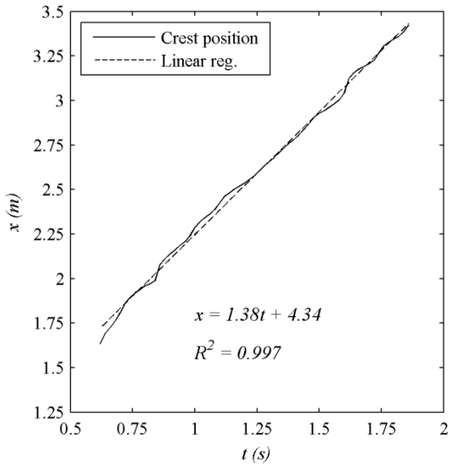

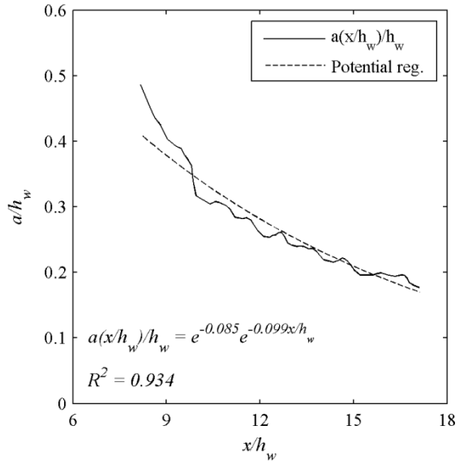

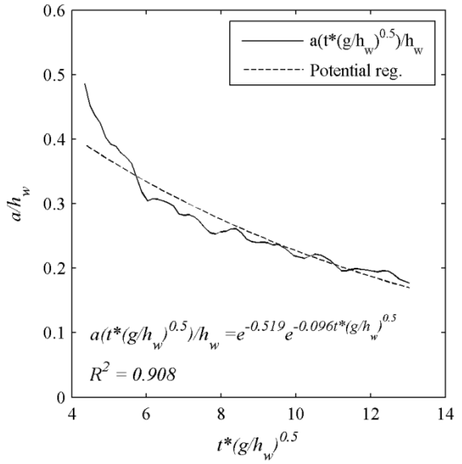

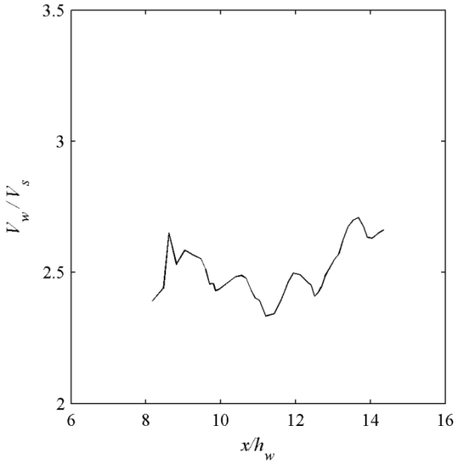

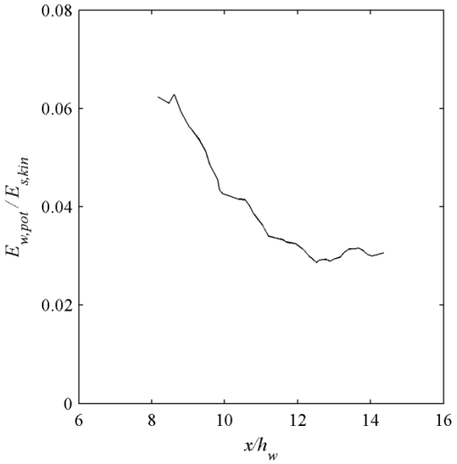

Name of Experiment	**Camera HS**					**Cameras HD**						**Green Laser**
	Shutter opening	**Speed (f/s)**	**Exposition (ms)**	**Img. size (pixels)**	**Lens**	**Img. size**	**Speed (f/s)**	**Exposition (s)**	**Shutter opening**	**ISO**	**Lenses**	**Power (V)**
Unique_M50_hs0.25_27.8deg	1.4F	500	2	800x800	Nikon50	C) HD	C) 50	C) 1/160	C) 4F	C) 400	C) Tamron 17-135	3/5

Red laser positions (m)								**Landslide's parameters**						**Final deposit (m)**			
1	**1-2**	**2-3**	**3-4**	**4-5**	**5-6**	**6**	**Total**	***α*** **(°)**	***m*** **(kg)**	$h_{s,ini}$ **(m)**	$l_{s,ini}$ **(m)**	w_s **(m)**	h_w **(m)**	a_d	b_d	***D***	$h_{s,fin}$
0.50	0.60	0.60	0.60	0.60	0.60	0.60	410	27.8	50	0.25	0.45	0.34	0.2	ND	ND	ND	ND

Observations

Calibration of HS same as *Unique_M50_hs0.15_27.8deg*. Calibration HD same as *Unique_M120_27.8deg*.

Unique_M75_hs0.10_27.8deg

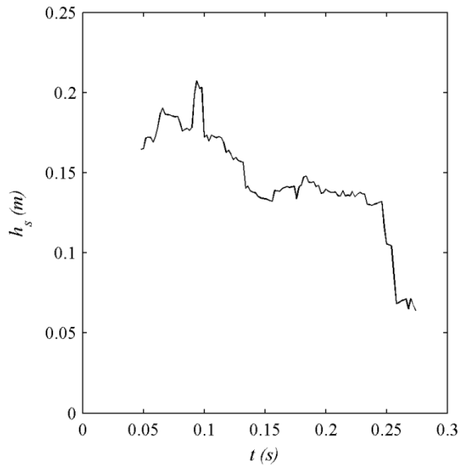

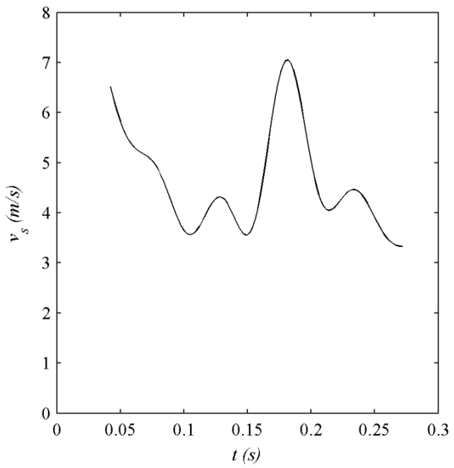

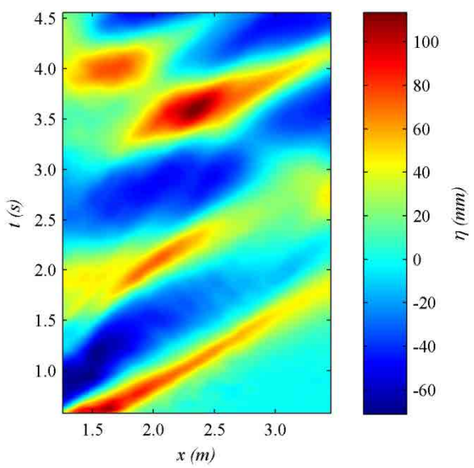

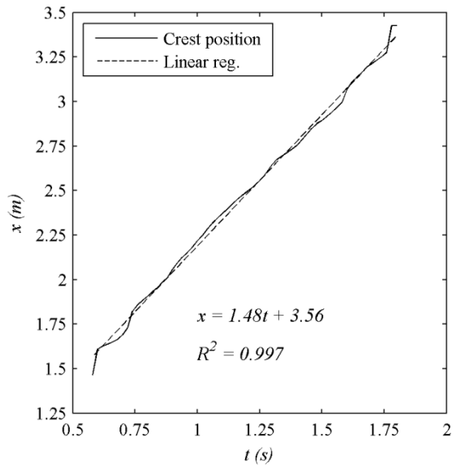

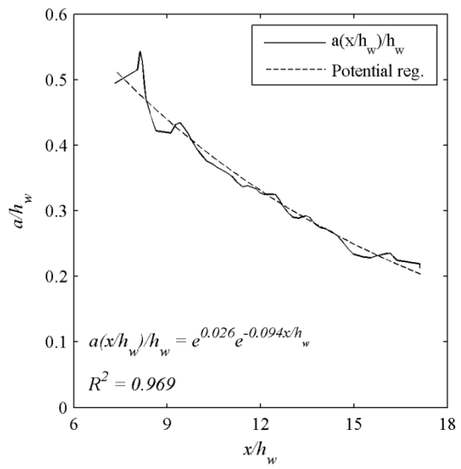

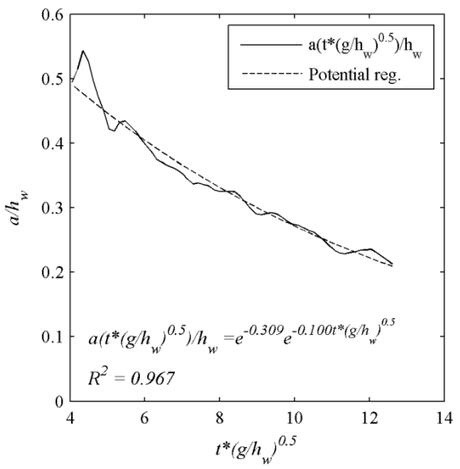

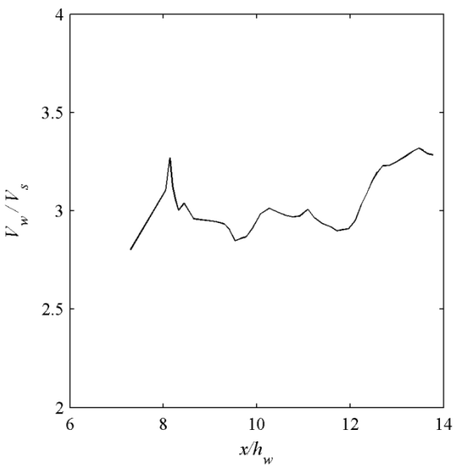

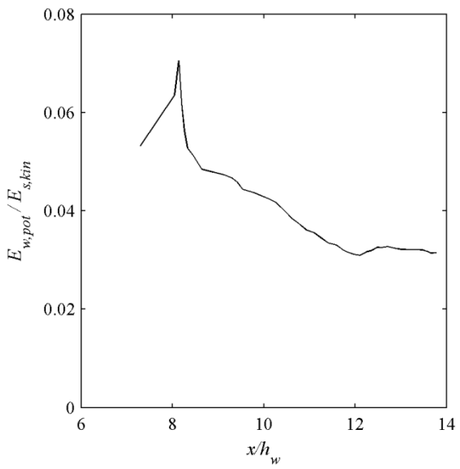

Name of Experiment	Camera HS					Cameras HD						Green Laser
	Shutter opening	Speed (f/s)	Exposition (ms)	Img. size (pixels)	Lens	Img. size	Speed (f/s)	Exposition (s)	Shutter opening	ISO	Lenses	Power (V)
Unique_M75_hs0.10_27.8deg	1.4F	500	2	800x800	Nikon50	C) HD	C) 50	C) 1/160	C) 4F	C) 400	C) Tamron 17-135	3/5

Red laser positions (m)								Landslide's parameters						Final deposit (m)			
1	1-2	2-3	3-4	4-5	5-6	6	Total	α (°)	m (kg)	$h_{s,ini}$ (m)	$l_{s,ini}$ (m)	w_s (m)	h_w (m)	a_d	b_d	D	$h_{s,fin}$
0.50	0.60	0.60	0.60	0.60	0.60	0.60	410	27.8	75	0.10	1	0.34	0.2	ND	ND	ND	ND

Observations

Calibration of HS same as *Unique_M50_hs0.15_27.8deg*. Calibration HD same as *Unique_M120_27.8deg*.

Unique_M75_hs0.15_27.8deg

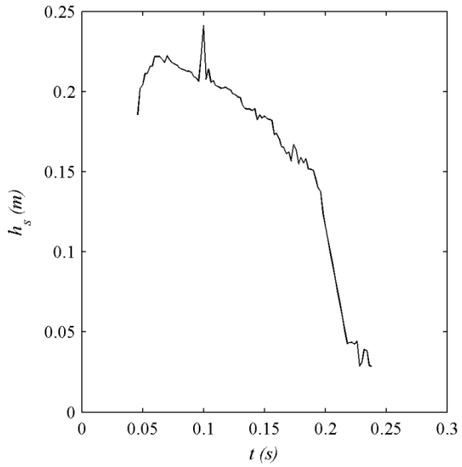

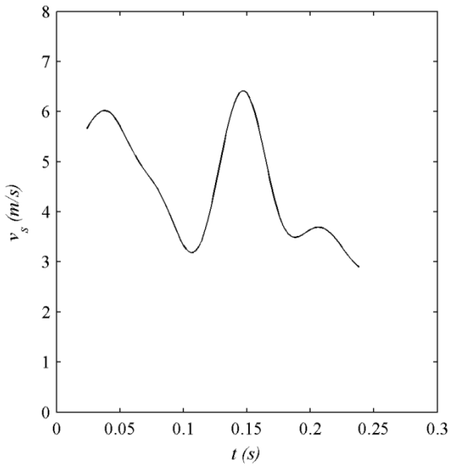

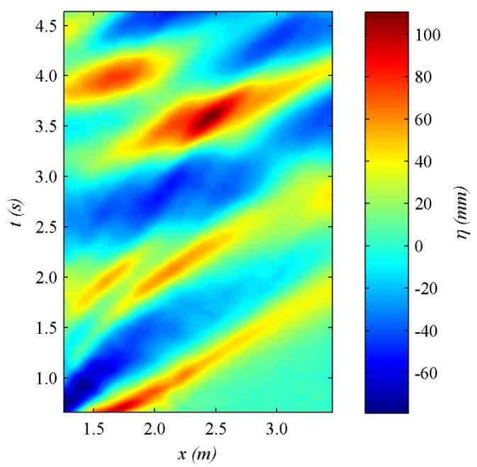

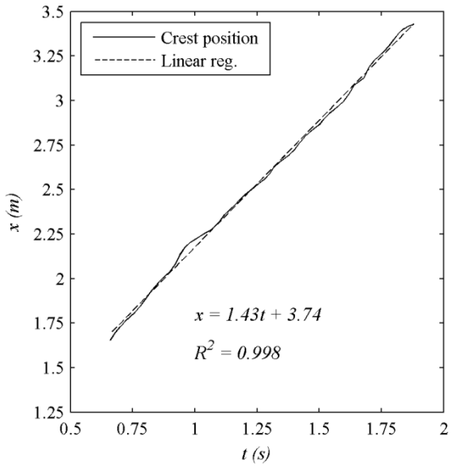

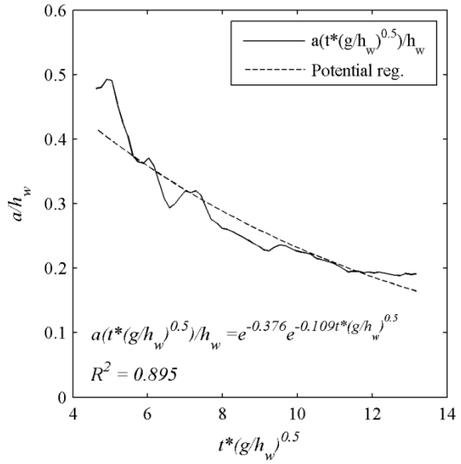

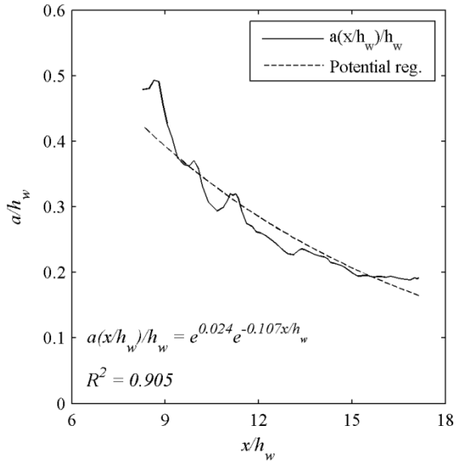

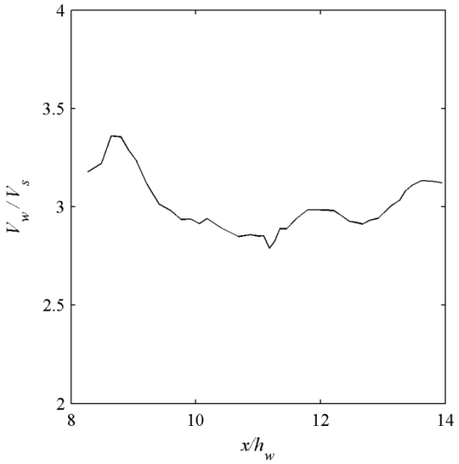

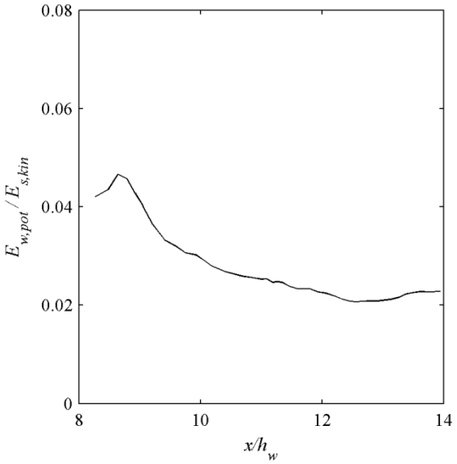

Name of Experiment	Camera HS					Cameras HD						Green Laser
	Shutter opening	Speed (f/s)	Exposition (ms)	Img. size (pixels)	Lens	Img. size	Speed (f/s)	Exposition (s)	Shutter opening	ISO	Lenses	Power (V)
Unique_M75_hs0.15_27.8deg	1.4F	500	2	800x800	Nikon50	C) HD	C) 50	C) 1/160	C) 4F	C) 400	C) Tamron 17-135	3/5

Red laser positions (m)								Landslide's parameters					Final deposit (m)			
1	1-2	2-3	3-4	4-5	5-6	6	Total	α (°)	m (kg)	$h_{s,ini}$ (m)	$l_{s,ini}$ (m)	w_s (m)	h_w (m)	a_d	b_d	D	$h_{s,fin}$
0.50	0.60	0.60	0.60	0.60	0.60	0.60	410	27.8	75	0.15	1	0.34	0.2	ND	ND	ND	ND

Observations

Calibration of HS same as *Unique_M50_hs0.15_27.8deg*. Calibration HD same as *Unique_M120_27.8deg*.

Unique_M75_hs0.20_27.8deg

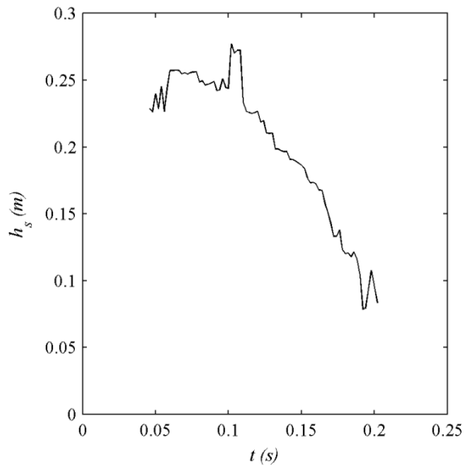

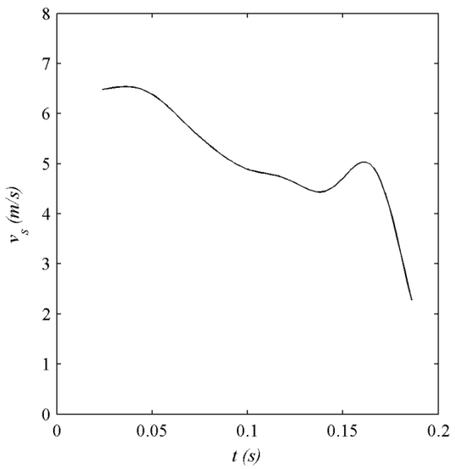

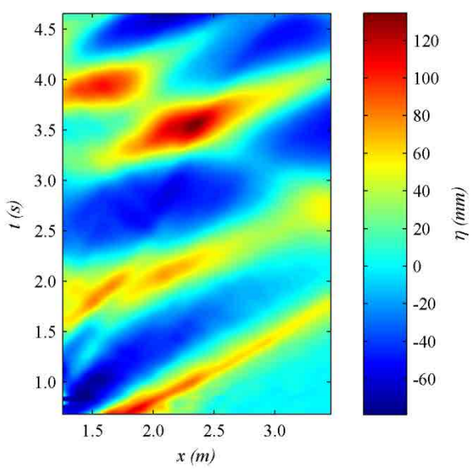

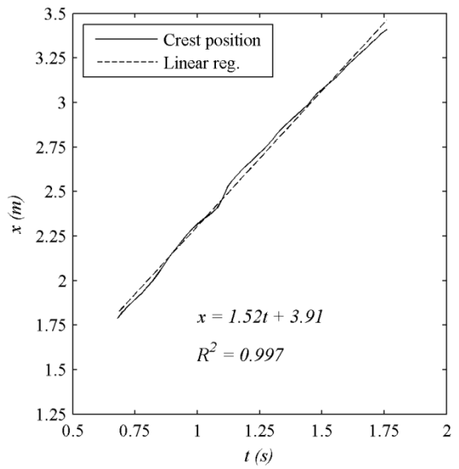

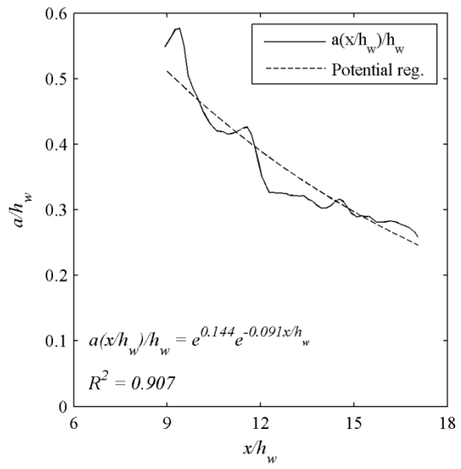

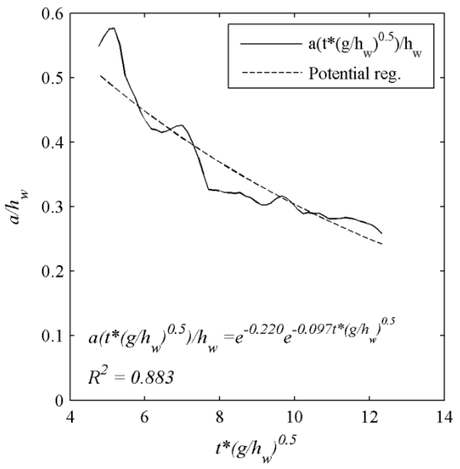

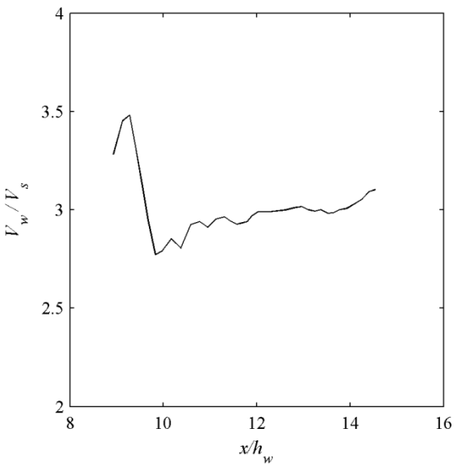

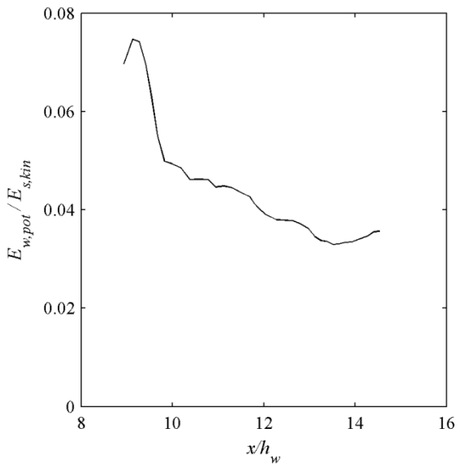

Name of Experiment	Camera HS					Cameras HD						Green Laser
	Shutter opening	Speed (f/s)	Exposition (ms)	Img. size (pixels)	Lens	Img. size	Speed (f/s)	Exposition (s)	Shutter opening	ISO	Lenses	Power (V)
Unique_M75_hs0.20_27.8deg	1.4F	500	2	800x800	Nikon50	C) HD	C) 50	C) 1/160	C) 4F	C) 400	C) Tamron 17-135	3/5

Red laser positions (m)							
1	1-2	2-3	3-4	4-5	5-6	6	Total
0.50	0.60	0.60	0.60	0.60	0.60	0.60	410

Landslide's parameters						Final deposit (m)			
α (°)	m (kg)	$h_{s,ini}$ (m)	$l_{s,ini}$ (m)	w_s (m)	h_w (m)	a_d	b_d	D	$h_{s,fin}$
27.8	75	0.20	0.75	0.34	0.2	1.50	1.25	ND	0.10

Observations

Calibration of HS same as *Unique_M50_hs0.15_27.8deg*. Calibration HD same as *Unique_M120_27.8deg*.

Unique_M75_hs0.25_27.8deg

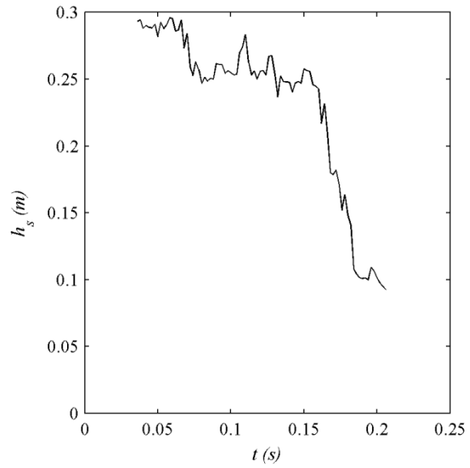

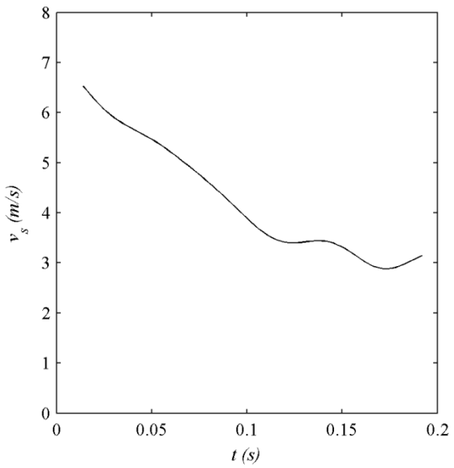

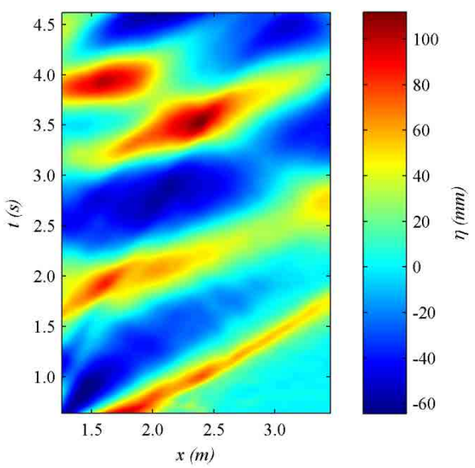

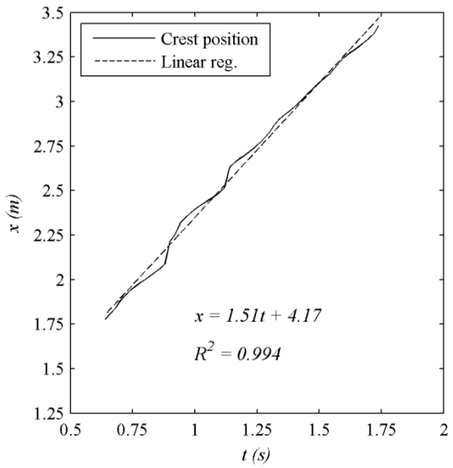

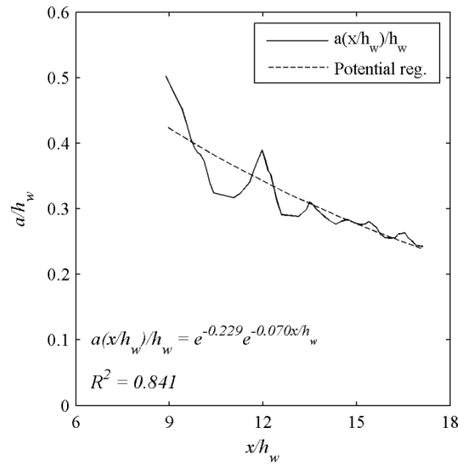

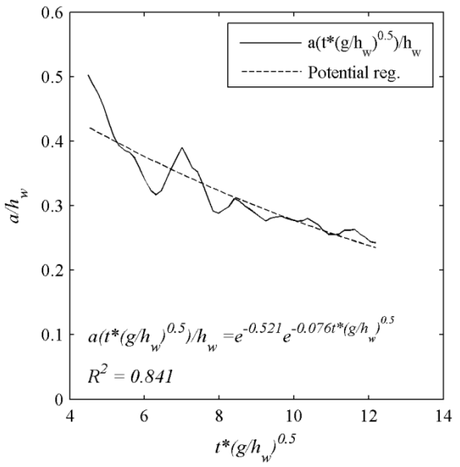

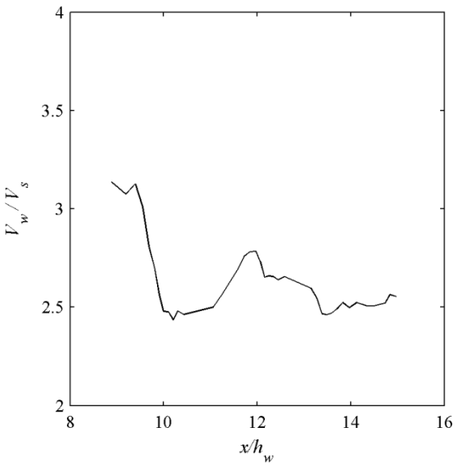

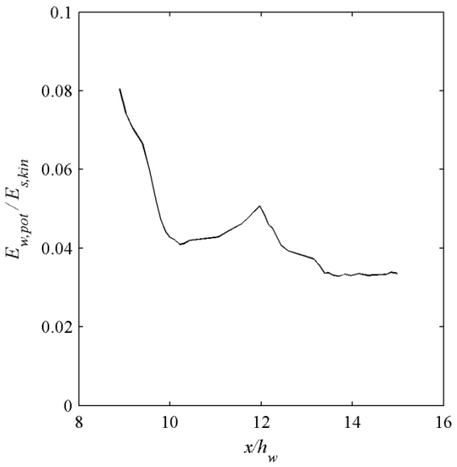

Name of Experiment	Camera HS					Cameras HD						Green Laser
	Shutter opening	Speed (f/s)	Exposition (ms)	Img. size (pixels)	Lens	Img. size	Speed (f/s)	Exposition (s)	Shutter opening	ISO	Lenses	Power (V)
Unique_M75_hs0.25_27.8deg	1.4F	500	2	800x800	Nikon50	C) HD	C) 50	C) 1/160	C) 4F	C) 400	C) Tamron 17-135	3/5

Red laser positions (m)								Landslide's parameters						Final deposit (m)			
1	1-2	2-3	3-4	4-5	5-6	6	Total	α (°)	m (kg)	$h_{s,ini}$ (m)	$l_{s,ini}$ (m)	w_s (m)	h_w (m)	a_d	b_d	D	$h_{s,fin}$
0.50	0.60	0.60	0.60	0.60	0.60	0.60	410	27.8	75	0.25	0.6	0.34	0.2	1.35	1.2	ND	0.12

Observations

Calibration of HS same as *Unique_M50_hs0.15_27.8deg*. Calibration HD same as *Unique_M120_27.8deg*.

Unique_M50_hs0.10_15.5deg

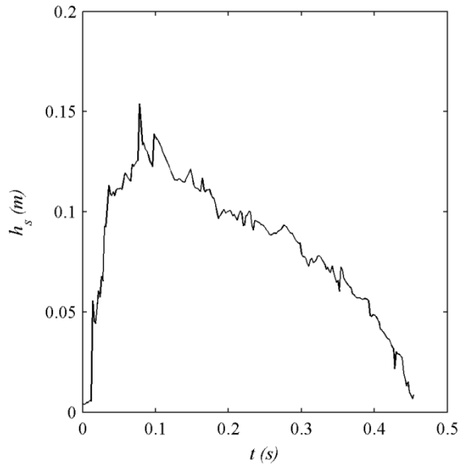

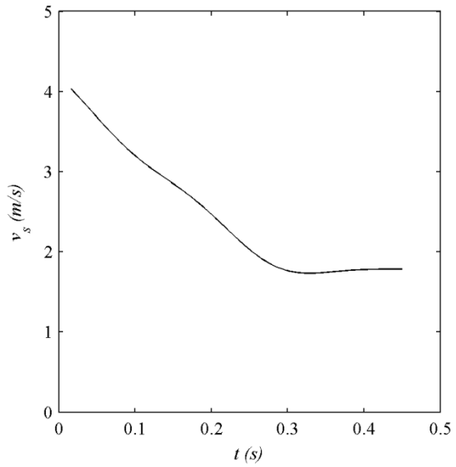

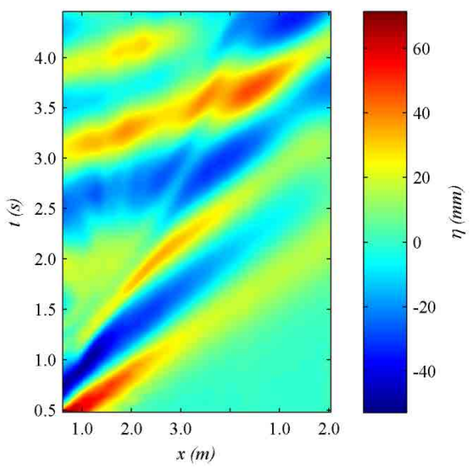

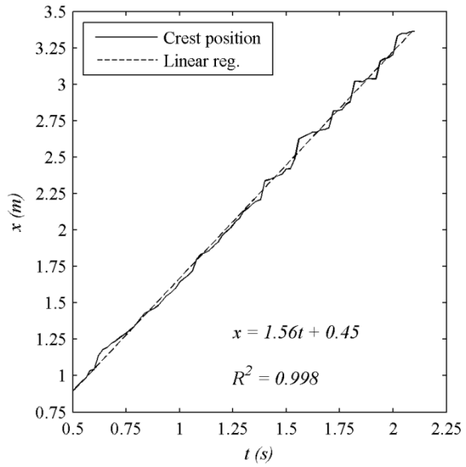

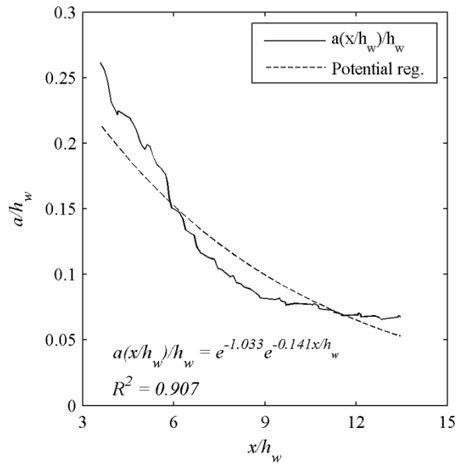

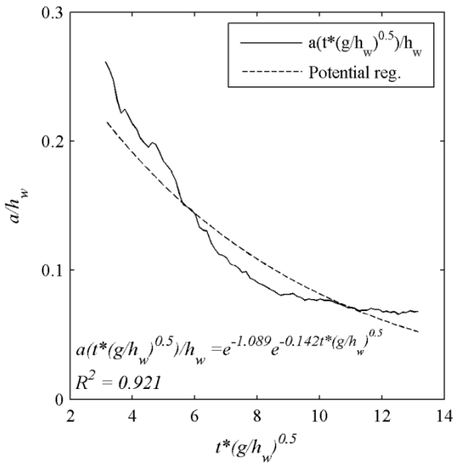

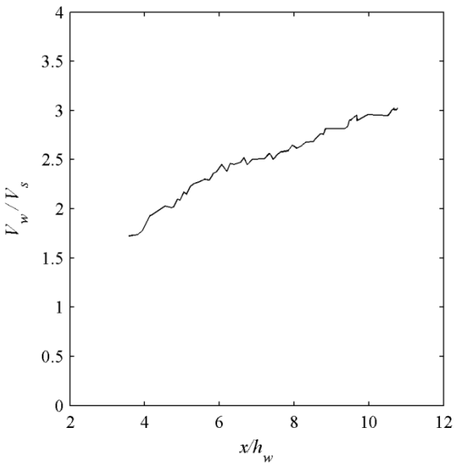

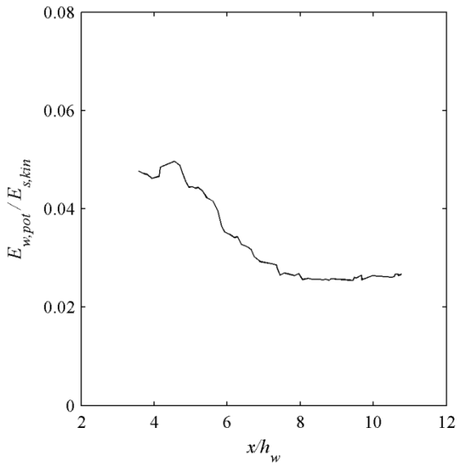

Name of Experiment	Camera HS					Cameras HD						Green Laser
	Shutter opening	Speed (f/s)	Exposition (ms)	Img. size (pixels)	Lens	Img. size	Speed (f/s)	Exposition (s)	Shutter opening	ISO	Lenses	Power (V)
Unique_M50_hs0.10_15.5deg	1.4F	500	2	800x724	Nikon50	C) HD	C) 50	C) 1/200	C) 4F	C) 400	C) Canon 18-55	4/5

Red laser positions (m)								Landslide's parameters						Final deposit (m)			
1	1-2	2-3	3-4	4-5	5-6	6	Total	α (°)	m (kg)	$h_{s,ini}$ (m)	$l_{s,ini}$ (m)	w_s (m)	h_w (m)	a_d	b_d	D	$h_{s,fin}$
0.50	0.60	0.60	0.60	0.60	0.60	0.60	410	15.5	50	0.10	1	0.34	0.25	1.25	0.98	ND	0.12

Observations

Calibration *ad-hoc*

Unique_M50_hs0.20_15.5deg

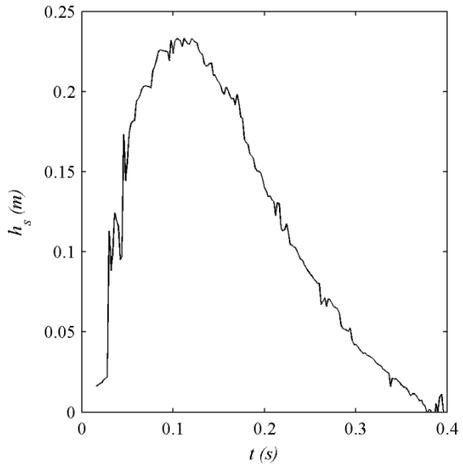

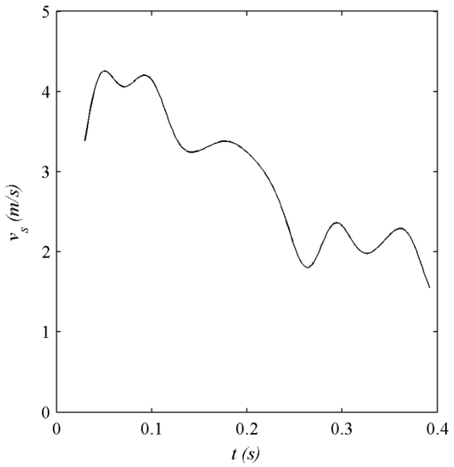

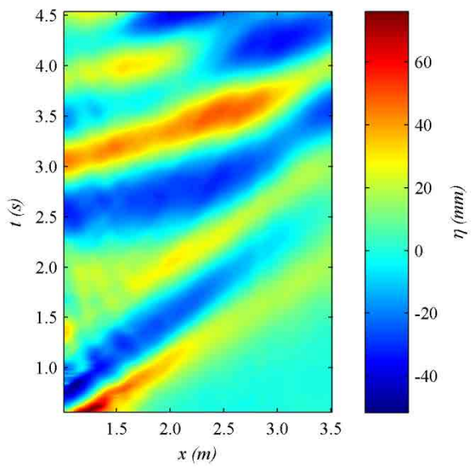

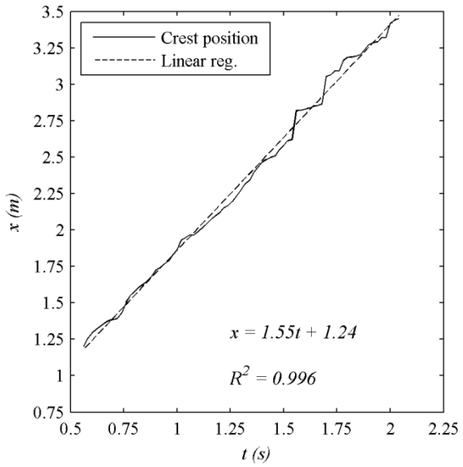

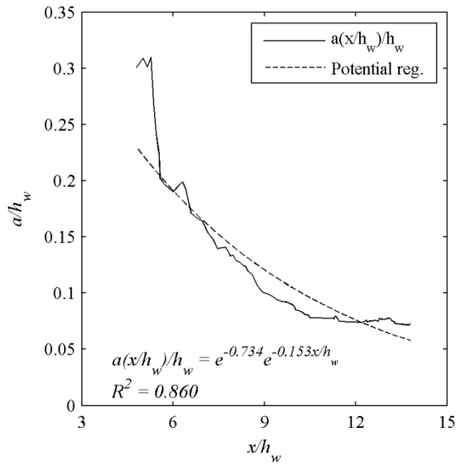

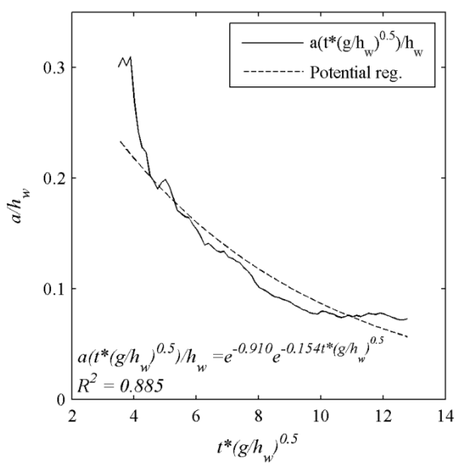

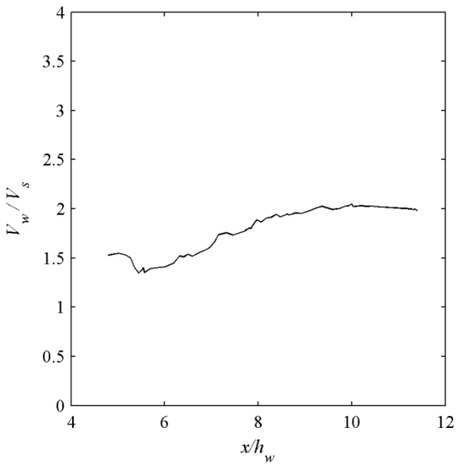

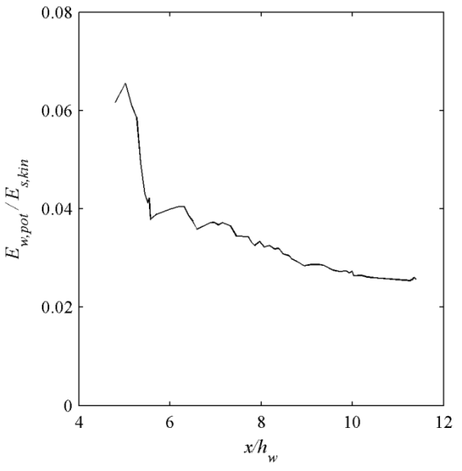

Name of Experiment	**Camera HS**					**Cameras HD**						**Green Laser**
Unique_M50_hs0.20_15.5deg	**Shutter opening**	**Speed (f/s)**	**Exposition (ms)**	**Img. size (pixels)**	**Lens**	**Img. size**	**Speed (f/s)**	**Exposition (s)**	**Shutter opening**	**ISO**	**Lenses**	**Power (V)**
	1.4F	500	2	800x724	Nikon50	C) HD	C) 50	C) 1/200	C) 4F	C) 400	C) Canon 18-55	4/5

Red laser positions (m)								**Landslide's parameters**						**Final deposit (m)**			
1	**1-2**	**2-3**	**3-4**	**4-5**	**5-6**	**6**	**Total**	***α*** **(°)**	***m*** **(kg)**	$h_{s,ini}$ **(m)**	$l_{s,ini}$ **(m)**	w_s **(m)**	h_w **(m)**	a_d	b_d	***D***	$h_{s,fin}$
0.50	0.60	0.60	0.60	0.60	0.60	0.60	410	15.5	50	0.20	0.5	0.34	0.25	1.25	0.98	ND	0.14

Observations

Calibration same of *Unique_M50_hs0.10_15.5deg*

Unique_M75_hs0.15_15.5deg

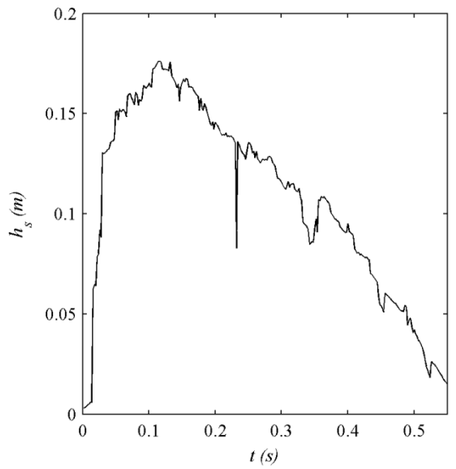

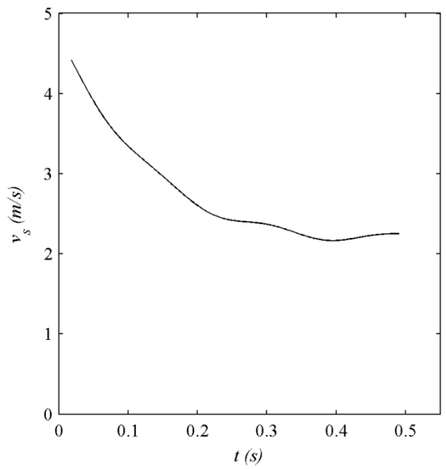

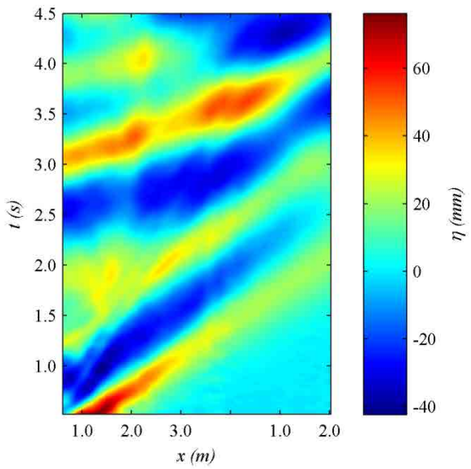

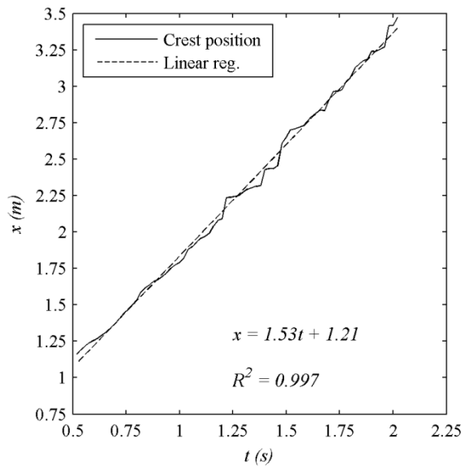

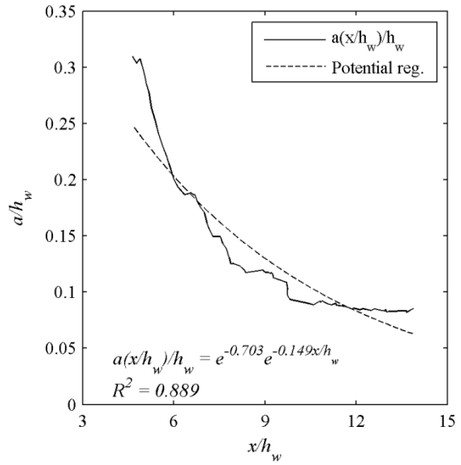

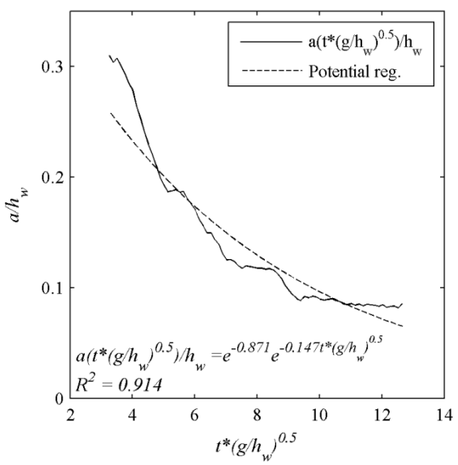

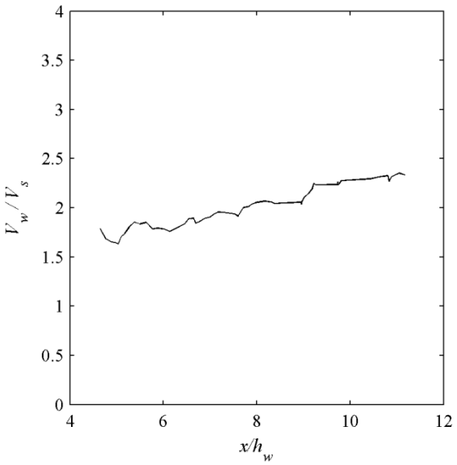

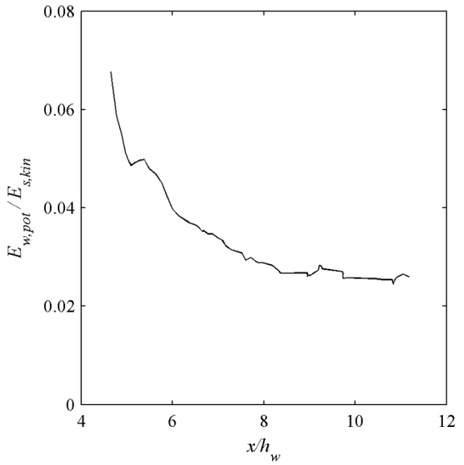

Name of Experiment	Camera HS					Cameras HD						Green Laser
Unique_M75_hs0.15_15.5deg	Shutter opening	Speed (f/s)	Exposition (ms)	Img. size (pixels)	Lens	Img. size	Speed (f/s)	Exposition (s)	Shutter opening	ISO	Lenses	Power (V)
	1.4F	500	2	800x800	Nikon50	C) HD	C) 50	C) 1/160	C) 4F	C) 400	C) Canon 18-55	4/5

Red laser positions (m)								Landslide's parameters						Final deposit (m)			
1	1-2	2-3	3-4	4-5	5-6	6	Total	α (°)	m (kg)	$h_{s,ini}$ (m)	$l_{s,ini}$ (m)	w_s (m)	h_w (m)	a_d	b_d	D	$h_{s,fin}$
0.50	0.60	0.60	0.60	0.60	0.60	0.60	410	15.5	75	0.15	0.6	0.34	0.25	1.4	0.95	ND	0.10

Observations

Calibration same *ad-hoc*

Unique_M100_hs0.20_15.5deg

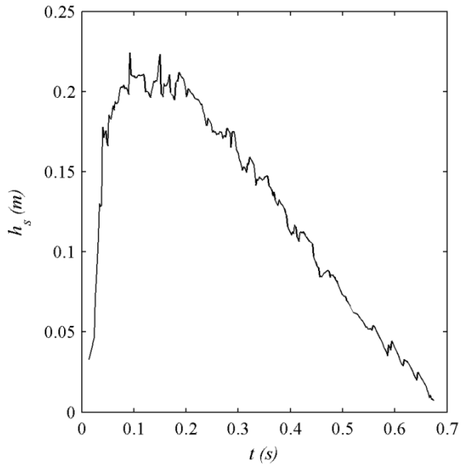

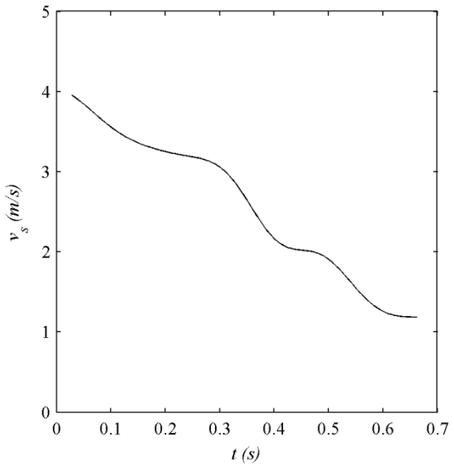

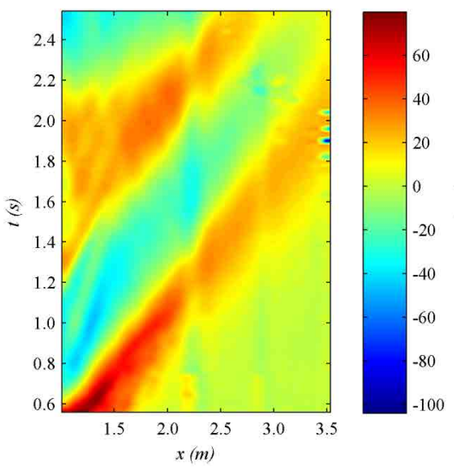

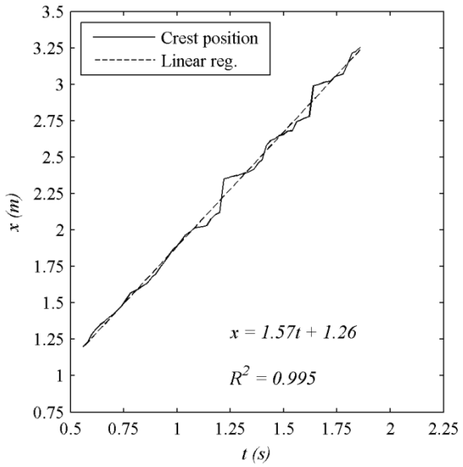

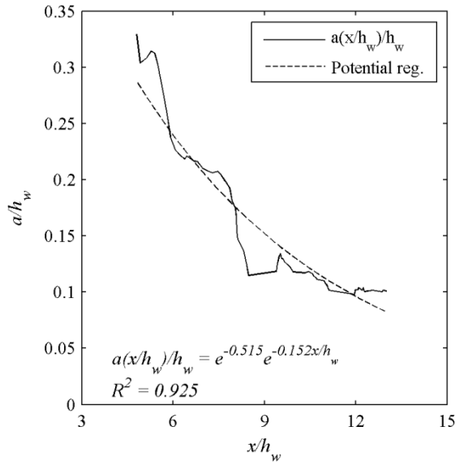

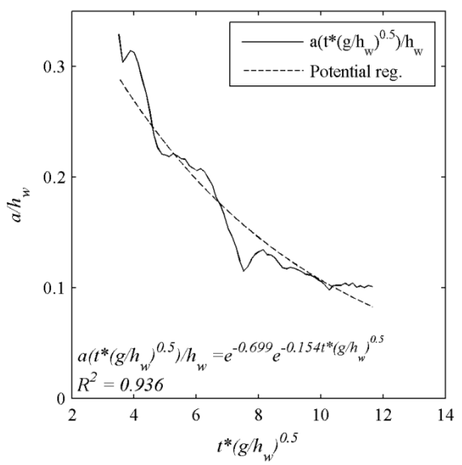

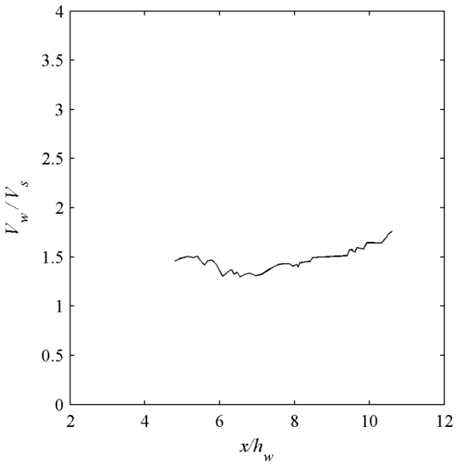

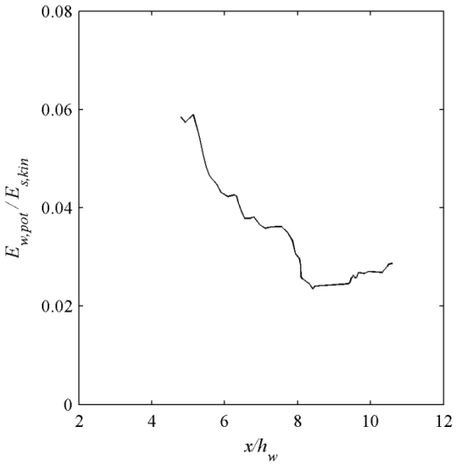

Name of Experiment	Camera HS					Cameras HD						Green Laser
Unique_M100_hs0.20_15.5deg	Shutter opening	Speed (f/s)	Exposition (ms)	Img. size (pixels)	Lens	Img. size	Speed (f/s)	Exposition (s)	Shutter opening	ISO	Lenses	Power (V)
	1.4F	500	2	800x800	Nikon50	C) HD	C) 50	C) 1/200	C) 4F	C) 400	C) Canon 18-55	4/5

Red laser positions (m)								Landslide's parameters						Final deposit (m)			
1	1-2	2-3	3-4	4-5	5-6	6	Total	α (°)	m (kg)	$h_{s,ini}$ (m)	$l_{s,ini}$ (m)	w_s (m)	h_w (m)	a_d	b_d	D	$h_{s,fin}$
0.50	0.60	0.60	0.60	0.60	0.60	0.60	410	15.5	100	0.20	0.6	0.34	0.25	1.55	1.10	ND	0.10

Observations

Calibration same *ad-hoc*. An amount of material remained inside the box.

Unique_M100bis_hs0.20_15.5deg

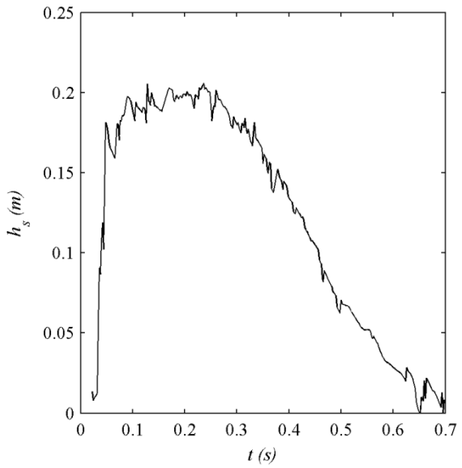

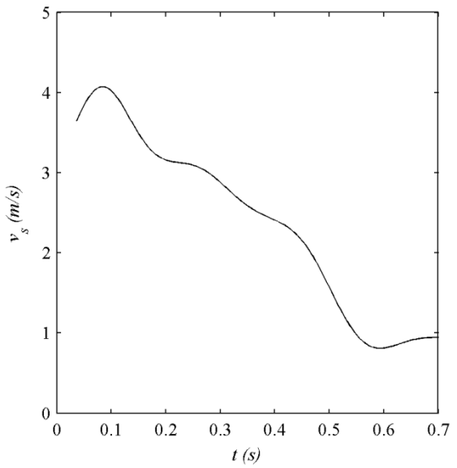

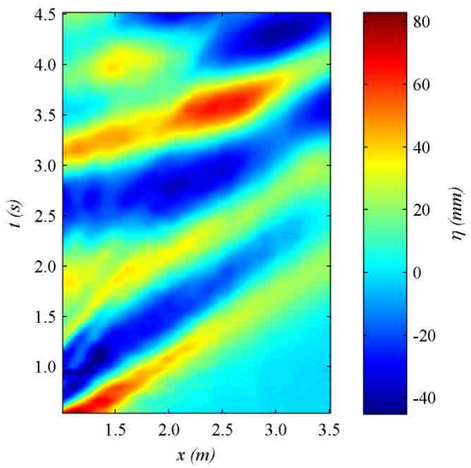

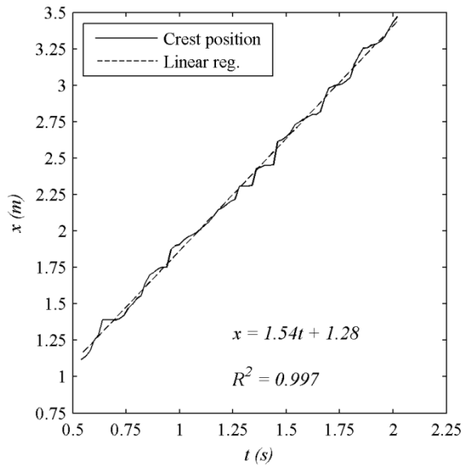

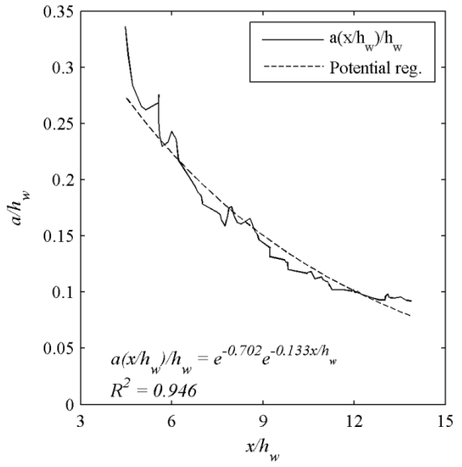

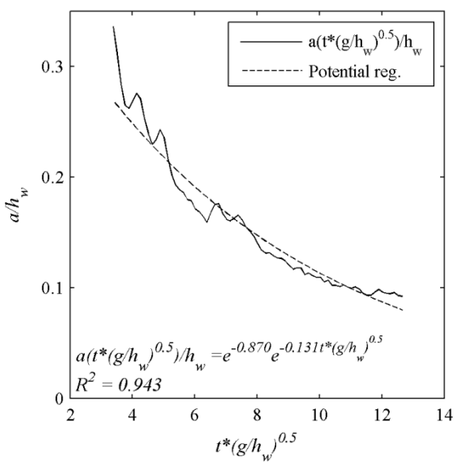

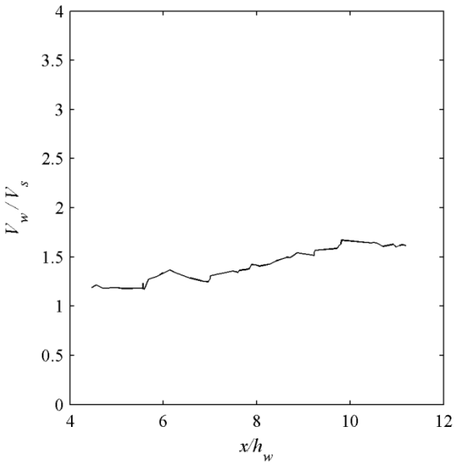

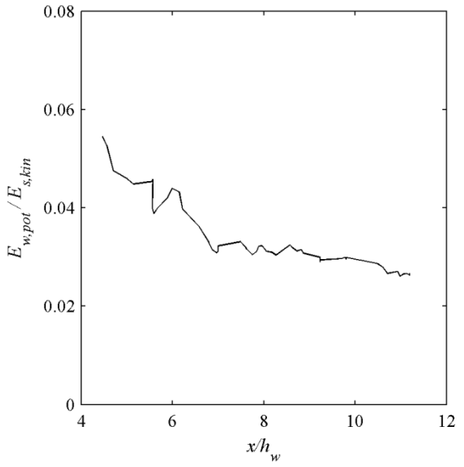

Name of Experiment	Camera HS					Cameras HD						Green Laser
	Shutter opening	Speed (f/s)	Exposition (ms)	Img. size (pixels)	Lens	Img. size	Speed (f/s)	Exposition (s)	Shutter opening	ISO	Lenses	Power (V)
Unique_M100bis_hs0.20_15.5deg	1.4F	500	2	800x800	Nikon50	C) HD	C) 50	C) 1/200	C) 4F	C) 400	C) Canon 18-55	4/5

Red laser positions (m)								Landslide's parameters						Final deposit (m)			
1	1-2	2-3	3-4	4-5	5-6	6	Total	α (°)	m (kg)	$h_{s,ini}$ (m)	$l_{s,ini}$ (m)	w_s (m)	h_w (m)	a_d	b_d	D	$h_{s,fin}$
0.50	0.60	0.60	0.60	0.60	0.60	0.60	410	15.5	100	0.20	0.6	0.34	0.25	1.50	1.10	ND	0.10

Observations

Calibration same *ad-hoc.* An amount of material remained inside the box.

Unique_M125_hs0.20_15.5deg

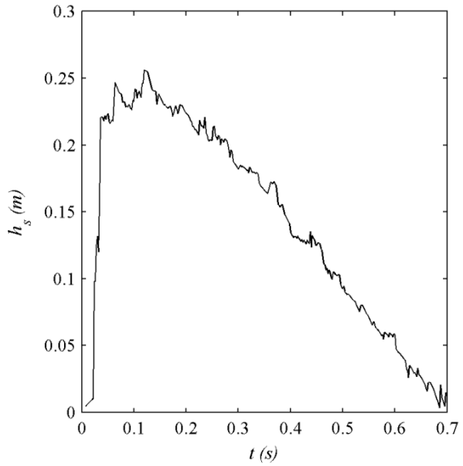

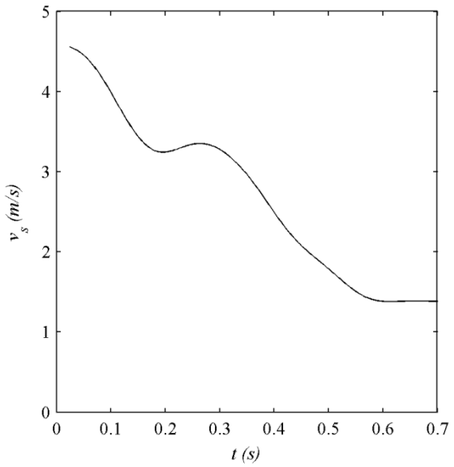

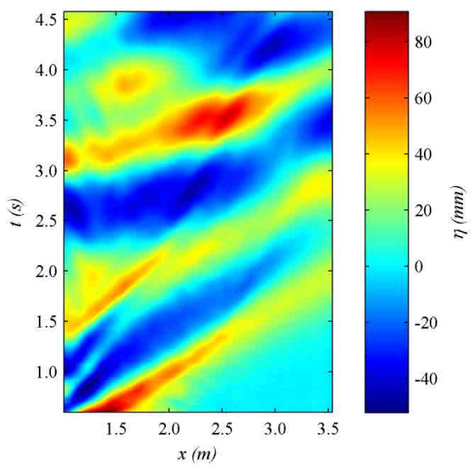

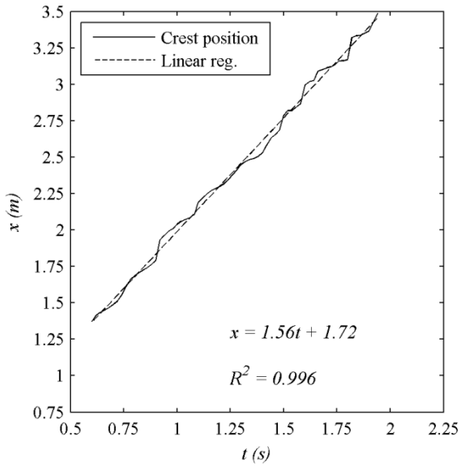

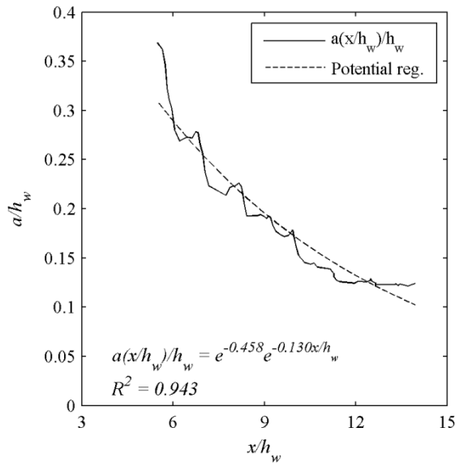

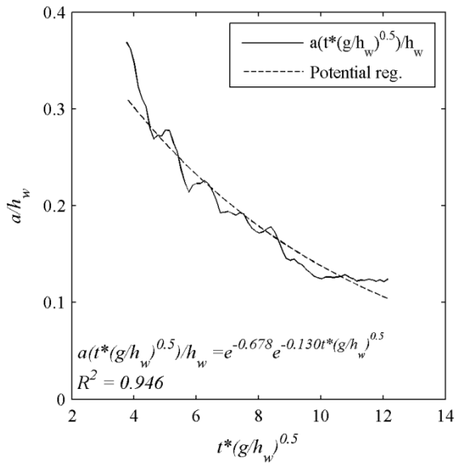

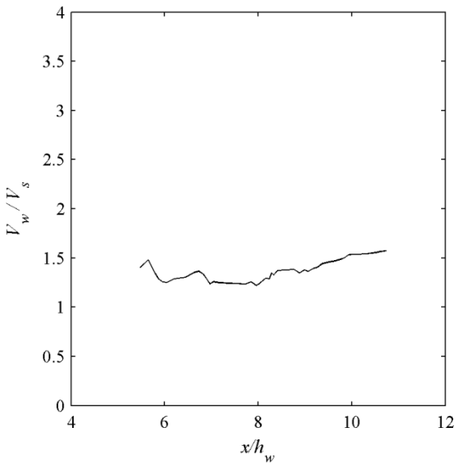

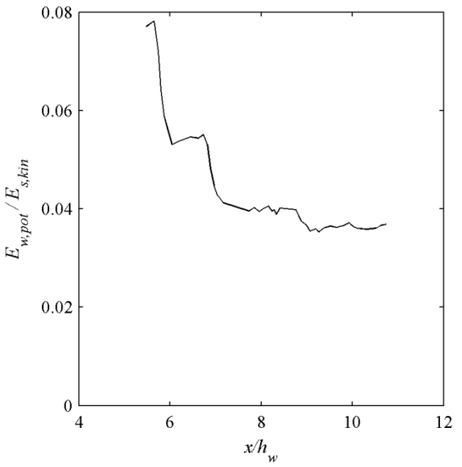

Name of Experiment	**Camera HS**					**Cameras HD**						**Green Laser**
Unique_M125_hs0.20_15.5deg	**Shutter opening**	**Speed (f/s)**	**Exposition (ms)**	**Img. size (pixels)**	**Lens**	**Img. size**	**Speed (f/s)**	**Exposition (s)**	**Shutter opening**	**ISO**	**Lenses**	**Power (V)**
	1.4F	500	2	800x800	Nikon50	C) HD	C) 50	C) 1/200	C) 4F	C) 400	C) Canon 18-55	4/5

Red laser positions (m)								**Landslide's parameters**						**Final deposit (m)**			
1	**1-2**	**2-3**	**3-4**	**4-5**	**5-6**	**6**	**Total**	***α*** **(°)**	***m*** **(kg)**	$h_{s,ini}$ **(m)**	$l_{s,ini}$ **(m)**	w_s **(m)**	h_w **(m)**	a_d	b_d	***D***	$h_{s,fin}$
0.50	0.60	0.60	0.60	0.60	0.60	0.60	410	15.5	125	0.20	0.6	0.34	0.25	1.68	1.15	2.30	0.12

Observations

Calibration same *ad-hoc*. An amount of material remained inside the box.

Unique_M143_hs0.25_15.5deg

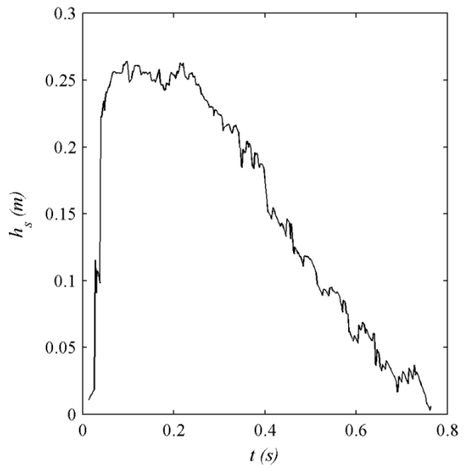

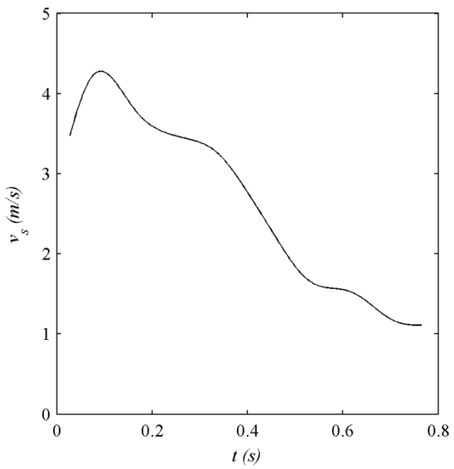

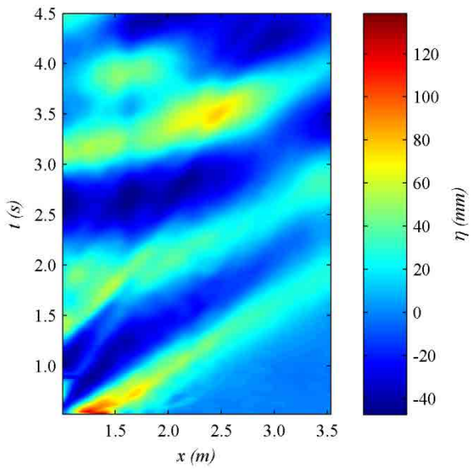

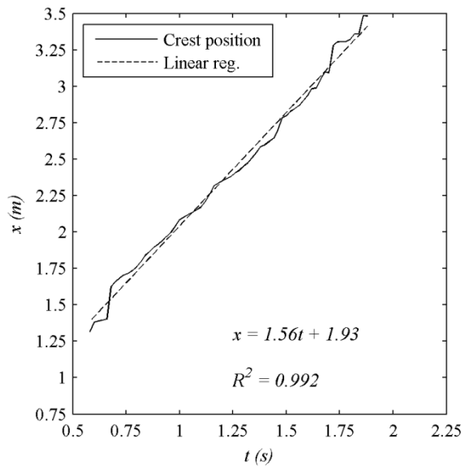

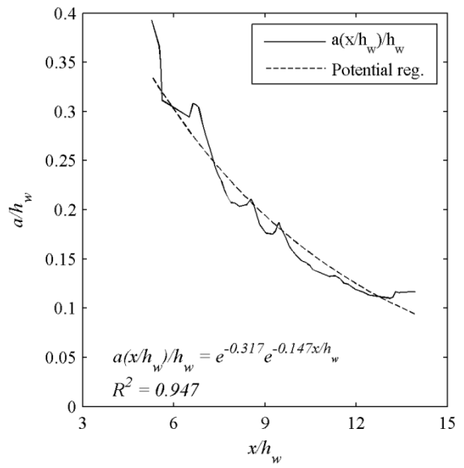

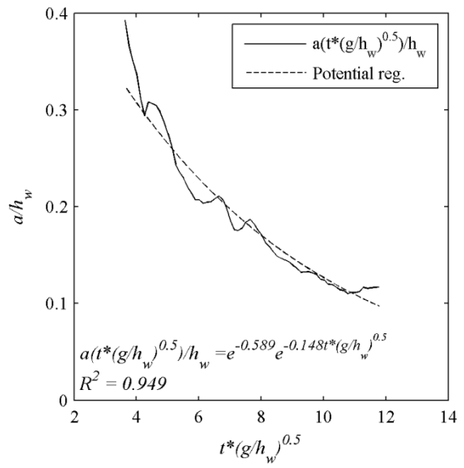

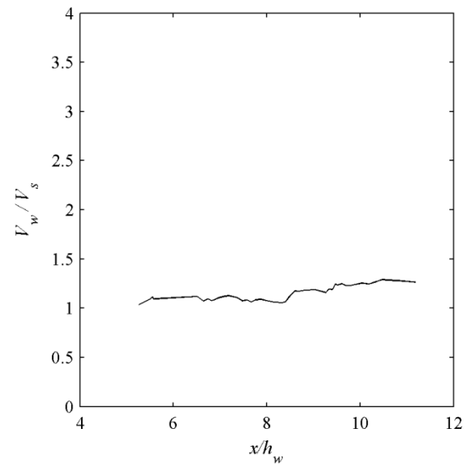

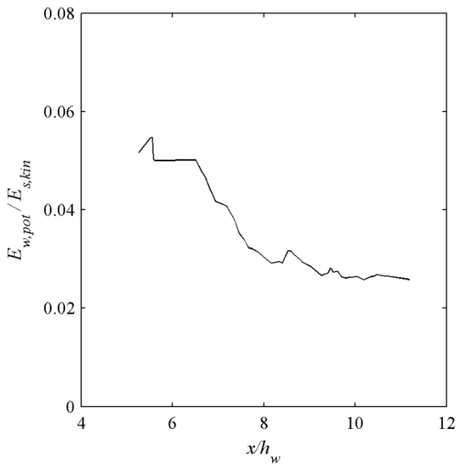

Name of Experiment	Camera HS					Cameras HD						Green Laser
	Shutter opening	Speed (f/s)	Exposition (ms)	Img. size (pixels)	Lens	Img. size	Speed (f/s)	Exposition (s)	Shutter opening	ISO	Lenses	Power (V)
Unique_M143_hs0.25_15.5deg	1.4F	500	2	800x800	Nikon50	C) HD	C) 50	C) 1/200	C) 4F	C) 400	C) Canon 18-55	4/5

Red laser positions (m)								Landslide's parameters						Final deposit (m)			
1	1-2	2-3	3-4	4-5	5-6	6	Total	α (°)	m (kg)	$h_{s,ini}$ (m)	$l_{s,ini}$ (m)	w_s (m)	h_w (m)	a_d	b_d	D	$h_{s,fin}$
0.50	0.60	0.60	0.60	0.60	0.60	0.60	410	15.5	143	0.25	0.6	0.34	0.25	1.70	1.20	2.40	0.12

Observations

Calibration same *ad-hoc.* An amount of material remained inside the box.

Unique_M120_27.8deg_no_wedge

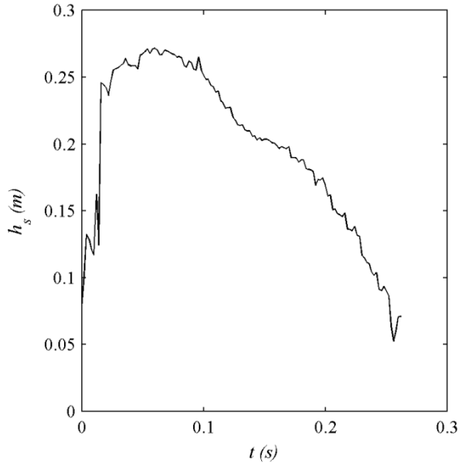

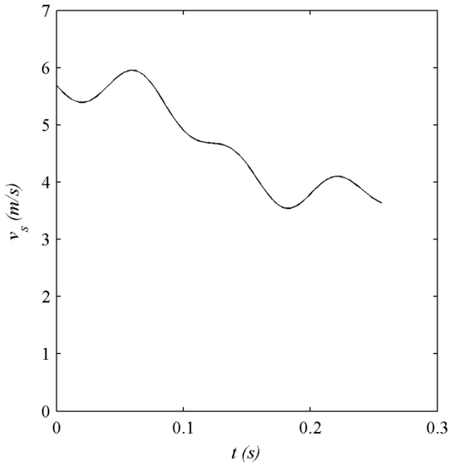

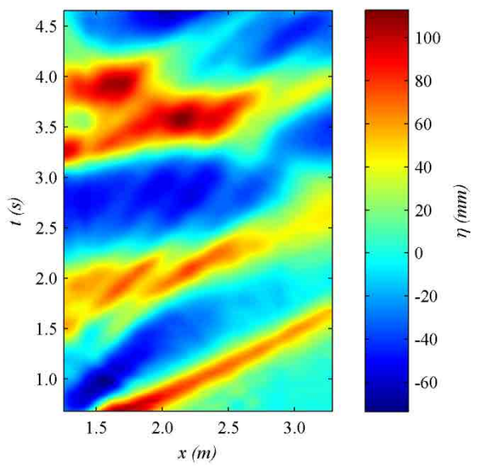

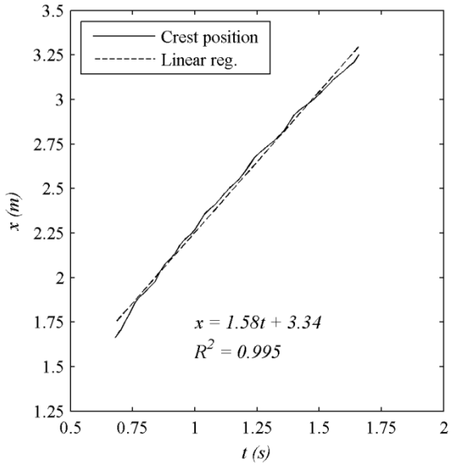

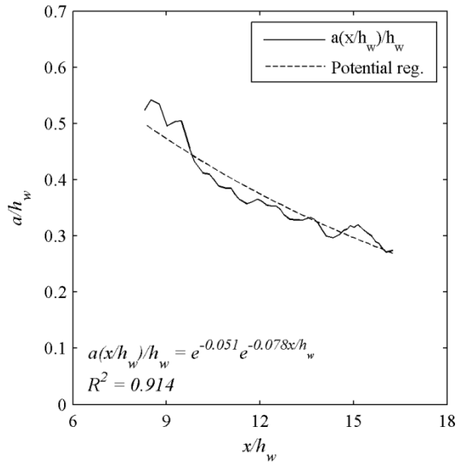

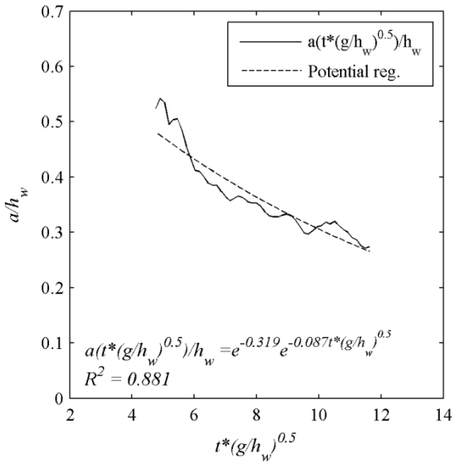

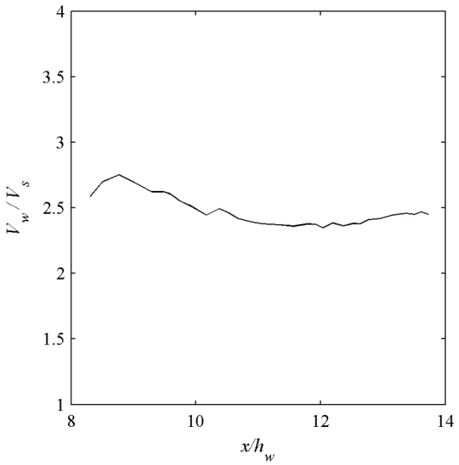

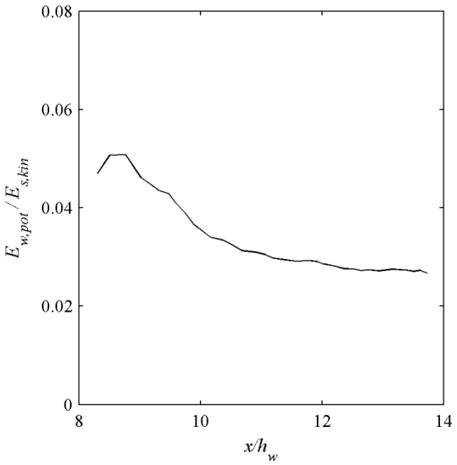

Name of Experiment	Camera HS					Cameras HD						Green Laser
Unique_M120_27.8deg_no_wedge	Shutter opening	Speed (f/s)	Exposition (ms)	Img. size (pixels)	Lens	Img. size	Speed (f/s)	Exposition (s)	Shutter opening	ISO	Lenses	Power (V)
	1.4F	500	2	800x800	Nikon50	C) HD	C) 50	C) 1/200	C) 4F	C) 400	C) Canon 18-55	4/5

Red laser positions (m)								Landslide's parameters						Final deposit (m)			
1	1-2	2-3	3-4	4-5	5-6	6	Total	α (°)	m (kg)	$h_{s,ini}$ (m)	$l_{s,ini}$ (m)	w_s (m)	h_w (m)	a_d	b_d	D	$h_{s,fin}$
0.50	0.60	0.60	0.60	0.60	0.60	0.60	410	27.8	120	0.20	0.6	0.34	0.20	1.85	1.45	2.70	0.13

Observations

Calibration *ad-hoc* for HS and HD. Without wedge.